

**COMPUTATIONAL INVESTIGATION OF THE EFFECT OF NOSE  
MOUNTED DEVICES ON THE AEROTHERMODYNAMICS OF A  
MISSILE SHAPED BODY FLYING AT HYPERSONIC SPEEDS**

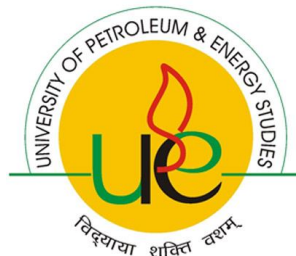
By

**Rajesh Yadav**

**(P500011012)**

**COLLEGE OF ENGINEERING**

*Submitted*



**IN PARTIAL FULFILMENT OF THE REQUIREMENT OF THE DEGREE OF  
DOCTOR OF PHILOSOPHY**

TO

**UNIVERSITY OF PETROLEUM AND ENERGY STUDIES**

**DEHRADUN**

**April, 2013**

## **ABSTRACT**

All hypersonic vehicles are subjected to severe aerodynamic heating even during flights through thin atmosphere. The interests of military establishments to develop kinetic energy missiles and human urge for a hypersonic commercial transport vehicle would require the vehicle to travel at hypersonic speeds through dense atmosphere. Under dense atmospheric conditions, the aerothermal conditions can bring about deformation of the configuration through ablation and fusion altering the aerodynamics and in turn flight dynamics of the vehicle. Such vehicles would also require to have a low drag in order to maximize range and to be economical. Various passive devices have been proposed in the literature which can reduce the aerodynamic heating of a blunt nose by modifying the flowfield structure in front of vehicle nose. One such device is a forward facing cavity mounted at the nose of such vehicles. One the drag reduction front, aerospikes mounted at the nose has been practically implemented for supersonic vehicles. For hypersonic vehicles however, the use of aerospikes cause severe reattachment heating on the main body, especially with turbulent flows. Effective management of thermal loads and drag is thus the primary goal of a hypersonic vehicle designer.

In the view of above problem, numerical experiments are carried out using a commercially available Computational Fluid Dynamics code, to investigate the turbulent aerodynamic heating of a hemisphere cylinder with a forward facing ellipsoid cavity at nose in dense atmospheric conditions. A wide range cavity shapes viz. parabolic, hemispherical, conical and ellipsoid cavity have been investigated for their effectiveness in reducing the aerodynamic heating of a hemisphere cylinder. All these forward facing cavities are placed axisymmetrically at the nose of a hemisphere cylinder with base diameter of 40 mm and overall length of 70 mm. The depth of these cavities has been varied from 2 mm to 40 mm with a lip radius between 2 mm and 18 mm. have been investigated. The use aerospikes can reduce the aerodynamic drag substantially;

however, at hypersonic speeds especially under turbulent flow conditions there is a detrimental rise at the reattachment point on the main body. So, an attempt has also been made to investigate the use of a double disk aerospike with two hemispherical caps in reducing the peak reattachment heat fluxes and the total heat transfer rates of the hemisphere cylinder. The overall length of these aerospike investigated has been limited to 1, 1.25 and 1.5 times the base diameter of the cylinder.

The geometries and meshes used in computations were made in the geometric modeling and mesh generator software Gambit<sup>®</sup> and ICEMCFD<sup>®</sup> available with ANSYS<sup>®</sup>. The meshes generated for all computations mapped are quadrilaterals except inside the cavity where paved quadrilaterals are used. The mapped mesh for the base body has a total of 40,000 quadrilaterals with 200 cells along the body and 200 cells in radial direction. A stretching is applied in the radial direction such that the mesh near the wall is dense enough to resolve the viscous heating accurately. The distance of the first cell from the body is  $1e-07$  m such that the non-dimensional cell-wall distance at the body,  $y^+ \approx 1$ . With the addition of cavity or aerospike at the nose the cell count for the subsequent geometries varies from 40,000 to 60,000 depending on the depth cavities or the length of aerospike.

For all configurations the surface pressure and heat flux distribution, total heat transfer rates, area weighted average of heat fluxes and drag were observed at zero degree angle of attack through a time marching solution of the axisymmetric Navier-Stokes equations using the FLUENT<sup>®</sup> code. In FLUENT<sup>®</sup>, the time dependent, axisymmetric Navier Stokes were solved simultaneously in a coupled manner using implicit scheme wherein each equation in the coupled set of governing equations is linearized implicitly with respect to all dependent variables in the set. The resultant block system of linear equations was solved using a point implicit linear equation solver in conjunction with an algebraic multi grid method. The iterative solution was assumed to have converged when the normalized residuals of all the equations fall below  $10^{-06}$  along with the iterative convergence of total heat transfer rate to the body. The time marching was started with a CFL number of 0.001 and the CFL value of, as

high as, 4 were used at later stages. All computations are done with second order upwind spatial discretization while the inviscid fluxes are computed using modified version of the Advection Upstream Splitting Method, viz. AUSM+. This flux formulation provides very high resolution of the shock discontinuity and is free of Gibbs error.

Since the thesis aims to minimize the aerodynamic heating problem in dense atmosphere, computations for all configurations have been performed at two different freestream conditions, first Mach 6.2 flow at sea level atmospheric conditions and second Mach 10.1 flow at a standard atmosphere of 11 km. The unit Reynolds number for both these conditions are high enough to have turbulent flow. The turbulence in the flow has been model with the modified version of the Spalart–Allmaras (SA) one equation model which incorporates both the strain and vorticity based production. The main advantage of using this model is the computational efficiency and insensitiveness to wall distance. This model accurately predicts wall bounded flows with adverse pressure gradients and is quite popular for hypersonic flow applications. The numerical simulations for sea level atmosphere has been done with the assumption of air as a thermally perfect gas while for the second set of freestream conditions, air has been treated as a chemically reacting mixture of N, NO, O, O<sub>2</sub> and N<sub>2</sub> in thermal equilibrium. The air chemistry has been modelled with Park's 5 species 17 reactions chemical kinetics model with fully catalytic walls at a temperature of 300K.

The steady state results shows that except for the peak heating on the inner cavity surface near the sharp, the use of forward facing cavity reduces all other aerodynamic heating parameters favourably. The maximum lip heating at Mach 6.2 is seen for deep ellipsoid cavities wherein the local heating is up to 80% higher than the peak heating of the base while for spherical and parabolic cavity, the lip heating is not severe and reduced in some cases by up to 30-40% lower than the peak heating of base model. The peak heating on the outer surface, total heat transfer rates and the AWA heat fluxes, on the other hand are significantly reduced for all cavity configurations investigated. All these aerodynamic heating parameters were observed to decrease with increasing depth



and the lip radius of the cavity. The maximum reduction of 64% in outer surface peak heat fluxes was seen for the deepest ellipsoid cavity while the deepest hemispherical, parabolic, ellipsoid and conical cavities investigated showed reductions of 32%, 26%, 26% and 23% respectively in total convective heat transfer rates at Mach 6.2. For the same depth, the parabolic cavities produce the maximum reduction in total heat transfer rates and AWA heat flux as well while the conical cavities showed the least reductions.

The effectiveness of forward facing cavities in reducing aerodynamic heating is reduced at Mach 10.1 with the assumption of fully catalytic wall. The local heating at the sharp lip worsens at Mach 10.1, with deep ellipsoid showing peak heating of as high as 2.7 times the peak heating of base configuration. The least heating at the sharp lip is seen for wide parabolic cavity with a worst heating of only 1.5 times the base configuration peak heating. Maximum reductions of only to 44%, 19%, 14% and 17% in total heat transfer rates for hemispherical, parabolic, conical and ellipsoid cavity respectively could be achieved at Mach 10.1 with similar reductions in AWA heat fluxes.

The drag of a hemisphere cylinder at is negligibly affected by the presence of a forward facing cavity. In fact for some moderate depth cavities, the drag is reduced by 2-4% owing to the direction of the viscous traction inside the cavity. The drag of the projectile increases for lip radius of more than 12 mm and drags of as much as 50% higher than the base configuration can be seen for very wide cavities. The trend is same for both Mach numbers as Mach number independence is seen for drag coefficient.

For the double-disk aerospike configurations, besides the total heat transfer rates, AWA heat fluxes and aerodynamic drag, the peak reattachment pressure and heat fluxes are also monitored. It was found that the peak reattachment pressure on the main body is reduced to 50 % of the base body stagnation pressure by the use of double disk aerospikes with overall length to diameter ratio of 1.5. For shorter spikes with length to diameter ratio of 1, the peak reattachment pressure is only marginally smaller than the stagnation pressure of the base body. The reattachment heat flux on the main body is observed to be larger than the peak heating of the base configurations for radii of rear cap less


than 6 mm irrespective of the length of aerospike. For the double disk aerospike configuration with radius of rear cap 6 mm, the peak reattachment heat flux and the total heat transfer rates are reduced by 22% and 15 % respectively for  $l/D$  ratio of 1.5. At Mach 10.1, the effectiveness of double disk aerospike in reducing reattachment heat flux is significantly reduced with even the best aerospike configuration of  $l/D=1.5$  and radius of rear cap 6 mm providing only 11% and 9% reductions in AWA heat fluxes and peak heat fluxes respectively. For shorter aerospike configurations, the aerodynamics heating is more than for base configuration without spike.

Favourable drag reductions are observed for all aerodisk aerospike configurations with longer aerospikes providing as high as 47% and 44% reductions in drag at Mach 6.2 and 10.1 respectively. Among the double disk aerospike configurations investigated the one with  $l/D=1.5$ ,  $r_1=6$  mm,  $r_2=3.5$  mm and  $l_1/l_2=1.5$  is observed to be the optimal configuration with 9% and 44% reductions in peak heat fluxes and drag respectively at Mach 10.1 and respective reductions of 22% and 47% at Mach 6.2.

*Dedicated to*  
*My son*

## DECLARATION

I do hereby declare that this submission is my own work and that, to the best of my knowledge and belief, it contains no material previously published or written by another person nor material which has been accepted for the award of any other degree or diploma of the university or other institute of higher learning, except where due acknowledgment has been made in the text.

A handwritten signature in black ink, appearing to read 'Rajesh Yadav', with a horizontal line underneath it.

**Rajesh Yadav**

**Date:** 1<sup>st</sup> April 2013

Department of Aerospace Engineering

University of Petroleum and Energy Studies

Dehradun-248007

## **THESIS COMPLETION CERTIFICATE**

This is to certify that the thesis on “**Computational Investigation of the Effect of Nose Mounted Devices on the Aerothermodynamics of a Missile Shaped Body Flying at Hypersonic Speeds**” by **Rajesh Yadav** in Partial completion of the requirements for the award of the Degree of Doctor of Philosophy is an original work carried out by him under my supervision and guidance.

It is certified that the work has not been submitted anywhere else for the award of any other diploma or degree of this or any other University.

A handwritten signature in black ink, appearing to be 'Ugur Guven', written over a horizontal line.

**Dr. Ugur Guven**

**Professor**

**Aerospace Engineering**

## ACKNOWLEDGEMENTS

With deepest gratitude, I would like to thank my Ph. D. supervisor **Professor Ugur Guven**, Department of Aerospace Engineering, University of Petroleum and Energy Studies, for his continuous motivation, encouragement, technical support and advice during this work. I sincerely acknowledge the strenuous efforts put by him at different stage of my thesis. I would like to thank him also for providing me the freedom to express my ideas and to experiment.

I would like to sincerely thank the Vice Chancellor of the University, **Dr. Parag Diwan**, to have encouraged me to join the doctoral programme. I would also like to thank him for financially supporting my research by availing me the Dell Workstations, CFD servers and the CFD Research licences of ANSYS FLUENT.

I would like to sincerely thank the Chancellor of the University, **Dr. S. J. Chopra**, to have introduced Prof. U. Guven as my Ph. D. mentor and to have shown continuous concern about my research and my comfort at the University.

I would also like to thank **Dr. Srihari**, Campus Director, COE, to have presided the Faculty Research Committee during my research reviews and to have provided valuable suggestions.

I am also thankful to my friend **Mr. Gurunadh Velidi**, to have provided me the logistic and moral support.

Finally, I acknowledge the efforts and sacrifices made by my wife and son to help me complete my work in time. Above all, I would like to thank the Almighty God to have helped me to overcome troubles in my life.

## TABLE OF CONTENTS

Abstract .....	i
Declaration .....	vii
Thesis Completion Certificate .....	viii
Acknowledgements .....	ix
Table of Contents .....	x
List of Figures.....	xvii
List of Tables .....	xxiii
1 INTRODUCTION .....	1
1.1 Overview.....	1
1.2 Recapitulation of the history .....	2
1.3 The Characteristics of Hypersonic Flow.....	6
1.4 Theoretical Predictions of Aerodynamic Heating.....	10
1.5 Heat and Drag Reduction Mechanisms.....	13
1.6 The Physics of Hypersonic forward facing Cavity.....	17
1.7 The Effect of Aerospike and Aerodisk.....	20
1.8 Motivation and objectives of current research .....	22
1.9 Structure of the Thesis .....	24
2 Literature Review.....	26
2.1 The Aerodynamic Heating Problem .....	26
2.2 The Effect of Forward Facing Cavity .....	30
2.3 The effect of aerospike and aerodisk .....	36
2.4 Conclusion of the Literature Review .....	51
3 The Governing Equations.....	53
3.1 The Continuity Equation.....	53
3.2 The Momentum Equations .....	54
3.3 The Energy Equation .....	56
3.4 The Equation of State .....	58
3.5 The Energy Equation for High Temperature Gas .....	60
3.6 Thermodynamic Properties of a Chemically Reacting Mixture .....	61
3.7 Transport Properties of a Chemically Reacting Mixture.....	62
3.8 The Chemical Non-Equilibrium.....	64

3.9	Turbulent Flows.....	67
3.9.1	Equations for Turbulence.....	68
3.9.2	Turbulence Modelling.....	69
3.9.3	Spalart-Allmaras Turbulence Model.....	72
3.9.4	Shear Stress Transport (SST) $k$ - $\omega$ Turbulence Model.....	74
3.10	Governing Equations in Vector Form.....	78
3.11	Summary of the Governing Equations.....	80
4	The Numerical Setup.....	82
4.1	Geometry and Grid Generation.....	83
4.1.1	Geometries Investigated.....	83
4.1.2	Grid Generation.....	87
4.2	The FLUENT Code.....	88
4.2.1	Descritization of transport equations.....	90
4.2.2	The Algebraic Multigrid Method.....	92
4.2.3	The AMG Restriction and Prolongation Operators.....	94
4.2.4	The F Cycle.....	95
4.2.5	The Flexible Cycle.....	95
4.2.6	The Gauss –Seidel Smoother.....	97
4.2.7	Incomplete Lower-Upper (ILU) Factorization.....	98
4.2.8	Full Multigrid Initialization.....	99
4.3	Spatial Descritization.....	100
4.3.1	Gradient Formulation.....	101
4.3.2	Gradient Limiters.....	101
4.4	Temporal Descritization.....	102
4.4.1	The Implicit Formulation for Steady State Computations.....	102
4.4.2	Implicit Formulation for Transient Simulations.....	104
4.4.3	Explicit Formulation.....	105
4.5	Evaluation of Convective Fluxes.....	105
4.6	Aero-chemistry Model.....	108
4.7	Boundary Conditions.....	109
4.8	Solver Validation and Verification.....	110
4.8.1	Flow over a Hemisphere-Cylinder.....	111
4.8.2	Flow over a Hemisphere Cylinder with a Cylindrical Cavity.....	112
4.8.3	A Large Angle Blunt Cone with Forward Facing Cavity.....	113
4.9	Grid Independence Study.....	114
5	Results and Discussion for flow at Mach 6.2.....	116



5.1	The Effect of Ellipsoid Cavity.....	116
5.1.1	Flowfield Around Hemisphere Cylinder with Ellipsoid Cavity .....	116
5.1.2	Effect of Ellipsoid Cavity on Surface Pressure Distribution.....	121
5.1.3	Effect of Ellipsoid Cavity on Heat Transfer Rates.....	123
5.1.4	The Effect of Flow Unsteadiness.....	129
5.2	The Effect of Parabolic Cavity .....	132
5.2.1	Flowfield Around Hemisphere Cylinder with Parabolic Cavity.....	132
5.2.2	Effect of Parabolic Cavity on Surface Pressure Distribution .....	134
5.2.3	The Effect of Parabolic Cavity on Surface Heat Transfer Rates .....	136
5.2.4	The Effect of Flow Unsteadiness.....	142
5.3	The Effect of Conical Cavity.....	143
5.3.1	Flowfield Around Hemisphere Cylinder with Conical Cavity .....	143
5.3.2	Effect of Conical Cavity on Surface Pressure Distribution.....	147
5.3.3	Effect of Conical Cavity on Surface Heat Flux Distribution.....	151
5.3.4	Effect of Conical Cavity on Total Heat Transfer Rates .....	156
5.3.5	Effect of Flow Unsteadiness.....	158
5.4	The Effect of Hemispherical Cavity .....	162
5.4.1	Flowfield Around Hemisphere Cylinder with Hemispherical Cavity.....	162
5.4.2	Effect of Hemispherical Cavity on Surface Pressure Distribution .....	165
5.4.3	Effect of Hemispherical Cavity on Surface Heat Transfer Rates .....	168
5.4.4	Effect of Flow Unsteadiness.....	172
5.5	The Effect of Double Disk Aerospike.....	173
5.5.1	The flowfield Around a Double Disk Aerospike .....	173
5.5.2	Effect of Double Disk Aerospike on Surface Pressure Distribution .....	176
5.5.3	Effect of Double Disk Aerospike on Surface Heat Fluxes.....	180
5.5.4	Comparisons with a Single Aerodisk Aerospike .....	184
6	Results and Discussion for Flow at Mach 10.1.....	188
6.1	The Effect of Parabolic Cavity .....	188
6.2	Effect of Ellipsoid Cavity in Chemically Reacting Air.....	198
6.3	Effect of Forward Facing Conical Cavities .....	208
6.4	Effect of Forward Facing Hemispherical Cavity.....	218
6.5	Effect of Double Disk Aerospike.....	226
7	Conclusion and Future Work .....	234
7.1	Conclusion .....	234
7.2	Future Work.....	238
	References .....	240

Appendix A: Axisymmetric Navier –Stokes equations.....	250
Appendix B: Publications.....	252
Manuscripts under Peer Review .....	253
Appendix C: FORTRAN Code for Computation of Laminar Heating Rates .....	254
Curriculum Vitae.....	280

## ***Nomenclature***

$\gamma$	=	<i>ratio of specific heat</i>
$\delta$	=	<i>kroncker delta function</i>
$\nabla$	=	<i>divergence, gradient</i>
$P$	=	<i>density, kg/m<sup>3</sup></i>
$\xi, \eta$	=	<i>coordinates in transformed plane</i>
$\mu$	=	<i>Molecular viscosity, kg/m-s</i>
$\theta$	=	<i>flow inclination angle, radian</i>
$\lambda$	=	<i>Characteristic wave length, m, second coefficient of viscosity, kg/m-s</i>
$k$	=	<i>turbulence kinetic energy, m<sup>2</sup>/s<sup>2</sup>,</i>
$\tau$	=	<i>shear stress, N/m<sup>2</sup>, pseudo time, s</i>
$\tau_F$	=	<i>characteristic flow time, s</i>
$\tau_C$	=	<i>characteristic chemical reaction time, s</i>
$\sigma$	=	<i>characteristic molecular diameter, m</i>
$\tilde{\nu}$	=	<i>modified turbulent viscosity, m<sup>2</sup>/s</i>
$\Omega$	=	<i>collusion Integral</i>
$\nu'_{r,i}$	=	<i>stoichiometric coefficients for reactants in r<sup>th</sup> reaction</i>
$\nu''_{r,i}$	=	<i>stoichiometric coefficients for products in r<sup>th</sup> reaction</i>
$\Omega$	=	<i>specific dissipation rate, 1/s</i>
$A_{f,r}$	=	<i>pre-exponential factor for r<sup>th</sup> reaction, m<sup>3</sup>/kg mol s</i>
$a$	=	<i>vertical distance between intersection of cavity surface and y axis from the origin, semi-major axis of elliptic cavity, base radius for conical cavity, m</i>
$b$	=	<i>semi-major axis of ellipsoid cavity, depth of cavity, m</i>
$\beta_{f,r}$	=	<i>temperature coefficient for r<sup>th</sup> reaction</i>
$c_i$	=	<i>Mass fraction of species i</i>
$c_p$	=	<i>specific heat at constant pressure, J/kg-K</i>
$c_{p,i}$	=	<i>specific heat at constant pressure for individual species, J/kg-K</i>
$c_v$	=	<i>specific heat at constant volume, J/kg-K</i>
$d$	=	<i>depth of cavity measured from stagnation point of base model, m</i>
$C_p$	=	<i>pressure coefficient</i>

$\mathcal{D}_{ij}$	=	diffusion coefficient if species $i$ into $j$
$\mathcal{D}_{im}$	=	diffusion coefficient if species $i$ into mixture
$D$	=	diameter of the base body, $m$ , Drag, $N$
$Da$	=	Damkohler number
$e$	=	internal energy, $J/kg$
$E_{a,f,r}$	=	activation energy for $r^{th}$ reaction, $J/kg\ mol$
$H$	=	specific enthalpy, $J/kg$
$k$	=	Thermal conductivity, $W/m-K$
$l$	=	overall length of aerospike, $m$
$l_1$	=	length of first aerospike, $m$
$l_2$	=	length of second aerospike, $m$
$l/D$	=	ratio of total length of aerospike to the diameter of the base
$L$	=	overall length of base body, $m$
$Le$	=	Lewis Number
$M$	=	Mach number, Reacting partner in chemical reaction
$\mathcal{M}_i$	=	Molecular weight of species $i$
$P, p$	=	pressure, $N/m^2$
$Pr$	=	Prandtl number, $(\mu c_p/k)$
$q$	=	wall heat transfer rate, $W/m^2$
$q_{peak}$	=	peak heat flux, $W/m^2$
$Q$	=	Total heat transfer rate, $\int q\ dA\ W$
$Q_{awa}$	=	Area weighted average of heat flux, $\frac{1}{A} \int q\ dA\ W/m^2$
$r$	=	lip radius of the cavity, $m$
$r_1$	=	radius of first hemispherical cap in the aerospike, $m$
$r_2$	=	radius of second hemispherical cap in the aerospike, $m$
$R_0$	=	nose radius of base configuration, $m$
$R, \mathcal{R}$	=	Universal gas constant = $8134\ J/(kg.mol\ K)$
$St$	=	Stanton number, $\frac{q}{\rho_\infty V_\infty c_p (T_{aw} - T_w)}$
$T$	=	temperature, $K$
$U$	=	axial velocity, $m/s$
$U_i$	=	Diffusion velocity of $i^{th}$ species, $m/s$

$v$	=	<i>radial velocity, m/s</i>
$V$	=	<i>volume of cell</i>
$x$	=	<i>axial coordinate</i>
$X_i$	=	<i>mole fraction of <math>i</math></i>
$y$	=	<i>radial coordinate, y-coordinate</i>

### *Subscripts*

$aw$	=	<i>adiabatic wall</i>
$awa$	=	<i>area weighted average of any quantity</i>
$e$	=	<i>edge of boundary layer</i>
$I$	=	<i>of <math>i^{th}</math> species</i>
$\infty, inf$	=	<i>freestream conditions</i>
$w$	=	<i>wall</i>
$x, y, z$	=	<i>along x, y- and z-directions respectively</i>
$0$	=	<i>stagnation, base</i>
$i, j, k$	=	<i>index along x, y and direction</i>

## LIST OF FIGURES

Figure 1.1 Hypersonic Flow Characteristics .....	9
Figure 1.2 Temperature behind normal shockwave as a function of freestream velocity at a standard altitude of 52 Km [3] .....	14
Figure 1.3 Schematic diagram of a Forward facing nose cavity.....	17
Figure 1.4 Schematic diagram of the steady flow over a spiked blunt body.....	21
Figure 1.5 Schematic of the unsteady flowfield around spiked blunt body .....	22
Figure 4.1 Base Configuration.....	84
Figure 4.2 Different Geometries investigated, hemisphere cylinder with a a) hemispherical cavity, b) parabolic cavity, c) conical cavity, d) ellipsoid cavity and e) double disk aerospike.....	86
Figure 4.3 Mesh generated a) base body, b) parabolic cavity, c) hemispherical cavity, d) conical cavity, e) ellipsoid cavity and f) double aerodisk model .....	88
Figure 4.4 The density based approach.....	89
Figure 4.5 A typical unstructured control volume or cell.....	91
Figure 4.6 Multigrid Cycles .....	95
Figure 4.7 Logic of a Flexible Multigrid Cycle [89] .....	96
Figure 4.8 The Full Multigrid Initialization .....	100
Figure 4.9 Surface heat flux on the hemispherical portion.....	112
Figure 4.10 Surface Stanton Numbers for 41° sphere cone.....	113
Figure 4.11 Mesh refinement heat flux distribution.....	115
Figure 5.1 Contours of a) Static pressure, b) Mach numbers and c) Temperature for ellipsoid cavity with a/b=3, d=9 mm.....	117
Figure 5.2 Streamlines inside ellipsoid cavity a/b=3, d=9 mm .....	118
Figure 5.3 Streamlines inside ellipsoid cavity with a) a/b=0.5, d=26 mm and b) a/b=0.67, d=24 mm .....	119
Figure 5.4 Contours of a) Pressure, b) Mach number and c) temperature for ellipsoid cavity a/b=1.5, d=21 mm.....	120
Figure 5.5 Surface pressure distribution for ellipsoid cavity with a/b=3 and d= a) 6-12 mm, b) 15-21 mm and c) 24-30 mm .....	121
Figure 5.6 Surface pressure distribution for ellipsoid cavity with a/b=2 and d= a) 4- 8 mm, b) 10- 14 mm, c) 16-20 mm and d) 22-26 mm.....	122

Figure 5.7 Surface pressure distribution for ellipsoid cavity with $a/b=1.5$ and $d =$ a) 3-9 mm, b) 12-18 mm and c) 21-24 mm.....	123
Figure 5.8 Surface heat flux distribution for ellipsoid cavities with $a/b=3$ and $d=$ a) 6-12 mm, b) 15-21 mm and c) 24-30 mm.....	124
Figure 5.9 Surface heat flux distribution for ellipsoid cavity with $a/b = 2$ and $d=$ a) 4-8 mm, b)10- 14 mm, c) 16-20 mm and d) 22-26 mm.....	125
Figure 5.10 Surface heat flux distribution for ellipsoid cavity with $a/b=1.5$ and $d=$ a) 3-9 mm, b) 12-18 mm and c) 21-24 mm .....	126
Figure 5.11 Peak heat flux on outer surface for various cavity models .....	127
Figure 5.12 Total heat transfer rates for various ellipsoid cavity configurations.....	128
Figure 5.13 AWA of heat fluxes for various cavity configurations.....	129
Figure 5.14 Cavity base pressure fluctuations for ellipsoid cavity with a) $a/b=1.5$ , $d=24$ mm and b) $a/b=2$ , $d=6$ mm.....	130
Figure 5.15 Surface heat flux for ellipsoid cavity with a) $a/b=3$ , $d=24$ mm and b) $a/b=1.5$ , $d=15$ mm .....	131
Figure 5.16 a) Mach Contours and b) Temperature Contours for $r/d=2.5$ , $d=2$ mm. ....	132
Figure 5.17 a) Mach contours and b) Temperature Contours for cavity depth 10 mm, $r/d=2$ .....	132
Figure 5.18 a) Pathlines for cavity depth 4 mm, $r/d=1.5$ and b) Pathlines for cavity depth 10 mm, $r/d=1.5$ .....	133
Figure 5.19 Surface pressure distribution for parabolic cavity of $r/d=1.5$ , a) $d= 2-4$ mm, b) $d= 5-7$ mm and c) $d=8-10$ mm .....	134
Figure 5.20 Surface pressure distribution for parabolic cavity of $r/d=2$ , a) $d= 1-3$ mm, b) $d= 4-6$ mm and c) $d=7-10$ mm.....	135
Figure 5.21 Surface pressure distribution for parabolic cavity of $r/d=2.5$ , a) $d= 1-3$ mm, b) $d= 4-6$ mm and c) $d=7-10$ mm .....	136
Figure 5.22 Surface heat flux distribution for parabolic cavity with $r/d=1.5$ , a) $d=2-4$ mm, b) $d=5-7$ mm and c) $d=8-10$ mm. ....	137
Figure 5.23 Surface heat flux distribution for parabolic cavity with $r/d=2$ , a) $d=1-3$ mm, b) $d=4-6$ mm and c) $d=7-10$ mm. ....	138
Figure 5.24 Surface heat flux distribution for parabolic cavity with $r/d=2.5$ , a) $d=1-3$ mm, b) $d=4-6$ mm and c) $d=7-10$ mm. ....	139
Figure 5.25 Peak heat fluxes on the outer surface for various cavity configurations.....	140
Figure 5.26 Total heat transfer rates for various cavity models.....	141
Figure 5.27 AWA heat fluxes for various cavity models .....	141

Figure 5.28 Base pressure history for parabolic cavities with a) $r/d=1.5$ , $d=7$ mm and b) $r/d=2.5$ , $d=4$ mm .....	142
Figure 5.29 Primary vortices inside shallow conical cavities.....	143
Figure 5.30 Pathlines for Cavity $\alpha=45^\circ$ , $d=20$ mm .....	144
Figure 5.31 Pathlines for cavity with $\alpha=18.45^\circ$ , $d=18$ mm .....	144
Figure 5.32 Vortices inside conical cavity $\alpha=14^\circ$ , $d=32$ mm .....	145
Figure 5.33 Contours of a) Mach number, b) Pressure and c) Temperature for conical cavity with $\alpha=26.6^\circ$ , $d=6$ mm.....	146
Figure 5.34 Contours of a) Mach number, b) Pressure and c) Temperature for conical cavity with $\alpha=14^\circ$ , $d=40$ mm.....	147
Figure 5.35 Surface pressure for conical cavity with $\alpha=45^\circ$ and $d=$ a) 2-6 mm, b) 8-12 mm and c) 14-20 mm .....	148
Figure 5.36 Surface pressure distribution for conical cavity with $\alpha=26.56^\circ$ and $d=$ a) 4-8 mm, b) 10-14 mm, c) 16-20 mm and d) 22-28 mm.....	149
Figure 5.37 Surface pressure distribution for conical cavity with $\alpha=18.45^\circ$ and $d=$ a) 6-12 mm, b) 15-21 mm and c) 24-30 mm .....	150
Figure 5.38 Surface pressure distribution for conical cavity with $\alpha=14^\circ$ and $d=$ a) 8-16 mm, b) 20-24 mm and c) 32-40 mm .....	151
Figure 5.39 Surface heat flux distribution for conical cavities with $\alpha=45^\circ$ .....	152
Figure 5.40 Surface heat flux distribution for conical cavities with $\alpha=26.56^\circ$ .....	153
Figure 5.41 Surface heat flux distribution over conical cavity with $\alpha=18.45^\circ$ .....	154
Figure 5.42 Surface heat flux distribution for conical cavity with $\alpha=14^\circ$ .....	155
Figure 5.43 Peak heat flux on outer surface .....	156
Figure 5.44 Total heat transfer rates for various conical cavity configurations.....	157
Figure 5.45 Area weighted average of surface heat transfer rates for various.....	157
Figure 5.46 Cavity pressure fluctuation inside conical cavity with a) $\alpha=45^\circ$ , $d=14$ mm, b) $\alpha=26.56^\circ$ , $d=6$ mm and c) $\alpha=18^\circ$ , $d=27$ mm.....	159
Figure 5.47 Drag oscillation for conical cavity with a) $\alpha=45^\circ$ , $d=14$ mm and .....	160
Figure 5.48 Comparison of unsteady and steady-state surface heat fluxes for conical cavity with a) $\alpha=26.56^\circ$ , $d=24$ mm and b) $\alpha=18^\circ$ , $d=27$ mm .....	161
Figure 5.49 Streamlines inside a hemispherical cavity of 3 mm .....	162
Figure 5.50 Streamlines inside hemispherical cavity of radius 10 mm.....	163
Figure 5.51 a) Pressure, b) Temperature and c) Mach number contours for 4 mm cavity.....	164
Figure 5.52 a) Pressure, b) Temperature and c) Mach number contours for hemisphere cylinder with 12 mm cavity .....	165



Figure 5.53 Surface Pressure distributions for various spherical cavities.....	167
Figure 5.54 Surface heat flux distribution for various spherical cavity .....	169
Figure 5.55 Peak surface heat flux for various cavity configurations.....	170
Figure 5.56 a) Total heat transfer rates and b) AWA of heat fluxes for various cavity depth.....	171
Figure 5.57 Variation of drag with spherical cavity depth .....	172
Figure 5.58 Cavity base pressure convergence for a) $d = 4$ mm and b) $d=14$ mm ...	172
Figure 5.59 Mean unsteady heat fluxes for hemispherical cavity with.....	173
Figure 5.60 Recirculating Flow between the spike and the main body.....	174
Figure 5.61 Contours of a) pressure, b) Tempeature and Mach number for Aerospike of $r_1=6$ mm, $r_2=3.5$ mm and $l/d=1.5$ .....	175
Figure 5.62 Surface pressure distribution for aerospike configurations with $r_1= 6$ mm, $r_2= 3.5$ mm and a) $l/D=1$ , b) $l/D =1.25$ and c) $l/D=1.5$ .....	177
Figure 5.63 Surface pressure distribution for aerospike configurations with $r_1= 5$ mm, $r_2= 3$ mm and a) $l/D=1$ , b) $l/D =1.25$ and c) $l/D=1.5$ .....	178
Figure 5.64 Surface pressure distribution for aerospike configurations with $r_1= 4$ mm, $r_2= 2.5$ mm and a) $l/D=1$ , b) $l/D =1.25$ and c) $l/D=1.5$ .....	179
Figure 5.65 Surface heat flux distribution for aerospike configurations with $r_1= 6$ mm, $r_2= 3.5$ mm and a) $l/D=1$ , b) $l/D =1.25$ and c) $l/D=1.5$ .....	181
Figure 5.66 Surface heat flux distribution for aerospike configurations with $r_1= 5$ mm, $r_2= 3$ mm and a) $l/D=1$ , b) $l/D =1.25$ and c) $l/D=1.5$ .....	182
Figure 5.67 Surface heat flux distribution for aerospike configurations with $r_1= 4$ mm, $r_2= 2.5$ mm and a) $l/D=1$ , b) $l/D =1.25$ and c) $l/D=1.5$ .....	183
Figure 5.68 Surface heat flux distribution for aerospike configurations with .....	185
Figure 5.69 Surface pressure distributions for aerospike configurations with .....	186
Figure 6.1 Temperature contours for parabolic cavities with a) $r/d=1.5$ , $d=6$ mm and (b) $r/d=2.5$ , $d=7$ mm .....	189
Figure 6.2 Contours of mass fractions of a) O, b)NO, c) N and O <sub>2</sub> for parabolic cavity with $r/d=1.5$ , $d=6$ mm.....	190
Figure 6.3 Contours of mass fractions of a) O, b)NO, c) N and O <sub>2</sub> for parabolic cavity with $r/d=2.5$ , $d=7$ mm.....	191
Figure 6.4 Species mass fraction along stagnation streamline for a) $r/d=1.5$ , $d=6$ mm and b) $r/d=2.5$ , $d=7$ mm.....	192
Figure 6.5 Surface heat flux distribution for various parabolic cavity configurations with $r/d=1.5$ .....	193

Figure 6.6 Surface heat flux distribution for various parabolic cavity configurations with $r/d=2.0$ .....	194
Figure 6.7 Surface heat flux distribution for various parabolic cavity configurations with $r/d=2.5$ .....	195
Figure 6.8 Post lip peak heat flux for parabolic cavity .....	196
Figure 6.9 Non dimensionalized a) total heat transfer rates and b) AWA of surface heat fluxes for various parabolic cavity configurations.....	197
Figure 6.10 Normalized drag for various parabolic cavity configurations.....	198
Figure 6.11 Contours of pressure for ellipsoid cavity with a) $a/b=3$ , $d=9$ mm and $a/b=2$ , $d=20$ mm .....	199
Figure 6.12 Mass fractions of a) O, b) N, c) NO and d) O <sub>2</sub> for ellipsoid cavity with $a/b=3$ and $d=9$ mm .....	200
Figure 6.13 Variation of species mass fraction along the stagnation streamline for ellipsoid cavity with a) $a/b =3$ , $d=9$ mm and b) $a/b=2$ , $d=20$ mm.....	201
Figure 6.14 Surface heat flux distribution for various cavity configurations with $a/b=3$ .....	202
Figure 6.15 Surface heat flux distribution for various cavity configurations with $a/b=2$ .....	203
Figure 6.16 Surface heat flux distribution for various cavity configurations with $a/b=1.5$ .....	204
Figure 6.17 Local surface heat flux at a point 5 mm aft of sharp lip .....	205
Figure 6.18 Non-dimensionalized a) total heat transfer rates and b) AWA heat fluxes for various ellipsoid cavity configurations at Mach 10.1 .....	206
Figure 6.19 Non-dimensional drag for various ellipsoid cavity models .....	207
Figure 6.20 Contours of a) pressure and b) temperature for a conical cavity model with $\alpha=45^\circ$ and $d=12$ mm .....	208
Figure 6.21 Contours of a) pressure and b) temperature for a conical cavity model with $\alpha=14^\circ$ and $d=36$ mm .....	209
Figure 6.22 Contours of mass fractions of a) O <sub>2</sub> , b) O, c)NO and N for a conical cavity model with $\alpha=14^\circ$ and $d= 36$ mm.....	210
Figure 6.23 Variation of species mass fractions along the stagnation streamline for conical cavity with a) $\alpha=45^\circ$ , $d=10$ mm, b) $\alpha=26.6^\circ$ , $d= 20$ mm, c) $\alpha=18.4^\circ$ , $d=27$ mm and d) $\alpha =14^\circ$ , $d=36$ mm .....	211
Figure 6.24 Surface heat flux distribution for models with conical cavity of $\alpha=45^\circ$	212
Figure 6.25 Surface heat flux distribution for models with conical cavity of $\alpha=26.6^\circ$ .....	213

Figure 6.26 Surface heat flux distribution for models with conical cavity of $\alpha = 18.4^\circ$ .....	214
Figure 6.27 Surface heat flux distribution for models with conical cavity of $\alpha = 14^\circ$ .....	215
Figure 6.28 Peak local heat flux on the outer surface of conical cavity models.....	216
Figure 6.29 a) Total heat transfer rates and b) AWA heat fluxes for various conical cavity configurations at Mach 10.1 .....	217
Figure 6.30 Non dimensional drag for various cavity models.....	218
Figure 6.31 Contours of a) pressure and b) temperature for 2 mm spherical cavity model at Mach 10.1 .....	219
Figure 6.32 Contours of a) pressure and b) temperature for 8 mm spherical cavity model at Mach 10.1 .....	219
Figure 6.33 Contours of mass fractions of a) O, b) NO, c) N and d)O <sub>2</sub> for a hemispherical cavity model of depth 8 mm .....	220
Figure 6.34 Variation of species mass fractions of a) NO and b) O <sub>2</sub> along the stagnation streamline for hemispherical cavity models .....	221
Figure 6.35 Surface heat flux distribution over a hemisphere cylinder with hemispherical cavity of different radii.....	223
Figure 6.36 Peak surface heat flux on the outer surface of various cavity models ..	224
Figure 6.37 a) Total heat transfer rates and b) AWA heat flux for various hemispherical cavity configurations.....	225
Figure 6.38 Normalized drag for various hemispherical cavity models .....	226
Figure 6.39 Contours of a) Mach number and b) Temperature for a double disk aerospike at Mach 10.1 .....	227
Figure 6.40 Diving streamlines for aerodisk with a) $l/D = 1.5$ and b) $l/D = 1$ .....	228
Figure 6.41 Surface pressure distribution for aerodisk configuration with $r_1 = 6$ mm and a) $l/D = 1.0$ , b) $l/D = 1.25$ and c) $l/D = 1.5$ .....	229
Figure 6.42 Surface pressure distribution for aerodisk configuration with $r_1 = 5$ mm and a) $l/D = 1.0$ , b) $l/D = 1.25$ and c) $l/D = 1.5$ at Mach 10.1 .....	230
Figure 6.43 Surface heat flux distribution for aerodisk configuration with $r_1 = 6$ mm, $r_2 = 3.5$ mm and a) $l/D = 1$ , b) $l/D = 1.25$ and c) $l/D = 1.5$ .....	231

## LIST OF TABLES

Table 4 A.....	109
Table 4 B.....	110
Table 4 C.....	110
Table 5 A .....	184
Table 5 B .....	187
Table 6 A .....	233

# 1 INTRODUCTION

## 1.1 OVERVIEW

Technological advancements in the 20<sup>th</sup> century have made hypersonic flights a realized human dream. It can be stated that the advent of hypersonic vehicles has minimized the gap between the atmospheric and trans-atmospheric flights. With the availability of hypersonic flight, a communion of both space flights and atmospheric flights have occurred causing great amount of research to be conducted in the area. While hypersonic flight actually became important with the availability of space flight: the gap between space flight and atmospheric flight will soon be bridged.

The desire to explore deep into space has led to many space exploration missions both manned and unmanned. The SPUTNIK I launched on 4<sup>th</sup> October, 1957 by the Soviet Union, was the first man made satellite. The Soviet Union also conducted unmanned explorations to Mars in 1960. In addition to reentry vehicles from space missions, there are other hypersonic vehicles on the horizon, such as hypersonic transport aircraft and the ramjet powered hypersonic missiles. On the civil transport horizon, there are many projects still in infancy to build trans-atmospheric hypersonic vehicle for human transport. All these hypersonic vehicles are based on the concept of single stage to orbit (SSTO). These include National Aerospace Plane (NASP) by the USA, Horizontal Take Off and Landing (HOTOL) by United Kingdom, Hypersonic Flight Experiment (HYFLEX) by Japan, SANGER of Germany and AVATAR of India.

On military grounds, the need for hypersonic missiles that travel through the dense atmosphere is unavoidable, so as to strike hostile enemy missiles. Such hypersonic missiles systems are already under development especially by the United States. In addition, for first strike capability, the utilization of hypersonic missiles gives an important advantage to the country that possesses such technology. The modern missiles that travel at hypersonic speeds are Inter

Continental Ballistic Missiles (ICBMs). The ICBMs can carry the pay loads to a distance in excess of 5000 nautical miles. Especially, the United States has many nuclear capable ICBMs all designed to fly at hypersonic speed in a sub-orbital flight path.

The payload of any ballistic missile that is included in the reentry body or reentry vehicle is referred to as the nose cone. Usually, the reentry vehicle is separated from the main airframe after the propelled flight of the airframe. The reentry vehicle with the payload then follows the ballistic trajectory through the space towards the target. On its way to the target, the vehicle accelerates to hypersonic velocities due the pull by the Earth, as the vehicle descends through the atmosphere. At these speeds, the aerodynamic heating becomes immense and the post shock temperatures ahead of the vehicle become extremely high, as the kinetic energy of the hypersonic missile is transformed into heat energy.

Most of the ballistic missiles that enter the Earth's atmosphere are disintegrated by ablation. This reemphasizes the importance of aerothermodynamic study of missiles. In order to protect the payload from this immense aerodynamic heating, an efficient thermal protection system needs to be designed. The aerodynamic heating is even severe during the ascent of aerospace planes and hypersonic missiles, as these vehicles have to travel through thicker atmosphere and as a result, the frictional forces are more predominant.

In these types of situations, the use of blunt nose is the most fundamental way to reduce the aerodynamic heating. At hypersonic speeds, even the slender bodies need to have blunt nose in order to reduce the stagnation point heat transfer rates. There has been many research for optimizing the shape and configuration of hypersonic vehicles, but the problem of aerodynamic heating stands there and some innovative concepts need to be introduced.

## **1.2 RECAPITULATION OF THE HISTORY**

It has just been over a century after humans have mastered the art of flying and fulfilled their long cherished dream. But, it has come out of relentless ef-

fort through centuries before and the human attitude of “never say no”. It is hard to trace the origin of human desire to fly like birds, but it has been there from almost the beginning of civilizations. According to a Greek myth, Daedalus and his son Icarus escaped from the island of Crete by means of wings fastened with wax. In Hindu mythology, Ravana, the King of Lanka, abducted Sita, wife of Ajodhya’s prince Rama, and flew to Lanka by Pushpak Vimana (aircraft), the aircraft. This incident is believed to have happened some six thousand years back.

Mythologies apart, Roger Bacon, an English philosopher, in 13<sup>th</sup> century wrote about possibility of making a flying instrument, so that a man sitting in the middle of the instrument and turning some mechanism might put it in some motion with artificial wings, which might beat the air like a flying bird. However, the first scientific design of a flying machine was given in 15<sup>th</sup> century by the famous Italian painter, philosopher-cum-engineer, Leonardo *da Vinci*. His notes contained as many as 35000 words and 500 sketches of ingenious mechanism for man-operated wing flapping devices and a variety of advanced conception design of a modern propeller. The human dream of flying literally came true on 21<sup>st</sup> November, 1783, when a hot air balloon carrying Pilatre de Rozier and the Marquis d’Arlandes ascended into the air and drifted 5 miles across Paris. This hot air balloon flight was designed and constructed by the Montgolfier brothers, Joseph and Etienne.

In 1799, George Cayley gave a revolutionary idea to include a fixed wing for generating lift, another separate mechanism for propulsion, and a combined horizontal and vertical tail for stability [1]. All modern airplanes are designed on this philosophy and George Cayley is indeed the parent of modern aviation. Cayley, in 1849, built and tested a full size airplane, named Boy Carrier. The triplane carried a ten year old boy and lifted several meters off the ground while gliding down the hill. He is believed to have made and flew a coachman carrying glider in 1853.

In April 1843, William Samuel Henson, published a design for a fixed-wing airplane powered by a steam engine driving two propellers, called the aerial steam carriage, which never flew. In 1857-1858, the French Naval officer and

engineer Felix Du Temple flew the first successful powered model airplane in the history. His airplane had a swept forward wing and powered by clockwork. In 1874, he designed a full-size airplane which took off with a pilot, but could not achieve a sustained flight.

Otto Lilienthal, in 1891, successfully flew his glider from a hill at Derwitz, Germany. He used cambered airfoil shapes on the wing and incorporated vertical and horizontal tail planes in the back for stability. Lilienthal made over 2000 successful glider flights, but on August 9, 1896, a gust stalled his glider, which crashed to the ground. He died because of the injury the next day. In 1896, Octave Chanute, inspired by Lilienthal, designed a biplane hang glider which employed the Pratt truss.

Samuel Pierpont Langley, secretary of the Smithsonian Institution, achieved the first sustained heavier-than-air, unmanned, powered flight in the history with his small scale Aerodrome in 1896. He also emphasized on the use of gasoline-fuelled engines and successfully flew a quarter-scale model aircraft with 3.2 hp, gasoline fuelled engine in 1903. But all his manned aircraft flights were unsuccessful.

On 17<sup>th</sup> December, 1903, at Kill Devil Hills in North Carolina, Orville and Wilbur Wright achieved the first controlled, sustained, powered, heavier-than-air, manned flight in the history of aviation. The Wright Flyer I, piloted by Orville Wright, flew for about 12 seconds covering a distance of 120 ft and rising up to a height of 10 ft. The Wright Flyer I was a biplane with a horizontal elevator mounted on struts in front of the wings, and a double vertical rudder behind the wings. It was powered by a 12 hp gasoline engine mounted on the top surface of the bottom wing. After the first historical flight, three more flights were made that day, with the last covering 852 ft and remaining in air for 59 seconds. The rest is history.

The human desire to fly higher and faster has been in existence much before the first successful powered manned flight by Wright Brothers in 1903. The unmanned non lifting flight of projectiles has been there for a very long past. The success story that started on 17<sup>th</sup> December 1903 with a sea level flight at 35 mi/h in 1903 has progressed exponentially to lunar return by Apollo at



36,000 ft/s in 1969. The flight speed achieved by the Wright Flyer was much less the speed at which the sound wave travels through the air, and called subsonic flight whereas the reentry of Apollo was at a speed that was 36 times speed of sound through the ambient air and flight at such speed is known as hypersonic flight.

On 24<sup>th</sup> February 1949, the V-2/WAC Corporal combination was test fired from the New Mexico Deserts in an attempt to demonstrate the use of multi-stage rocket for achieving higher speed and altitude. In this combination, a slender needle like rocket WAC Corporal was mounted on the top of a V-2 rocket, wherein the WAC Corporal served as second stage to the V2 rocket. The pen plotters track the V-2 to an altitude of 100 miles at a velocity of 3500 mph, at which point the WAC Corporal is ignited. This second stage rocket accelerates to a maximum velocity of 5150 mph, and reaches an altitude of 244 miles [2]. In doing so, it becomes the first machinery object of human origin to achieve hypersonic flight. By the 1950's, intercontinental ballistic missiles were flying at Mach 25 during entry tests of their nose cones.

On 12<sup>th</sup> April 1961, the world's first spaceship Vostok I, with a man on board was launched into the orbit from the Soviet Union. After attaining the first escape velocity and the separation of the last stage carrier rocket, the spaceship went into free flight on around the earth orbit. After the announcement of first successful space flight, the Vostok I is slowed by the firing of a retro rocket, and enters the atmosphere at a speed in excess of 25 times the speed of sound. After 30 minutes, the pilot-navigator, Major Yuri Gagarin, becomes the first man to fly in space, to orbit the earth and return safely. He also becomes the first human being to experience hypersonic flight [2]. The same year 1961, on 23<sup>rd</sup> June, U.S. Air force test pilot Major Robert White flies the X-15 airplane at a speed in excess of Mach 5. He extends his own record on 9<sup>th</sup> November 1961, by flying the X-15 at Mach 6. In these efforts, W White accomplishes the first miles per second flight in an airplane.

### 1.3 THE CHARACTERISTICS OF HYPERSONIC FLOW

In aerodynamics, one of the most complex and energetic regimes is hypersonic flow. As the aircraft starts moving from rest and gains speed, the flow field around it changes continuously from an incompressible flow to highly compressible flow, especially as it nears the speed of sound. At the speed of sound, the pressure waves emanated from the aircraft coalesce in front of the aircraft to form a strong shock wave, which was once believed to be impenetrable. This results in a sharp increase in drag due to discontinuous jump in pressure across the shock wave. It requires some special design and sufficient engine power to overcome the sound barrier. The pressure jump across the shock wave is also accompanied by a rise in temperature, density as well as entropy. As the speed is further increased above the sonic speed, the jump across the shock becomes higher and higher. A stage is reached, depending upon the design of the vehicle, when the jump in physical properties across the wave is such that the phenomena like shock layer-viscous interaction, aerodynamic heating, high temperature gas effects etc. become important; such flows are called *hypersonic flows* [3]. As a result, in hypersonic flows, special methods and equations will need to be implemented for accurate results.

P. L. Roe in 1970 during a lecture at the von Karman Institute, Belgium [2] stated that, “Almost everyone has their own definition of the term hypersonic. If we were to conduct something like a public opinion poll among those present, and asked everyone to name a mach number above which the flow of gas should properly be described as hypersonic there would be majority of answers round about five or six; but it would be quite possible for someone to advocate, and defend, numbers as small as three, or as high as 12”. Though in general; the flows over Mach number 5 are treated as hypersonic flows, nothing spectacular happens when the flow passes from a speed of Mach 4.99 to Mach 5.1. Instead hypersonic flows are separated from the supersonic ones on the basis of phenomena that are associated with hypersonic flows and not generally found in supersonic flows.

Hypersonic flows can be distinguished from supersonic flows by the thinness of its shock layer. Due to higher post shock density, the flow between shock wave and body, squeeze through a smaller area close to the body to adjust for a constant mass flow rate. This brings the oblique shock closer to the body making the shock layer i.e. the flow between the shock and the body, quite thin. Such a shock wave can merge with the thick boundary layer forming a viscous shock layer, which complicates the hypersonic flow.

The presence of normal shock in front of a blunt nose in hypersonic flow results in extreme temperature behind the shock. These temperatures are high enough to alter the physicochemical and thermodynamic properties of the air. At temperatures above 800 K, the vibrational energy of the air molecules gets excited, which makes the specific heats  $c_p$  and  $c_v$  functions of temperature and the assumption of calorifically perfect gas fails. As the temperature is further increased,  $\gamma$  becomes a function of both temperature and pressure. At about 2000 K and 1 atm pressure, the  $O_2$  molecules start to dissociate into O atoms and the flow is said to be chemically reacting. The oxygen molecule is totally dissociated at 4000 K and the  $N_2$  dissociation begins approximately at this temperature, which is complete at about 9000 K. Any further increase in temperature results in the ionization of oxygen and nitrogen atoms into positively charged ions and associated electrons. If the vibrational excitation and the chemical reactions take place at a rate faster than the time taken for a fluid element to move out of the flowfield, the flow is said to be in vibrational and chemical equilibrium. However, if it is just the other way round, the flow is said to be in non-equilibrium.

Another important aspect of the hypersonic flow over a blunt body is the presence of an entropy layer. The streamlines passing through the shock wave closer to the stagnation streamline have larger entropy increase, as compared to the streamlines away from it. This creates a large entropy gradient normal to the body and flows downstream. This is called entropy layer and it alters the boundary layer properties substantially.

Hypersonic flows are also characterized by the presence of phenomena called the viscous interaction. When a hypersonic flow is slowed by the viscous effect of a fluid, a part of kinetic energy that has been lost by the fluid is utilized in increasing the internal energy and hence the temperature of the fluid. The increase in temperature in turn increases the viscosity of the fluid resulting in a thicker boundary layer. The increase in temperature inside decreases the density in boundary layer, which has no pressure gradient normal to the surface. This further adds up to the thickening of hypersonic boundary layer due to larger area requirement for specified mass flow rate. The extreme thickening of hypersonic boundary layer alters the assumed inviscid flow outside the boundary layer, which in turn affects the boundary layer flows. This interaction between the outer inviscid flow and the viscous boundary layer flow is called the viscous interaction. Viscous interaction not only affects the lift, drag and stability of hypersonic vehicles by altering the pressure distribution over the vehicle body, but also increases skin friction and surface heat transfer.

Another aspect of hypersonic flow is the presence of rarefied atmosphere, which can be called as high altitude effect. Almost all of the vehicles that travel at hypersonic speed are reentry vehicles viz. space shuttle, Inter-Continental Ballistic Missiles (ICBMs), crew return vehicle (CRVs), etc. The reentry takes place at very high altitude where the density of atmosphere is very low. At these altitudes, the mean free path of air molecules becomes very high and the assumption of continuum flow is no more valid and the equations, aerodynamics concepts and results on such assumptions begin to break down. The popular Navier Stokes equations no more governs the fluid dynamic motion, new formulations based on the kinetic theory of gases needs to be implemented instead. This regime is also termed as *low density flows* or it can be also defined as *molecular flow*. The flow in the nose region of a space shuttle cannot be treated by purely continuum assumption above 92 km altitude [4]. Under these conditions, the *velocity slip* occurs wherein the velocity of fluid adjacent to body is not zero even for viscous flows. When the altitude is progressively increased, there comes a point where the continuum flow equations by themselves are invalid and method from kinetic theory must be used to

predict aerodynamics behaviour. If for density, the altitude is further increased, the air density can become low enough so that only a few molecules impact the surface of vehicle per unit time, and get reflected from the surface without interacting with the incoming molecules. Such flows are called *free molecular flows*. For the space shuttle, the free molecular flow occurs at an altitude above 150 km.

These wide range of phenomena associated with hypersonic flow distinguishes it from a supersonic flow and makes a closed form solution of hypersonic flows an almost impossible task. These hypersonic phenomena can be summarized with an example of a flow over a generic hypersonic vehicle as demonstrated in Figure. 1.1[2]

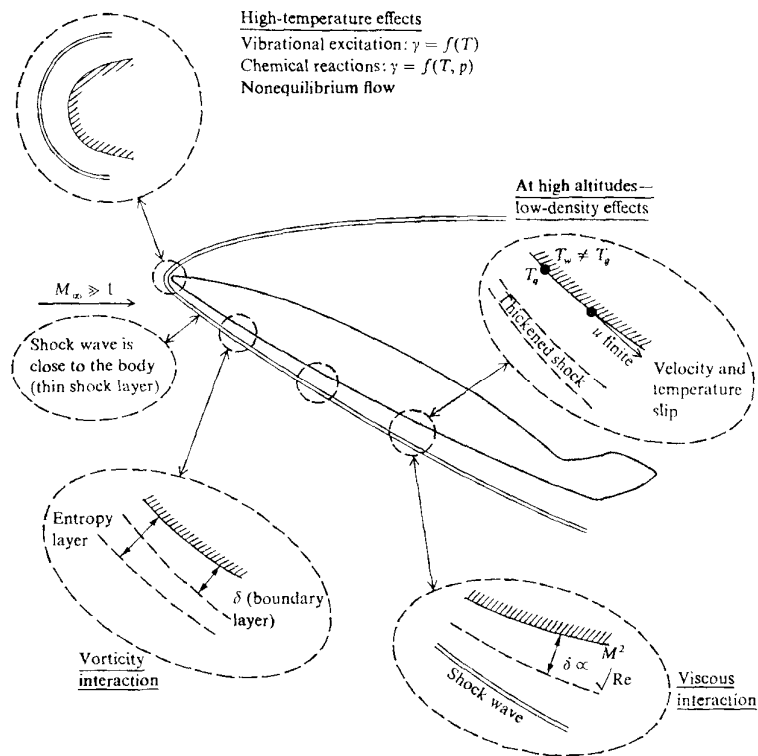


Figure 1.1 Hypersonic Flow Characteristics

A sharp pointed nose is generally used to overcome the large wave drag associated with supersonic flows, as it makes the shock weaker by aligning it at

low angles to the freestream and hence close to the body. At higher speeds the shock wave and the boundary layer merges to form a shock layer that result in increased skin friction and aerodynamic heating of the body. This can be reduced by making the nose blunt which creates a strong bow shock with greater temperature jump, but at some distance from the body and hence a reduced heat transfer to the body [2]. The need of a blunt nose to reduce the aerodynamic heating was first proposed by H. Julian Alley, before which hypersonic flows were merely treated as higher supersonic flows.

#### 1.4 THEORETICAL PREDICTIONS OF AERODYNAMIC HEATING

A large number of investigations have been reported in the literature attempting to predict the aerodynamic heating analytically. There are a number of correlations that can predict laminar stagnation point heat transfer rates for hypersonic flows. The prediction of local heat transfer rates for laminar flows can be done quite closely for convex axisymmetric bodies using Lee's correlation. However, for the prediction of local laminar heat transfer requires the knowledge of local pressure distribution over the surface. An approximate analytical estimate of the pressure distribution over a convex body revolution can be obtained from the modified Newtonian theory [2]. The so called generalized Newtonian Theory was postulated by Sir Isaac Newton as the fluid dynamic theory 1687, where he modelled the fluid flow as stream of particles in rectilinear motion. This postulate has been modified to obtain the pressure distribution over an inclined plane in a continuum flow as a function of local inclination of the surface to the freestream. This famous sine-squared law is given by

$$C_p = 2 \sin^2 \theta \quad (1.1)$$

where  $C_p$  is the local pressure coefficient and  $\theta$  is the local deflection angle.

This relation gives a good result for the stagnation point pressure coefficient at very large Mach numbers. Lester Lees [5] modified the Newtonian theory to give more accurate predictions of the surface pressure distribution at nominal hypersonic mach numbers. The modified Newtonian theory gives

$$C_p = C_{p \max} \sin^2 \theta \quad (1.2)$$

where

$$C_{p \max} = \frac{2}{\gamma M_\infty^2} \left\{ \left[ \frac{(\gamma + 1)^2 M_\infty^2}{4\gamma M_\infty^2 - 2(\gamma - 1)} \right]^{\gamma/\gamma-1} \left[ \frac{1 - \gamma - 2M_\infty^2}{\gamma + 1} \right] - 1 \right\} \quad (1.3)$$

Lester Lees [6] in 1956 studies the laminar heat transfer rates over blunt nosed bodies in hypersonic flows and established a correlation between the stagnation point heat transfer rates and heat transfer rates along the wall of body. He suggested a self similar solution of the laminar hypersonic boundary layer using the *Lee- Dorodnitsyn* transformations

$$\xi = \int_0^x \rho_x u_e \mu_e r^2 dx \quad (1.4)$$

$$\eta = \frac{u_e r}{\sqrt{2\xi}} \int_0^y \rho dy \quad (1.5)$$

where  $x$ ,  $y$  and  $\xi, \eta$  are the coordinates in physical and transformed planes respectively and  $\rho_e, u_e$  and  $\mu_e$  are the density, velocity and the viscosity coefficients respectively at the edge of the boundary layer and  $r$  is the vertical coordinate measured from the centreline for axisymmetric bodies. This leads to equations for axisymmetric stagnation point viz. equations (1.6) and (1.7).

$$(Cf''')' + ff'' = \frac{1}{2} [(f')^2 - g] \quad (1.6)$$

$$\left(\frac{C}{Pr} g'\right) + fg' = 0 \quad (1.7)$$

This leads to the theoretical heat transfer distribution over the wall of a sphere

$$q_w = 0.763 Pr^{-0.6} (\rho_e \mu_e)^{\frac{1}{2}} \sqrt{\frac{du_e}{dx}} (h_{aw} - h_w) \quad (1.8)$$

Lees [6] also gave a correlation for the ratio the stagnation point heat transfer rates to the heat transfer rates at other locations along the curve surface of a blunt axisymmetric cone, which is given by

$$\frac{\dot{q}_w}{\dot{q}_0} = \frac{\left(\frac{1}{2}\right) \left(\frac{p_w}{p_s}\right) \left(\frac{u_e}{u_\infty}\right) \left(\frac{r}{r_0}\right)}{\left[\int_0^{\xi} \left(\frac{p_w}{p_s}\right) \left(\frac{u_e}{u_\infty}\right) \left(\frac{r}{r_0}\right)^2 d\xi\right]^{\frac{1}{2}}} \left[\frac{u_\infty^2 \rho_s}{2(p_s - p_\infty)}\right]^{\frac{1}{4}} \quad (1.9)$$

The stagnation point heat transfer rates in turn can be estimated using the correlation given by Fay and Riddell [7] in 1958 which essentially is valid for hypersonic boundary layers in dissociated gas. Fay and Riddell [7] obtained a self similar solution for laminar boundary layer using the *Lee-Dorodnitsyn* transformations using the wall properties in place properties at the boundary layer edge, given by equations (1.10) and (1.11)

$$\xi = \xi(x) = \int_0^x \rho_w \mu_w u_e r^2 dx \quad (1.10)$$

$$\eta = \eta(x, y) = \frac{ru_e}{\sqrt{2\xi}} \int_0^y \rho dy \quad (1.11)$$

They gave a correlation based on large number of computations for stagnation point heat transfer rates in chemically reacting equilibrium and frozen boundary layers. The correlation for spherical blunt body is given by



$$\dot{q}_0 = \frac{0.763}{Pr_w^{0.6}} (\rho_e \mu_e)^{0.4} (\rho_w \mu_w)^{0.1} \sqrt{\frac{du_e}{dx}} (h_{0e} - h_w) \left[ 1 + (Le^{0.52} - 1) \left( \frac{h_D}{h_{0e}} \right) \right] \quad (1.12)$$

In the above equation,

$$h_D = \sum_i c_{i_e} (\Delta hf)_i^0 \quad (1.13)$$

Lewis number,

$$Le = \rho D_{12} c_{pf} / k \quad (1.14)$$

The axial velocity gradient in the above equation can be determined by the Newtonian approach, i.e.

$$\left( \frac{du_e}{dx} \right)_s = \frac{1}{R} \sqrt{\frac{2(p_e - p_\infty)}{\rho_e}} \quad (1.15)$$

## 1.5 HEAT AND DRAG REDUCTION MECHANISMS

Hypersonic vehicles are designed to withstand severe heat loads. Peak heat transfer rates and hence the maximum material ablation typically occurs at the nose tip. Hypersonic projectiles can have large penetration depths into armour due to their very high kinetic energy at impact and consequently the United States is interested in their development. Between 1.5 km/sec and 2 km/sec at sea level, the projectile nose tip can withstand the aerodynamic heating provided a high melting point material like tungsten is used. However, in flight regime 2-4 km/sec, the projectile nose tip experiences severe heat transfer rates and shape change due to ablation of the nose tip material. The shape change can produce unacceptable perturbations in the aerodynamics and the flight path and also reduce penetration characteristics. As an example of the severity of the heat transfer rates, the stagnation temperatures at sea level corresponding to a velocity of 3.1 km/sec is equal to the melting point of tungsten

(3680 K). Figure 2 shows the post shock temperature for different hypersonic vehicles as a function of forward velocity at a standard altitude of 52 km, assuming air as both calorically perfect gas and non equilibrium chemically reacting mixture of gases [3].

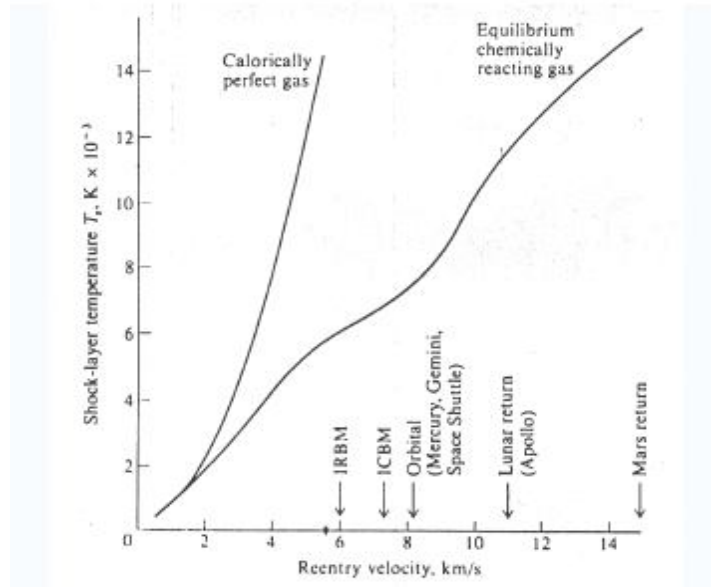


Figure 1.2 Temperature behind normal shockwave as a function of freestream velocity at a standard altitude of 52 Km [3]

Consequently, to extend the flight regime above 2 km/sec at sea level, there is a need to develop active or passive heat reduction techniques. Commonly used cooling techniques include ablative heat shields, heat sinks, active cooling and passive cooling. Atmospheric reentry studies in the early 1950s revealed the requirement of engineered heat shields called the thermal protection system. Further studies led to the conclusion that blunt bodies with high drag coefficients were better at surviving high heat fluxes. Allen and Eggers [8] in early 1950s discovered that the aerodynamic heating experienced by an object is inversely proportional to the drag coefficient, suggesting that the most thermally efficient reentry vehicle would be a blunt body. It followed that the first manned atmospheric reentry vehicle was a blunt nosed capsule.

In hypersonic flows, the kinetic energy of the oncoming flow molecules must be conserved when they come to rest or low subsonic values at and around the stagnation point. The kinetic energy is converted to thermal energy, heating the vehicle through both convection and radiation. Heat sinks are mechanism designed to absorb high heat fluxes during reentry and then reradiate and convect the heat back to the atmosphere to cool the vehicle once the heat pulse is over. The main drawback of using heat sink as thermal protection system is that they require a large amount of material to store the heat and therefore reduces the amount of payload that can be carried.

Ablative heat shields on the other hand works by pushing the post shock gases away from the vehicle and cooling the boundary layer through blowing. The actual process which occurs during ablation is the pyrolysis of ablative materials like char, which produces gases in the boundary layer blocking convective heat flux. For ablative heat shields to work effectively, the surface temperatures must reach the minimum required for the pyrolysis of the ablator material. The gases released by the pyrolysis create a flow across the vehicle surface, convectively cooling the post shock area. To protect against radiative heat fluxes, carbon ablative heat shields are used, which increase the amount of carbon in the boundary layer which in turn increases the opacity and therefore reduces the amount of radiative heat flux to the hypersonic vehicle.

Besides these, there are a number of ways in which heat transfer to the hypersonic vehicles can be reduced by modifying the flow field ahead of the stagnation point. The use of axisymmetric forward facing cavity has been under investigation for a long time now. There is a speculation that the introduction of a forward facing axial cavity at the nose of a hypersonic blunt body can reduce the peak heat transfer rates. This speculation is based on two observations. Firstly, there is substantial experimental evidence that the stagnation point heat transfer rate is decreased for certain cavity configurations. It has been observed that the heat transfer rates the cavity base is lower than the standard nose tip stagnation point heat transfer rates. Secondly, there are also some experimental evidences that the heat transfer along the outer surface, near the cavity leap, is significantly reduced for certain nose cavity configura-

tions compared to the spherical nose tip. Finally, there is enough experimental evidence that some configurations of nose cavity flow resonates strongly at a discrete frequency. It is strongly believed that this resonance affects the boundary layer in such a way that there is net reduction in the mean heat transfer rates at the stagnation region.

The use blunt nose for the reduction of heat fluxes associated with hypersonic flow comes with a severe penalty of increased drag. The two most critical design requirements for hypersonic vehicles like missiles and projectiles are the reduced wave drag and lower heat fluxes. Unfortunately, these two objectives are often conflicting. On one hand, sharp and slender nose design reduces the drag and ensures longer ranges and more economical flights. However, they are more vulnerable to aerodynamic heating. On the other hand, blunt nosed bodies produce more drag, though they are preferred as far as aerodynamic heating is concerned. Hence the effective management of heat transfer rates and aerodynamic drag is the primary element to the success of any hypersonic vehicle design. Spikes ahead of the blunt nose of the bodies of revolution have been considered as a means of drag reduction by a number of investigations. A forward facing spike attached to the nose of a blunt body creates a region of separated flow over the nose that reduces the drag due to the reduced dynamic pressure in the separated region at supersonic and hypersonic speeds. The spike establishes a conical separated flow zone when it has a proper length. The heat transfer tests conducted with the presence of drag reducing spikes has shown that the presence of a separated region ahead of the blunt body produce by the presence of spike causes a detrimental increase in the heat transfer to a hemispherical nose. However, some recent investigations on spiked blunt bodies at high mach numbers have shown that the heat transfer rates are reduced as compared to the blunt body without spike. A greater heat flux across a separated turbulent boundary, and then across an attached turbulent boundary has been theoretically predicted at low mach numbers; but it was shown that the ratio of heat flux of the separated boundary to that of attached boundary is a strong function of Mach number.

## 1.6 THE PHYSICS OF HYPERSONIC FORWARD FACING CAVITY

A forward facing axial cavity can be regarded as a resonance tube [9]. There have been a large number of experimental and numerical investigations to study the mechanism of flow oscillations in forward facing cavity [9], [10], [11], [12]. Though, majority of these investigations are based on cylindrical cavities, the physics unearthed is very useful in understanding the heat reduction mechanism due the presence of forward facing cavity. There are many experimental evidences that suggest that the forward facing nose cavity resonates at a discrete frequency. And it is strongly believed that it is this resonance that affects the flow field in such a manner, so that the mean heat transfer rate to the nose is reduced [11]. Figure 3 shows one such cavity studied for the resonance phenomena.

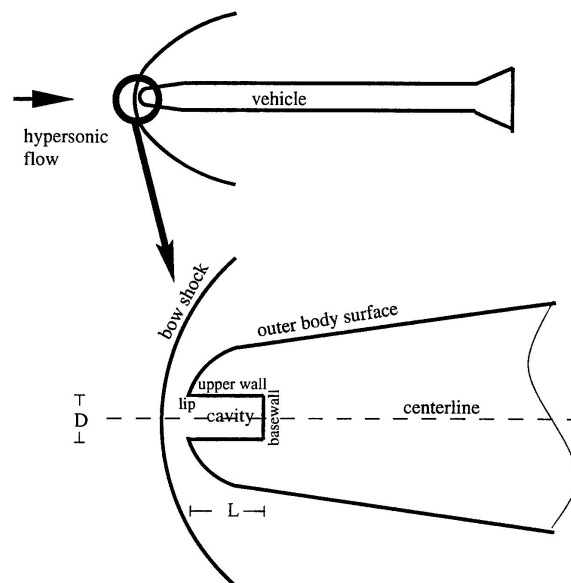


Figure 1.3 Schematic diagram of a Forward facing nose cavity

The fundamental frequency of oscillation of an axial cylindrical cavity such as shown in figure 1.3 can be approximated from the resonant tube theory by considering the speed of sound inside the cavity ( $a_0$ ) and the characteristic wavelength ( $\lambda$ ) of the cavity.

$$f_n = \frac{a_0}{\lambda} \quad (1.16)$$

For modestly large diameter cavities, the pressure waves travel between the bow shock and the base of the cavity. These pressure waves are reflected off the base of the wall and reflected off the bow shock. Consequently, the characteristic wavelength is approximately four times the distance between the mean bow shock position and the cavity base along the centreline.

$$\lambda = 4L^* \quad (1.17)$$

The flow inside the cavity is close to stagnation conditions and thus stagnation temperature can be used to find the speed of sound inside the cavity. Hence the frequency of oscillation can be given as

$$f_n = \frac{\sqrt{\gamma RT_0}}{4L^*} \quad (1.18)$$

Most of the oscillation energy is contained in the fundamental mode of oscillation. When the cavity depth is increased the oscillations become cleaner and stronger. At  $L/D=3.0$ , the cavity exhibits a quasi static bow shock motion in which the bow shock remains fixed at the mouth of the cavity during the inflow and at an upstream position during outflow and moves abruptly between these two positions.

When freestream noise is present, the oscillation strength for shallow cavities ( $L/D \leq 1.0$ ), increases gradually with increase in depth ( $L$ ). The medium depth cavities ( $0.4 \leq L/D \leq 0.7$ ) exhibit two modes of resonance. In these cavities, the pressure oscillations switches between a strong resonance mode and a weak resonance mode at random time intervals. For these shallow cavities, the free stream noise is the only mechanism which drives the shock oscillations. So, the relatively shallow cavities will not oscillate in case if free stream noise

is not present. For example, if a sinusoidal noise is present in the freestream; during the first half cycle the freestream stagnation pressure is larger than the mean value, while during the next half cycle it is less than the mean value. The increase in the freestream pressure during the first half results in a larger inflow momentum reaching the cavity mouth. This relatively large momentum encourages the cavity inflow and increases the cavity pressure gradients. During cavity inflow, the bow shock is moving downstream towards the mouth of the cavity. During the second half, the decreased freestream pressure results in a smaller momentum reaching the cavity mouth. This decreased momentum encourages a cavity outflow; during which the bow shock moves upstream away from the cavity mouth. The cavity reversal occurs after each half cycle. As the flow begins, during the start up, both the strength of the pressure oscillations inside the cavity and the bow shock oscillations grows with each input cycle. Eventually a pseudo –steady state is achieved, where the pressure within the cavity simply oscillates symmetrically about the steady-state stagnation pressure. The bow shock wave also oscillates about its steady-state position. During each oscillation cycle, the cavity base pressure reaches a maximum shortly after the bow shock reaches the maximum downstream position. For steady flows, the total mass of air inside the cavity is constant; however for unsteady flows involving shallow cavities, the total mass inside the cavity oscillate moderately about  $\pm 20\%$  of the mean value.

However, deeper cavities resonate strongly even without freestream noise and such oscillations are called as *self sustained oscillations*. The strength of self sustained oscillations is independent of the amount of noise present in the freestream and the movement of the bow shock cannot be ignored. The momentum losses across the bow shock increase with forward shock motion and decrease with aft shock motion. It follows that the inflow momentum is larger during the cavity inflow than the outflow. Consequently, during cavity inflow, the freestream flow momentum tends to reinforce the cavity flow and during the outflow the freestream momentum opposes the cavity flow. Thus, due to the relative imbalance in losses across the moving shock, even symmetric bow shock oscillations tend to add energy to the cavity fluid oscillations. This en-

ergy addition increases with mean bow shock speed and acts like a reverse dissipation.

Basically, during the cavity inflow, there is relatively low pressure and high velocity downstream of the bow shock and the incoming airstream flows directly into the cavity without significant radial flow. In contrast during the outflow, there is relatively high pressure and low velocity downstream of the bow shock and the incoming airstream tends to flow radially around the blunt nose. This is peculiar of deep cavities where the phenomenon of reverse dissipation exists.

## 1.7 THE EFFECT OF AEROSPIKE AND AERODISK

An aerospike is a needle like body mounted at the nose tip of the main blunt body. Sometimes a disk of small radius, called the aerodisk is fitted at the tip of spike for an improved performance [13].

A physical spike attached at the nose of a blunt body reduces its drag drastically by reducing the dynamic pressure of separated flow ahead of the nose. However, this reduced drag configuration comes with a penalty of increased heat loads. An aerospike with variable length could one of the solutions for the combined problem of aerodynamic heating and drag reduction. The flowfield over a spiked blunt body in hypersonic flow can either be steady or unsteady depending on the  $L/D$  (length of spike to the diameter of cylinder) ratio and the shape of the spike tip. **Bogdnhoff and Vas** in 1959 [14] reported that two distinct forms of flow unsteadiness exist at different critical lengths dependent on the geometry of the base blunt body. The flow over a blunt body with protruding spike is stable if the length of the spike is greater than the critical length for which the *oscillation mode* is observed. As the spike length to the body diameter ratio is decreased below this critical value the *oscillation* regime is obtained. If the length is further decreased, a flow transition from *oscillation mode* to *pulsation mode* occurs. If the length of spike is further decreased to a value such that the spike does not penetrate the bow shock formed by the base blunt body, a stable flow is once again achieved.



In the *pulsation mode*, the conical separation bubble formed on the concave part of the body inflates periodically and expands radially, thereby taking a hemispherical shape. In the *oscillation mode*, wherein the unsteadiness is milder, the conical foreshock, which envelops the separation bubble, and the accompanying shock layer oscillate laterally and their shape changes periodically from concave to convex [15]. The pulsation mode is typical of shorter spikes with  $L/D$  ratio between 0.2 and 1.5 while the oscillation mode occurs in relatively longer spikes with  $L/D$  ratio of 1.5 to 3. Figure 1.4 and figure 1.5 shows the schematic of the steady and unsteady flowfield around a spiked blunt body in hypersonic flow respectively.

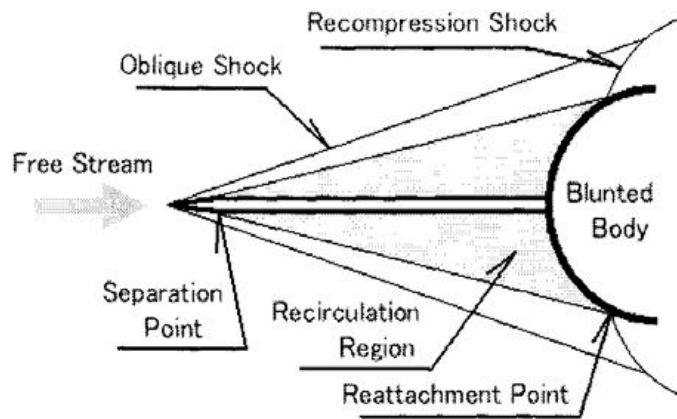


Figure 1.4 Schematic diagram of the steady flow over a spiked blunt body

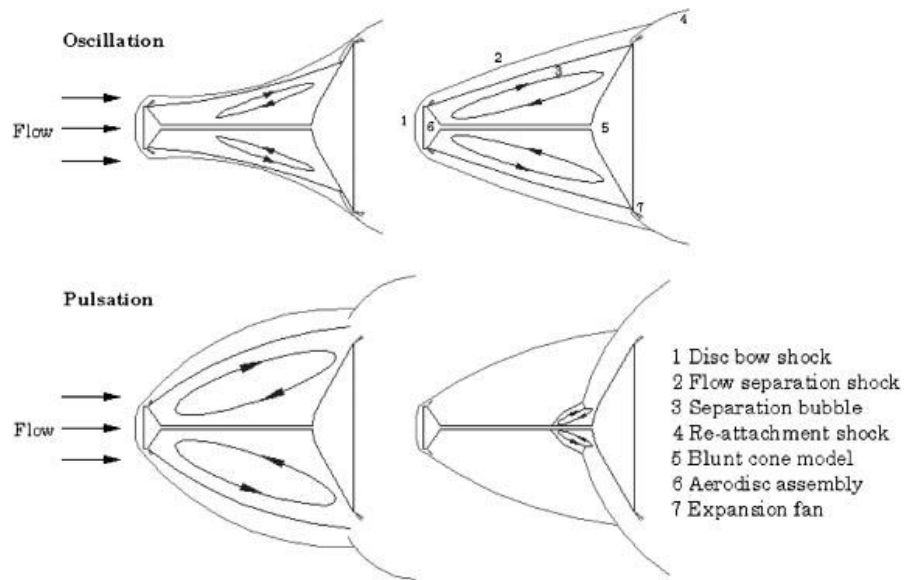


Figure 1.5 Schematic of the unsteady flowfield around spiked blunt body

## 1.8 MOTIVATION AND OBJECTIVES OF CURRENT RESEARCH

The hypersonic research dates back to the 1940s as a consequence of the World War II. In the 1940s and early 1950s, hypersonic aerodynamics practice was viewed as a high speed extension of supersonic aerodynamics practice, where slender bodies with sharp leading edges were employed to produce the weakest possible shock wave with an attendant low wave drag. However, at hypersonic speeds, the aerodynamic heating becomes a dominant factor and the heat transfer to a sharp nosed body becomes severe enough to melt the body of the vehicle. A breakthrough came in the mid 1950s, when H. Julian Allen proposed the use of blunt nose to reduce the severe aerodynamic heating, though it was kept secret for many years by the United States. The use of blunt nose is also advantageous for its higher volumetric efficiency and better accommodation of payloads. However the use of blunt nose drastically increases the wave drag and hence reduces the range of the missiles and also the payload that can be carried. A proper compromise to optimize the nose geometry has been the objective of many hypersonic researches. Today, the research of hypersonic missiles and projectiles is becoming more widespread among

the developed and developing nations due to their usage for scientific, commercial and military purposes.

With the advent of high speed digital computers, the hypersonic research has re-emerged on the global scenario in the backdrop of renewed focus on some exciting concepts like the hypersonic transport vehicles, atmospheric orbital transfer vehicles, reusable launch vehicles, space recovery experimental modules, wave riders, kinetic energy penetrators and the hypersonic cruise and ballistic missiles. Over the last two decades, the thrust for hypersonic systems for military applications has changed from emphasis on aerospace planes for the delivery of rapid reaction force over a long range to relatively short range response to critical targets. While, the need for hypersonic studies for systems involved in exo-atmospheric flights has not changed, since the requirement to reach orbital velocities and re-entry back to atmosphere introduces the traditional hypersonic problems; there has been a renewed emphasis on the ground and air launched hypersonic missile defence systems. These missiles are launched at speeds between 2 to 3 km/sec at ground level. At these moderate hypersonic speeds, the combination of dense atmosphere and high velocity imposes a severe heat transfer environments at the stagnation region of nose tip which require considerable research endeavours. Hence, there is a need to develop feasible, cost effective and innovative techniques to reduce the aerodynamics heating. There are a number of techniques which have been used to modify the structure of the hypersonic flow field ahead of the nose tip. Some of these techniques are use of retractable aerospike, forward facing cavity, forward facing jets among many others. There have been many investigations with an objective of optimizing the nose geometry, so as modify the flow field in order to achieve a reduced heat transfer rates in stagnation region of the hypersonic vehicles. But most of these investigations were carried at the flight conditions that exist at points along the reentry trajectory of different trans-atmospheric vehicles. Among various nose mounted mechanisms for the reduction of stagnation point heat fluxes, the use of forward facing cavity is the most popular one. There are recent efforts to investigate the use of blunt shaped aerospikes to reduce the aerodynamic heating. Pointed aerospikes has

been traditionally used to reduce the wave drag associated with supersonic and hypersonic flows. As the hypersonic flight is generally associated with high altitude, most of the research data available on heat reduction mechanism are for rarefied or very low density atmosphere. But, due to the advent of hypersonic systems like Ballistic Missile Defence systems, there is a need to reassess these heat reduction mechanisms that is valid for low altitude hypersonic speeds.

In backdrop of above discussion, the objective of the current research is two-fold:

Firstly, to investigate numerically the effect of shape and size of forward facing axisymmetric cavity at the nose of a sphere-cylinder on the stagnation point heat transfer rates.

Secondly, to investigate numerically the effects of some innovative aerospikes designs and geometrical modifications at the nose of a sphere-cylinder on the stagnation point heat transfer rates and the total wave drag.

## **1.9 STRUCTURE OF THE THESIS**

The thesis begins with the introduction of the hypersonic flow phenomena and the associated aerodynamic heating problems in chapter 1. Also a brief history of human flight endeavours and hypersonic flight achievements are illustrated.

The detailed review of the available literature in the field of heat reduction mechanism by modification of flow field is presented in chapter 2. The literatures on different allied and close researches have been reviewed. These include the experimental and numerical aerothermodynamics of blunt bodies at hypersonic speeds and various techniques for reduction of stagnation region heating. The physics of forward facing cavity and blunt head aerospike is introduced in this chapter with the help of existing literature on these topics. A survey has also been made on the state of the art of the numerical schemes for the simulations of blunt body aerothermodynamics in hypersonic flow.

The governing equations of viscous hypersonic flow are described in detail in chapter 3. This includes various forms of the unsteady Navier Stokes equations and the scalar transport equations for turbulence. The chapter also presents the models for thermodynamic and transport properties of high temperature gas.

Chapter 4 presents the comprehensive details of the numerical methodology employed in the study of the current problem. This includes various strategies adopted for the time integration of unsteady Navier Stokes equations, the flux models used and the modeling of turbulence. This chapter also includes the explanation of the geometry, grid used and the boundary conditions employed for the study. The solver validation and verification along with mesh independence study are also presented.

Chapter 5 presents in detail, the results obtained numerically using commercially available code for the convective heat transfer rates on hemisphere-cylinder with different nose geometry modifications like the forward facing cavity and the blunt nosed aerospike at Mach 6.2. A detailed discussion is also made on the results obtained with the aerodynamic and aerothermodynamic perspective.

Chapter 6 presents the results for the effect of forward facing cavities and aerospikes on the aerothermodynamics of a hemisphere cylinder for a chemically reacting air at Mach 10.1. This includes the presentation of surface pressure distribution, surface heat flux distribution and total heat transfer rates for various configurations.

After a detailed discussion of the results in chapter 5 and 6, a conclusion is drawn on the basis of the results obtained in chapter 5 and 6. The conclusion addresses both the aerodynamic heating and the wave drag of the hemisphere-cylinder and recommend the best possible design for the reduction heat fluxes. Further recommendations are made for the further study that needs to be done to complement the current research.

## 2 LITERATURE REVIEW

### 2.1 THE AERODYNAMIC HEATING PROBLEM

In 1954, the designers of the Atlas, the ICBM intended for carrying hydrogen bomb, for the first time faced the problem of aerodynamic heating during reentry. A suitably designed lightweight nose cone that could protect the warhead against the heat of atmospheric entry was the requirement of the day. The solution to the problem of nose cone design came from George Sutton who introduced the concept of ablation [16]. An important attribute of the nose cone design was its shape, and the prevailing design in early 1950 was needle-nose streamlining for ultimate reduction in the drag. This intuitive design fell apart 1953 when NACA-Ames aerodynamicists **H. Allen Julian** and **Alfred Eggers** carried out an elegant analysis of the motion and heating of a re-entry nose cone [8]. They calculated the total heat input to a re-entry vehicle, seeking shapes that would minimize it. Their analysis falsified the concept that a slender sharply pointed nose was the best nose cone design. For a lightweight nose cone that would slow down significantly in the atmosphere due to drag, they found that the best shape, minimizing the total heat input, was a blunt rather than sharp. It was also found that to reduce the maximum heat transfer rate averaged over the entire vehicle surface, a nose cone of realistic weight might be either very sharp or very blunt. Missiles of intermediate slenderness gave considerably higher heating rates and as a result, they ought to be avoided. But the peak heat transfer rates were concentrated at the nose-cone tip and it was important to minimize the peak heating at the nose tip. Again their analysis showed that the blunt nose was the best. They also suggested that not only the pointed nose should be avoided; but the blunt nose with largest possible nose radius must be used.

Many prototypes were built and flight tested by the United States to verify and quantify this breakthrough finding. Immediate application of this finding was that all the space probe designs to follow had a blunt reentry nose cone. Since

then a wide range of experiments were conducted by different researcher to predict the aerodynamic heating on blunt nose at hypersonic speeds.

**Crawford and McCauley** [17] in 1956 investigated the laminar aerodynamic heat transfer to a non isothermal hemisphere cylinder at a mach number of 6.8 and a Reynolds number of  $0.14 \times 10^5$  to  $1.06 \times 10^6$  based on the diameter and the freestream conditions. They obtained the heat transfer coefficients, which were slightly less over the whole body than those predicted by the theory of Stine and Wanlass [18] for an isothermal surface. For stations within  $45^\circ$  of the stagnation point, the heat transfer coefficients could be correlated by a single relation between the local Stanton number and the local Reynolds number. The pressure distribution obtained over the sphere cylinder verified that the local Mach number or the velocity outside the boundary layer required in the theories may be computed from the surface pressures using isentropic flow relations and conditions immediately behind a normal shock. The experimental pressure distribution at a Mach number of 6.8 was closely predicted by the modified Newtonian theory.

**Diaconis et. al.** [19] in 1957 studied the heat transfer parameters and the boundary layer transition on a hemisphere cone cylinder and a  $120^\circ$  included angle cone cylinder at a freestream Mach number of 3.2 and a freestream Reynolds number of  $12.92 \times 10^5$  per inch. The wall temperature of the body was kept approximately equal to the freestream temperature. The values of Stanton number obtained for both configurations with smooth walls were in good agreement with the theory. With the increase in surface roughness to 130 micro inches, the heat transfer parameter in the spherical region of the hemisphere-cone cylinder increased significantly and the ratio of experimental to theoretical stagnation point heat transfer rate appeared to be a function of roughness Reynolds number.

**William E. Stoney** [20] in 1958 studied the aerodynamic heating of blunt nose shapes at Mach numbers up to 14. The results obtained through flight tests and wind tunnel tests showed that a flat faced cylinder has about 50 percents the stagnation point heating rates of the hemisphere over the entire Mach number range. Experiments done at a Mach number of 2 on a series of bodies made up

of hemispherical segments of varying radius of curvature showed that the slight amounts of curvature can reduce the local heating rates at the edge of the flat faced cylinder with only slight increase in the stagnation point heating rates. Also the total heat transfer to such slightly curved bodies is somewhat smaller than the total heat transfer rates to a flat faced cylinder. Tests on flat faced cylinders at a mach number of 2.49 and at angles of attack up to 15° showed that with an increase in angle of attack the apparent stagnation points moves towards the windward side reaching at a point 50 percent away from the center of the nose at an angle of attack of 15°. At this attitude, the heat transfer rate near the windward edge increases by an amount of 30 percent while decreases by an amount of 20 percent near the leeward edge.

Some preliminary investigations done by Stoney on concave nose shapes indicated a possibility of extremely low heating rates significantly lower than the flat faced cylinder.

**John O. Reller** [21] in 1960 investigated the convective heat transfer rates on a large number of bodies of revolution to determine the effect of variations in the body shape on the overall heat transfer rates. This investigation included the studies of the effect of changes in the body fineness ratio, ratio of nose to base diameters, and nose profile including the addition of spikes. The nose to base diameter ratio was varied from 0 to 1 while the body fineness ratio was varied from 0.3 to 2.0. All the tests were done in an ideal gas flow at Mach number from 3 to 6 and Reynolds number from  $0.4 \times 10^6$  to  $2.4 \times 10^6$  based on diameter.

It was found that the heat transfer data for blunt shapes with laminar flow expressed as the product of Stanton number and the square root of Reynolds number are essentially independent of freestream Mach number and body shape. It was also suggested that if the Reynolds number is such that the transition occurs somewhere on the body, bluntness can significantly reduce the heat transfer rates by increasing the length of laminar run. Conversely nose shapes having small radii of curvature in the shoulder region can cause early transition to turbulent flow and significantly increase the total heat transfer rates. Another important finding of this investigation was that the heat transfer



rates to a blunt shape was increased by concave stagnation regions having depth in excess of 0.3 times the nose diameter due to development of large scale unsteadiness in the flow. Also the stagnation point spikes up to 2 diameters length increased in heat transfer rates significantly for both steady and large scale oscillations.

**Scala and Warren [22]** in 1961 studied the stagnation point convective heat transfer rates in dissociated air. The heat transfer rates were obtained on a  $\frac{3}{4}$ " hemisphere cylinder at hypervelocity both analytically using a new theory developed by Scala. The results supported by experimental data suggested that the convective stagnation heat transfer rates in dissociated air are twice as large as predicted using older theories.

**Griffith and Lewis [23]** in 1963 studied the heat transfer distribution on a  $9^\circ$  half angle spherically blunted cone and a hemisphere cylinder at Mach numbers between 17 and 20 and freestream Reynolds number between 100,000 and 800,000 per inch. All the tests were conducted in the arc driven tunnels of the von Karman Gas Dynamics Facility, AEDC. The data obtained showed a strong dependence of heat transfer distribution on pressure distribution, Mach number and the half cone angle.

**Bushnell et. al [24]** in 1968 studied the local heat transfer rates and pressure distribution over a conical portion of a  $25^\circ$  half angle cone at angles of attack up to  $90^\circ$ . The investigation was conducted at a Mach number of 8.0 and a Reynolds number of  $0.37 \times 10^6$  and  $1.65 \times 10^6$  based on the base diameter. The heat transfer distributions over the windward surface for angles of attack up to  $45^\circ$  were in good agreement with predictions using small cross flow theory of Beckwith whereas the distributions at higher angles of attack are in fair agreement with swept cylinder theory based on the local diameter of the cone.

**Marvin and Akin [25]** in 1965 studied the pressure distribution and convective heat transfer on a hemisphere-cylinder, a blunted  $30^\circ$  cone and the afterbody of a capsule type shape in air, carbon dioxide, nitrogen and argon. It was found that the pressure distribution on hemisphere-cylinder did not vary significantly in the various test gases, but the heat transfer rate in argon was approximately 30 percent higher than that of other gases.

**Baker and Kramer** [26] in 1982 did an optimization study to determine fixed fineness ratio nose tip shape contours for a vehicle with specified ballistic coefficient and nose tip scale, which minimizes the total trajectory nose tip laminar and turbulent heat transfer.

**Andrushchenko et. al.** [27] in 2007, studied the problem of a chemically equilibrium three dimensional boundary layer on a blunt body moving in a dense atmosphere. They suggested the solution of the system of equations for the boundary layer by the method of successive approximations, and provided simple analytical expressions in the first approximation for the surface friction and heat flux coefficients. They also obtained formulae for estimating the convective heat flux in the neighbourhood of the critical point of spherical blunting.

**Sravanan et. al.** [28] in 2009 studied the convective heat transfer rates over a missile shaped body at mach numbers of 5.75 and 8.0 at an angle of attack of zero degrees. The experimental results were supported with the numerical simulations. It was found that the measured stagnation point heat transfer rates were always lower for both Mach numbers as compared with the Fay Riddell correlation. It was found that the non dimensional heat flux distribution along the model surface is essentially dependent on the freestream mach numbers.

## **2.2 THE EFFECT OF FORWARD FACING CAVITY**

The primary concern in the design of a future hypersonic vehicle is the effective management of heat transfer rates and the aerodynamic drag. From the work of Allen, it is well established that to avoid extremely severe heat transfer rates to the body at reentry velocity the use of blunt nose is unavoidable. A blunt body in hypersonic flow generates a strong bow shock in front of the body with the shock standing at some distance from the body. This takes away the heat from the flow to the air surrounding the body leaving behind only a fraction of thermal energy to heat up the blunt body. Even though the presence of stronger bow shock reduces the heat fluxes to the body, it is associated with a large increase in the overall drag of the blunt body. For a hypersonic blunt body, most of its drag owes to the large pressure rise across the strong de-

tached bow shock ahead of it. The locally normal bow shock not only increases the drag drastically, but also produces very high stagnation temperatures behind the shock, which in turn results in a very severe heat fluxes in the stagnation region and is a matter of great concern. The idea behind this passive technique of employing a forward facing nose cavity is to modify the flow field ahead of the blunt body so as the stagnation temperatures, heat fluxes to the body and the aerodynamic drag are optimized.

There have been many researches in the last five decades that were focused at finding the effectiveness of forward facing cavity in reducing the aerodynamic heating of hypersonic vehicles. **Cooper et. al.** [29] in 1958 measured the heat transfer rates and the pressure fluctuations at Mach numbers of 1.98 and 4.95 at the stagnation point of a concave hemispherical nose for a Reynolds number range from  $2 \times 10^6$  to  $10 \times 10^6$ . Both the steady state and unsteady effects were studied and it was found that for angles of attack less than  $2^\circ$  either of steady or unsteady flow conditions could occur, while for angles of attack more than  $2^\circ$  the flow was observed to be steady. The steady flow heat transfer coefficients observed were 20 to 50 percent of the heat transfer coefficients associated with convex nose shape.

**Hopko and Strauss** [30] also in 1958 studied the aerodynamic heating on convex and concave hemispherical nose shapes and hemispherical depressions on a  $30^\circ$  blunted nose cone. The data obtained at Mach numbers up to 8.5 indicates that the heating of the stagnation point of the concave hemispherical nose is one-third of a convex hemispherical shape at Mach number of 2 and one-tenth at Mach number of 8.

**Stalling and Burbank** [31] in 1959 measured the heat transfer coefficients and pressure distribution for a 4.56 inch diameter cylinder with concave nose for a Mach number range of 2.49 to 4.44. Two types of flows were observed in this investigation; a steady flow condition and a non predictable, sporadic unsteady flow condition. The study revealed that the stagnation point heat transfer coefficient on concave nose were 20 percent of those for hemispherical nose under steady state flow conditions. However the heat transfer coefficients increased by a factor of 6 for the unsteady flow conditions.

**Tyner** [32] in 1959 obtained the heating data on a 5 inch diameter cylinder cone having a flat faced cone with four different hemispherical depressions, using flight tests. The experimental results show that, although the heating rates in the depressions nearest the stagnation point are lower than those in the pits near the edge of the model, the flow is more nearly turbulent about the inboard pit than the outward pit. The behaviour of the heating rates in the depressions on this model contrasts greatly with the behaviour in pits at the stagnation point. The results indicate an increase in heating rates up to 93 percent at the depressions.

**Nestler** [33] in 1981 studied experimentally the cavity flow on sharp and blunted cones at Mach 8 over a wide range of Reynolds number providing both laminar and turbulent flow upstream of a rectangular cavity on a  $9^\circ$  cone. The pressure measurements that were done on the cavity floor and downstream of the cavity were shown to be sensitive to the cavity aspect ratio.

**Sambamurthi et. al** [34] in 1987 studied the flow field around a  $9^\circ$  blunt cone with a nose cavity at Mach 10 at the Von Karman gas Dynamic facility. They presented both the analytical and experimental results and correlated them with numerical results. The results indicate that the bow shock oscillate at the natural frequency of the cavity with low amplitude and the heat transfer rate to the base of the cavity is reduced as compared to the rim of the nose cone. The correlation obtained between the experimental results and the numerical results obtained using computational code RAVEN was exceptional.

**Huebner and Utreja** [12] in 1993 studied the bow shock behaviour associated with a conical walled cavity with a flat circular base at a Mach number 10. In this experimental investigation, the measurement of shock oscillation frequency and amplitude, as well as the shock wave shape, were recorded by a number of techniques. The oscillation frequency was found to be inversely proportional to cavity depth and corresponds to the natural acoustic frequency of the cavity, with a wavelength that was 4 times the distance from the base to the mean shock standoff position. The mean shock standoff distance was found to a function of cavity size but not the depth and it was suggested that the flow sees the nose cavity configuration as if it possessed a flat face. It was

further shown that varying the angle of attack did not alter the shock shape, standoff distance and the amplitude. The amplitude of the oscillating shock was found to be directly proportional to the Reynolds number and varies from 9 to 21 percent of the mean shock standoff distance.

**Engblom and Goldstein** [10] in 1996 conducted experimental and numerical investigation of the effect of forward facing nose cavity on the heat fluxes to the surface of a blunt nose. They found that for sufficiently deep cavities that the local surface heat flux was reduced everywhere on the surface when strong longitudinal pressure oscillations within the cavity, induced large bow shock oscillations. During the downstream movement of the bow shock towards the cavity, the relative Mach number is decreased which allows the relatively cool gas to enter the cavity. As the bow shock moves upstream away from the cavity, the relative Mach number is increased and the hot gas present behind the shock wave is convected away from the cavity lip by cooler gases leaving the cavity.

**Engblom et. al.**[11] in 1997 studied with the time accurate numerical simulations of hypersonic flow over the nose of a blunt body with forward facing cavity. It was shown that the freestream noise is the mechanism that drives the resonant pressure oscillations within relatively shallow cavities. However, sufficiently deep cavities oscillate strongly even without any freestream noise. For shallow cavities, it was found that there is a strong dependence of the oscillation strength on the freestream noise frequency. They showed that the oscillation strength increases nearly proportional to the amplitude of the input noise, increases rapidly with the cavity depth and increases with Mach number up to a certain limit. They also verified the numerical result that there is a critical cavity length to diameter ratio, beyond which the bow shock oscillations are self sustaining.

**Ladon et. al** [9] in 1998 studied experimentally the physics of resonance in a supersonic forward facing cavity at Mach 4. Many cylindrical cavities with different L/D ratios, but fixed diameter were studied. A fast response pressure transducer was placed at the base of the cavity to measure pressure fluctuations inside the cavity. It was observed that under the conventional wind tunnel

conditions, the root mean square (RMS) of the pressure fluctuations was 0.4% of the mean base pressure while under the quiet-flow conditions; the RMS of the pressure fluctuations was of the order of 0.04% of the mean pressure. To study the effect of freestream disturbances on the pressure fluctuations, a laser induced perturbation system was used which created controlled, repeatable and localized upstream disturbances upstream of the bow shock wave. These disturbances were convected with the flow, impinged on the nose cavity and caused damped cavity oscillations. The small damped oscillations present under the quiet-flow conditions seem to explain the low heat transfer rates observed in flight tests. The large pressure fluctuations observed under noisy wind tunnel conditions are artefacts of the large noise levels present in the freestream and are not realistic under normal flight conditions.

**Perng and Dolling** [35] in 1997 measured the fluctuating surface pressures in a forward facing cavity at a Mach number of 5 and a Reynolds number of  $9.65 \times 10^5$  based on the turbulent boundary layer thickness. The cavity length to depth ratio ( $L/H$ ) was varied from 3 to 4 while the cavity width to depth ratio was held fixed at 3. Many geometrical modifications were tried at the front and rear walls to see their effectiveness in suppressing cavity pressure oscillations. Certain 2-D slanted rear walls were very effective.

**Kim and Park** [36] in 2000 carried out a numerical study of hypersonic inviscid flow past a blunt cone with forward facing, cylindrical cavity to examine the characteristics of resonant flow oscillations inside the cavity. The numerical simulations were carried out using the weighted ENO scheme with 5<sup>th</sup> order accuracy for spatial and third order total variation diminishing Runge-Kutta explicit method for time integration. In this computational study the effects of the length of the cavity, freestream Mach number and the diameter of the cavity on flow oscillations were accomplished. It was found that when the freestream Mach number was decreased the cavity flow oscillations subsided to steady flow, however the frequency of transient flow oscillations decreased with Mach number. It was also found that the increase in cavity diameter for a fixed  $L/D$  (length of the cavity to the diameter of the cavity) ratio resulted in an increase in damping of the oscillations to yield non oscillatory flow.

**Silton and Goldstein** [37] in 2005 did a combined numerical and experimental investigation of the ablation onset in unsteady hypersonic flow about a nose tip of a hemisphere cylinder body with forward facing cylindrical cavity. This parametric study investigated the effect of cavity length, cavity lip radius and cavity diameter on ablation onset times. Each parameter was first investigated experimentally and optimized independently followed by a time intense numerical simulation for geometries indicating most delayed ablation onset. It was found that a forward facing cavity at the nose tip could delay the ablation onset beyond that of baseline sphere cylinder nose tip. It was also observed that the best cavity length, for a given nose diameter, was four times the cavity diameter. The best cavity lip radius was found to be a quarter of the difference between the nose diameter and the cavity diameter. The numerical results suggested that the cavity diameter that increased the ablation onset time the most, with both the cavity length and the cavity lip radius optimized was half the nose diameter.

**Bazyma and Kuleshov** [38] in 2006 carried out an experimental and numerical study of the supersonic flow past cylinder with cavity of  $L/D$  (length of the cavity to the diameter of the cylinder) ratio ranging from 0.3 to 1.6. The experimental investigations were done at a Mach number of 3 and a Reynolds number greater than  $10^6$ . The bow shock oscillation was observed for all configurations with the oscillation frequency proportional to the cavity depth and approximately equal to the fundamental acoustic frequency for  $L/D$  ratios greater than 0.4. For the case of  $L/D = 0.4$ , a non steady regime for bow shock oscillation was observed which was bimodal in nature. The bow shock for this configuration was found to be non axisymmetric with bulges on one and/or another side. For  $L/D$  ratio greater than 0.8 the bow shock was found to be axisymmetric.

**Seiler et. al.** [39] in 2007 studies the heat flux to a blunt nosed supersonic projectile equipped with cavity. The heat fluxes were measured by thermocouples at the bottom of the tapered cavity of different geometry in a shock tunnel using a Mach 4.5 contoured nozzle. The flow conditions of a real flight at altitudes of 0 km, 2 km and 5 km were simulated in the shock tunnel. The ex-

perimental results were validated against those obtained with Laminar Fluent Code. The results suggest that the deepest cavity has the smallest heat flux.

**Sravanan et. al.** [40] in 2009 studies the structure of the hypersonic flow over a forward facing cavity at the nose a missile shaped body at Mach 8. The experimental and numerical investigations were done to investigate the bow shock behaviour associated with two different cavities. For each of the tests performed with a cavity, the bow shock oscillated during the test. The mean shock standoff distance was shown to be dependent on the cavity diameter. The net reduction of 35% to 40% in surface convective heating transfer rates was observed for cavity configurations near the stagnation zone at zero angle of attack. Cavity configurations with an L/D ratio of four resulted in approximately 5% reduction the drag, whereas with an L/D ratio of 2, 10% increase in aerodynamic drag was observed. The addition of small diameter cavity resulted in slight increase in the L/D (lift to drag) ratio, and it increases at higher angles of attack for both cavity configurations. The important finding of this investigation is that the smaller diameter cavity has the highest lift to drag ratio, whereas the medium diameter cavity has the highest heat flux reduction.

**Lu and Liu** [41] in 2012 studied the effect of forward facing cavity on the aerodynamic heating of hypersonic vehicle nose using computational fluid dynamics (CFD). The CFD results obtained shows that the forward facing cavity configurations are very effective in cooling the nose of a hypersonic vehicle especially at the stagnation point region. It was observed that deeper the cavity, the smaller is the heat flux and the mean heat fluxes increases along the body surface to reach a peak value near the sharp lip and then decreases rapidly. The point maximum heat flux along the surface does not coincide with the sharp cavity lip; it is located after the lip instead. Also no effect of the length of the cavity on the location of peak heat flux has been established.

### **2.3 THE EFFECT OF AEROSPIKE AND AERODISK**

The use of blunt nose is unavoidable in hypersonic flow to reduce the aerodynamic heating. But the requirement of low drag during ascent for reduced fuel consumption in ballistic missile demands a reinvestigation into the problem.



The use of aerospikes or aerodisks of certain geometric configurations can reduce both aerodynamic heating and aerodynamic drag [42]. Conceptually, a spike introduces two major modifications to the flowfield ahead of the blunt forebody. Firstly, it replaces a strong detached bow shock wave with a system of weaker oblique shock waves. Secondly, it acts as a flow separator as the spike encourages the separation of boundary layer from its surface and the creation of a shear layer. This shear layer propagates downstream, reattaches with the blunt forebody surface, and envelops a zone of recirculation in which the flow attains a low value of pressure and velocity. This zone covers a considerable portion of the blunt forebody surface, and results in significant drop in surface pressure and temperatures. However, at the point of shear layer reattachment to the surface, the local heating rates and surface temperature are considerably higher. An additional shock wave is formed in the reattachment region to turn the flow outside the shear layer parallel to the blunt forebody surface. The formation of reattachment shock wave results in pressure jump downstream of the shock. All these phenomena result in reduced aerodynamic heating and aerodynamic drag. Sometime a blunt faced aerospikes, called the aerodisk is used to enhance the effectiveness of an aerospike.

Due to the above mentioned possibilities, there have been a large number of studies to investigate of the effect of aerospikes and aerodisks. The first study in this regard can be traced back to 1947 where a number of firing tests were done on a blunt and sharp nose bodies at the Langley pilotless Aircraft Research Division [43]. It was suggested in this study that mounting a thin rod with a relatively larger cap on a blunt body could increase the effective fineness ratio of the body and a reduced drag was reported for such vehicles as compared to bodies without spikes but larger than those with pointed spikes.

However, the first comprehensive in this field was done by **Mair** in 1952 [44]. He experimentally studied the flowfield around spiked blunt bodies with flat and hemispherical face. The experiments were conducted at a Mach number of 1.96 and a Reynolds number of  $1.65 \times 10^5$ . The ratio of length of the conically pointed spike to the diameter of model,  $L/D$ , was varied up to 6 in the study. He presented a fine structure of the flowfield around a spiked blunt body and

discussed the impact of the spike length on the structure of the flowfield. Mair, for the first time recorded the flow instability around a spiked blunt body with flat face. He observed that for a certain range of spike length, a significant flow instability is invoked in which the shock wave at the tip changes its shape in a self sustained manner. He also proposed an explanation of this oscillating behaviour of the shock wave based on the pressure difference between flow downstream of the reattachment shock and the flow inside the recirculation zone.

**J.J. Jones**, also in 1952 [45] experimentally investigated the flow around conical blunt bodies with a sharp pointed spike attached to the hemispherical nose at a freestream Mach number of 2.72. The length of the spike named as the “protruding rod” was varied from 1 to 6 times the nose radius of the blunt forebody. Jones, for the first time suggested that there is a single streamline that stagnates on the forebody surface at the reattachment point.

**Piland and Putland** [46] in 1954 coined the term “spike” for the protruding rod at the nose of a blunt body during their analysis of the firing tests of projectiles. They conducted the tests for hemispherical nosed projectile with and without sharp pointed spikes at Mach numbers ranging 0.7 to 1.3 and Reynolds number in the range of  $1.44 \times 10^5$  to  $2.44 \times 10^5$ . The results on two spike lengths showed that there was no reduction in the drag of the vehicle in Mach number range investigated.

The first study on the effect of the aerospike on the aerothermodynamics of a blunt body was done by **Stadler and Neilsen** in 1954 [47]. In this breakthrough investigation, tests were conducted to study the effect of attaching an aerospike at the nose of a hemispherical nosed body on the average heat transfer rates, average recovery temperatures and the pressure distribution on the surface. The spikes used in this investigation were primarily conical nosed spikes with semi-vertex angle of  $10^\circ$ , however some capped spikes with flat face and blunt cones with semi-vertex angle of  $40^\circ$  were also investigated. The length of the spike to the diameter of the spike body was varied between 0.5 and 2.0. All these investigations were conducted in a Mach number range of 0.12 to 5.04 and Reynolds number between  $1.55 \times 10^5$  to  $9.85 \times 10^5$  based on

the diameter of the body and the freestream conditions. It was found that regardless of the length of spike and spike configuration, the addition of spikes at the nose of a hemispherical nosed body approximately doubles the heat transfer rates to the blunt nose as compared to the blunt nose without spike. It was also found that this increase in heat transfer is confined mainly to the forward half area of the hemispherical nose. It was also found that the average temperature recovery factors are lowered due to the addition of spikes, decreasing with increasing the spike length. In regards to the pressure distribution, they found that the addition of spikes reduced the pressure drag of the body by approximately 45 percent for the best configuration. This minimum drag was obtained for the longest spike with which the separation occurred on the shoulder.

**Jones** in 1955 [48] studied the drag coefficients of round noses with conical spikes, called windshields at a Mach number of 2.72 and a Reynolds number of  $1.83 \times 10^6$ . The diameters of the windshield rods investigated were 0.415, 1.125 and 1.464 times the model base diameter. A wide range of lengths and angles of the conical windshields were investigated and it was found that the drag reduction was dependent on both the rod diameter and the windshield geometry. It was also found that for long rods the windshield loses its benefits in reducing drag.

**Beastall and Turner** in 1957 [49] conducted a series of wind tunnel tests at Mach numbers 1.5, 1.6 and 1.8 and Reynolds number of  $1.125 \times 10^6$  on a flat faced cylinder equipped with spikes. The models investigated had either pointed ogive tips or conical aerodisks of variable vertex angles. The protruding spikes used had L/D ratio of up to 4.5. They concluded that the drag of the cylindrical body was reduced considerably by the use of spikes with a conical head. The minimum drag coefficient was obtained with the  $15^\circ$  semi-angle conical nose piece. They also reported hysteresis phenomena during the flow evolution. The drag on the model for a specific spike length was found to be dependent on whether the spike was extended or retracted. They also observed two types of flow unsteadiness with one being violent oscillations while the other being a much milder. It was found that the violent oscillation occurs with

the ogive and the  $15^\circ$  semi-angle conical nose pieces but the mild oscillation does not depend on the nose piece and might occur for any spike extension where there is a dead-air space between the stem and the body. The factors determining the existence of violent oscillations were found to be the cone angle of the nose piece, the position of the nose piece relative to the body and the Mach number and the shape of the body.

**Heramach et. al.** in 1957 [50] studied the impact of violent oscillations on the aerothermal characteristics of the spiked bodies and called these oscillations as ‘pulsating flow’. Their investigation included the study of the effect of pointed spikes of variable tip design and L/D ratio up to 2 fitted on a flat cylindrical model at Mach number of 3.5 and Reynolds number of  $1.73 \times 10^6$ . They found that, for a certain optimum spike length, the pulsating flow could produce up to 22 percent reduction in the temperature recovery factor compared to the laminar boundary layer. Also the frequency of the pulsating flow was found to decrease monotonically with the spike length.

**Bogdnhoff and Vas** [14] in 1959 conducted an important experimental investigation of the pressure and heat transfer distribution on spiked bodies. They studied two models in this investigation; a flat faced cylinder and a hemisphere cylinder in a helium flow at a Mach number of 14 and a Reynolds number of  $3.6 \times 10^5$ . The spike length to body diameter ratio of the pointed spike was varied from 0 to 8 and it was found that the heat transfer to a spiked blunt body is significantly reduced if the separated shear layer remains laminar until reattachment.

**Crawford** in 1959 [51] conducted an exhaustive study of the shape and nature of the flow over a spike-nose hemisphere-cylinder at a Mach number of 6.8 and Reynolds number in the range of  $0.12 \times 10^6$  to  $1.5 \times 10^6$  based on the freestream conditions and the diameter of the base. This investigation was aimed at exploring the effect of the spike length and geometry upon the shape and nature of the flow boundaries, the pressure distribution and the aerodynamic heating on the surface for wide range of Reynolds number including laminar, transitional and turbulent flow regimes. The results showed that the heat transfer to the spiked-nosed hemisphere was greatly influenced by the

nature of the flow over the separated boundary layer. The integrated heat transfer to the hemisphere was increased by the presence of the spike over the greater part of the Reynolds number range studied, but was decreased at lower Reynolds number from  $0.14 \times 10^6$  to  $0.17 \times 10^6$ . The reason for this was that at lower Reynolds numbers the flow was almost laminar at the location of reattachment while at higher Reynolds numbers the flow was turbulent at the reattachment location. The results for pressure distribution showed that the drag coefficient of a hemisphere cylinder was reduced with the increase in spike length until a minimum value is reached. Further increase in spike length caused an increase in the drag coefficient at high Reynolds numbers due to transition in the separation region. The ratio of drag to heat transfer was reduced by the spike in every test regardless of the spike length and the location of transition.

In all the cases, the model's surface pressure and the local heat flux attained their peak values at the reattachment point. The pressure peak attained remained well below the stagnation pressure whereas the peak heat flux ranged from half (at lowest Reynolds number) to double (at highest Reynolds number) the heat transfer rate at the stagnation point of the unspiked model for all spike lengths.

**D J Maull** in 1960 [52], was the first to study the effect of shape of the body nose on the unsteadiness that occurs in the flowfield of a spiked blunt bodies for certain range of spike length to body diameter. He studied the impact of rounding the shoulder of a spiked flat cylindrical model on the flow oscillations at a Mach number of 6.8 and Reynolds number of  $8.5 \times 10^4$ . The  $l/D$  ratio (spike length to body diameter) of the pointed spike was varied from 0 to 3 while the ratio of shoulder radius to the body diameter was varied from 0 (for the flat face) to 0.5 (for hemispherical nose). It was found that for a flat faced cylinder the flow oscillations occur when the spike length is in the range  $0.25 < l/D \leq 2.5$ . It was suggested that the oscillation begins when the spike protrudes through the detached bow shock. However the flow around a spiked body with hemispherical nose was found to be steady for all spike lengths, but for all the bodies with shoulder radius less than half the diameter of the cylin-

drical body, the flow was found to be oscillatory for a certain range of spike lengths. He also explained the mechanism of these oscillations in terms of boundary layer separation and the pressure distribution on the surface. The oscillation starts with the boundary layer on the spike separating near the nose forming a approximately conical dead air region, which if continued to the face of the body would strike it well below the shoulder. To turn the flow just outside just outside the separated layer up the nose of the body a detached shock wave is required. The pressure ratio across this shock and the area behind the shock through which air may be reversed into the dead air region are too high for equilibrium to occur with the mass of air scavenged from the dead air region before the shock. Thus, a non-equilibrium condition occurs with air flowing into the dead air region down the body nose. This enlarges the dead air region forming a nearly normal shock wave at the spike tip which grows and replaces the conical shock wave. The flow into the dead air region goes along the spike and the strong shock wave grows from the spike tip as more air is fed into the dead air region. As it grows the intersection with the bow shock wave of the body moves towards the shoulder of the body. The dead air region by this time is not conical, but blunt in shape, with the reattachment region moving up the face of the body. As the dead air region broadens, the angles through which the external flow must be turned at the end of it pass round the nose decreases and the pressure ratio across the shock decreases and the feeding of air into the dead air region stops. The dead air region collapses and the blunt shock wave moves towards the body and grows weaker. As this shock moves downstream along the spike, separation once again occurs at the spike tip and shock wave becomes conical again. When the excess air in the dead air region has escaped and the strong shock wave originally at the tip has become the bow shock wave of the body the cycle begins again.

Another landmark investigation was done by **C. J. Wood** [53] in 1961 in which he studied the effect of varying spike length and model geometry on the flowfield around a spiked body at Mach 10 and Reynolds number of  $0.5 \times 10^5$ . The model studied was a cone cylinder with vertex angle varying from  $30^\circ$  to  $180^\circ$  and the L/D ratio of the spike was varied up to 5. The investigation

showed that the shape and size of the separated flow is controlled primarily by the flow near the reattachment point, where the dividing streamline is brought to rest by the reattachment pressure rise. He argued that the flow pattern around the spiked cones can be classified into five different categories depending on the spike length and model's semi-vertex angle. For small cone angles the flow does not separate from the spike and the angle of the conical shock wave is the same as that of the conical wave formed without the presence of a spike. As the cone angle is increased, the flow separates from the spike and reattaches on the conical face of the body. As the cone angle is further increased the size of the separated region increases and the reattachment point moves downstream. This continues until the reattachment point reaches the shoulder of the body. If the cone angle further increased such that the semi-apex angle is greater than the shock detachment angle, an oscillatory flow occurs. As the bluntness increases the oscillations become more violent. The last category of flow observed for very short spikes is similar to flow without spikes as the spike does not penetrate the bow shock wave.

**Holden** in 1966 [54] experimentally investigated the heat transfer to spiked axisymmetric bodies in at Mach numbers of 10 and 15 and a Reynolds number of  $0.27 \times 10^6$ . The three models used were hemisphere cylinder, flat cylinder and a cone cylinder with semi-vertex angles of  $30^\circ$ ,  $45^\circ$ ,  $60^\circ$  and  $75^\circ$ . All these models had a pointed spike with  $l/D$  ratio varying up to 4. He extended and refined the classification of flowfield pattern around spiked cones suggested by Wood to higher Mach numbers and Reynolds numbers. He recorded a new flow pattern for the conical models called them mild oscillations. He also showed that the peak heat transfer rate at the reattachment point is directly proportional to the reattachment angle which is dictated by both the spike length and the cone vertex angle.

**Khlevnikov** in 1986 [55] measured the heat transfer rates to spiked spherical models at Mach number of 3 and Reynolds number of  $1.4 \times 10^6$ . The spherical models investigated were equipped with spikes having conical and pyramidal aerodisks and the  $l/D$  ratio of these spikes was varied between

0.283 and 1.78. He concluded that the value of peak heat flux varies inversely with its distance from the spike root.

**McGhee and Staylor** [56] in 1969 investigated the role of mounting a very short pointed spike to blunt conical models at Mach numbers of 3, 4 and 6 and a Reynolds number of  $1.83 \times 10^6$ . They investigated the flow over two conical models with a vertex angle of  $120^\circ$ , and blunt nose radii of 0.25 and 0.5 times the base radius. Three pointed spike configurations with semi vertex angles of  $20^\circ$ ,  $30^\circ$  and  $40^\circ$ , were used in the study. The length of the spikes was varied from 0.055 to 0.083 times the model's base diameter while two different spike diameters of 0.044 and 0.011 times the base diameter were used in the investigation. These models were investigated at  $0^\circ$ ,  $2^\circ$  and  $5^\circ$  angles of incidence. It was concluded that with such short spikes the impacts of both spike tip angle and the diameter of pressure distribution on the model were insignificant.

**Staylor** [57] extended this research to a Mach numbers of up to 9.6 and Reynolds number ranging between  $6 \times 10^4$  and  $23 \times 10^6$ . The tests confirmed that most flow phenomena produced by the spikes were a function of the parameter  $l/d$ , the ratio of spike cylinder length to the bow shock stand-off distance at the stagnation point. For  $l/d \leq 0.7$ , the flow was detached from the spike tip and steady and for  $1.1 \leq l/d \leq 2.2$ , the flow was attached and steady while unsteady flow occurred for all other  $l/d$  values. The heat transfer studies revealed that the heat flux distribution for both the spiked and unspiked cases were independent of Reynolds number. For detached spike flow, the heating distributions were essentially unchanged from those measured on the unspiked models. For attached spike flow, the maximum heating values were generally less than the unspiked stagnation point values and occurred at the point of attachment to the model surface. The total integrated heating of the models increased with the spike length and for steady attached spike flows, the integrated heating ranged from about 1.1 to 1.3 times the unspiked value.

**Huebner et. al.** [13] in 1995 experimentally investigated the range of incidence angles within which the spike would perform the best in terms of drag and aerodynamic heating reduction. The model tested in the investigation was a cylinder with a hemispherical cap with a spike protruding along the axis of



the model. A flat aerodisk was fitted at the tip of the spike and angles of attack were varied from  $0^\circ$  to  $40^\circ$ . A series of wind tunnel tests were conducted at a Mach number of 6 and freestream Reynolds number of  $8.0 \times 10^6/\text{ft}$  to obtain the surface pressure and the temperature rise data. The results obtained indicated that the aerospike is effective for very low angles of attack i.e. less than  $5^\circ$ . For angles of attack more than  $5^\circ$ , the impingement of the aerospike bow shock and the flow separation shock from the recirculation region created by the aerospike causes pressure and temperature rise on the windward side of the dome which exceed the values observed in the same region with the aerospike removed.

**Yamauchi et. al.** [58] in 1995 studied numerically the effect of spike length, Mach number and angle of attack on the flowfield around spiked blunt bodies at supersonic speeds. It was found that the flow at zero degree angle of attack is characterized by the presence of conical shock wave, a separated region in front of the body and the resulting reattachment shock wave. It was found that the drag is greatly influenced by the length of the aerospike, which affects the pressure of the surface in the separated region on the front face of the blunt body. The area of the separated region is extended by the longer spike, but is not influenced by the Mach number. It was found that there is the reduction in the pressure levels in the separated region which causes a reduction in drag. It was also found that at slightly higher angles of attacks the flow becomes spiral and complex but the drag coefficients remain at low values.

**R. C. Mehta** in 2000 [59] carried out numerical simulations over a forward facing spike attached to a blunt body in the Mach number range between 1.3 and 4.5. The time dependent solutions of the axisymmetric Navier Stokes equations were obtained using the Runge-Kutta time integration scheme. It was found that the peak in the pressure and the heat flux is found on the blunt nose region at the same location for all Mach numbers. The shear layer created on the spike region passes through the reattachment shock wave, which is influenced by the conical shock-reattachment interaction, giving rise to the peak surface pressure and heat flux on the heat shield.

**Motoyama et. al.** [60] in 2001 experimentally investigated the pressure and heat flux distribution over a spiked hemisphere-cylinder body at a Mach number of 7 and Reynolds number of  $4 \times 10^5$ . In this elaborate experimental investigation the effect of conical, rounded, and flat end and hemispherical and flat aerodisk of two different sizes and two spike lengths were tested for the heat transfer and drag reduction on the main body besides the effect of pointed spikes on the drag and pitching moments at various angles of attack up to 8 degrees.

**Milicev and Pavlovic** [61] in 2001 and Milicev et. al. [62] in 2002 examined experimentally the effect of modifying the tip of a plain aerospike at a Mach number of 1.89 and a Reynolds number of  $3.8 \times 10^5$ . The model investigated was a hemisphere cylinder with an aerospike of  $l/D=1$  but having different tip shapes viz. pointed cylindrical, rounded cylindrical and conical with two different vertex angles. The angle of incidence of the model was varied from  $-4^\circ$  to  $10^\circ$  and it was found that the spike with the rounded tip has the maximum drag reduction along a favorable increment in lift coefficient.

**Menezes et. al.** [63], [64] studied both experimentally and numerically the effect of an aerodisk on the drag reduction of large angle blunt cones flying at hypersonic speeds. A drag reduction of more than 50 percent was observed at a freestream Mach number of 5.75 for a  $120^\circ$  apex angle blunt cone with a forward facing aerospike having a flat faced aerodisk at moderate angles of attack. However an increase in drag was observed at higher angles of attack. It was suggested that this increase was because of the impingement of the flow separation shock on the windward side of the cone.

**Gopalan et. al.** [65] in 2005 studied the flowfield around a  $120^\circ$  apex angle blunt cone with a forward facing retractable spike at hypersonic Mach numbers. Two different spikes were used in the investigation, one with disc tip while the other with a conical tip, however the ratio of the total length of the spike to the model base diameter was same for both and equal to one. The experiments conducted at a Mach number of 6.99 and a Reynolds number of  $2.46 \times 10^6$  per unit length indicated the presence of slight shock oscillations near the edge of the cone when it is equipped with a disc spike, and pro-

nounced shock oscillations when the model is equipped with a conical spike. However, no pulsation mode oscillations were observed during the experimental investigations.

**Maru et. al. [66]** in 2007 proposed the addition of multiple stabilizer disks to the shaft of the conventional aerospike and designated it as *multiple-row disk*. They experimentally studied the flow oscillation characteristics of aerospikes with such multiple disks. It was suggested that the device can achieve an enhanced aerodynamic controllability and a reduction of flow instability by dividing a single flow separation region into multiple conical cavities. It was also suggested that the pressure oscillations downstream of the cavities were caused by the inside cavity oscillations through the vortices flowing over the cavity. The downstream oscillation level was found to be large only in the case where  $L/D$  is large and freestream Mach number is transonic. Dividing the cavity into multiple parts could reduce the downstream oscillation level of the cavity with  $L/D = 4.0$ . This result verified the effect of stabilizer disks on the reduction of pressure oscillations in the conical cavity flow.

**Kobayashi et. al.[67]** in 2007 studied the aerodynamic characteristics of telescoping aerospikes with multiple stabilizer disks at Mach numbers in the range between 1.1 and 5.1 and Reynolds number in the range of  $0.845 \times 10^7$  to  $2.31 \times 10^7$  per meter. It was found that the disks on the spike shaft produce stable recirculation regions by dividing the single separation flow region into several conical cavity flows, making the flow stable irrespective of the spike length. It was also suggested that adding disks to the aerospike is effective in decreasing zero lift drag and induced drag and the cavities on the conical surface improves the aerodynamic stability of the spiked body as well as the effective control of the retractable aerospike.

**Kalimuthu et. al.** in 2008 [68] and 2010 [69] studied the lift, drag and pitching moment of a spiked hemisphere cylinder at a Mach number of 6 and a Reynolds number of  $9.44 \times 10^5$  at angles of incidences up to 8 degrees. The effect of variable length spike with pointed conical, hemispherical and flat aerodisk was investigated and it was confirmed that the aerodisks are superior to plain conical aerospikes at non zero angles of attack. It was found that the

flowfield immediately behind the flat aerodisk is complex due to back disk geometry. It was suggested that the reattachment point of the shear layer on the body should be moved backwards by choosing the optimal spike length and suitable geometric configuration of the spike tip for an efficient drag reduction. The aerodisk aerospike with  $l/D = 2$  was found to be the most efficient in reducing the drag among those tested.

**Gauer and Paull in 2008** [70] investigated numerically the effect of aerospike at different Mach numbers and different altitudes on the flowfield over the nose cone of a blunt body. They evaluated the heat load reduction and the drag reduction for a large number of aerospike lengths, geometry and configurations at Mach numbers of 5.0, 7.0 and 10.0. The ratio of length of the spike to the diameter of the dome of the nose cone was varied between 1 and 4. The shape of the spike nose tip was chosen either to be a sharp front, a blunt spike or an aerodome mounted on the tip of the spike. Depending on the spike length and the altitude of simulation, the drag reduction was found to be between 2% for the shortest spike to 53% for the longest spike. The blunt spike with  $l/D$  ratio equals to 1 induces a conical bow shock which impinges on the surface of the nose cone. It was found that the sharp spikes can reduce the drag by 35 % but with sharper conical wave. It was suggested that the aerodome can reduce the drag by up to 62% with no shock impingement. On the heat transfer front, it was found that the aerodome configuration can reduce the peak heat load by up to 85% and is most effective. However, the sharp pointed spikes increase the peak heat fluxes drastically.

**Panaras and Drikasis** [15] in 2009 investigated the unsteady supersonic and hypersonic flows around spiked blunt bodies, including the investigation of the effect of flowfield initialization on the flow characteristics. It was concluded that if the geometry of the blunt body is such that a detached bow shock appears, then if the spike is sufficiently long to penetrate through the bow shock, the resulting foreshock-aftershock interaction may lead to unsteady flow. This unsteady flow was characterized by periodic radial inflation of the conical separation bubble which is formed around the forebody. In absence of any freestream noise the separation bubbles collapse downstream leading to

freestream conditions and a new of the so called pulsation mode restarts. When the spike length is increased the pulsation mode is abruptly transformed into the oscillation mode which is characterized by mild radial oscillation of the conically shaped shock system and the accompanying shear layer. During the numerical computations, it was found that the direct implementation of the time accurate procedure in conjunction with uniform freestream conditions lead to spurious pulsation mode. On the other hand the use non –uniform, approximate steady state solutions as initial values leads to physical, experimentally observed behavior.

**Humieres and Stollery** [71] in 2010 investigated the effect of spike on the drag of a 1:100 scaled down model of Apollo program reentry vehicle at hypersonic speeds. The experiments conducted at a Mach number of 8.2 and a Reynolds number of  $9.01 \times 10^6$  per meter could not detect any flow unsteadiness for the range of spike lengths tested. It was also suggested that the drag benefit appears for the shorter spikes length than with a hemispherical body. They further suggested that the drag created by such spiked body can be approximated by the pressure drag generated by a solid cone, with some correction.

**Ahmed and Qin** [72] in 2010 conducted a numerical investigation on a hemispherical body equipped with a spike of variable length and a hemispherical aerodisk of variable size in laminar hypersonic freestream conditions. In this investigation, the spike length was varied up to 2.5 times the base diameter whereas the aerodisk diameter was varied up to 0.4 times the body diameter. Based on the numerical results a novel approach was used to explain the mechanism of drag reduction for both pointed spikes and aerodisks. In this approach, the dividing streamline of the shear layer was assumed to be the outline of the effective body that replaces the original spiked blunt body. It was found that the shape of the effective body and flow stability depend on the energy level of the dividing streamline expressed by its total pressure. It was suggested that the aerodisk are superior to aerospikes firstly as it encourages the separation of the dividing streamline and pushes the separation point radially away from the spike axis, thereby yielding a more slender effective body

and secondly as it reduces the overall downstream pressure by the action of an expansion fan at the aerodisk shoulder. Also the optimum size of the aerodisk for maximum reduction in drag was found to be inversely proportional to the spike length.

**Wang et. al.** [73] in 2010 numerically investigated the influences of the nose configurations such as conical, hemispherical and flat headed spike and the  $l/D$  ratio of the spike on the aerodynamic drag and heating of blunt bodies. It was found that for certain values of  $l/D$  ratio the thermal protective effect of conical spike was superior as compared to hemispherical and flat-headed spikes. The temperature and pressure contour plots for both hemispherical and flat-headed spike were observed to be similar and their aerodynamics drag reduction capabilities were better than those of conical spikes.

**Ahmed and Qin** [74] in 2010 investigated four surrogate models for the design optimization of spiked blunt bodies in hypersonic flight with two design objectives of drag and aerodynamic heating evaluated separately. They found that optimizing the spike design could produce 92% and 13% reduction in drag and aerodynamic heating respectively, compared to the unspiked blunt body. Both optimized designs were found to favor very large spike lengths order of 6 times the diameter of blunt nose, thus it could be concluded that the two design parameters are not strongly competing each other. However, the lengths of optimized spikes are impractical due to structural reasons.

**Gerdroodbary and Hosseinalipour** [75] in 2010 numerically investigated the effectiveness of aerodisk/ aerospike assemblies as retractable drag and heat reduction devices for large angle blunt cones at different angles in hypersonic flow. They obtained full three dimensional solutions of the compressible Navier Stokes equations with  $k-w$  turbulence model at a Mach number of 5.7 and angles of attack of 3, 7, 10 and 12. It was concluded that the drag reduction can be increased by increasing the spike length in the range  $0.3 \leq l/D \leq 1.5$ . It was also observed that the spike with the hemispherical aerodisk exhibit the higher drag reduction as compared to blunt and cut spikes. The drag reductions for all spikes were found to increase with angles of attack. The heat transfer studies revealed that that hemispherical aerodisk spike exhibits the

best heat reduction characteristics. They have recommended the use of aerodome with hemispherical aerodisk with an  $l/D$  ratio of 1 for optimum drag and heat reduction.

## 2.4 CONCLUSION OF THE LITERATURE REVIEW

Based on an extensive literature survey on the aerothermodynamics of blunt bodies with and without passive heat and drag reduction devices like forward facing cavity and aerospikes and aerodisks the following conclusion can be drawn.

- The stagnation point heat transfer rates for spherical blunt bodies can be closely approximated using Lee's Theory.
- The flat faced blunt body has the minimum stagnation point heat transfer rates as compared to other blunt shapes but has a high local heat flux at the sharp corner. The flowfield around a forward facing cavity resembles to that of a flat faced blunt body.
- The reduction in heat transfer rates for deep cylindrical forward facing cavities is because of the oscillation of the bow shock wave. There is a substantial reduction in heat transfer rates for hemispherical cavities as well but very explanation of the heat reduction mechanism could not be found in the literature.
- No recent work on heat reduction by hemispherical cavities and concave nose could be found in the literature. The reduction of drag by plain and aerodisk aerospikes is well established with the aerodisks being superior to pointed aerospikes.

Some investigations have shown that for certain length and tip design the aerospikes can reduce aerodynamic heating to some extent. However, many investigations have shown that some spike lengths can cause an increment in surface heating.

In view of above literature survey the following topics warrant a detailed investigation.

- The effect of hemispherical, parabolic, elliptic and conical cavities on the heat transfer rates and the drag of a blunt body
- The design of an aerodisk aerospike that can substantially reduce the heat transfer rates along with suitable drag reduction of a blunt body.



### 3 THE GOVERNING EQUATIONS

This thesis primarily investigates the effect of cavities and protrusions on the aerothermodynamics of a blunt body in dense atmosphere and thus the fluid model assumed for the investigation is continuum. All continuum flows are primarily governed by the general Navier-Stokes equations which in turn are the mathematical statements of the conservations of mass, momentum, energy and species concentrations. The Navier-Stokes equations can be expressed in different forms and notations depending upon the coordinate system and the model of fluid.

#### 3.1 THE CONTINUITY EQUATION

The divergence form of the global continuity equations can be obtained by applying the law of conservation of mass to an infinitesimally small volume of fluid fixed in space. It is written in vector form as in equation 3.1

$$\frac{\partial \rho}{\partial t} + \nabla \cdot (\rho \vec{V}) = 0 \quad (3.1)$$

In the Cartesian coordinate system, with  $u$ ,  $v$  and  $w$  representing the  $x$ ,  $y$  and  $z$  components, respectively, of the velocity vector  $\vec{V}$  and  $\rho$  representing the density of fluid, the above equation becomes

$$\frac{\partial \rho}{\partial t} + \frac{\partial(\rho u)}{\partial x} + \frac{\partial(\rho v)}{\partial y} + \frac{\partial(\rho w)}{\partial z} = 0 \quad (3.2)$$

### 3.2 THE MOMENTUM EQUATIONS

The gradient form of the momentum equation can be obtained by applying Newton's second law of motion to an infinitesimal control volume of fluid fixed in space. This momentum equation is the statement of the conservation of linear momentum of the fluid volume as can be written as

$$\frac{\partial(\rho V)}{\partial t} + \nabla \cdot (\rho V) \mathbf{V} = \rho \cdot \mathbf{f} + \nabla \cdot \mathbf{\Pi}_{i,j} \quad (3.3)$$

In equation 3.3,  $\rho \cdot \mathbf{f}$  is the body force per unit volume and  $\mathbf{\Pi}_{i,j}$  is the stress tensor which consists of normal and shearing stresses which in turn are represented by the components of stress tensor as expressed in equation 3.4.

$$\Pi_{i,j} = -p\delta_{ij} + \mu \left( \frac{\partial u_i}{\partial x_j} + \frac{\partial u_j}{\partial x_i} \right) + \delta_{ij} \lambda \frac{\partial u_k}{\partial x_k} \quad (i, j, k=1, 2, 3) \quad (3.4)$$

where  $p$  is the pressure and  $\delta_{ij}$  is the Kronecker delta function;  $u_1, u_2$  and  $u_3$  represents the three components of the velocity vector  $\mathbf{V}$ ;  $\mu$  is the molecular viscosity coefficient and  $\lambda$  is the second coefficient of viscosity.

The molecular viscosity coefficient and the second viscosity coefficient are related to each other through the coefficient of bulk viscosity  $\kappa$ , as hypothesized by Stokes, given in equation 3.5.

$$\kappa = \frac{2}{3}\mu + \lambda \quad (3.5)$$

However, the coefficient of bulk viscosity is often negligibly small for Newtonian fluids, yielding equation 3.6

$$\lambda = -\frac{2}{3}\mu \quad (3.6)$$

With above relation the momentum equation can be rewritten with substantial derivative notation as equation 3.7.

$$\rho \frac{DV}{Dt} = \rho \cdot \mathbf{f} - \nabla \cdot p + \frac{\partial}{\partial x_j} \left[ \mu \left( \frac{\partial u_i}{\partial x_j} + \frac{\partial u_j}{\partial x_i} \right) - \frac{2}{3} \delta_{ij} \mu \frac{\partial u_k}{\partial x_k} \right] \quad (3.7)$$

or,

$$\rho \frac{DV}{Dt} = \rho \cdot \mathbf{f} - \nabla \cdot p + \frac{\partial}{\partial x_j} [\boldsymbol{\tau}_{ij}] \quad (3.8)$$

where  $\boldsymbol{\tau}_{ij}$  is the viscous stress tensor.

In Cartesian coordinate system, the above equation can be written, with  $u$ ,  $v$  and  $w$  respectively as the  $x$ ,  $y$  and  $z$  component of the velocity, as

X-momentum:

$$\frac{\partial(\rho u)}{\partial t} + \nabla \cdot (\rho u \mathbf{V}) = -\frac{\partial p}{\partial x} + \frac{\partial \tau_{xx}}{\partial x} + \frac{\partial \tau_{yx}}{\partial y} + \frac{\partial \tau_{zx}}{\partial z} + \rho \cdot \mathbf{f}_x \quad (3.9a)$$

Y-momentum:

$$\frac{\partial(\rho v)}{\partial t} + \nabla \cdot (\rho v \mathbf{V}) = -\frac{\partial p}{\partial y} + \frac{\partial \tau_{xy}}{\partial x} + \frac{\partial \tau_{yy}}{\partial y} + \frac{\partial \tau_{zy}}{\partial z} + \rho \cdot \mathbf{f}_y \quad (3.9b)$$

Z-momentum:

$$\frac{\partial(\rho w)}{\partial t} + \nabla \cdot (\rho w \mathbf{V}) = -\frac{\partial p}{\partial z} + \frac{\partial \tau_{xz}}{\partial x} + \frac{\partial \tau_{yz}}{\partial y} + \frac{\partial \tau_{zz}}{\partial z} + \rho \cdot \mathbf{f}_z \quad (3.9c)$$

In above equations the components of the viscous stress tensor are given by

$$\tau_{xx} = \lambda(\nabla \cdot \mathbf{V}) + 2\mu \frac{\partial u}{\partial x} \quad (3.10a)$$

$$\tau_{yy} = \lambda(\nabla \cdot \mathbf{V}) + 2\mu \frac{\partial v}{\partial y} \quad (3.10b)$$

$$\tau_{zz} = \lambda(\nabla \cdot \mathbf{V}) + 2\mu \frac{\partial w}{\partial z} \quad (3.10c)$$

$$\tau_{xy} = \tau_{yx} = \mu \left[ \frac{\partial v}{\partial x} + \frac{\partial u}{\partial y} \right] \quad (3.10d)$$

$$\tau_{xz} = \tau_{zx} = \mu \left[ \frac{\partial w}{\partial z} + \frac{\partial u}{\partial x} \right] \quad (3.10e)$$

$$\tau_{yz} = \tau_{zy} = \mu \left[ \frac{\partial w}{\partial y} + \frac{\partial v}{\partial z} \right] \quad (3.10f)$$

### 3.3 THE ENERGY EQUATION

The energy equation for a viscous hypersonic flow can readily be obtained by applying the law of conservation energy i.e. the first law of thermodynamics to an infinitesimally small volume of fluid fixed in space. The energy equation in conservation form is given by equation 3.11.

$$\frac{\partial E_t}{\partial t} + \nabla \cdot E_t \mathbf{V} = \frac{\partial Q}{\partial t} - \nabla \cdot \mathbf{q} + \rho \mathbf{f} \cdot \mathbf{V} + \nabla \cdot (\Pi_{ij} \cdot \mathbf{V}) \quad (3.11)$$

where  $E_t$  is the total energy per unit volume of fluid and is given by

$$E_t = \rho(e + V^2 + \text{potential energy} + \text{vibrational energy} + \dots) \quad (3.12)$$

with  $e$  as the internal energy per unit mass.

The first term of the left hand side of the energy equation 3.11 represents the rate of change of total energy per unit volume of the fluid while the second

term on the same side is the energy lost per unit volume by convection through the control surfaces. The term  $\frac{\partial Q}{\partial t}$  represents the rate at which heat is supplied to the unit volume of fluid and term  $\nabla \cdot \mathbf{q}$  denotes the rate at which heat is lost through the control surfaces, per unit volume, by the process of conduction. The heat transfer per unit volume  $\mathbf{q}$  is related to the temperature gradient by the Fourier Law expressed as

$$\mathbf{q} = -k\nabla T \quad (3.13)$$

where  $k$  is the coefficient of thermal conductivity and  $T$  is the temperature. The third and fourth term of the energy equation (3.11) represent the work done on the fluid per unit volume by the body forces and the surface forces respectively.

For a Cartesian coordinate system, the conservation form of the energy equation can be rewritten as

$$\begin{aligned} & \frac{\partial E_t}{\partial t} - \frac{\partial Q}{\partial t} - \rho(f_x u + f_y v + f_z w) + \frac{\partial}{\partial x}(E_t u + pu - u\tau_{xx} - v\tau_{xy} - w\tau_{xz} + \mathbf{q}) \\ & + \frac{\partial}{\partial y}(E_t v + pv - u\tau_{xy} - v\tau_{yy} - w\tau_{zy} + \mathbf{q}) \\ & + \frac{\partial}{\partial z}(E_t w + pw - u\tau_{xz} - v\tau_{yz} - w\tau_{zz} + \mathbf{q}) = 0 \end{aligned} \quad (3.14)$$

In the above equation, the heat flux vector,

$$\mathbf{q} = q_x \mathbf{i} + q_y \mathbf{j} + q_z \mathbf{k} \quad (3.15)$$

where,

$$q_x = -k \frac{\partial T}{\partial x} \quad (3.16a)$$

$$q_y = -k \frac{\partial T}{\partial y} \quad (3.16b)$$

$$q_z = -k \frac{\partial T}{\partial z} \quad (3.16c)$$

### 3.4 THE EQUATION OF STATE

In order to close the system of equations governing the physics of compressible viscous flow, viz. the Navier Stokes equations, additional equations are required that establish the relations between the thermodynamic variables and between the thermodynamics variables and the transport properties viz. viscosity ( $\mu$ ) and thermal conductivity ( $k$ ). The thermodynamic state of a fluid with a fixed chemical composition can be determined by any two independent thermodynamic variables. Thus, for a gas mixture without any finite rate chemical reaction or diffusion, the *equation of state*, assuming negligible intermolecular forces can be given equations 3.17.

$$p = \rho RT \quad (3.17)$$

where  $R$  is the gas constant. For air, at standard conditions,  $R=287 \text{ m}^2/(\text{s}^2\text{K})$ . The gases which obey the above equation of state are called as *perfect gases*. An additional equation required to close the system of Navier Stokes equations, can be obtained by assuming the perfect gas to be at relatively low temperatures wherein the specific heats at constant pressure ( $c_p$ ) and at constant volume ( $c_v$ ) remains constant for the gas. Such gases with constant values of  $c_p$ ,  $c_v$  and thus constant  $\gamma$  are called *calorifically perfect gases*. For a calorifically perfect gas, the internal energy can be related to the temperature through equation (3.18).

$$e = c_v T \quad (3.18)$$

The coefficients of viscosity and thermal conductivity can be related to the thermodynamic variables using the kinetic theory for gases. According to the Sutherland's formula these quantities can be given by equations (3.19a) and (3.19b) respectively.

$$\mu = C_1 \frac{T^{3/2}}{T + C_2} \quad (3.19a)$$

$$k = C_3 \frac{T^{3/2}}{T + C_4} \quad (3.19b)$$

where  $C_1$ ,  $C_2$ ,  $C_3$  and  $C_4$  are constants for a given gas. The values of these constants for air at moderate temperatures are:

$$C_1 = 1.485 \times 10^{-06} \text{ kg}/(\text{m s } \sqrt{\text{K}}), \quad C_2 = 110.4 \text{ K},$$

$$C_3 = 2.495 \times 10^{-03} \text{ (kg m)} / (\text{s}^3 \text{ K}^{3/2}) \quad \text{and} \quad C_4 = 194 \text{ K}$$

Most often a non-dimensional parameter called the *Prandtl number* ( $Pr$ ) is used to define the relation between the above two coefficients. This relation is known as Reynolds Analogy given by equation (3.20).

$$k = \frac{\mu c_p}{Pr} \quad (3.20)$$

The Prandtl number is approximately constant for most gases; for air at standard conditions  $Pr=0.72$ .

### 3.5 THE ENERGY EQUATION FOR HIGH TEMPERATURE GAS

The energy equation and the closure equations given in section 3.1.3 are valid only up to moderate temperatures. Hypersonic flow is generally associated with very high temperatures of the order of thousand degrees Celsius. As the temperature of the gas is increased to higher values, the assumption of calorifically perfect gas is no longer valid and the gas becomes *thermally perfect*. A thermally perfect gas is one whose specific heats are functions only of temperature. For air this happens at about 800 K at sea level standard pressure, wherein the vibrational energy of the molecule gets excited. If the temperature is further increased, the chemical reactions begin to occur. For air at sea level pressure, its O<sub>2</sub> molecules starts to dissociate into O atoms at about 2000 K, and the assumption of thermally perfect gas fails on the onset of this temperature.

Taking into account the effect of high temperatures, the governing energy equation 3.13 should be modified to accommodate the diffusion terms. The total energy  $E_t$  should now include the vibrational, rotational, translational and electronic energies as well. The resultant Energy equation can be given in substantial derivative form by equation 3.21.

$$\begin{aligned} \rho \frac{DE_t}{Dt} = \frac{\partial Q}{\partial t} - \nabla \cdot \mathbf{q} - \nabla \cdot p\mathbf{V} + \frac{\partial}{\partial x}(u\tau_{xx}) + \frac{\partial}{\partial y}(u\tau_{yx}) + \frac{\partial}{\partial z}(u\tau_{zx}) + \frac{\partial}{\partial x}(v\tau_{xy}) \\ + \frac{\partial}{\partial y}(v\tau_{yy}) + \frac{\partial}{\partial z}(v\tau_{zy}) + \frac{\partial}{\partial x}(w\tau_{xz}) + \frac{\partial}{\partial y}(w\tau_{yz}) + \frac{\partial}{\partial z}(w\tau_{zz}) \end{aligned} \quad (3.21)$$

where the heat flux vector  $\mathbf{q}$  also includes the energy flux due to diffusion and radiation as given by equation 3.22

$$\mathbf{q} = -k\nabla T + \sum_i \rho_i U_i h_i + \mathbf{q}_R \quad (3.22)$$



In equation 3.22, the second term represents the energy flux due to diffusion is the summation energy fluxes due to diffusion of all species present in the mixture. The variables  $\rho_i$ ,  $U_i$ , and  $h_i$  respectively are the density, diffusion velocity and the enthalpy of the  $i^{\text{th}}$  species in the mixture. The term  $q_R$  represents the energy transport through the phenomenon of radiation.

### 3.6 THERMODYNAMIC PROPERTIES OF A CHEMICALLY REACTING MIXTURE

For most of the chemically reacting gases, each species in the mixture can be assumed to obey the perfect gas equation of state with negligible intermolecular forces. Additionally the gas can be assumed to be a mixture of thermally perfect gases. The equation of state for a mixture of perfect gases can be given by

$$p = \frac{\mathcal{R}}{\mathcal{M}} T \quad (3.23)$$

where  $\mathcal{R}$  is the universal gas constant (8314.34 J/kg mol K) and  $\mathcal{M}$  is the molecular weight of the mixture. The molecular weight of the mixture in equation (3.24) can be calculated using equation 3.24

$$\mathcal{M} = \left( \sum_{i=1}^n \frac{c_i}{\mathcal{M}_i} \right)^{-1} \quad (3.24)$$

In equation (3.24)  $c_i$  is the mass fraction of the  $i^{\text{th}}$  species and  $\mathcal{M}_i$  is the molecular weight of each species.

The thermodynamic properties of a mixture of gases in thermo-chemical equilibrium is a function two state variable only viz. Temperature and pressure. The thermodynamic properties of a mixture of perfect gases in thermal equilibrium and chemical non-equilibrium on the other hand are dependent on the

mass fraction of each species as well. The specific enthalpy and specific heat of each species in the mixture are given respectively by equations 3.25 and 3.26.

$$h_i = C_{1,i}T + h_i^0 \quad (3.25)$$

$$c_{p,i} = C_{2,i} \quad (3.26)$$

where the coefficients  $C_{1,i}$  and  $C_{2,i}$  for each species is a functions of temperature and  $h_i^0$  is enthalpy of formation of individual species. The coefficients for the curve fits of piecewise polynomial variations of specific heats and enthalpy of individual species is readily available in the literature [76, 77]. The enthalpy and specific heat of the mixture of perfect gases in turn are given by equations 3.27 and 3.28.

$$h = \sum_{i=1}^n c_i h_i \quad (3.27)$$

$$c_p = \sum_{i=1}^n c_i c_{p,i} \quad (3.28)$$

### 3.7 TRANSPORT PROPERTIES OF A CHEMICALLY REACTING MIXTURE

For a multispecies gas mixture such as found in chemically reacting hypersonic flow, the values of coefficients of viscosity  $\mu$  and thermal conductivity  $k$  for the mixture must be found from the values of  $\mu_i$  and  $k_i$  of each chemical species  $i$  in the mixture by means of *mixture rules*. Equation (3.29) represents a general mixture rule called the *Wilke's rule* for the coefficient of viscosity

$$\mu = \sum_i \frac{X_i \mu_i}{\sum_j X_j \phi_{ij}} \quad (3.29)$$

with

$$\phi_{ij} = \frac{1}{8} \left( 1 + \frac{\mathcal{M}_i}{\mathcal{M}_j} \right)^{-\frac{1}{2}} \left[ 1 + \left( \frac{\mu_i}{\mu_j} \right)^{\frac{1}{2}} \left( \frac{\mathcal{M}_i}{\mathcal{M}_j} \right)^{\frac{1}{4}} \right]^2 \quad (3.30)$$

In equations (3.29) and (3.30),  $\mathcal{M}_i$  and  $X_i$  are the molecular weight and mole fraction of the  $i^{\text{th}}$  species respectively and  $i$  and  $j$  are subscripts denoting various species. The molecular viscosity of individual species  $\mu_i$  appearing in equations 3.29 and 3.30 can be derived from the kinetic theory of gases as

$$\mu_i = \frac{2.6693 \times 10^{-06} \sqrt{\mathcal{M}_i T}}{\sigma_i^2 \Omega_{\mu i}} \quad (3.31)$$

where,  $\sigma_i$  and  $\Omega_{\mu i}$  are characteristic molecular diameter and Collision integrals respectively for the  $i^{\text{th}}$  species. In a similar manner, the coefficient of thermal conductivity of the mixture,  $k$  can be given by

$$k = \sum_i \frac{X_i k_i}{\sum_j X_j \phi_{ij}} \quad (3.32)$$

where,  $\phi_{ij}$  is same as given by equation 3.30. The thermal conductivity of individual species  $k_i$  is given by

$$k_i = \frac{15}{4} \left( \frac{\mu_i R}{\mathcal{M}_i} \right) \left( \frac{4}{15} \frac{c_{p,i} \mathcal{M}_i}{R} + \frac{1}{3} \right) \quad (3.33)$$

Finally the multi-component diffusion coefficient of a species  $i$  into the multi-species mixture,  $\mathcal{D}_{im}$  can be computed using the binary diffusion coefficients  $\mathcal{D}_{ij}$  of individual species as given in equation 3.34.

$$\mathcal{D}_{im} = \frac{(1 - X_i)}{\sum_j \left( X_j / \mathcal{D}_{ij} \right)} \quad (3.34)$$

The binary diffusion coefficients for diffusion of species  $i$  into species  $j$ , can be derived from the kinetic theory as,

$$\mathcal{D}_{ij} = 0.0018583 \frac{\sqrt{T^3 \left( \frac{1}{\mathcal{M}_i} + \frac{1}{\mathcal{M}_j} \right)}}{p \sigma_{ij}^2 \Omega_{D,ij}} \quad (3.35)$$

### 3.8 THE CHEMICAL NON-EQUILIBRIUM

A chemically reacting mixture of gases can be classified as to be under frozen, non equilibrium and equilibrium conditions depending on the characteristic time scales of the chemical reactions and the flow. The ratio of characteristic flow time  $\tau_F$  and characteristic chemical time scale  $t_C$ , called as Damkohler number  $Da$ , is often used to define the chemical state of a flow.

If  $Da = \tau_F / t_C \ll 1$ , no reactions take place and the flow is said to be *frozen*. If, one the other hand,  $Da = \tau_F / t_C \gg 1$ , the chemical reactions are significantly faster than the characteristic flow time and there are enough collisions to complete all chemical reactions, the flow is termed as chemical *equilibrium* flows. For chemical equilibrium flows, the concentration of individual chemical species is a function of local pressure and temperature only. Between the two extreme cases, if  $Da = \tau_F / t_C \approx 1$ , the reaction rates are finite and there are not

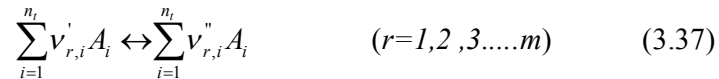
enough collision between the reactant to complete the reactions. Such flows are called to be in *chemical non equilibrium*.

For chemical nonequilibrium flows, since the concentrations of different species are continuously changing due to the production of new species and the destruction of old species, additional species continuity equations are required for each species. Applying the law of conservation of mass, the following equation is readily obtained.

$$\rho \frac{Dc_i}{Dt} + \nabla \cdot (\rho_i \mathbf{U}_i) = \dot{w}_i \quad (3.36)$$

where  $\rho_i$  is the species density,  $\mathbf{U}_i$  is the species diffusion velocity,  $c_i$  is species mass fraction and  $\dot{w}$  is the rate of production of species  $i$ . The rate of production of each species  $\dot{w}$  can be evaluated by using an appropriate chemistry model that can simulate the chemical reactions.

A chemistry model consisting of  $m$  reactions,  $n$  species and  $n_t$  reactants can be symbolically represented by



where  $\nu'_{r,i}$  and  $\nu''_{r,i}$  are the stoichiometric coefficients and  $A_i$  is the chemical symbol of the species.

Once the chemical reaction mechanism is set up, the rate of production of each species  $i$  can be computed using the Law of Mass Action which can be given by

$$\dot{w}_i = \mathcal{M}_i \sum_{r=1}^m (\nu''_{r,i} - \nu'_{r,i}) \left[ K_{f,r} \prod_{j=1}^{n_t} (\rho \gamma_j)^{\nu'_{r,j}} - K_{b,r} \prod_{j=1}^{n_t} (\rho \gamma_j)^{\nu''_{r,j}} \right] \quad (3.38)$$

where  $K_{f,r}$  and  $K_{b,r}$  are the forward and backward reaction rates for the  $r^{\text{th}}$  reaction and  $\gamma_j$  is the mole mass ratio of the reactants given by equation 3.39.

$$\gamma_j = \begin{cases} \frac{c_j}{\mathcal{M}_j} & j = 1, 2, \dots, n \\ \sum_{i=1}^n Z_{j-n,i} \gamma_i & j = n+1, n+2, \dots, n_t \end{cases} \quad (3.40)$$

where  $Z_{j-n,i}$  are the third body efficiencies. The forward and backward reaction rates in equation 3.38 can be computed using the Arrhenius formula. The Arrhenius formula for the forward reaction rate is given by equation 3.41.

$$K_{f,r} = A_{f,r} \bar{T}^{\beta_{f,r}} e^{\left( \frac{E_{a,f,r}}{RT} \right)} \quad (3.41)$$

In equation 3.41,  $A_{f,r}$ ,  $\beta_{f,r}$  and  $E_{a,f,r}$  are the pre-exponential factor, temperature exponent and activation energy for the reaction respectively while  $\bar{T}$  is the rate controlling temperature which for thermal equilibrium is equal to  $T$ .

The backward reaction rates in equation 3.40 can be computed from the forward reaction rates using relation 3.42.

$$K_{b,r} = \frac{K_{f,r}}{K_r} \quad (3.42)$$

The equilibrium constant for the  $r^{\text{th}}$  reaction  $K_r$ , can be computed from equation 3.43.

$$K_r = \exp\left( \frac{\Delta S_r}{R} - \frac{\Delta H_r}{RT} \right) \left( \frac{P_{atm}}{RT} \right)^{\sum_{i=1}^{n_t} (v_{r,i}'' - v_{r,i}')} \quad (3.43)$$

where the term within the exponential function are given by

$$\frac{\Delta S_r}{R} = \sum_{i=1}^{n_i} (v_{r,i}'' - v_{r,i}') \frac{S_i}{R} \quad (3.44)$$

$$\frac{\Delta H_r}{R} = \sum_{i=1}^{n_i} (v_{r,i}'' - v_{r,i}') \frac{h_i}{RT} \quad (3.45)$$

In equations 3.44 and 3.45,  $S_i$  and  $h_i$  are the entropy and enthalpy of the  $i^{th}$  species evaluated at temperature  $T$  and atmospheric pressure  $p_{atm}$ .

### 3.9 TURBULENT FLOWS

The unsteady Navier-Stokes equations are generally sufficient to solve the turbulent flowfield completely in a continuum regime. All levels of turbulence can be captured by the *Direct Numerical Simulation* (DNS) of the transient Navier stokes equations. The DNS require that all length scales of turbulence are resolved, from the smallest eddies to scales of the order of the physical dimensions of the problem under consideration. For the direct numerical simulation, all computations need to be done in three dimensions with grid and time step small enough to capture the small scale motions in a time accurate manner. These requirements put a large demand on the computer resources and such simulations are practically impossible for any real engineering problem with present day computer capabilities. Thus, the present day researches intend to capture the turbulence flow through the time averaged Navier-Stokes equations. In this statistical method, commonly called as *Reynolds averaged Navier-Stokes* (RANS) equations, the time averaging of flow variables is carried out in order to separate the time-mean quantities from the fluctuations. This averaging introduces new variables in the system of equations, thus require additional equations to close the system of equations. The new equations can be formulated by what is called the *turbulence modeling*. Two types averaging is currently in use viz. classical Reynolds averaging and mass weighted averaging, of which the later is primarily used for compressible flows.

### 3.9.1 Equations for Turbulence

The mass weighted (Favre) averages for any variable  $f$  is given by

$$f = \tilde{f} + f'' \quad (3.46)$$

where the mean quantity  $\tilde{f}$  and the fluctuating part  $f''$  are respectively given by

$$\tilde{f} = \frac{\overline{\rho f}}{\rho} \quad (3.47a)$$

$$f'' = \frac{\overline{\rho' f'}}{\rho} \quad (3.47b)$$

and the fluctuating part has the property

$$\overline{\rho f''} = 0 \quad (3.48)$$

With mass averages for the dependent variable the Navier-Stokes equations can be written as

Continuity equation:

$$\frac{\partial \bar{\rho}}{\partial t} + \frac{\partial (\bar{\rho} \tilde{u})}{\partial x} + \frac{\partial (\bar{\rho} \tilde{v})}{\partial y} + \frac{\partial (\bar{\rho} \tilde{w})}{\partial z} = 0 \quad (3.49)$$

Momentum Equations(x-only):

$$\begin{aligned} \frac{\partial}{\partial t} (\bar{\rho} \tilde{u}) + \frac{\partial}{\partial x} (\bar{\rho} \tilde{u} \tilde{u}) + \frac{\partial}{\partial y} (\bar{\rho} \tilde{u} \tilde{v}) + \frac{\partial}{\partial z} (\bar{\rho} \tilde{u} \tilde{w}) = - \frac{\partial \tilde{p}}{\partial x} + \frac{\partial}{\partial x} (\tilde{\tau}_{xx} - \overline{\rho u'' u''}) \\ + \frac{\partial}{\partial y} (\tilde{\tau}_{yx} - \overline{\rho u'' v''}) + \frac{\partial}{\partial z} (\tilde{\tau}_{zx} - \overline{\rho u'' w''}) \end{aligned} \quad (3.50)$$

where the mean viscous stresses  $\tilde{\tau}_{ij}$  can be given, neglecting the fluctuations in viscosity, as



$$\tilde{\tau}_{ij} = \mu \left[ \left( \frac{\partial \tilde{u}_i}{\partial x_j} + \frac{\partial \tilde{u}_j}{\partial x_i} \right) - \frac{2}{3} \delta_{ij} \frac{\partial \tilde{u}_k}{\partial x_k} \right] + \mu \left[ \left( \frac{\partial \overline{u''_i}}{\partial x_j} + \frac{\partial \overline{u''_j}}{\partial x_i} \right) - \frac{2}{3} \delta_{ij} \frac{\partial \overline{u''_k}}{\partial x_k} \right] \quad (3.51)$$

where  $i, j, k$  are dummy variables representing  $x, y$  and  $z$  directions respectively.

Energy equation:

The energy equation for turbulent flows in compact tensor notation employing Einstein summation convention can be written as

$$\begin{aligned} \frac{\partial}{\partial t} (\overline{\rho c_p \tilde{T}}) + \frac{\partial}{\partial x_j} (\overline{\rho c_p \tilde{T} \tilde{u}_j}) = & \frac{\partial \overline{p}}{\partial t} + \tilde{u}_j \frac{\partial \overline{p}}{\partial x_j} + \overline{u''_j \frac{\partial p}{\partial x_j}} \\ & + \frac{\partial}{\partial x_j} \left( k \frac{\partial \tilde{T}}{\partial x_j} + k \frac{\partial \overline{T''}}{\partial x_j} - c_p \overline{\rho T'' u''_j} \right) + \overline{\Phi} \end{aligned} \quad (3.52)$$

where

$$\overline{\Phi} = \overline{\tau_{ij} \frac{\partial u_i}{\partial x_j}} = \tilde{\tau}_{ij} \frac{\partial \tilde{u}_i}{\partial x_j} + \overline{\tau_{ij} \frac{\partial u''_i}{\partial x_j}} \quad (3.53)$$

### 3.9.2 Turbulence Modelling

Turbulence models to close the Reynolds averaged N-S equations can broadly be divided into two groups depending on whether the model is based on *Boussinesq assumption* or otherwise. As per Boussinesq assumption, the apparent turbulent shearing stresses are related to the rate of mean strain through an eddy viscosity. For a general Reynolds stress, the Boussinesq assumption gives

$$-\overline{\rho u'_i u'_j} = 2\mu_T S_{ij} - \frac{2}{3} \delta_{ij} \left( \frac{\mu_T \partial u_k}{\partial x_k} + \rho \bar{k} \right) \quad (3.54)$$

where  $\mu_T$  is the turbulent viscosity. The turbulent kinetic energy  $\bar{k}$  and the rate mean strain tensor  $S_{ij}$  in equation 3.54 are respectively given by

$$\bar{k} = \frac{\overline{u'_i u'_j}}{2} \quad (3.55)$$

and

$$S_{ij} = \frac{1}{2} \left( \frac{\partial u_i}{\partial x_j} + \frac{\partial u_j}{\partial x_i} \right) \quad (3.56)$$

The above assumption is commonly known as eddy- viscosity approach. By applying the eddy-viscosity approach to the Favre-averaged Navier Stokes equations, the dynamic viscosity coefficients in viscous stress tensor (equations 3.10 a-f) is simply replaced by the sum of a laminar and a turbulent component i.e.

$$\mu = \mu_L + \mu_T \quad (3.57)$$

In above formulation, the laminar viscosity can be computed using the kinetic theory of gases or by some empirical formulations like the Sutherland's formula. Similarly, using the Reynolds Analogy the thermal conductivity in equations 3.15 (a-c) can be evaluated as

$$k = k_L + k_T = c_p \left( \frac{\mu_L}{Pr_L} + \frac{\mu_T}{Pr_T} \right) \quad (3.58)$$

where  $Pr_L$  and  $Pr_T$  are laminar and turbulent Prandtl numbers corresponding to laminar and turbulent viscosities  $\mu_L$  and  $\mu_T$ . Once the value of eddy viscosity  $\mu_T$  is known, the Navier Stokes equations for turbulent flows can be solved by adding the eddy viscosity to the laminar viscosity terms.

The turbulence models that use Boussinesq eddy-viscosity assumption are referred as first order models and those not based on this assumption are referred to as second order models. Most of the engineering simulations at

present are done with first order models. Further the first order models can be classified as zero-equation, one equation and two-equations depending on the number of closure equations.

Since this thesis primarily investigates the aerodynamic heating under dense atmospheric conditions the flow is assumed to be turbulent and a suitable turbulence model needs to be implemented. A wide range of turbulence closures, based on the order of closer and the number of additional equations can be found in the literature [78]. The computational expense increases with the increasing number of equations with increased accuracy of the predicted results. Among the first order closer models, the most widely used model of hypersonic applications that have been implemented in the Fluent Code are the one equation Spalart-Allmaras (SA) model [79, 80], two-equation Wilcox  $k-\omega$  [78] model and the Menter Shear Stress Transport  $k-\omega$  (Menter  $k-\omega$  SST) model[81]. A detailed validations and assessments of these turbulence models for use in hypersonic flow conditions can be found in the literature [82-86]. The one equation SA model is not only computationally cheap but also very robust and provides reasonably accurate results for the hypersonic flows. The main advantage besides the computational expenses, of using this turbulence model for most of the simulations is its insensitiveness to the wall  $y^+$  value and the freestream turbulence [84]; however it produces the most accurate results for  $y^+ \leq 1$ . The Wilcox  $k-\omega$  model over predicts the turbulent heating along with being very sensitive to freestream turbulence intensities. The Menter SST version of the  $k-\omega$  turbulence model combines the near wall model of the Wilcox  $k-\omega$  model and the shear layer and freestream formulation of the  $k-\epsilon$  turbulence model and produces very accurate results for a wide range of hypersonic applications. The Menter SST  $k-\omega$  model besides being more sensitive to the wall  $y^+$  distance, freestream turbulence intensity and grid resolution as compared to the SA model, also tends to over predict the turbulent shear stresses and heating rates. Because of the above mentions reasons the Menter SST  $k-\omega$  turbulence model has been used in this research for only limited cases for verification of results produced by the SA turbulence model.

### 3.9.3 Spalart-Allmaras Turbulence Model

The transported quantity  $\tilde{\nu}$ , in the SA model is called as the *Modified Turbulent Viscosity* which is identical to the turbulent kinematic viscosity except in the near wall region. The transport equation for the modified turbulent viscosity  $\tilde{\nu}$ , is given as,

$$\frac{\partial}{\partial t}(\rho\tilde{\nu}) + \frac{\partial}{\partial x_i}(\rho\tilde{\nu}u_i) = G_v + \frac{1}{\sigma_{\tilde{\nu}}} \left[ \frac{\partial}{\partial x_j} \left\{ (\mu + \rho\tilde{\nu}) \frac{\partial \tilde{\nu}}{\partial x_j} \right\} + C_{b2}\rho \left( \frac{\partial \tilde{\nu}}{\partial x_j} \right)^2 \right] - Y_v + S_{\tilde{\nu}} \quad (3.59)$$

In equation (3.59),  $G_v$  represents the production of turbulent viscosity;  $Y_v$  represents the destruction of turbulent viscosity due to viscous damping and wall blocking,  $\sigma_{\tilde{\nu}}$  and  $C_{b2}$  are the model constants and  $S_{\tilde{\nu}}$  is the user defined source term.

#### Computing Turbulent Viscosity

The turbulent viscosity,  $\mu_T$  is computed from the modified turbulence viscosity through relation (3.49)

$$\mu_T = \rho\tilde{\nu}f_{v1} \quad (3.60)$$

where

$$f_{v1} = \frac{\chi^3}{\chi^3 + C_{v1}^3} \quad (3.61a)$$

and

$$\chi = \frac{\tilde{\nu}}{\nu} \quad (3.61b)$$

#### Modeling Production of Turbulence

The production of turbulent kinematic viscosity in the SA model is given as,

$$G_v = C_{b1} \rho \tilde{S} \tilde{v} \quad (3.62)$$

with

$$\tilde{S} \equiv S + \frac{\tilde{v}}{\kappa^2 d^2} f_{v2} \quad \text{and} \quad f_{v2} = 1 - \frac{\chi}{1 + \chi f_{v1}} \quad (3.63)$$

where  $C_{b1}$  and  $\kappa$  are model constants  $d$  is the nearest distance from the wall and  $S$  is a scalar measure of the deformation tensor. The quantity  $S$  for a strain-vorticity based production scheme can be given as,

$$S \equiv |\Omega_{ij}| + C_{prod} \min(0, |S_{ij}| - |\Omega_{ij}|) \quad (3.64)$$

where

$$C_{prod} = 2.0; \quad |\Omega_{ij}| \equiv \sqrt{2\Omega_{ij}\Omega_{ij}} \quad \text{and} \quad |S_{ij}| \equiv \sqrt{2S_{ij}S_{ij}} \quad (3.65)$$

The mean rate of rotation tensor  $\Omega_{ij}$  and the mean strain rate  $S_{ij}$  appearing in equation 3.65 are defined respectively as,

$$\Omega_{ij} = \frac{1}{2} \left( \frac{\partial u_i}{\partial x_j} - \frac{\partial u_j}{\partial x_i} \right) \quad (3.66)$$

$$S_{ij} = \frac{1}{2} \left( \frac{\partial u_i}{\partial x_j} + \frac{\partial u_j}{\partial x_i} \right) \quad (3.67)$$

### Modeling Destruction of Turbulence

The destruction term  $Y_v$  in equation (3.59) can be modelled as,

$$Y_v = C_{w1} \rho f_w \left( \frac{\tilde{v}}{d} \right)^2 \quad (3.68)$$

with

$$f_w = g \left[ \frac{1 + C_{w3}^6}{g^6 + C_{w3}^6} \right]^{1/6} \quad (3.69a)$$

$$g = r + C_{w2} (r^6 - r) \quad (3.69b)$$

and

$$r = \frac{\tilde{v}}{\tilde{S} \kappa^2 d^2} \quad (3.69c)$$

where  $C_{w1}$ ,  $C_{w2}$  and  $C_{w3}$  are constants and  $\tilde{S}$  is given by equation (3.63).

### Model Constants

The values of constants used in equations (3.59) to (4.69) are given as

$$C_{b1} = 0.1355, \quad C_{b2} = 0.622, \quad \sigma_{\tilde{v}} = \frac{2}{3},$$

$$C_{v1} = 7.1, \quad C_{w1} = \frac{C_{b1}}{\kappa^2} + \frac{(1 + C_{b2})}{\sigma_{\tilde{v}}}, \quad C_{w2} = 0.3, \quad (3.70)$$

$$C_{w3} = 2.0 \quad \text{and} \quad \kappa = 0.4187$$

### **3.9.4 Shear Stress Transport (SST) $k$ - $\omega$ Turbulence Model**

The second model used in this research, primarily to do the turbulence model independence study, is shear stress transport model proposed by Menter [81]. This model overcomes the freestream turbulence intensity dependence of the standard  $k$ - $\omega$  model while retaining the robust near-wall formulation of the standard  $k$ - $\omega$  model. The SST model incorporates the transport of turbulence kinetic energy ( $k$ ) and specific dissipation rate ( $\omega$ ).

$$\frac{\partial}{\partial t} (\rho k) + \frac{\partial}{\partial x_i} (\rho k u_i) = \frac{\partial}{\partial x_j} \left( \Gamma_k \frac{\partial k}{\partial x_j} \right) + \tilde{G}_k - Y_k + S_k \quad (3.71)$$

and

$$\frac{\partial}{\partial t}(\rho\omega) + \frac{\partial}{\partial x_i}(\rho\omega u_i) = \frac{\partial}{\partial x_j} \left( \Gamma_k \frac{\partial \omega}{\partial x_j} \right) + G_\omega - Y_\omega + D_\omega + S_\omega \quad (3.72)$$

### Modeling the Production of Turbulence

In equation (3.71) the term  $\tilde{G}_k$  represents the production of turbulent kinetic energy and  $G_\omega$  in equation (3.72) represents the generation of  $\omega$ , given respectively by equations (3.73) and (3.74)

$$\tilde{G}_k = \min(G_k, 10\rho\beta^*k\omega) \quad (3.73)$$

$$G_\omega = \frac{\alpha}{\nu_T} \tilde{G}_k \quad (3.74)$$

with

$$G_k = -\rho \overline{u'_i u'_j} \frac{\partial u_j}{\partial x_i} \quad (3.75)$$

### Calculation of the Effective Diffusivity

The effective diffusivities of  $k$  and  $\omega$  appearing in equations (3.71) and (3.72) is computed using,

$$\Gamma_k = \mu + \frac{\mu_T}{\sigma_k} \quad (3.76)$$

$$\Gamma_\omega = \mu + \frac{\mu_T}{\sigma_\omega} \quad (3.77)$$

where turbulent Prandtl numbers for turbulence kinetic energy and the specific dissipation rate  $\sigma_k$  and  $\sigma_\omega$  and the turbulent viscosity  $\mu_t$  are computed respectively using the relations 3.78 (a)-(c).

$$\sigma_k = \frac{1}{F_1 / \sigma_{k,1} + (1 - F_1) / \sigma_{k,2}} \quad (3.78a)$$

$$\sigma_{\omega} = \frac{1}{F_1 / \sigma_{\omega,1} + (1 - F_1) / \sigma_{\omega,2}} \quad (3.78b)$$

$$\mu_T = \frac{\rho k}{\omega} \frac{1}{\max\left[\frac{1}{\alpha^*}, \frac{SF_2}{\alpha_1 \omega}\right]} \quad (3.78c)$$

In above equations the coefficient  $\alpha^*$  and the blending functions  $F_1$  and  $F_2$  are the calculated respectively using,

$$\alpha^* = \alpha_{\infty}^* \left( \frac{\alpha_0^* + \text{Re}_T / R_k}{1 + \text{Re}_T / R_k} \right) \quad (3.79)$$

$$F_1 = \tanh(\phi_1^4) \quad (3.80a)$$

$$F_2 = \tanh(\phi_2^4) \quad (3.80b)$$

with

$$\phi_1 = \min \left[ \max \left( \frac{\sqrt{k}}{0.09\omega y}, \frac{500\mu}{\rho y^2 \omega} \right), \frac{4\rho k}{\sigma_{\omega,2} D_{\omega}^+ y^2} \right] \quad (3.81)$$

$$D_{\omega}^+ = \max \left[ 2\rho \frac{1}{\sigma_{\omega,2}} \frac{1}{\omega} \frac{\partial k}{\partial x_j} \frac{\partial \omega}{\partial x_j}, 10^{-10} \right] \quad (3.82)$$

and

$$\phi_2 = \max \left[ 2 \frac{\sqrt{k}}{0.09\omega y}, \frac{500\mu}{\rho y^2 \omega} \right] \quad (3.83)$$



where  $y$  is the distance next to the surface and the  $D^+_{\omega}$  is positive component of the cross diffusion term. Also the coefficient  $\alpha_{\infty}$  appearing in equation (3.79) is evaluated as

$$\alpha_{\infty} = F_1 \alpha_{\infty,1} + (1 - F_1) \alpha_{\infty,2} \quad (3.84)$$

where, with  $\kappa=0.41$

$$\alpha_{\infty,1} = \frac{\beta_{i,1}}{\beta_{\infty}^*} - \frac{\kappa^2}{\sigma_{w,1} \sqrt{\beta_{\infty}^*}} \quad (3.85a)$$

$$\alpha_{\infty,2} = \frac{\beta_{i,2}}{\beta_{\infty}^*} - \frac{\kappa^2}{\sigma_{w,2} \sqrt{\beta_{\infty}^*}} \quad (3.85b)$$

### Modeling Turbulence Dissipation

The term  $Y_k$  representing the dissipation of  $k$  and the term  $Y_{\omega}$  representing the dissipation of  $\omega$  in equations (3.71) and (3.72) are defined respectively as

$$Y_k = \rho \beta^* k \omega \quad (3.86)$$

$$Y_{\omega} = \rho \beta \omega^2 \quad (3.87)$$

where

$$\beta = \beta_i \left[ 1 - \frac{\beta_i^*}{\beta_i} \zeta^* F(M_T) \right] \quad (3.88a)$$

$$\beta_i^* = \beta_{\infty}^* \left( \frac{4/15 + \left( \frac{\text{Re}_T}{R_{\beta}} \right)^4}{1 + \left( \frac{\text{Re}_T}{R_{\beta}} \right)^4} \right) \quad (3.88b)$$

and

$$\beta_i = F_1 \beta_{i,1} + (1 - F_1) \beta_{i,2} \quad (3.88c)$$

and the compressibility function,

$$F(M_T) = \begin{cases} 0 & M_T \leq M_{T0} \\ M_T^2 - M_{T0}^2 & M_T > M_{T0} \end{cases} \quad (3.89)$$

### Model Constants

Finally the model constants for the Shear Stress Transport turbulence model, appearing in equations (4.71)-(4.89) have the following values,

$$\begin{aligned} \sigma_{k,1} &= 1.176, \quad \sigma_{\omega,1} = 2.0, \quad \sigma_{k,2} = 1.0, \quad \sigma_{\omega,2} = 1.168, \\ \alpha_1 &= 0.31, \quad \beta_{i,1} = 0.075, \quad \beta_{i,2} = 0.0828, \quad \alpha_\infty^* = 1, \\ \alpha_\infty &= 0.52, \quad \alpha_0 = \frac{1}{9}, \quad \beta_\infty^* = 0.09, \quad R_k = 6, \quad R_\omega = 2.95, \\ \zeta^* &= 1.5 \text{ and } M_{T0} = 0.25 \end{aligned} \quad (4.90)$$

### **3.10 GOVERNING EQUATIONS IN VECTOR FORM**

Most often it is convenient to write the governing equations of compressible viscous flow in strong conservation form. This is especially useful while solving the compressible flowfield with shock capturing approach [87]. In Cartesian coordinates the governing equations for a three dimensional viscous flow of a mixture of chemically gases can be written as

$$\frac{\partial U}{\partial t} + \frac{\partial(F_i - F_v)}{\partial x} + \frac{\partial(G_i - G_v)}{\partial y} + \frac{\partial(H_i - H_v)}{\partial z} = S \quad (3.91)$$

where  $U$  is the solution vector,  $F_i$ ,  $G_i$  and  $H_i$  are the vectors of inviscid fluxes in  $x$ ,  $y$  and  $z$  directions respectively,  $F_v$ ,  $G_v$  and  $H_v$  are the vectors of viscous fluxes in  $x$ ,  $y$  and  $z$  directions respectively and  $S$  represent the source term vector. The vectors appearing in equation (3.91) are given respectively as

$$U = \begin{bmatrix} \rho \\ \rho u \\ \rho v \\ \rho w \\ \rho E_t \\ \rho c_1 \\ \vdots \\ \rho c_i \end{bmatrix} \quad (3.92)$$

$$F_i = \begin{bmatrix} \rho u \\ p + \rho u^2 \\ \rho uv \\ \rho uw \\ (\rho E_t + p)u \\ \rho c_1 u \\ \vdots \\ \rho c_i u \end{bmatrix} ; F_v = \begin{bmatrix} 0 \\ \tau_{xx} \\ \tau_{xy} \\ \tau_{xz} \\ u\tau_{xx} + v\tau_{xy} + w\tau_{xz} + q_x + \sum h_i \rho D_i \frac{\partial c_i}{\partial x} \\ \rho D_1 \frac{\partial c_1}{\partial x} \\ \vdots \\ \rho D_i \frac{\partial c_i}{\partial x} \end{bmatrix} \quad (3.93)$$

$$G_i = \begin{bmatrix} \rho v \\ \rho vu \\ p + \rho v^2 \\ \rho vw \\ (\rho E_t + p)v \\ \rho c_1 v \\ \vdots \\ \rho c_i v \end{bmatrix} ; G_v = \begin{bmatrix} 0 \\ \tau_{yx} \\ \tau_{yy} \\ \tau_{yz} \\ u\tau_{yx} + v\tau_{yy} + w\tau_{yz} + q_y + \sum h_i \rho D_i \frac{\partial c_i}{\partial y} \\ \rho D_1 \frac{\partial c_1}{\partial y} \\ \vdots \\ \rho D_i \frac{\partial c_i}{\partial y} \end{bmatrix} \quad (3.94)$$

$$H_i = \begin{bmatrix} \rho w \\ \rho u w \\ \rho v w \\ p + \rho w^2 \\ (\rho E_t + p)w \\ \rho c_1 w \\ \vdots \\ \rho c_i w \end{bmatrix}; H_v = \begin{bmatrix} 0 \\ \tau_{zx} \\ \tau_{zy} \\ \tau_{zz} \\ u\tau_{zx} + v\tau_{zy} + w\tau_{zz} + q_z + \sum h_i \rho D_i \frac{\partial c_i}{\partial z} \\ \rho D_1 \frac{\partial c_1}{\partial z} \\ \vdots \\ \rho D_i \frac{\partial c_i}{\partial z} \end{bmatrix} \quad (3.95)$$

$$\text{and} \quad S = \begin{bmatrix} 0 \\ 0 \\ 0 \\ 0 \\ 0 \\ \dot{w}_1 \\ \vdots \\ \dot{w}_i \end{bmatrix} \quad (3.96)$$

The shearing stresses  $\tau_{ij}$  and the heat fluxes  $q_i$  appearing in equations (3.93)-(3.95) can be calculated using equations (3.10a)-(3.10f) and equations (3.16a)-(3.16c).

### 3.11 SUMMARY OF THE GOVERNING EQUATIONS

The governing equations of a compressible viscous flow for a non reacting gas are given by the equations for conservation of mass (equation 3.2), conservation of momentum (equations 3.9a-3.9c) and the conservation of energy (equation 3.10), commonly called as Navier-Stokes equations. Additional equations are also required to close the system of Navier-Stokes equations that provides relation between various thermodynamic variables and relation between thermodynamic variables and the transport properties. These equations

can be provided by the equation of state for a calorifically perfect gas and the kinetic theory of gases respectively. At higher temperatures, however, the governing equation for the conservation of energy should be modified to include the vibrational and the electronic energy excitation of the of the gas molecule. Additionally, the heat flux vector must include the heat flux due to diffusion and radiation. The energy equation for hypersonic flow at moderate temperatures is given by equation (3.21) in conjunction with equation (3.22). The thermodynamic properties and the transport properties of such hot gases can however be evaluated assuming a mixture of perfect gases. For temperatures above 2000 K, air becomes a chemically reacting mixture of perfect gases, and additional equation of continuity of mass fraction of each species must be included in the system of Navier Stokes equations (3.36). For a chemically reacting mixture of gases the thermodynamic properties and the transport properties also become variable and should be computed through empirical relations.

The system of Navier Stokes equations completely describes the viscous hypersonic flow. However, due to computational limitations the direct Numerical simulation of these equations is not possible at present. So the fluctuations in the flow field variables need to be modelled through turbulence modeling. Most of the currently used turbulence models are based on the eddy-viscosity hypothesis where the coefficients of viscosity and thermal conductivity is assumed to be constituent of laminar and turbulent part. The turbulent component can be modelled through various turbulent models like Spalart-Allmaras and Shear Stress Transport turbulence models.

## 4 THE NUMERICAL SETUP

The closed form analytical solution of the general Navier-Stokes Equations described in chapter 3 does not exist as of now. Most of the physical explanation of the real fluid dynamic and heat transfer phenomena in the literature are based on experimentations. Though the experimental fluid dynamics is developed enough to decode the complex flow phenomena at subsonic and supersonic speeds, the experimental facilities to explore complex hypersonic phenomena is scarce. Most of these hypersonic wind tunnels are intermittent operation wind tunnels operating for only a fraction of second. These facilities can rarely simulate the continuous hypersonic flows with various associated complex phenomena like finite rate chemistry, high altitude effects and high temperature effects. In view of this, the numerical solution of the complete Navier-Stokes equations for the prediction of complex hypersonic phenomena has become the ultimate choice of scientists and engineers. However, extreme care should be taken in choosing the numerical schemes and discretization so as to obtain a converged, reliable and stable solution of the governing equations. These numerical simulations are also very demanding the computational resources and thus selection of suitable method is the key to success with this tool called *Computational fluid Dynamics*.

The computational fluid dynamic solution of any complex physical phenomena involves three basic processes viz. geometry and grid generation, defining physics for flow solver and post processing of results. All the numerical simulations in this investigation are performed using the commercially available general purpose flow solver Ansys Fluent for which unstructured grid are developed using Gambit available with Fluent. An overview of this code is given in the next section with the details of numerical formulations.

## **4.1 GEOMETRY AND GRID GENERATION**

All the geometries used in this investigation are constructed using the commercially available Gambit Grid generation software available with Ansys Fluent. Gambit is a state-of-the-art pre-processor for complex computational fluid dynamic analysis. Gambit possesses advanced geometry and meshing tools in a powerful, tightly integrated and easy to use interface. Although a large number formats for CAD geometry import are available, complex models can directly be created within Gambit solid geometry modeler also. It also possesses a comprehensive set of highly automated and size function driven tools for mesh generation such that structured, unstructured and hybrid meshes can be generated with relative ease.

The general sequence of operations required for mesh generation in Gambit includes following steps

- Solver selection, units, default parameters
- Geometry creation
- Mesh generation including edge mesh followed by face and/or volume mesh
- Mesh examination
- Zone assignment
- Mesh export

### **4.1.1 Geometries Investigated**

This thesis primarily investigates the effect of protrusion and cavities at the nose on the aerothermodynamics of a missile shaped blunt body. The blunt body selected here is a hemisphere-cylinder, primarily because of the large number of experimental data available for the validation of computational results. To reduce the computational expenses, the solver chosen is based on an axisymmetric formulation and thus two dimensional geometries and meshes are created in Gambit. The base blunt body model is a hemisphere cylinder with base diameter of 40 mm and an overall length of 70 mm as shown in Figure 4.1.

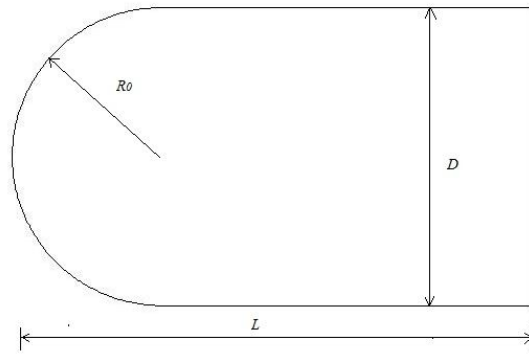
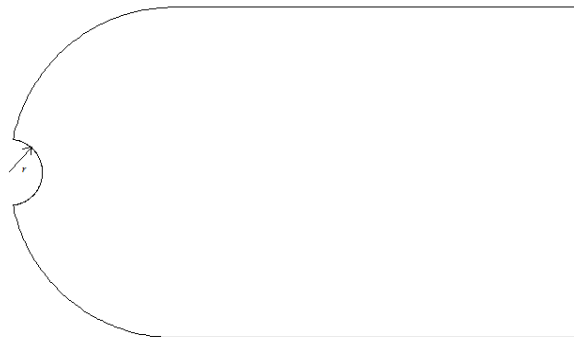


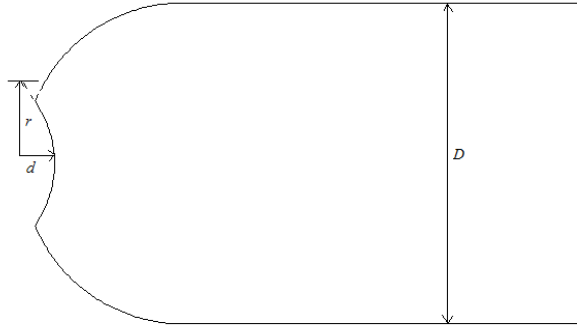
Figure 4.1 Base Configuration

The geometrical modifications at the nose of the hemisphere-cylinder are incorporated by either placing cavities or adding spikes at the nose of the hemisphere cylinder. All the cavities introduced are axisymmetric and forward facing with spherical, elliptic or conical shape. Apart from the cavity models geometries with a double disk aerospike at nose is also investigated. Different modifications incorporated at the nose of the base model are shown in figure 4.2 (a-e).

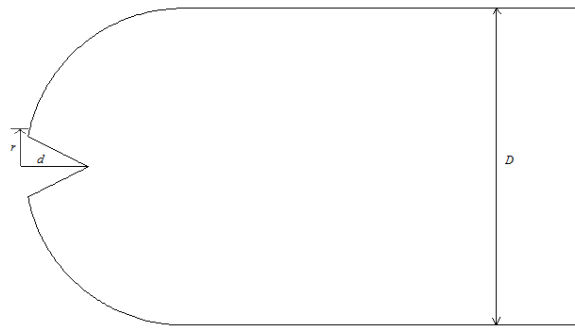


(a)

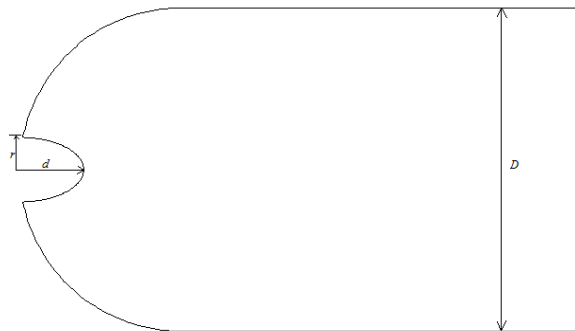




(b)



(c)



(d)

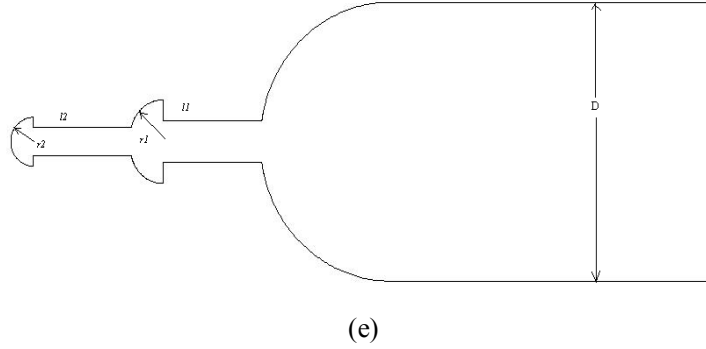


Figure 4.2 Different Geometries investigated, hemisphere cylinder with a  
 a) hemispherical cavity, b) parabolic cavity, c) conical cavity, d) ellipsoid cavity and  
 e) double disk aerospike

The size of a cavity of given shape is varied based on two parameters viz. the lip radius at origin,  $r$  and the depth of cavity  $d$ . For models with parabolic cavity, three different  $r/d$  ratio viz. 1.5, 2.0 and 2.5 of cavities with depth between 1 to 10 mm have been investigated. The lip radius at origin  $r$  and depth  $d$  also represent the semi-minor and semi-major axes for the ellipsoidal cavities. Again three different  $r/d$  ratios of 0.33, 0.5 and 0.67 have been chosen for ellipsoidal cavities whose depth is varied from 3mm to 30 mm. For models with conical cavities the depth of cavity is varied from 2 mm to 36 mm for  $r/d$  ratios of 0.25, 0.33, 0.5 and 1. The semi-vertex angle of these conical cavities is given by  $\tan^{-1}(r/d)$ . For the hemispherical cavities,  $r/d$  ratio is always equal to 1 and the depth of these cavities has been varied from 2 mm to 22 mm.

Only one type of protrusions has been investigated in this dissertation, i.e. a double-disk aerospike. The double disk aerospike has a hemispherical capped aerospike coming out of the spherical nose of the blunt body. A second aerospike protrudes out of the cap of the first aerospike, making a double disk aerospike. Nine different combinations of the lengths of first aerospike  $l_1$  and the length of second aerospike  $l_2$  along with 3 different radii of hemispherical disks have been investigated.

#### 4.1.2 Grid Generation

Almost all computations are done on meshes with mapped quadrilaterals except inside the cavities where paved quadrilateral are used. The mapped mesh for the base body has a total of 40,000 quadrilaterals with 200 cells along the body and 200 cells in radial direction. A stretching of 1.2 is applied in the radial direction such that the mesh near the wall is dense enough to resolve the viscous heating accurately. The distance of the first cell from the body is  $1e-07$  m such that the non dimensional cell-wall distance at the body,  $y^+ \approx 1$  for turbulent computations. With the addition of cavities or aerodisk at the nose the cell count for the subsequent geometries varies from 40,000 to 60,000 depending on the depth and lip radius of the cavities or the length of the aerodisk. Most of the meshed in the work are generated with the help of geometric modeling and pre-processor for the FLUENT code, viz. GAMBIT. GAMBIT is a state of art pre-processor with automated grid generation capabilities. To ensure the quality of grids produced by Gambit, few models were meshed in ANSYS ICEMCFD, grid generator, which generates high quality multi-block structured grids. Apart from the axisymmetric models with normal grid spacing, very fine grids were also generated for the grid independence study. The Grid independence studies done on four models suggest that the grid fineness discussed above is sufficient to capture the aerodynamic heating as well as the essential features of the flow. The axisymmetric meshes used for different configurations as shown in Figure 4.3 (a) - (f).

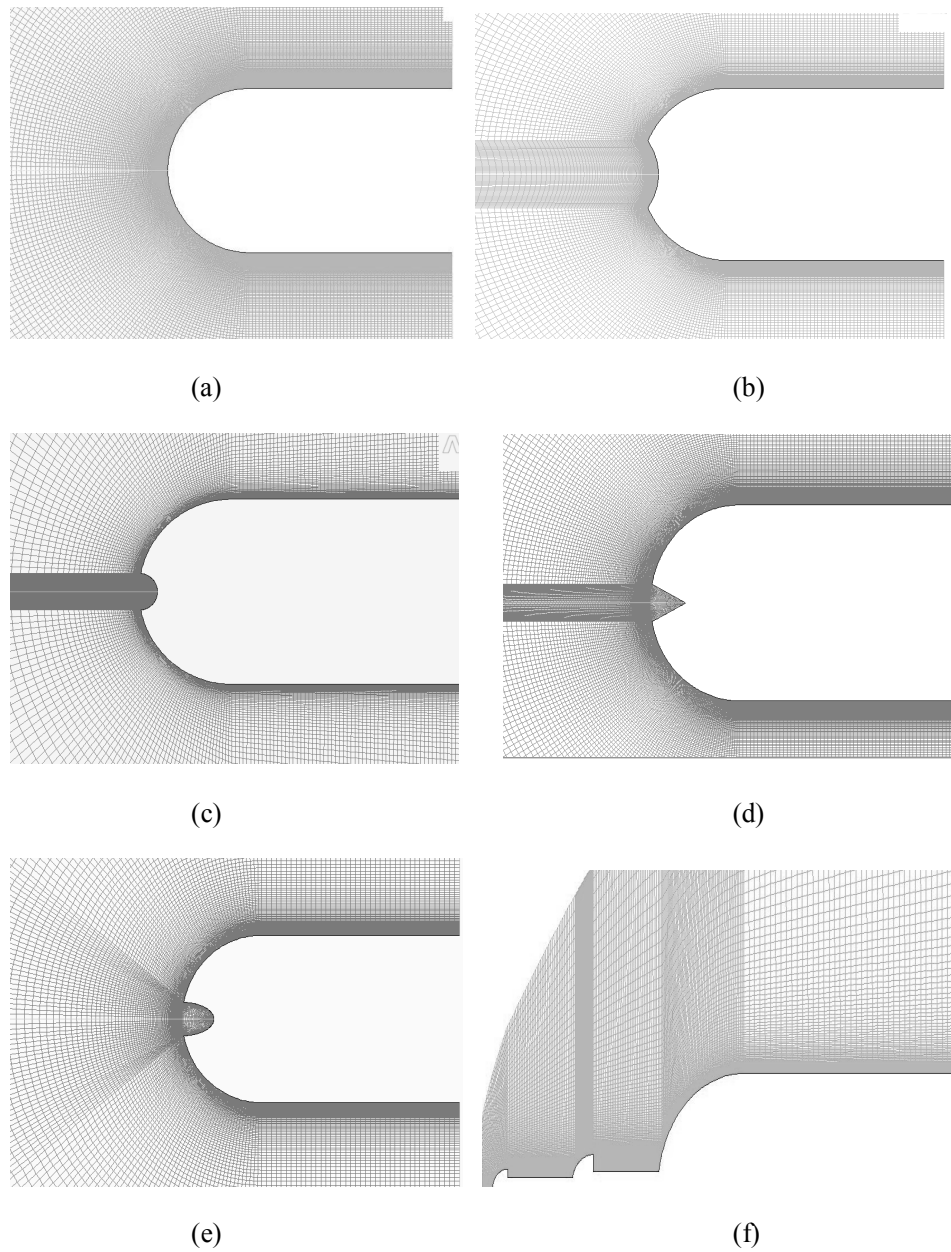


Figure 4.3 Mesh generated a) base body, b) parabolic cavity, c) hemispherical cavity, d) conical cavity, e) ellipsoid cavity and f) double aerodisk model

## 4.2 THE FLUENT CODE

Ansys Fluent is an advanced industrial flow solver with sophisticated modeling capabilities for wide range of applications including incompressible and compressible, laminar and turbulent and subsonic to hypersonic flows. Ansys

Fluent incorporates a broad range of mathematical models for transport phenomena including heat transfer and chemical reactions that can be implemented on any complex geometry. Since this thesis investigates highly compressible flows over blunt nose, a density based implicit solver has been used to compute the flowfield. In the density based approach, the governing equations of fluid flow viz. continuity, momentum and energy equations are solved simultaneously, while the governing equations for additional scalars viz. turbulence in this case is solved afterwards. In this approach, the resulting system of equations is highly coupled and nonlinear, hence an iterative procedure is adopted to reach a solution of desired accuracy. The density based procedure can be summarized via flowchart shown in Figure 4.3

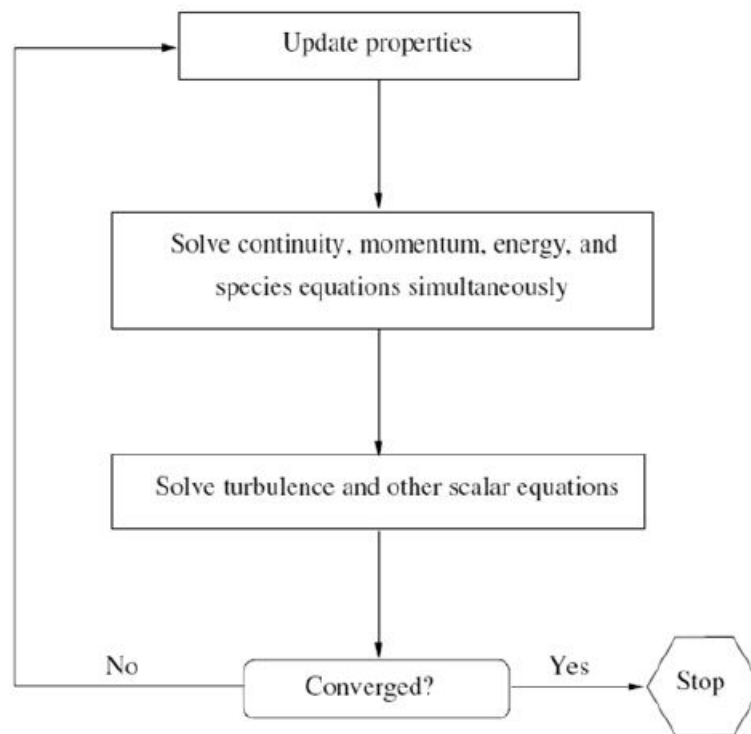


Figure 4.4 The density based approach

The discretized coupled non linear equations of fluid flow can be linearized either in an implicit or an explicit manner. As the implicit schemes are highly

stable and allow the use of large time steps to reach the solution faster, the majority of computations in this research have been done using the implicit discretization, unless the transient behaviour of the flow is captured. In the implicit approach, each equation is linearized implicitly with respect to all the dependent variables in the set of equations. This results in a system of linear equations with a total of  $N$  linear equations for each cell or control volume in the domain, where  $N$  is the number equations in the coupled nonlinear set of governing equations. The resultant block system of linear equations is solved for all variables in each cell using a point implicit linear equation solver which utilizes an Incomplete Lower-Upper (ILU) Factorization scheme in conjunction with an Algebraic Multigrid (AMG) method.

#### 4.2.1 Descritization of transport equations

In FLUENT, a control volume based technique is used to convert the generic scalar transport equation given by equation (4.1) to an algebraic equation [89]. In the control volume technique, the transport equation is integrated over each control volume, yielding a discretized algebraic equation which expresses the conservation of mass, momentum and energy in each control volume.

$$\int_V \frac{\partial \rho \phi}{\partial t} dV + \oint \rho \phi \mathbf{V} \cdot d\mathbf{A} = \oint \Gamma_\phi \nabla \phi \cdot d\mathbf{A} + \int_V S_\phi dV \quad (4.1)$$

where  $\rho$ ,  $V$ ,  $dV$ ,  $\mathbf{V}$ , and  $\mathbf{A}$  respectively are the density, control volume, differential control volume, velocity vector and area vector while  $\Gamma_\phi$  and  $S_\phi$  are diffusion coefficient for  $\phi$  and source of  $\phi$  per unit volume respectively. Equation (4.1) is applied and integrated over each cell in the flow domain as shown in Figure 4.2.

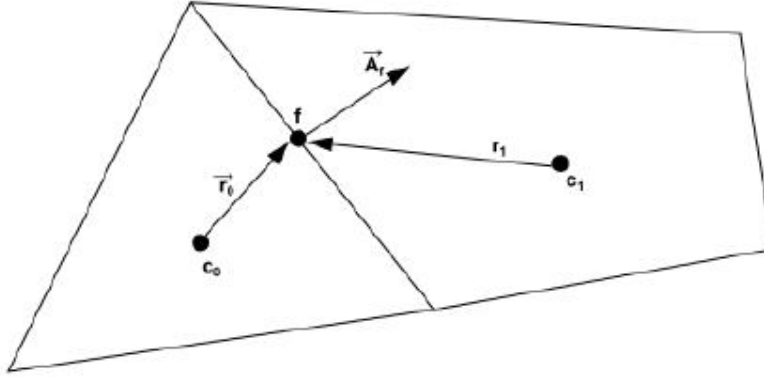


Figure 4.5 A typical unstructured control volume or cell

The discretization of equation (4.1) over a typical control volume yields equation (4.2).

$$\frac{\partial \rho \phi}{\partial t} V + \sum_f^{N_{faces}} \rho_f \mathbf{V}_f \phi_f \cdot \mathbf{A}_f = \sum_f^{N_{faces}} \Gamma_\phi \nabla \phi_f \cdot \mathbf{A}_f + S_\phi V \quad (4.2)$$

where,

$N_{faces}$  = number of faces enclosing cell

$\phi_f$  = value of  $\phi$  convected through face  $f$

$\mathbf{A}_f$  = Area vector for face  $f$

$V$  = cell volume

The discretized transport equation (4.2) contains the unknown scalar variable  $\phi$  at the centre of the control volume,  $c_0$  and also at the centre of neighbouring cells. The linearization of equation (4.2) results in equation of the form of equation (4.3)

$$a_p \phi = \sum_{nb} a_{nb} \phi_{nb} + b \quad (4.3)$$

where  $a_p$  and  $a_{nb}$  are the linearized coefficients of variable  $\phi$  and the subscript  $p$  and  $nb$  represents the cell under consideration and the neighbouring cells respectively.

Equation (4.3) is when written for each cell in the mesh, results in a block system of linear algebraic equations which is solved using a point implicit linear equation solver in conjunction with an Algebraic Multigrid Method.

#### 4.2.2 The Algebraic Multigrid Method

A Multigrid approach has been used in the CFD simulations to accelerate the convergence of the solver. In this approach, the low frequency errors or the global errors are reduced by using a series of successively coarser meshes. With Multigrid approach, the low frequency error that exists on fine mesh is represented on a coarser mesh where it becomes accessible as local or high frequency error because of faster communication of global corrections on a coarser mesh. Computations on the coarser mesh can be achieved at very low expense in terms of CPU time and memory storage requirements and thus the global errors are efficiently reduced at faster rate.

The concept of a Multigrid can be illustrated considering a set of linearized equations given by equation (4.4)

$$A\phi_e + b = 0 \quad (4.4)$$

where  $\phi_e$  is the exact solution of equations (4.4). Let  $\phi$  be an intermediate approximate solution of equation (4.4) such that a defect  $d$  exist which is given by equation (4.5)

$$A\phi + b = d \quad (4.5)$$

In the Multigrid strategy, we seek a correction  $\psi$  to  $\phi$  such that

$$\phi_e = \phi + \psi \quad (4.6)$$

Substituting equation (4.6) into equation (4.4), we get

$$A(\phi + \psi) + b = 0 \quad (4.7)$$

Or

$$A\psi + (A\phi + b) = 0 \quad (4.8)$$

Using equation (4.5), we get



$$A\psi + d = 0 \quad (4.9)$$

Equation (4.9) is the equation for the correction  $\psi$  in terms of the fine level operator  $A$  and defect  $d$ . With the high frequency errors sufficiently damped by the relaxation on the fine level mesh, the correction  $\psi$  can be smoothly obtained on the coarser mesh.

The application any Multigrid strategy involves three basic steps; transfer of defects from fine level mesh to a coarser mesh, computation of corrections on the coarser mesh and finally the transfer of corrections back to the finer mesh. The transfer of defects from the finer mesh to coarse mesh is called as *restriction* and the transfer of corrections from the coarser mesh to finer mesh is called *prolongation*.

The equation for the coarse level correction  $\psi^H$  can be written as [89],

$$A^H\psi^H + Rd = 0 \quad (4.10)$$

Where the superscript  $H$  represents the coarser level and  $R$  is the restriction operator with  $A$  being the original operator. The restriction operator  $R$  transfers the fine level defects to the coarser level. The solution of equation (4.10) yields the correction  $\psi^H$ , which is transferred to the fine level mesh using a prolongation operator  $P$ .

This is followed by the update of the solution on the finer mesh as given by equation (4.11)

$$\phi^{new} = \phi + P\psi^H \quad (4.11)$$

where  $\phi^{new}$  is the updated value of the unknown scalar variable  $\phi$ .

### 4.2.3 The AMG Restriction and Prolongation Operators

In the algebraic Multigrid scheme the coarse level equations are obtained without any re-descretization on the coarser levels and thus no hierarchy of mesh is required. This is highly advantageous for application to unstructured grids where it is difficult to establish the hierarchy of meshes. The AMG method also eliminates the necessity of construction and storage of coarse mesh and the associated flux and source terms.

The restriction and the prolongation operators employed in the Algebraic Multigrid Algorithm is based on the *Additive-Correction* (AC) strategy proposed by **Hutchinson and Raithby** [88]. The additive correction strategy gets its name from the fact that the defect in any coarse level cell is given by the sum of defects from the fine level cells it is parent to. In this method, the transfer of defects from the fine level to coarse level is obtained using piecewise constant interpolation and prolongation while the transfer of corrections from coarse mesh to fine level is accomplished by injection of the coarse level values. Thus, the prolongation operator in AC strategy is given as the transpose of the restriction operator [89]

$$P = R^T \quad (4.12)$$

In the restriction operation, two or more, equal numbers of fine level cells are grouped together with their strongest neighbours to form a coarse level cell. The strength of a neighbour cell  $j$  with respect to the current cell  $i$  is determined by the magnitude the coefficient of  $A_{ij}$ . The measure of the magnitude of the block matrix  $A_{ij}$  in turn is given by the magnitude of its first element. The restriction is followed by the computation of the coarse level defect using the coarse level operator  $A^H$ . The construction of the coarse level operator  $A^H$  is done by simply performing the summation of the diagonal and the corresponding off-diagonal blocks of all fine level mesh cells within the group to form the diagonal block of the coarse level cell. The coarse level operator is thus, given by equation (4.13)

$$A^H = RAP \quad (4.13)$$

#### 4.2.4 The F Cycle

A Multigrid cycle is a recursive procedure that is applied at each grid level as the computation moves through the grid hierarchy [89]. The F-cycle at each grid level is performed by a combination of V-cycle and W-cycle, where the logic of V-cycle and W-cycle are as shown in Figure 4.6

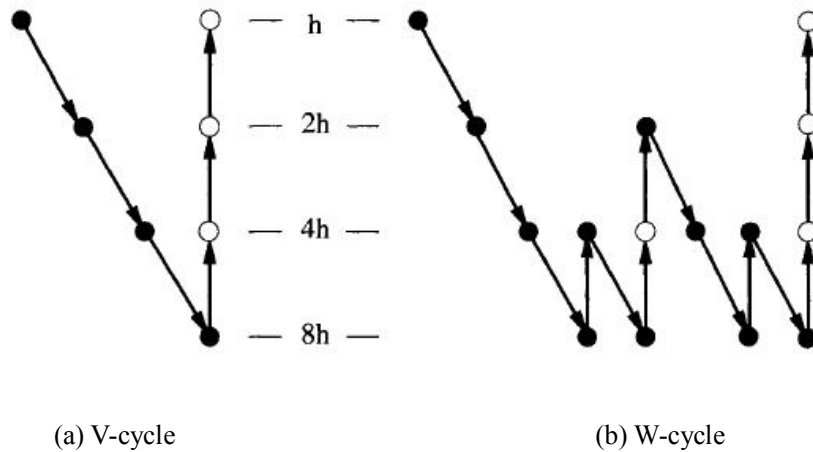


Figure 4.6 Multigrid Cycles

In Figure 4.6, the black circles represent the state after the restriction operation while the white circles represent the state after the prolongation operation and  $h$  represents the hierarchy of meshes with  $8h$  being the coarsest grid. A typical Multigrid operation with an F-cycle is achieved by successive application of a W-cycle and a V-cycle between the restriction and the prolongation operations as shown below.

**Pre-sweep → Restrict → W Cycle → V Cycle → Prolongate → Post sweep**

#### 4.2.5 The Flexible Cycle

In a flexible cycle the coarser grid calculations are invoked only when the rate of convergence or residual reduction on the current level is very slow. Also the flexible cycle logic ensures the change of grid level to finer level only after

the solution has sufficiently converged on the coarser level. The first of the above two decisions are controlled by parameters  $\beta$ , commonly referred to as *residual rate reduction tolerance* and the second decision is controlled by the parameter  $\alpha$  which is known as the *termination criteria*. Thus, with the flexible cycle, a grid level is repeatedly visited until both the conditions are satisfied. The logic of a flexible Multigrid cycle can be illustrated through Figure 4.7 [89].

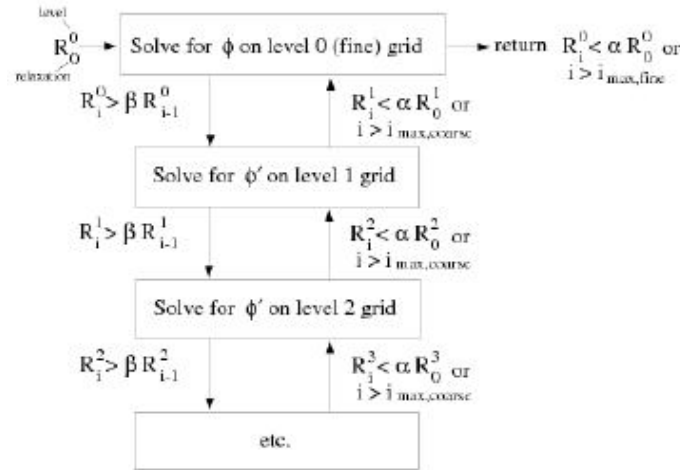


Figure 4.7 Logic of a Flexible Multigrid Cycle [89]

The error reduction rate on any grid level is considered to slow enough to move to next coarser grid if,

$$R_i > \beta R_{i-1} \quad (4.14)$$

where  $R_i$  is the absolute summation of the individual cell defects on the current grid level computed after  $i$  relaxation sweeps, and  $R_{i-1}$  is the absolute defect summation after  $i-1$  relaxation sweeps. Thus with the value of  $\beta$  between 0 and 1, the next coarser grid is visited when the ratio of defects or residuals between two successive iterations becomes less than the residual rate reduction parameter  $\beta$ .

The switching to finer grid level during prolongation on the other hand is accomplished when the correction equations are sufficiently converged on the

current grid level. The correction equations are assumed to be sufficiently converged when the ratio of the defect in the correction solution to the original defect falls below the termination criteria value  $\alpha$ . Thus, with  $\alpha$  between 0 and, the termination criteria can be given as,

$$R_i < \alpha R_0 \quad (4.15)$$

where  $R_i$  is the residual on the current grid level after  $i$  iterations and  $R_0$  is the original defect on the current grid level at the current global iteration.

#### 4.2.6 The Gauss –Seidel Smoother

Gauss- Seidel relaxation technique is primarily used to solve linear system of scalar equations viz. Turbulence equation. In this scheme, the previously computed values of unknowns are used, as soon as they are available. The Gauss-Seidel procedure performs one sweep in the forward direction and one sweep in the backward direction on the unknown variables. The Gauss- Seidel technique is capable of handling both the scalar and coupled equations with its point implicit and block method respectively.

Consider a linear system of scalar equations represented by equation (4.16)

$$a_{ij}x_j = b_i \quad (4.16)$$

The forward sweep of the Gauss-Seidel algorithm for the above scalar system can be given as equation (4.17)

$$x_i^{k+1/2} = \left( b_i - \sum_{j<i} a_{ij}x_j^{k+1/2} - \sum_{j>i} a_{ij}x_j^k \right) / a_{ii} \quad (i=1,2\dots N) \quad (4.17)$$

The forward sweep is followed by a backward sweep which can be written as

$$x_i^{k+1} = \left( b_i - \sum_{j<i} a_{ij}x_j^{k+1/2} - \sum_{j>i} a_{ij}x_j^{k+1} \right) / a_{ii} \quad (4.18)$$

Substituting equation (4.17) into equation (4.18), the symmetric Gauss-Seidel procedure in matrix form can be expressed as a two step recursive solution as given in equation (4.19),

$$(D_A + L_A)D_A^{-1}(D_A + U_A)(x^{k+1} - x^k) = b - Ax^k \quad (4.19)$$

where  $D_A$ ,  $L_A$  and  $U_A$  respectively are the diagonal, lower tridiagonal and upper tridiagonal components of matrix  $A=[a_{ij}]$ .

#### 4.2.7 Incomplete Lower-Upper (ILU) Factorization

The Gauss-Seidel method, though simple, does not provide good convergence rates for coupled equations viz. density based flow equations. For a coupled AMG solver, a smoother based on the Incomplete Lower-Upper Decomposition technique is more effective.

Let us consider a system of equations given by equation (4.20),

$$Ax = b \quad (4.20)$$

The iterative solution of the above system can be given as,

$$M(x^{k+1} - x^k) = b - Ax^k \quad (4.21)$$

where the matrix  $M$  is an approximate and incomplete factorization of the original matrix  $A$  of the system such that,

$$M = LU = (D + L_A)D^{-1}(D + U_A) \quad (4.22)$$

In equation (4.22), matrices  $L$  and  $U$  are the factors of matrix  $M$ . Also  $L_A$  and  $U_A$  are the lower and upper tridiagonal parts of the characteristic matrix  $A$  respectively and  $D$  is a diagonal matrix computed in a manner to satisfy

$$D_M = D_A \quad (4.23)$$

For the system given by equation (4.20) the elements of the Diagonal matrix D can be given by,

$$d_{ii} = a_{ii} - \sum_{j<i} \left( \frac{a_{ij}a_{ji}}{d_{jj}} \right) \quad (4.24)$$

With the elements of the diagonal matrix computed using equation (4.24) during the construction of grid levels, the value of new solution can be computed by one forward and one backward sweep as with the Gauss-Seidel procedure.

#### 4.2.8 Full Multigrid Initialization

A good initial guess of the solution can enhance the stability and convergence of a solver and reduce the computational expenses favourably. The full Multigrid (FMG) initialization provides a reasonable initial solution of the flowfield at a very low computational cost by utilizing *Full Approximation Storage* (FAS) Multigrid scheme [90]. In the FAS scheme both the fine grid solution  $\phi$  and the defect  $d$  are restricted to the coarse grid level. In the restriction process, the solution for the coarse level cell is obtained by taking the volume average of the solution values in fine grid cells and the coarse grid defect is computed by summation of defects of fine grid cells contained inside a coarse level cell. The prolongation operation on the other hand is accomplished by setting fine grid corrections to the associated coarse grid values.

The FMG initialization process, starting from the initial guess of the solution, proceeds by constructing a desirable number of grid levels by coalescing group of cells on the finer levels to form a coarse grid cell by cell *agglomeration*. The initial solution is restricted all the way down to the coarsest grid level where the FAS cycles are applied until a desired reduction in the residuals are achieved. The solution on the coarsest grid level is then interpolated to one grid level up every time and the FAS cycle is applied between the current

level all the down to the coarsest level. This recursive process is done until the solution has been interpolated to the finest level. A typical FMG initialization procedure can be illustrated through Figure 4.8 which shows FMG initialization on a 4 level Multigrid, 0 representing the finest grid level.

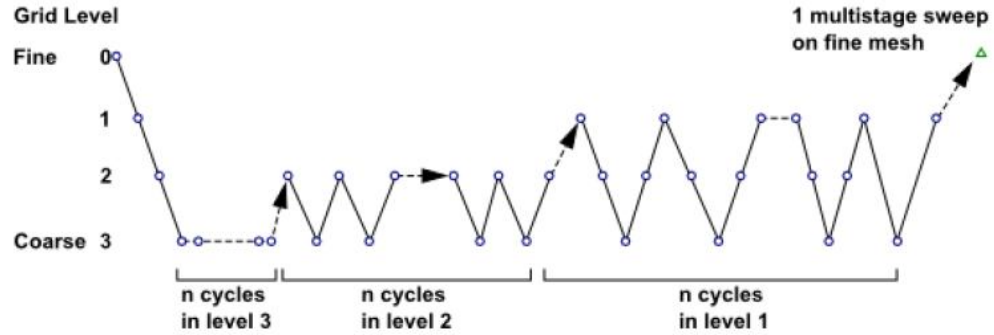


Figure 4.8 The Full Multigrid Initialization

### 4.3 SPATIAL DESCRITIZATION

In a control volume approach, the discrete value of scalar variable  $\phi$  is generally stored at the centroid of each cell. The evaluation of the convective term of the general scalar transport equation (4.2), however, requires the value of the scalar variable at the cell interface  $\phi_f$  to be known. The value of  $\phi_f$  can be interpolated from the  $\phi$  values at the cell centres using different spatial description schemes.

In this work, a *second order upwind* description has been implemented so as to obtain reasonably accurate solution to the convection dominated flow problem. In this scheme, the quantities at the cell faces are computed by using a multidimensional linear reconstruction approach through the Taylor series expansion of the cell centred solution about the cell centroid [91]. The face value  $\phi_f$  can thus be computed using equation (4.25)

$$\phi_{f,SOU} = \phi + \nabla \phi \cdot \vec{r} \quad (4.25)$$



where  $\phi$  and  $\nabla\phi$  are the cell centred value and its gradient in the upstream cell respectively and  $\vec{r}$  is the displacement vector joining the upstream cell centroid to the current cell face centroid.

#### 4.3.1 Gradient Formulation

Using the *Green-Gauss Theorem*, the gradient of a scalar at the cell centroid can be computed using equation (4.26)

$$(\nabla\phi)_{c0} = \frac{1}{V} \sum_f \bar{\phi}_f \mathbf{A}_f \quad (4.26)$$

where subscript  $c0$  represents the cell centroid,  $\bar{\phi}_f$  is the value of the scalar at the face centroid and  $\mathbf{A}_f$  is the area vector normal to the face.

For a *Cell-based gradient formulation*, the average face value of scalar  $\bar{\phi}_f$  in equation (4.26) can be assumed to be the arithmetic mean of the values at neighbour cells. Thus,

$$\bar{\phi}_f = \frac{\phi_{c0} + \phi_{c1}}{2} \quad (4.27)$$

And for a node based formulation, it can be given as the weighted average of the scalar values at the nodes of the face. Thus,

$$\bar{\phi}_f = \frac{1}{N_f} \sum_n^{N_f} \bar{\phi}_n \quad (4.28)$$

where  $N_f$  is the number of nodes in the face.

#### 4.3.2 Gradient Limiters

The second order upwind schemes are inherently are not *Total Variation Diminishing* and thus susceptible to spurious oscillations near the shock and discontinuities. The use of *Gradient limiters* or Slope limiters can prevent such spurious oscillation by enforcing the monotonicity principle. This is achieved by preventing the flow variables at the cell faces from exceeding the maximum or the minimum values of the neighbouring cells by a linear reconstruction of flow variables at the cell faces.

The Standard Gradient limiter used in this work is a *non differentiable limiter* that uses a Minimum Modulus (Minmod) function to clip and limit the reconstructed solution. This gradient limiter uses a *cell to face limiting* of the reconstruction gradient which is determined at the centroid of the cell face. Thus the second order upwind scheme with a gradient limiter evaluates the face value of the scalar as,

$$\phi_{f,SOU} = \phi + \psi \nabla \phi \cdot \vec{r} \quad (4.29)$$

where  $\psi$  is the scalar that limits the gradient of scalar  $\phi$ .

#### 4.4 TEMPORAL DESCRITIZATION

The coupled Navier Stokes equations are descritized in time for both the steady state as well as the transient flow simulations for an iterative solution. For the steady state simulations, however, the temporal accuracy is not desired and the flow is assumed to reach a steady state where the flow derivatives with respect to time vanish. This allows the use of large time steps for steady state simulations and hence has faster convergence. The temporal descritization of the coupled set of governing equations can be done in either an explicit or implicit manner.

##### 4.4.1 The Implicit Formulation for Steady State Computations

The implicit formulation offers a better choice for the steady state solution of coupled equations as the time accuracy is not desired. The solution can progressed with larger time steps and CFL number to reach the steady state as a faster rate.

Let us consider preconditioned Navier-Stokes equations in vector form given by equation (4.30)

$$\Gamma \frac{\partial}{\partial t} \int_V Q dV + \oint [F_i - F_v] \cdot dA = \int_V S dV \quad (4.30)$$

where the preconditioning matrix  $\Gamma$  is given by,

$$\Gamma = \frac{\partial U}{\partial Q} = \begin{bmatrix} \Theta & 0 & 0 & 0 & \rho_T \\ \Theta u & \rho & 0 & 0 & \rho_T u \\ \Theta v & 0 & \rho & 0 & \rho_T v \\ \Theta w & 0 & 0 & \rho & \rho_T w \\ \Theta H & \rho u & \rho v & \rho w & \rho_T H + \rho c_p \end{bmatrix} \quad (4.31)$$

with

$$\Theta = \left( \frac{1}{V_r^2} - \frac{\rho_T}{\rho c_p} \right) \quad (4.32)$$

The Euler implicit time discretization of equation (4.30), combined with the Newton-type linearization of the fluxes, results in a linearized system in residual form given by equation (4.33)

$$\left[ D + \sum_j^{N_{faces}} S_{j,k} \right] \Delta Q^{n+1} = -R^n \quad (4.33)$$

where the centre and off-diagonal coefficient matrices  $D$  and  $S_{j,k}$  are given respectively by,

$$D = \frac{V}{\Delta t} \Gamma + \sum_j^{N_{faces}} S_{j,i} \quad (4.33)$$

$$S_{j,k} = \left( \frac{\partial F_{i,j}}{\partial Q_k} - \frac{\partial F_{v,j}}{\partial Q_k} \right) A_j \quad (4.34)$$

while the residual vector  $R^n$  and the time step  $\Delta t$  are given respectively by,

$$R^n = \sum_j^{N_{faces}} (F(Q^n) - G(Q^n)) A_j - VH \quad (4.35)$$

$$\Delta t = \frac{2 \text{ CFL} \cdot V}{\sum_f \lambda_f^{\max} A_f} \quad (4.36)$$

where  $V$  is the cell volume,  $A_f$  is the face area and  $\lambda_f^{\max}$  is the maximum of the local eigenvalues.

The descritized implicit equation (4.33) is solved using Algebraic Multigrid Method in conjunction with Incomplete Lower Upper Factorization to obtain the steady state solution.

#### 4.4.2 Implicit Formulation for Transient Simulations

The implicit time descritization of unsteady Navier Stokes equations for the transient solution is done by introduction of a pseudo time variable  $\tau$  and the associated preconditioned time derivative term, thus giving a *dual time* stepping scheme. Thus the coupled Navier-Stokes equations with preconditioned pseudo time derivative term can be written as,

$$\frac{\partial}{\partial t} \int_V U dV + \Gamma \frac{\partial}{\partial \tau} \int_V Q dV + \oint [F_i - F_v] \cdot dA = \int_V S dV \quad (4.37)$$

In equation (4.37),  $t$  represents the physical time and  $\tau$  represents the pseudo-time variable. In the implicit transient formulation, the transient terms in equation (4.37) are descritized using the second order Euler backward difference scheme. The semi-descritized Navier-Stokes equations using dual time stepping formulation is given by,

$$\left[ \frac{\Gamma}{\Delta \tau} + \frac{\varepsilon_0 \partial U}{\Delta t \partial Q} \right] \Delta Q^{k+1} + \frac{1}{V} \oint [F_i - F_v] \cdot dA = S - \frac{1}{\Delta t} (\varepsilon_0 U^k - \varepsilon_1 U^n + \varepsilon_2 U^{n-1}) \quad (4.38)$$

where  $\varepsilon_0 = 3/2$ ,  $\varepsilon_1 = 2$ ,  $\varepsilon_2 = 1/2$ , are the coefficients for the second order accuracy,  $k$  is the inner iteration counter and  $n$  is the physical time step counter.

The temporal accuracy is achieved by driving the pseudo-time derivative to zero at each physical time step level by performing a number of inner iterations in an implicit manner. During the inner iterations,  $U^n$  and  $U^{n+1}$  are held constant while  $U^k$  is computed from the knowledge of  $Q^k$ . As the pseudo time derivative vanishes, the solution at the next physical time step  $n+1$  is given by  $U^k$ . The choice of physical time step  $\Delta t$  depends on the level of temporal accuracy desired and the value of pseudo-time step  $\Delta \tau$  is computed based on the CFL number provided in the implicit time marching procedure.

#### 4.4.3 Explicit Formulation

The explicit formulation is primarily used for computations where a high degree temporal accuracy is desired. A higher order discretization of the transient terms can be obtained using a multi-stage Runge-Kutta time stepping method [92].

With the explicit knowledge of solution of preconditioned Navier-Stokes equation (4.30) at physical time level  $n$ , the solution at new physical time step  $n+1$  can be given using  $m$ -stage Runge-Kutta method as,

$$\begin{aligned} Q^0 &= Q^n \\ \Delta Q^i &= -\alpha_i \Delta t \Gamma^{-1} R^{i-1} \\ Q^{n+1} &= Q^m \end{aligned} \quad (4.39)$$

with

$$\Delta Q^i = Q^i - Q^n \quad (4.40)$$

where  $i$  is the stage counter,  $\alpha_i$  is the multi-stage coefficient for the  $i^{\text{th}}$  stage and  $R^i$  is the residual for the intermediate solution  $Q^i$ .

#### 4.5 EVALUATION OF CONVECTIVE FLUXES

The viscous fluxes appearing in the Navier-Stokes equations are diffusive in nature and always evaluated using the central difference stencils. The inviscid

fluxes on the other hand are convection dominated and evaluated using upwind stencils. The upwinding is generally achieved through *Flux vector splitting* (FVS) of negative and positive component of flux based on the sign of propagation of associated waves [93, 94]. Though many flux vector splitting schemes are available in the literature, the *Advection Upstream Splitting Method* (AUSM) provides a high resolution solution at the shock. The AUSM scheme was first introduced by Liou and Steffen in 1993 [95], where in the inviscid fluxes are split into convective and pressure parts. In this scheme, the cell interface Mach number based on the characteristic speeds from the neighbouring cells is used to evaluate the upwind extrapolation for the convection part of the inviscid fluxes. In the original AUSM scheme, proposed in reference 95, a separate Mach number splitting is used for the pressure term. Though popular, this scheme suffered from spurious oscillations near shock and was susceptible to carbuncle phenomena. An advanced version of the AUSM scheme, AUSM+, proposed by Liou [96] uses a generalized Mach number based splitting of fluxes to provide exact shock capturing.

In the AUSM based schemes [95-97], the inviscid flux appearing in the Navier Stokes equation is split as the sum of convection part and pressure part,

$$F_i = F_c + P \quad (4.41)$$

where,

$$F_c = Ma \begin{pmatrix} \rho \\ \rho u \\ \rho h_t \end{pmatrix} \quad \text{and} \quad P = \begin{pmatrix} 0 \\ p \\ 0 \end{pmatrix} \quad (4.42)$$

Correspondingly the discrete numerical flux the cell interface for the AUSM+ formulation is given as,

$$f_{j+1/2} = a_{j+1/2} \left[ \frac{1}{2} m_{j+1/2} (\Phi_j + \Phi_{j+1}) - \frac{1}{2} |m_{j+1/2}| (\Phi_{j+1} - \Phi_j) \right] + p_{j+1/2} \quad (4.43)$$

where,

$$\Phi_{j+1/2} = \begin{cases} \Phi_j & \text{if } m_{j+1/2} \geq 0, \\ \Phi_{j+1} & \text{otherwise;} \end{cases} \quad (4.44)$$

with

$$\Phi = \begin{pmatrix} \rho \\ \rho u \\ \rho h_t \end{pmatrix} \quad (4.45)$$

The quantities  $m_{j+1/2}$ ,  $p_{j+1/2}$ , and  $a_{j+1/2}$  in equation (4.43) are defined respectively as below.

The cell interface mass flux  $m_{j+1/2}$  is defined as,

$$m_{j+1/2} = \mathcal{M}^+(M_j) + \mathcal{M}^-(M_{j+1}) \quad (4.46)$$

In equation (4.46), split mach numbers are given by

$$\mathcal{M}^\pm(M) = \begin{cases} \frac{1}{2}(M \pm |M|), & \text{if } |M| \geq 1 \\ \mathcal{M}_\beta^\pm(M), & \text{otherwise} \end{cases} \quad (4.48)$$

with

$$\mathcal{M}_\beta^\pm(M) = \pm \frac{1}{2}(M \pm 1)^2 \pm \beta(M^2 - 1)^2, \quad -\frac{1}{16} \leq \beta \leq \frac{1}{2} \quad (4.49)$$

The interface pressure flux  $p_{j+1/2}$  is defined as,

$$p_{j+1/2} = \mathcal{P}^+(M_j)p_j + \mathcal{P}^-(M_{j+1})p_{j+1} \quad (4.50)$$

where the split pressures are given by,

$$\mathcal{F}^\pm(M) = \begin{cases} \frac{1}{2}(M \pm \text{sign}(M)), & \text{if } |M| \geq 1 \\ \mathcal{F}_\alpha^\pm(M), & \text{otherwise} \end{cases} \quad (4.51)$$

with

$$\mathcal{F}_\alpha^\pm(M) = \frac{1}{4}(M \pm 1)^2(2 \mp M) \pm \alpha M(M^2 - 1)^2, \quad -\frac{3}{4} \leq \alpha \leq \frac{3}{16} \quad (4.52)$$

And finally, the common interface speed of sound is computed as,

$$a_{j+1/2} = a_j^{*2} / u_j \quad (4.53)$$

where  $a_j^*$  is the critical speed sound.

The AUSM+ scheme, though sensitive to mesh cell shape, does not require the use of artificial dissipation and does not produce any oscillations near shock to produce reasonably accurate results for hypersonic heat transfer problems [98].

#### 4.6 AERO-CHEMISTRY MODEL

The flow at Mach 6.2 computations air is assumed to be a perfect gas with specific heats as a polynomial function of temperature [76, 77]. At Mach 10.1 the post shock temperature is high enough to result in appreciable dissociation of molecules and air behaves as a chemically reacting mixture of N, NO, O, O<sub>2</sub> and N<sub>2</sub> [99]. The ionization of air the however, does not occur even at this conditions and assumption of 5 species reacting air is thermal equilibrium is appropriate to include the real gas effects [2, 99].

Many chemical reaction mechanisms for multispecies chemically reacting air have been proposed in the literature [100-105]. In the current work the chemical kinetics has been modelled as 5 species 17 elementary reactions [100] with single temperature. The detailed reaction mechanism and constants for use in the Arrhenius formula (equation 3.41) for each elementary reaction are presented in Table 4A.



Table 4A: Reaction Rate Parameters

<i>Reactions</i>	$A_{f,r}$	$\beta_{f,r}$	$E_{a,f,r}$	<i>Third body efficiencies</i>
$N_2 + M \leftrightarrow N + N + M$	$3.00 \times 10^{19}$	-1.6	$9.412 \times 10^8$	$O_2=N_2=NO=0.233,$ $O=N=1$
$O_2 + M \leftrightarrow O + O + M$	$1.00 \times 10^{19}$	-1.5	$4.947 \times 10^8$	$O_2=N_2=NO=0.2,$ $O=N=1$
$NO + M \leftrightarrow N + O + M$	$1.10 \times 10^{14}$	0	$6.277 \times 10^8$	$O_2=N_2=0.05,$ $O=N=NO=1$
$NO + O \leftrightarrow N + O_2$	$2.40 \times 10^6$	1	$1.598 \times 10^8$	-----
$N_2 + O \leftrightarrow NO + N$	$1.80 \times 10^{11}$	0	$3.193 \times 10^8$	-----

In above reactions,  $M$  is the reaction partner which can be any one of five species viz. O, O<sub>2</sub>, N, NO and N<sub>2</sub> from the mixture.

#### 4.7 BOUNDARY CONDITIONS

For a cylindrical geometric at zero angles of attack the computational efforts can be drastically reduced by assumption of axisymmetric flows when a 2D mesh can be used for computation. The governing Navier-Stokes equations in axisymmetric form can be found in Appendix A. An axis boundary condition has been implemented on the longitudinal axis of the hemisphere-cylinder in this problem across which the following conditions hold.

$$\rho v = 0 \quad \text{and} \quad \frac{\partial u}{\partial y} = \frac{\partial T}{\partial y} = \frac{\partial p}{\partial y} = 0 \quad (4.54)$$

All the axisymmetric simulations have been performed at two different sets of freestream conditions. For both the thermally perfect and chemically reacting gas simulations, the body of the hemisphere-cylinder is to be an isothermal wall at a temperature of 300 K with a no slip velocity condition ( $u=0, v=0$ ). Additionally, for computations involving chemical reactions, a fully catalytic wall is assumed with mass fraction of each species equal to freestream values at the wall.

All other boundaries of the flow domain are assumed to be pressure farfield with the freestream Mach number, static pressure and temperature specified. The details of freestream boundary conditions applied at the inlet for the thermally perfect gas simulations and the chemically reacting flow simulations are given in tables 4B and 4C respectively. The freestream conditions in Table 4C represent a typical ballistic reentry trajectory point of ELECTREE at an altitude of 13.24 Km [106]. The variables at the outlet farfield are obtained through extrapolation from the interior of the domain. Apart from the farfield boundary conditions, the above values are used as initial guesses for all cells to initialize the solution.

Table 4B: Freestream Parameters for perfect gas simulations

	Symbol	Units	Values
Mach number	M	-----	6.02
Temperature	T	K	288.16
Pressure	P	N/m <sup>2</sup>	101325
Molecular Viscosity	$\mu$	Kg/m-s	1.7895e-05
Reynolds Number	Re	m <sup>-1</sup>	1.44e+08

Table 4C: Freestream Parameters for Chemically Reacting Flow

	Symbol	Units	Values
Mach number	M	-----	10.1
Temperature	T	K	216.65
Pressure	P	N/m <sup>2</sup>	16066
Molecular Viscosity	$\mu$	Kg/m-s	1.7894e-05
Reynolds Number	Re	m <sup>-1</sup>	4.29e+07
Mass fraction of O <sub>2</sub>	c <sub>O2</sub>	----	0.23
Mass fraction of N <sub>2</sub>	c <sub>N2</sub>	-----	0.77

#### 4.8 SOLVER VALIDATION AND VERIFICATION

The Fluent<sup>®</sup> Solver has been validated for a wide range of complex hypersonic flows including the flow over a hypersonic projectile with either a forward

facing cavity [39], or an aerospike [107]. Despite this, a code validation study has been carried out for four different cases of hypersonic flow over a projectile with either a forward facing cavity or an aerospike at the nose. These cases incorporate wide range hypersonic phenomena and their experimental data are available in the literature for validation of CFD software. The cases investigated for the solver validation are as follows:

#### **4.8.1 Flow over a hemisphere-cylinder**

The flowfield over a hemisphere cylinder in a supersonic or hypersonic flow is a classical problem. A large number of experimental investigations were carried out in 1950s and 1960s to find the pressure and heat flux distribution over the surface of a hemisphere cylinder. Along with these experimental investigations, many analytical correlations were also developed in this era to compute the stagnation point heat transfer rates including those for chemically reacting boundary layers. The empirical correlations given by Fay and Riddell [7] and Lees [6] are the most popular and still extensively used to verify the experimental or numerical heat transfer rates at the stagnation point of spherical and spherically blunted cones.

The heat transfer results for the base configuration i.e. a hemisphere cylinder has been compared with the Fay and Riddell correlation for the stagnation point case and with that of Lees theory for surface heat flux distribution using equations (1.12) and (1.9) respectively. The pressure distribution require for these theories are obtained using the modified Newtonian theory. A strong agreement between the analytical and the computational results has been found with a difference of only 8% for the stagnation point heat transfer value while the heat flux distribution over the surface of the hemisphere cylinder differs from the Lees distribution by 2-20% as shown in Fig.4.9. The laminar stagnation point heat transfer rate was computed, using Fay and Riddell correlation, to be  $1.15 \times 10^7 \text{ W/m}^2$  while the FLUENT axisymmetric Navier-Stokes solver over predicted the heating to be  $1.24 \times 10^7 \text{ W/m}^2$ . A comprehensive code has been written to implement the correlations given Fay and Riddell [7] for the stagnation point heating and Lee's theory[6] for surface hat flux distribu-

tion. The code listed in Appendix C, is capable of computing laminar heat transfer rates over hemispheres and sphere-cones for ideal gas as well as real gas in thermo-chemical equilibrium. The coefficients of polynomial curve fits for relation between thermodynamic properties have been obtained from reference [108].

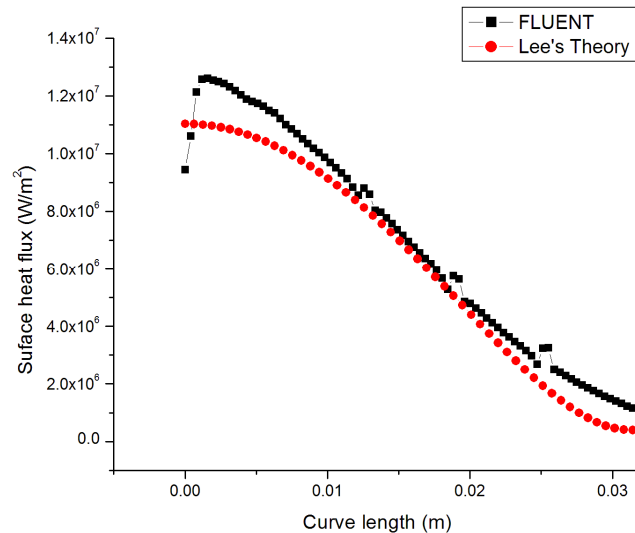


Figure 4.9 Surface heat flux on the hemispherical portion

#### 4.8.2 Flow over a hemisphere cylinder with a cylindrical cavity

A 5.08 cm diameter hemisphere cylinder with various forward facing cylindrical cavities of varying length of cavity to the diameter of the cavity ( $L/D$ ) have been investigated both experimentally and numerically in reference 10. In this classical work done by Engblom et. Al [10], the experiments were conducted in a Mach 5 blow down wind tunnel at a freestream pressure, temperature and Reynolds number of 4694 K, 64K and  $5.0e+07/m$  respectively. The heat transfer data for a hemisphere cylinder with a cavity of  $L/D=0.25$  and having sharp lip has been used to validate the FLUENT Code. A good agreement between the FLUENT results and the numerical results in reference [10] has been observed.

### 4.8.3 A large angle blunt cone with forward facing cavity

A recent experimental investigation over a large angle blunt hemispherical cone with and without a forward facing cylindrical cavity has been conducted by Sravanan et. al. in reference [40]. The Surface Stanton number based on the freestream conditions for the blunt cones at Mach 8 is obtained using an axisymmetric solver with perfect gas assumptions and compared with those obtained in reference [40]. As can be seen from Fig. 4.10 the computational results for surface Stanton number distribution over a blunt cone agrees closely with the experimental values within the limitations of CFD capabilities.

With the 2D axisymmetric formulation, the FLUENT solver over predicts the convective heat transfer by 0-20% with highest difference at the stagnation region as can be seen from Fig. 4.10.

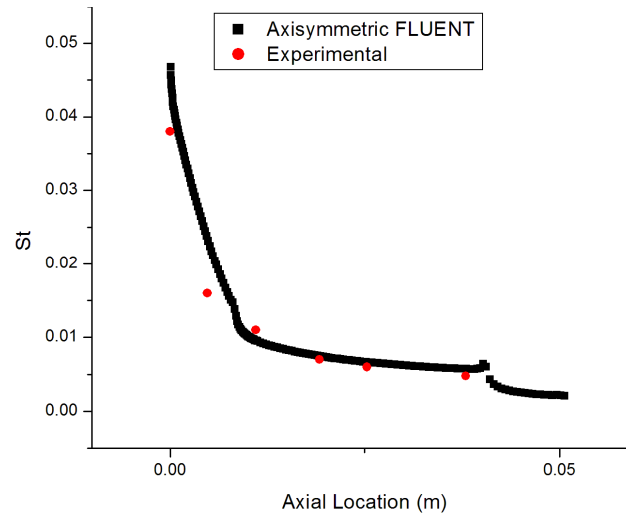


Figure 4.10 Surface Stanton Numbers for 41° sphere cone

Owing to uncertainties in the numerical setup, experimental setup and the round off errors, it can be assumed that the FLUENT code provides reasonably acceptable results.

#### 4.9 GRID INDEPENDENCE STUDY

The flowfield around the base hemisphere cylinder model has been discretized into 200 x 200 mapped quadrilateral cells with other models having more cells depending on either the depth of cavity or the length of aerodisk. For cavities there are 200 points in both axial and radial directions outside the cavity. A separate meshing has been done inside the cavity with number of cells depending on the depth of cavity. For aerodisk configurations the number of divisions is 200 in the radial direction normal to body while the number of grid points on the body varies depending on the length of the aerodisk. A grid independence study has been conducted on three cavity configurations and one aerodisk configuration. For three cavity configurations the grid points in both the directions have been doubled i.e. made 400 x 400 outside the cavity keeping the stretching factor and the first cell distance same as required by the  $y^+$  requirement. The number of grid points on each edge of cavity is also doubled during the grid independence study. A similar refinement of grid is used for the spiked configuration as well.

The comparison of coarse and fine mesh results for total surface heat transfer rates and the surface heat flux distribution shows that the 200 x 200 mesh is sufficient to resolve the viscous heating. The total heat transfer rates and the AWA heat flux for fine and coarse meshes were found to differ by only 0.5% while comparison of the surface heat flux distribution is shown in Figure 4.11 a-c.

From Fig. 4.11, it is clear that no extra insights into the physics is achieved by refining the mesh from 200 x 200 cells to 400 x 400 cells and thus meshes 200 x 200 cells have been used in this investigation to minimize computational expenses.

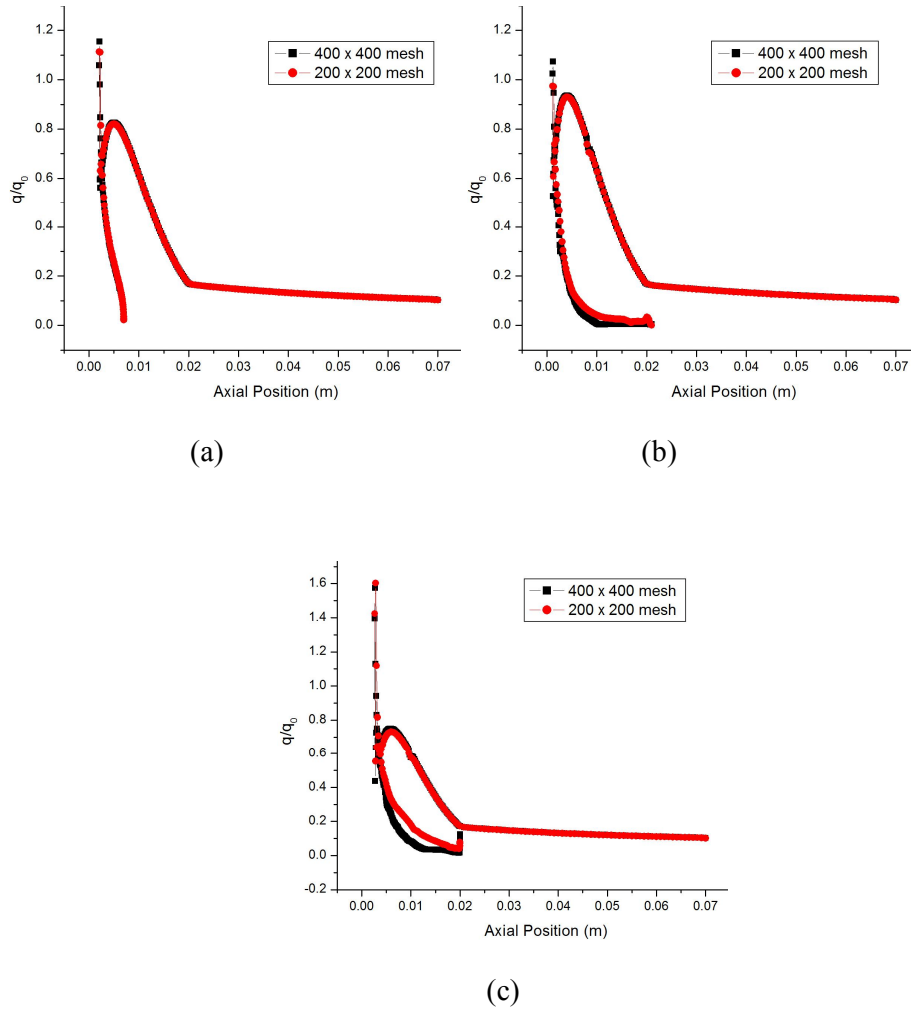


Figure 4.11 Mesh Refinement Heat Flux Distribution for a) Parabolic Cavity  $r/d=1.5$ ,  $d=7$  mm, b) Conical Cavity  $r/d=0.33$ ,  $d=21$  mm and c) Ellipsoid Cavity  $r/d=0.5$ ,  $d=20$  mm

## 5 RESULTS AND DISCUSSION FOR FLOW AT MACH 6.2

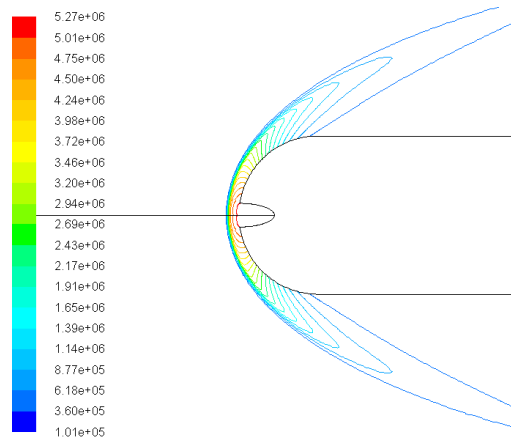
### 5.1 THE EFFECT OF ELLIPSOID CAVITY

The ellipsoid cavity at the nose of the base body is obtained by the axisymmetric formulation of an elliptic cavity. The ratios of the major axis ( $a$ ) to the minor axis ( $b$ ) of these elliptic cavities are fixed to be 3, 2 or 1.5. The minor axis  $b$  is slightly smaller than the lip radius  $r$  of the ellipsoid cavity due to intersection of ellipse and hemispherical cap at positive abscissa, while the major axis also represents the depth of these ellipsoid cavities. The effect of introducing an ellipsoid cavity at the nose of a hemisphere cylinder is reported through the change in the flowfield structure along with the surface heat flux and pressure distribution.

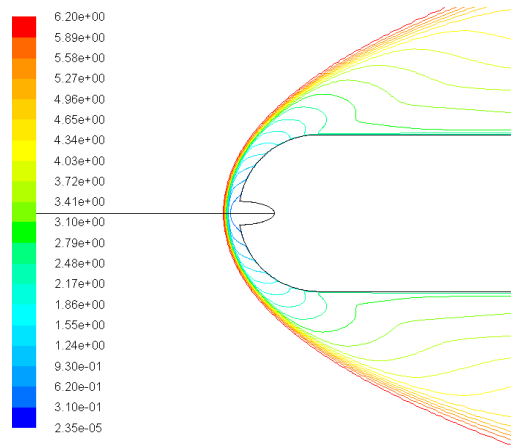
#### 5.1.1 Flowfield around hemisphere cylinder with ellipsoid cavity

The steady state flowfield around a hemisphere cylinder with a forward facing ellipsoid cavity can be best illustrated via the contours of various flow variables. Figure 5.1 (a-c) respectively shows the contours of pressures, Mach numbers and temperatures for an ellipsoid cavity with depth of 9 mm and  $a/b$  equal to 3. For cavities with very small lip radius the steady state bow shock wave shape remains similar to that of blunt body without cavity. The stagnation conditions prevail in the entire cavity with maximum pressure being almost equal inside whole cavity. The temperature however, inside the cavity is lower than that of the stagnation temperatures with a cool ring seen along the cavity surface. The temperature inside the cavity increases away and outwards from the stagnation point reaching a maximum in the vicinity of sharp lip. The Mach number shows almost stationary flow inside the cavity due to high speed of sound inside the cavity.

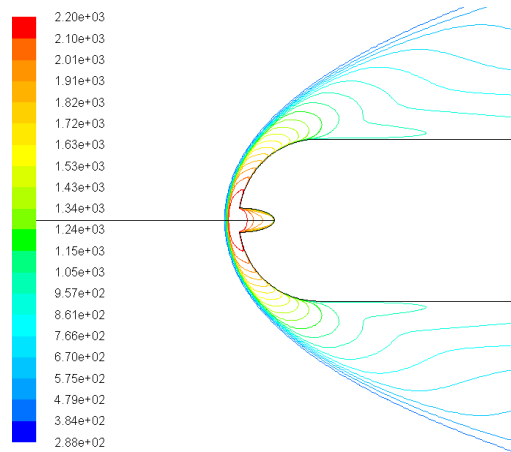




(a)



(b)



(c)

Figure 5.1 Contours of a) Static pressure, b) Mach numbers and c) Temperature for ellipsoid cavity with  $a/b=3$ ,  $d=9$  mm

Though the Mach numbers inside the cavity is infinitely small a pair of recirculating flow rotating in opposite directions can be observed near the mouth of the cavity as shown in Figure 5.2. The direction of rotation of these recirculating fluids is such that the flow direction adjacent to the stagnation line is opposite to freestream flow. The flow inside the cavity that is not a part of recirculating fluid region follows the curvature of the cavity and moves out of the cavity at the sharp lip. The presence recirculating fluid ensures a very little fluid entering the cavity such that the flow directed initially towards the cavity are all turned towards the sharp lip. This results in large deceleration of the fluid particles in the vicinity of the sharp lip along with high temperature gradients near the lip.

Though the Mach numbers inside the cavity is very small a pair of recirculating flow rotating in opposite directions can be observed near the mouth of the cavity as shown in Figure 5.2.

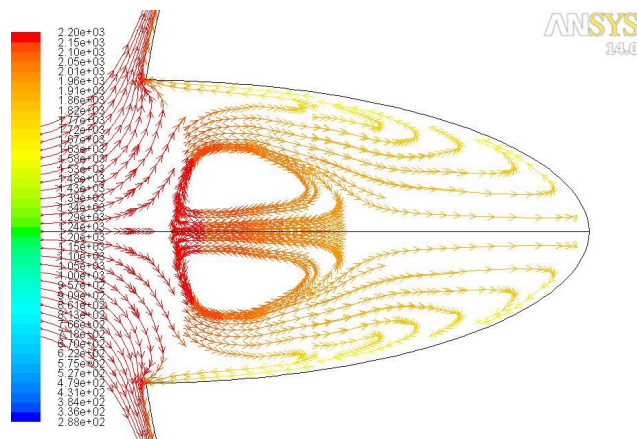


Figure 5.2 Streamlines inside ellipsoid cavity  $a/b=3$ ,  $d=9$  mm

The direction of rotation of these recirculating fluids is such that the flow direction adjacent to the stagnation line is opposite to freestream flow. The flow inside the cavity that is not a part of recirculating fluid region follows the curvature of the cavity and moves out of the cavity at the sharp lip. The presence recirculating fluid ensures a very little fluid entering the cavity such that the flow directed initially towards the cavity are all turned towards the sharp lip.

This results in large deceleration of the fluid particles in the vicinity of the sharp lip along with high temperature gradients near the lip. Another consequence of the recirculation zone is the formation of singular points along the axis of the body, near the opening of the cavity.

As the depth of cavity is increased keeping  $a/b$  ratio fixed, the size of the recirculating fluid region relative to the lip radius decreases allowing more fluid enter the cavity. As a consequence the temperature inside the cavity is more uniformly distributed to a relatively large surface area with lesser crowding of streamlines at the sharp lip.

Increasing the ratio of minor axis to major axis ( $a/b$ ) of the ellipse increases the mouth radius of the cavity which pushes the recirculation fluid region towards the cavity surface. The shape of the recirculation zone which is longitudinally stretched for small mouth opening becomes radially stretched as shown in Figure 5.3. As can be seen from Figure 5.3 the size of the recirculation zone is highly reduced with the singular moving further inside the cavity along the axis.

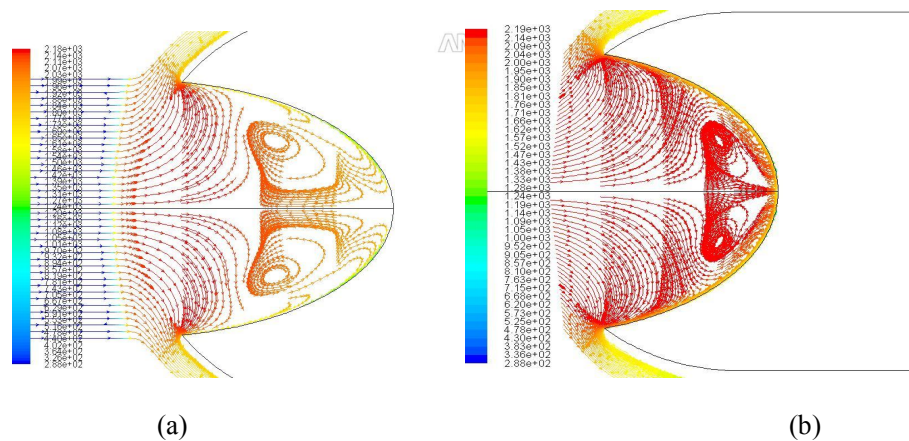


Figure 5.3 Streamlines inside ellipsoid cavity with a)  $a/b=0.5$ ,  $d=26$  mm and b)  $a/b=0.67$ ,  $d=24$  mm

With larger mouth radius the bow shock wave no more looks like one for a spherically blunt body, rather its becomes a normal shock almost up to the shoulder region of the hemisphere cylinder as shown in Figures 5.4 (a-c) .

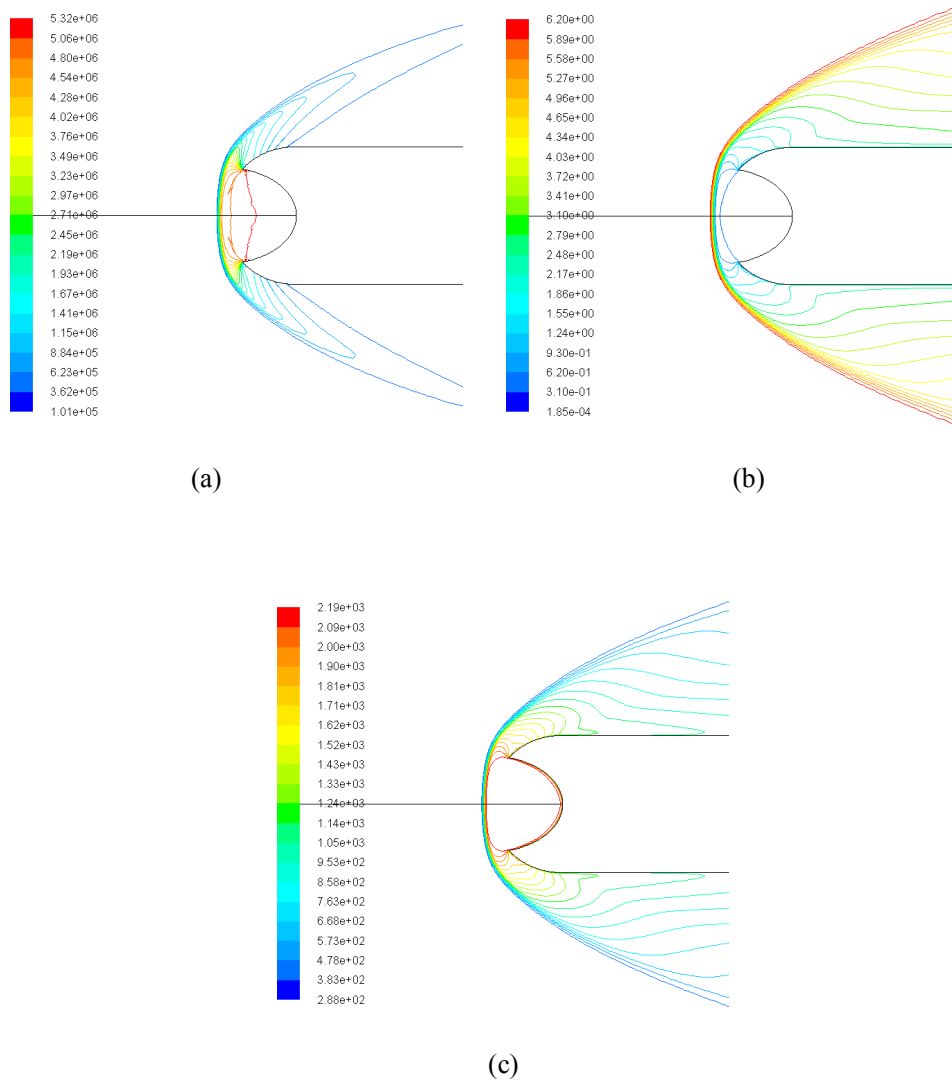


Figure 5.4 Contours of a) pressure, b) Mach number and c) temperature for ellipsoid cavity  $a/b=1.5$ ,  $d=21$  mm

This has a favourable effect in that the deceleration of the fluid particle in the vicinity of sharp lip is not very large causing less severe local heating at the sharp lip. Also it has been observed that for the same mouth radius the deeper cavities have larger region of relatively cold fluid inside the cavity.

### 5.1.2 Effect of Ellipsoid Cavity on Surface Pressure Distribution

The pressure distribution along the cavity surface of an ellipsoid cavity remains unchanged with depth or lip radius. The pressure along the surface of cavity remains constant up to the sharp lip and equal to the stagnation pressure for the blunt body without any cavity. The surface pressure distributions for different ellipsoid cavity configurations, non-dimensionalized with respect to the freestream pressure are shown in Figures 5.5 (a-c), 5.6(a-d) and 5.7(a-c). Figures 5.5, 5.6 and 5.7 respectively show the surface pressure distribution for ellipsoid cavities with  $a/b=3$ , 2 and 1.5.

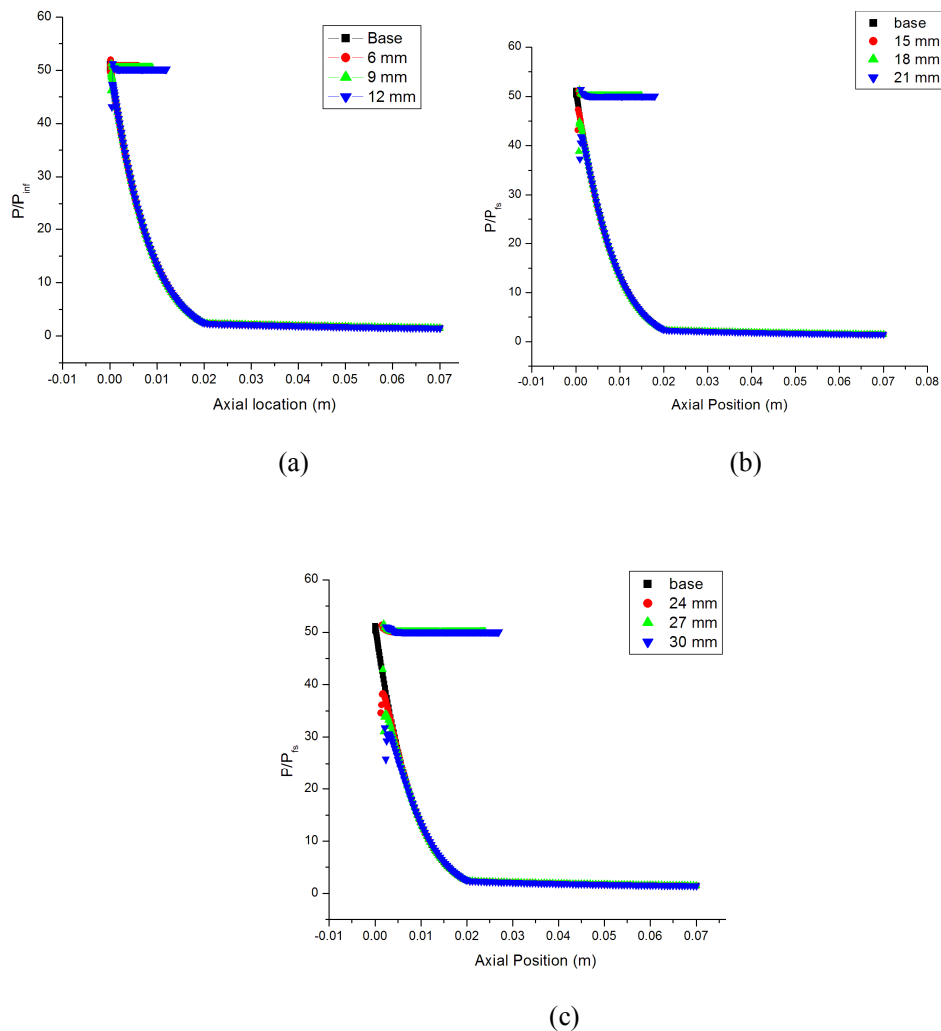


Figure 5.5 Surface pressure distribution for ellipsoid cavity with  $a/b=3$  and  $d=$  a) 6-12 mm, b) 15-21 mm and c) 24-30 mm

As can be seen in figures 5.5 -5.7, there is a sudden drop in surface pressure aft of the infinitely sharp lip due to expansion flow in order to follow the curvature of the blunt body. This sudden drop in surface pressure aft of sharp lip increases with increasing depth of ellipsoid cavity for fixed ratio of semi-major to semi-minor axis of the ellipse.

Increasing the mouth radius or decreasing  $a/b$  ratio, further exaggerates the pressure drop with pressure drop for deepest and widest cavities falling to about 5 % of the stagnation values.

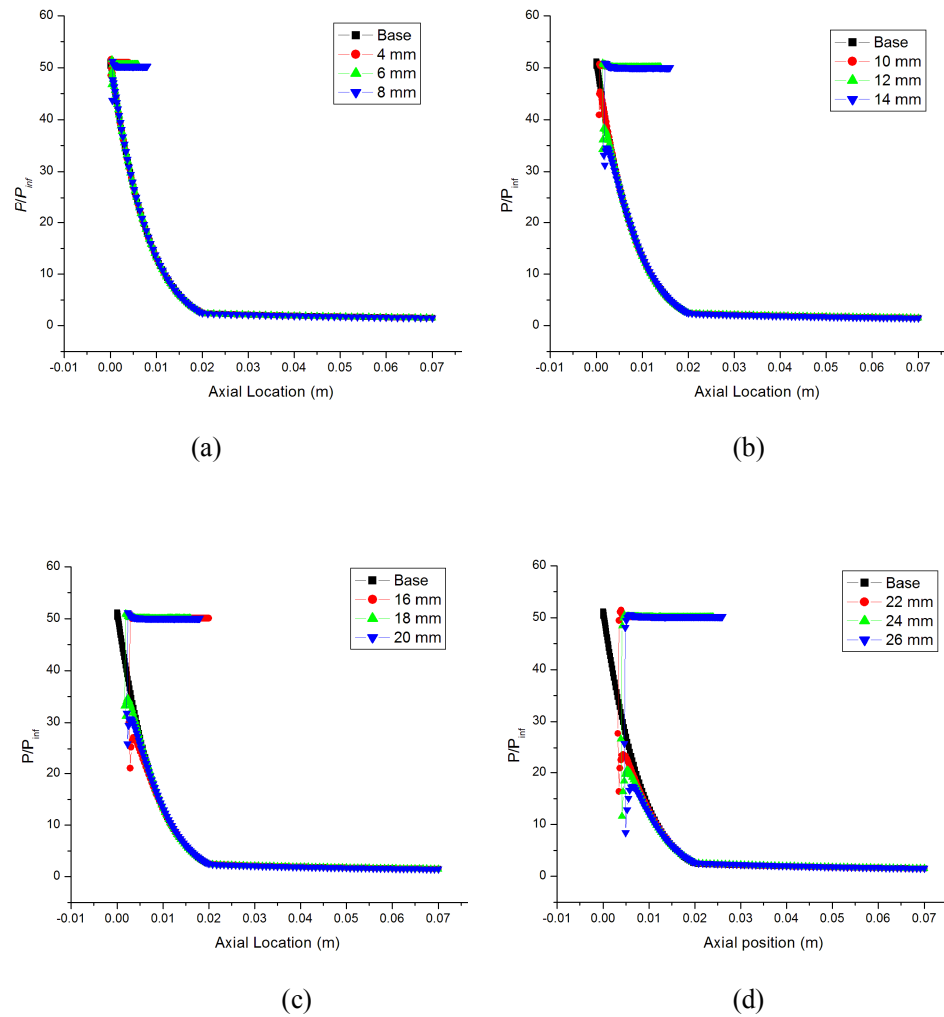


Figure 5.6 Surface pressure distribution for ellipsoid cavity with  $a/b=2$  and  $d=$  a) 4- 8 mm, b) 10- 14 mm, c) 16-20 mm and d) 22-26 mm

After the sharp drop at the in the vicinity of lip, there is a strong recovery in the pressure which reaches to a post lip maximum before another expansion along the hemispherical surface. The pressure along the surface, post peak pressure, decreases gradually up to the hemisphere-cylinder junction. The pressure after the junction remains almost constant with only marginal drop over the length of cylinder.

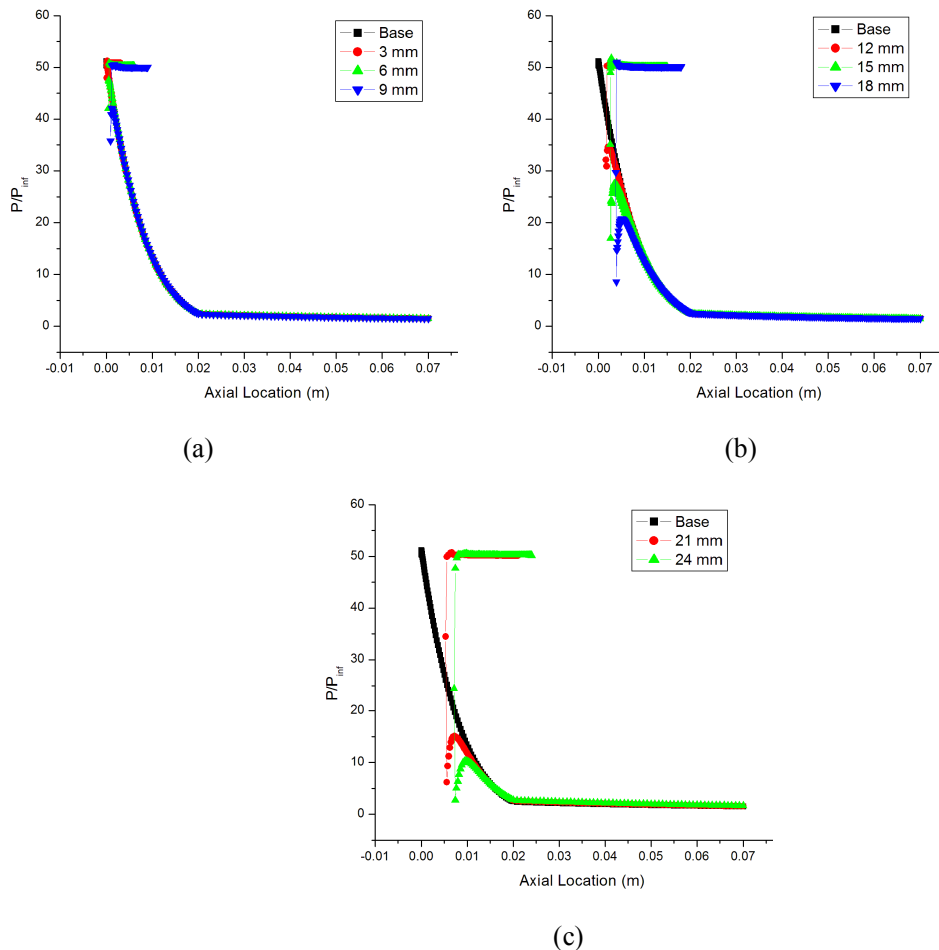


Figure 5.7 Surface pressure distribution for ellipsoid cavity with  $a/b=1.5$  and  $d =$   
a) 3- 9 mm, b) 12-18 mm and c) 21-24 mm

### 5.1.3 Effect of Ellipsoid Cavity on Heat Transfer Rates

The surface heat flux distribution follows directly from the temperature and pressure field around the blunt body. The stagnation point heat flux is dramatically reduced by the presence of an ellipsoid cavity at the nose a hemisphere

cylinder. This reduction is due to the formation a pair of recirculating fluid regions in the stagnation region inside the cavity which insulates the stagnation point from the high enthalpy flow upstream. The surface heat flux distributions for hemisphere cylinder with various cavity configurations are shown in Figures 5.8 – 5.10. The values of surface heat flux are non-dimensionalized with the peak heat value for a hemisphere cylinder with no cavity.

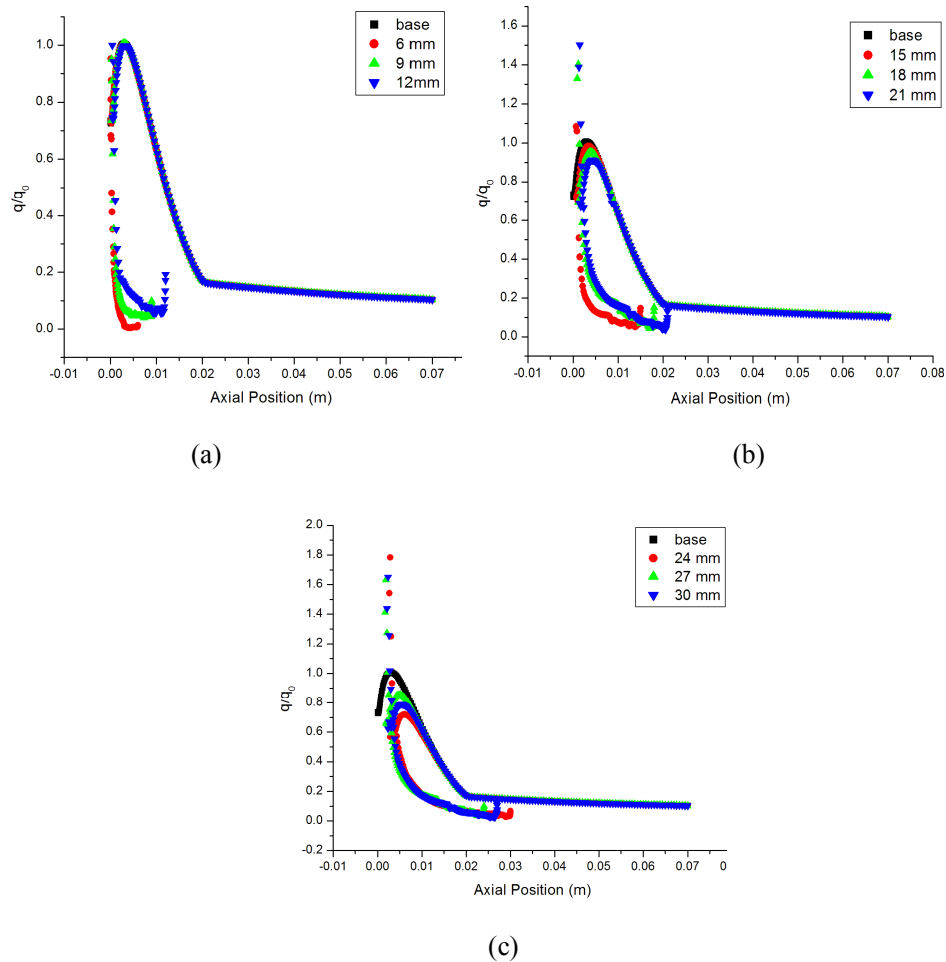


Figure 5.8 Surface heat flux distribution for ellipsoid cavities with  $a/b=3$  and  $d= a)$  6-12 mm, b) 15-21 mm and c) 24-30 mm

The surface heat flux along the cavity differs from the pressure distribution in that it is not constant along the cavity surface inside the cavity. A very low heat flux at the stagnation point drops slightly first and then rises sharply



along the surface up to the sharp lip to reach a maximum at the infinitely sharp lip. The detrimental rise in the heat flux observed at the sharp lip is probably due surface slope discontinuity and volumetric inefficiency arising from a vanishingly small surface area to conduct the heat. The detrimental rise at sharp lip is highly dependent on the depth of the cavity and the value of  $a/b$ .

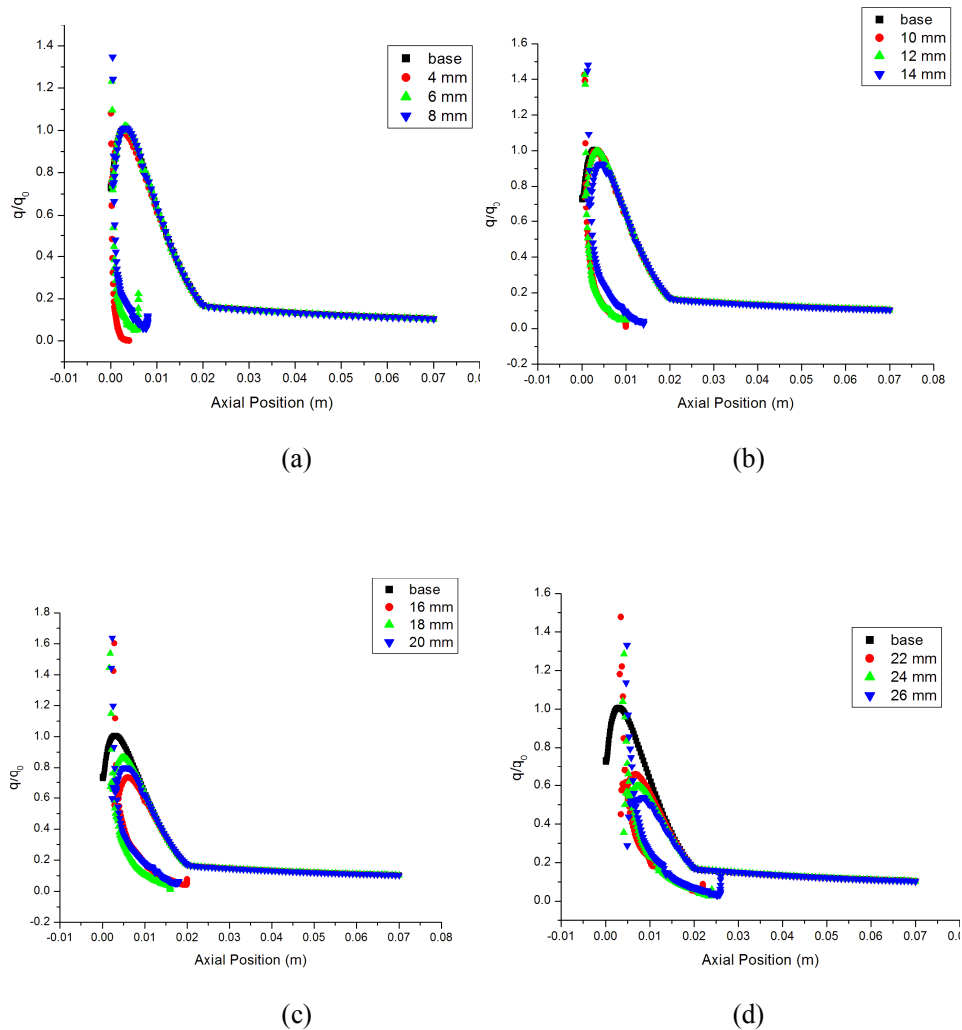


Figure 5.9 Surface heat flux distribution for ellipsoid cavity with  $a/b = 2$  and  $d = a$  4-8 mm, b) 10- 14 mm, c) 16-20 mm and d) 22-26 mm

For cavity of small depths with small lip radius, the rise is not detrimental at all and the heat flux rise is of the order of the peak heat flux for the base body. As the lip radius is or the depth of cavity is increased, the heat flux rise at the lip increases in magnitude. This is probably due to the pushing of the initially

longitudinal region of recirculating fluid into the cavity such that more of the incoming streams are directed towards the lip.

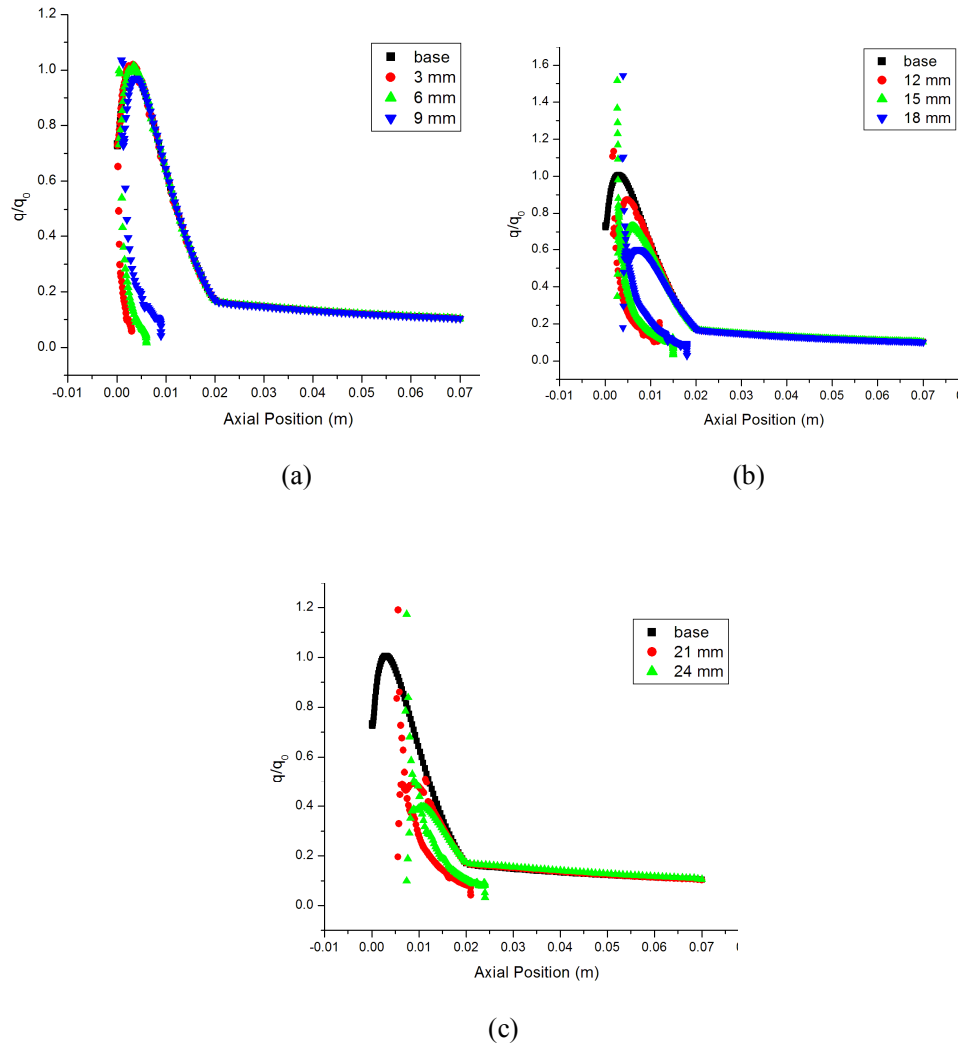


Figure 5.10 Surface heat flux distribution for ellipsoid cavity with  $a/b=1.5$  and  $d=$  a) 3-9 mm, b) 12-18 mm and c) 21-24 mm

Some respite is observed for sufficiently deep cavities with wider mouth opening i.e. large lip radius. In this case the counter rotating fluid regions is pushed very close to the stagnation region and is diminished in size; this allows the heat transfer from the incoming stream to be more evenly distributed to a larger area inside cavity, thus reducing the local heat flux at the sharp lip. Immediately after the sharp lip, there is an abrupt drop in the surface heat flux

as seen for the pressure distribution. This erratic change in the heat flux across the sharp lip can be smoothed by employing a rounded lip.

After the dramatic drop, the heat flux on the outer surface increases quickly to reach another maximum followed by an equally steep drop along the hemispherical surface up to the hemisphere- cylinder junction. Aft of the junction the surface heat flux remains almost constant with very slow drop along the length of the cylinder.

Ignoring the abnormal heat flux rise at the sharp lip which is highly exaggerated due to infinite sharpness which would not be the case with a physical projectile nose, the second peak heat flux on the hemispherical surface is decreased favorably with increasing depth and lip radius of the cavity. Figure 5.11 shows the peak heat flux on the outer surface of the hemisphere cylinder for various ellipsoid cavity configurations normalized with respect to peak heat flux for the base model. As can be seen from Fig. 5.11, the peak heat flux on the outer surface is of the same order of the base body peak heat flux for cavity depths up to 10 mm. For deeper cavities the reduction in peak heat flux becomes apparent and decreases almost linearly with depth. Most favorable heat flux reductions are obtained for cavities with  $a/b = 1.5$ , with the deepest cavity producing a reduction of about 55 percent in surface peak heat flux.

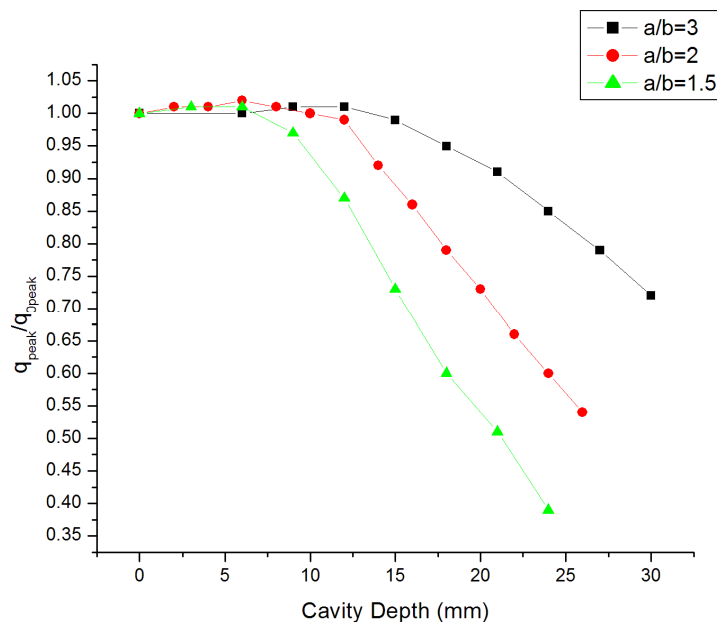


Figure 5.11 Peak heat flux on outer surface for various cavity models

The two most important aerodynamic heating parameters that are frequently discussed in literature are the *Total Heat Transfer Rate* and the *Area Weighted Average (AWA)* of heat fluxes over the body surface. Figures 5.12 and 5.13 show the total heat transfer rates and the AWA of the heat fluxes respectively, normalized with the respective values for base body. The trends seen in Figures 5.12 and 5.13 are similar to those for outer surface heat flux. Little or no reduction in both the quantities is obtained for small depth cavities even for large lip radius. With deepest ellipsoid cavities investigated a reductions of 26 percent and 30 percent in the total heat transfer rate and AWA of heat fluxes respectively is observed for cavity with  $a/b=1.5$  and having a depth of 24. The approximate lip radius,  $r$  of this cavity is 16 mm.

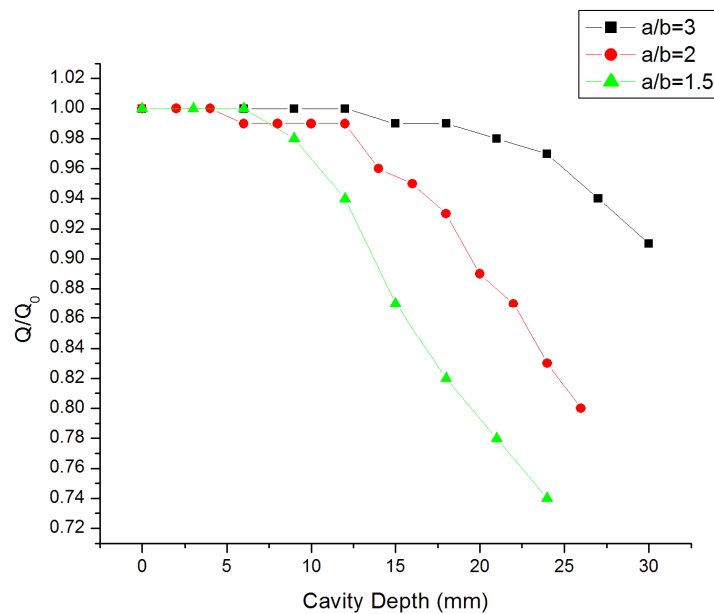


Figure 5.12 Total heat transfer rates for various ellipsoid cavity configurations

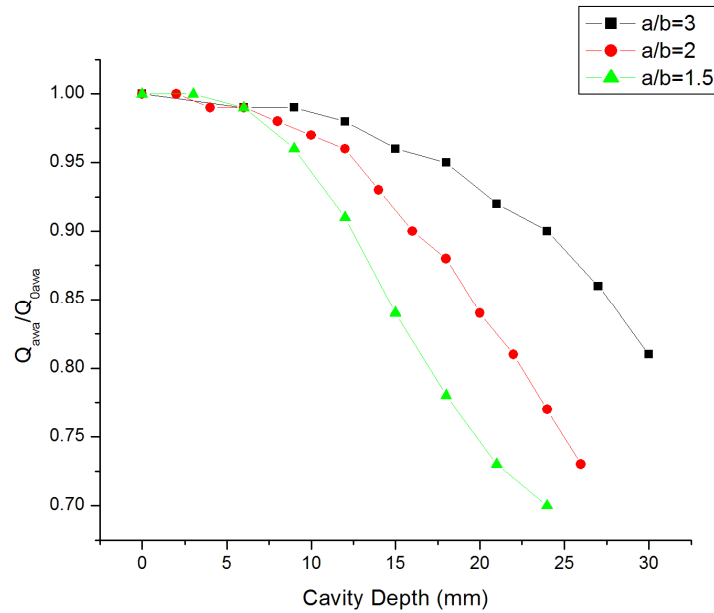
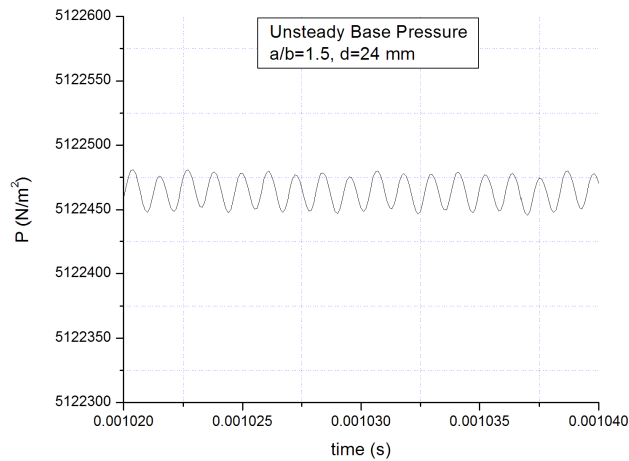


Figure 5.13 AWA of heat fluxes for various cavity configurations

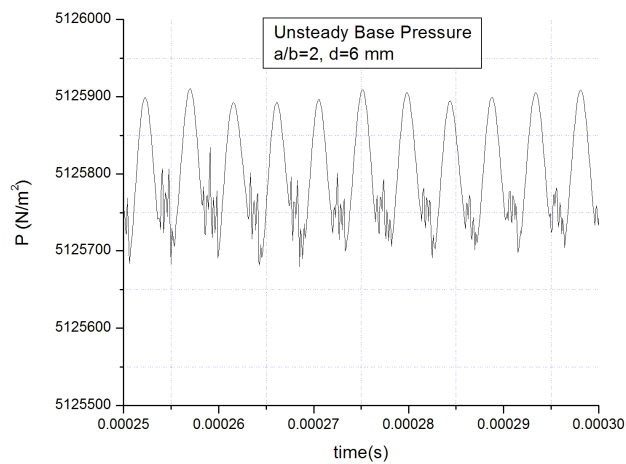
#### 5.1.4 The Effect of Flow Unsteadiness

The axisymmetric formulation does not allow for computation of lift or pitching moment even for unsteady case by forcing flow symmetry about longitudinal axis. The steady-state drag of a hemisphere cylinder with forward facing ellipsoid seems to be unaffected by the depth of the cavity. For lip radii up to 14 mm the drag remains constant with even slight drop (2-4%) for moderately deep cavities due to reversed direction of shear stresses inside the cavity. The aerodynamic drag for configurations with lip radii larger than 14 mm rises abruptly for all cavity depths.

The flow unsteadiness was captured by time marching from the steady state solution at a time step of  $1e-07$  seconds until a pseudo steady state flow were obtained. At the pseudo steady-state, the base pressure, the total heat transfer rates and the aerodynamic drag fluctuates about their respective steady state values. The maximum base pressure was found to oscillate about its mean value by less than 0.1 % in all cases as shown in Fig. 5.14 (a) and (b). The frequency of these fluctuations was observed to decrease with both an increase in lip radius for fixed depth and an increase in cavity depth for fixed lip radius.



(a)

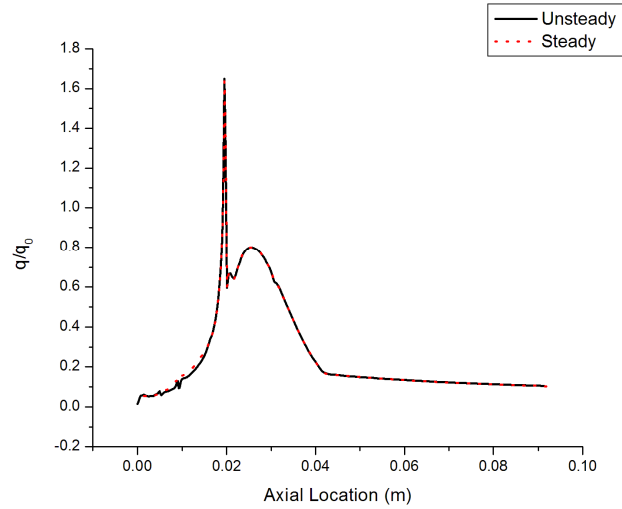


(b)

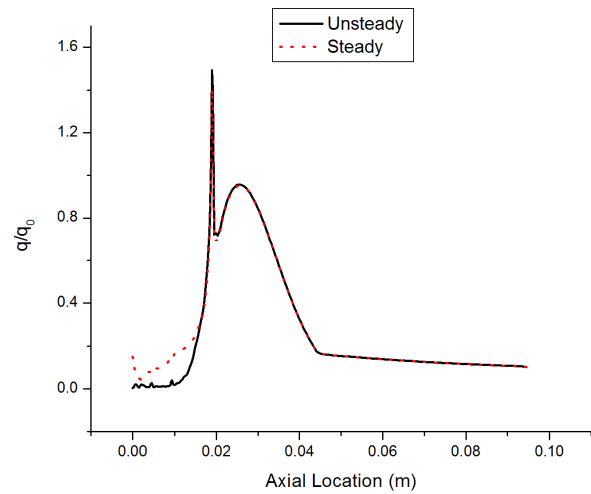
Figure 5.14 Cavity base pressure fluctuations for ellipsoid cavity with a)  $a/b=1.5$ ,  $d=24$  mm and b)  $a/b=2$ ,  $d=6$  mm

The small fluctuations in the cavity pressure ensure that unsteady drag remains close to the steady state values with fluctuations of less than 1% about the mean drag. The local surface heat flux also seems to be unchanged by the unsteadiness of the cavity flow, except for a small drop in local heating inside the cavity due to exchange of air in and out of cavity as can be seen in Fig. 5.15

and b. The reduction in total heat transfer rates to the entire body of about 1 % is achieved by the unsteady fluctuations in local surface heating.



(a)



(b)

Figure 5.15 Surface heat flux for ellipsoid cavity with a)  $a/b=3$ ,  $d=24$  mm and b)  $a/b=1.5$ ,  $d=15$  mm

## 5.2 THE EFFECT OF PARABOLIC CAVITY

### 5.2.1 Flowfield around hemisphere cylinder with parabolic cavity

The flowfield around a blunt body is significantly altered by the presence of a parabolic cavity. For smaller cavity depths, the steady state bow shock shape remains similar to that of a blunt body without any cavity as shown in Fig. 5.16 (a) and (b) which shows the Mach number and Temperature contours respectively for a cavity depth of 2 mm and  $r/d$  ratio of 2.5.

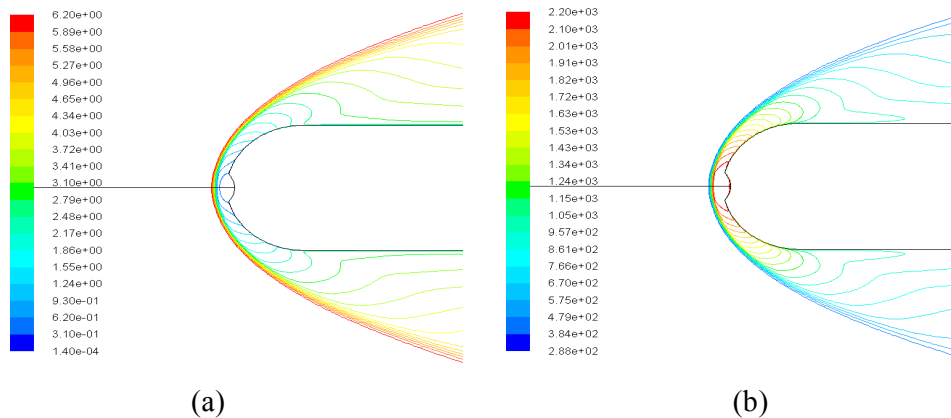


Figure 5.16 a) Mach Contours and b) Temperature Contours for  $r/d=2.5$ ,  $d=2$  mm

However as the size of the cavity opening increases the bow shock wave becomes nearly normal up to the sharp lip of the cavity as can be seen from the Mach number and temperature contours for a cavity of depth 10 mm and  $r/d$  value of 2.0 shown in Figures 5.17 (a) and (b).

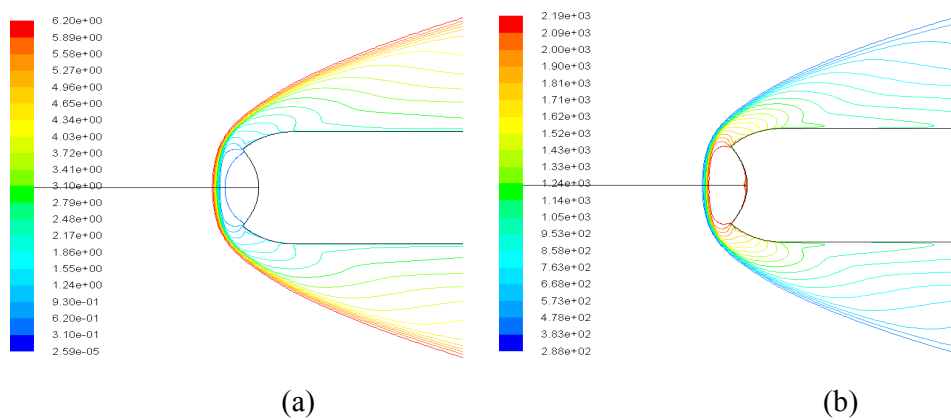


Figure 5.17 a) Mach contours and b) Temperature Contours for cavity depth 10 mm,  $r/d=2$



For all cavity configurations investigated a small region of relatively cold air is seen at the stagnation region which diminishes with the increasing opening of the cavity. For cavities with  $r/d$  ratio of 2.5 the flow that of a flat face flow-field with the flow following the curvature of the cavity smoothly before turning at the sharp lip of the cavity. For these very shallow cavities, a very small region of recirculating flow is observed at the stagnation region forming a singular point on the symmetry line very close to the surface of the cavity. As the  $r/d$  ratio is reduced to 2.0 and 1.5, a dominant pair of recirculating fluid region is formed inside the cavity which pushes the incoming flow away from the body. As a result of this the singular point on the symmetry line forms at some distance from the body. For the same  $r/d$  ratio as the cavity depth is decreased the relative size of the recirculating flow increases and the flow is pushed further away from the stagnation region. An adverse effect of growing recirculation zone in small depth cavities, however, is that the external flow converges near the sharp lip inside the cavity with a detrimental rise in local heat fluxes near the sharp lip. The particle Pathlines for cavity depths of 4 mm and 10 mm with  $r/d$  ratio of 1.5 are shown respectively in figure 5.18 (a) and (b).

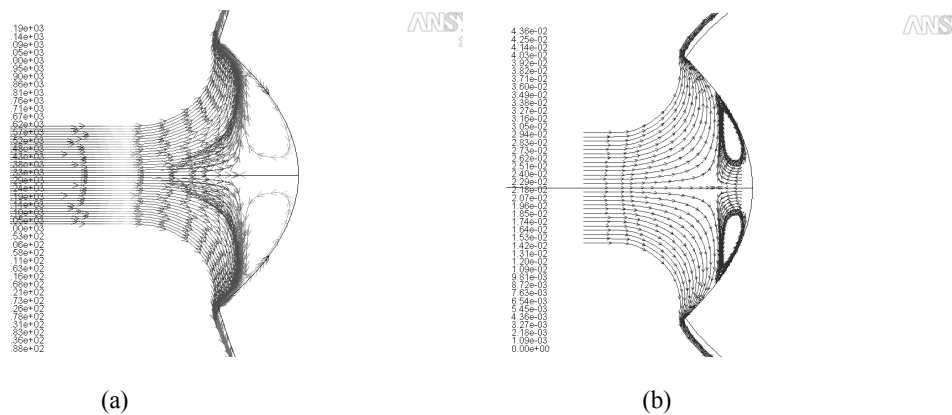


Figure 5.18 a) Pathlines for cavity depth 4 mm,  $r/d=1.5$  and b) Pathlines for cavity depth 10 mm,  $r/d=1.5$

### 5.2.2 Effect of Parabolic Cavity on Surface Pressure Distribution

The pressure distributions for all configurations with parabolic cavity investigated were found to follow a similar trend. The surface pressure inside the cavity increases slightly along the inner surface of to attain stagnation values at the inner side of the sharp lip. Figures 5.19-5.21 show the surface pressure distributions for hemisphere cylinder with parabolic cavities of  $r/d$  value 1.5, 2 and 2.5 respectively. The numbers appearing in the legends in these figures represent the depth of cavity.

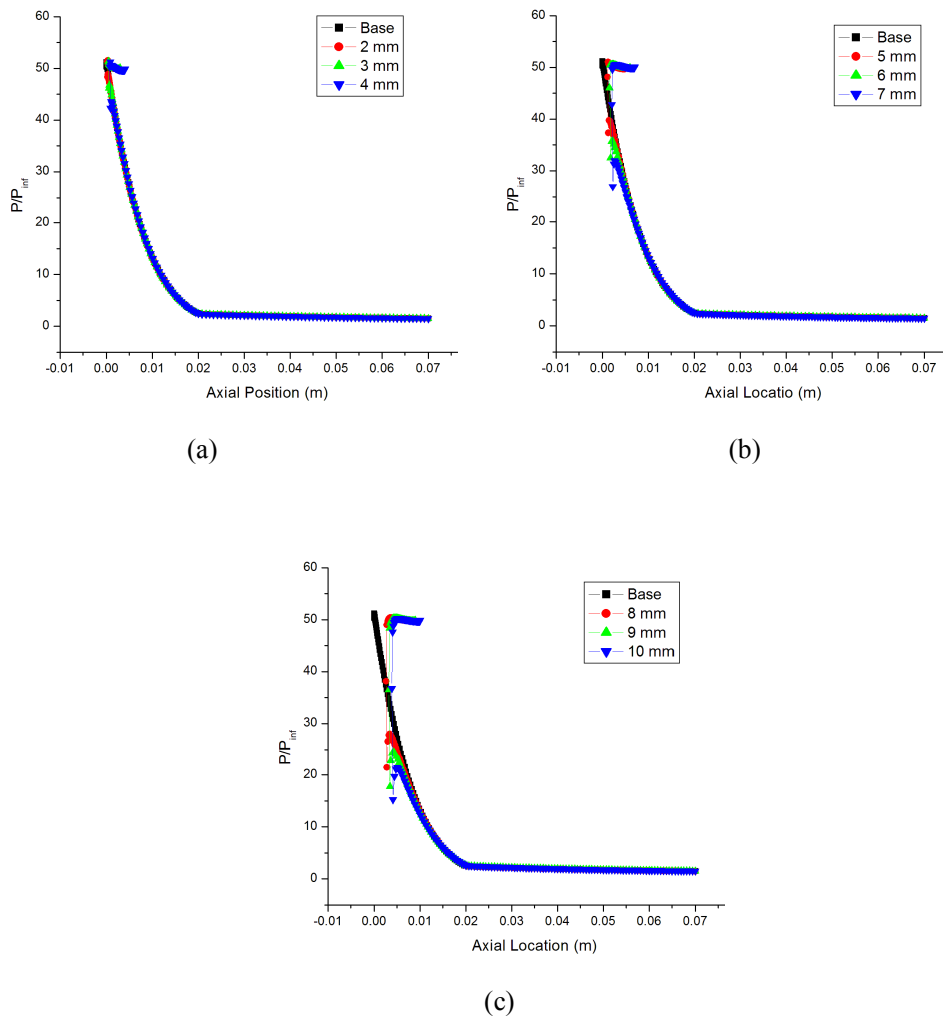


Figure 5.19 Surface pressure distribution for parabolic cavity of  $r/d=1.5$ , a)  $d= 2-4$  mm, b)  $d= 5-7$  mm and c)  $d=8-10$  mm

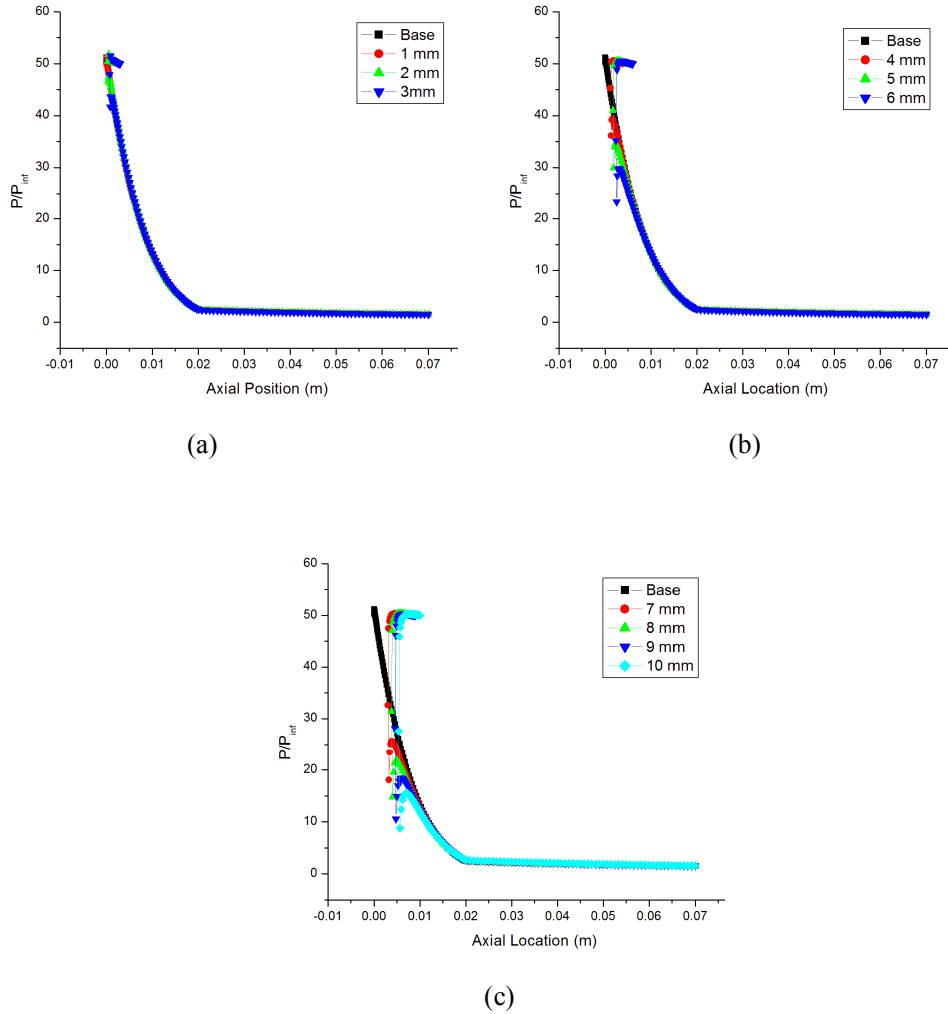


Figure 5.20 Surface pressure distribution for parabolic cavity of  $r/d=2$ , a)  $d= 1-3$  mm, b)  $d= 4-6$  mm and c)  $d=7-10$  mm

As can be seen in Figs. 5.19-5.21, there is a discontinuous drop in the surface pressure at the sharp lip of the cavity. The magnitude of drop in the surface pressure across the sharp lip is observed to be proportional to the lip radius  $r$ ; more the lip radius larger the pressure drop. For the widest cavity investigated the pressure drop to about 10% across the sharp lip. Downstream of the sharp lip, there is slight recovery in the surface pressure before the gradual expansion along the hemispherical surface. The continuous decrease in pressure stalls at the hemisphere-cylinder junction. The surface pressure thereafter and remains almost constant with only a marginal drop across the length of the cylinder.

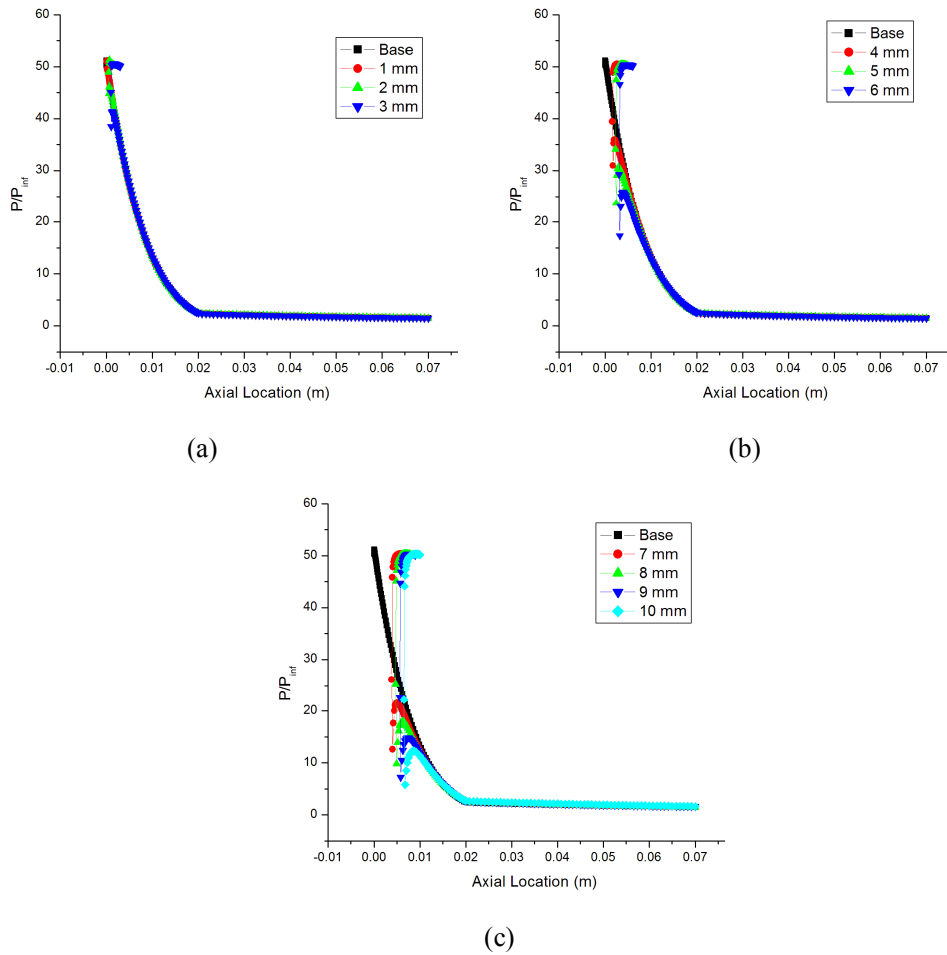


Figure 5.21 Surface pressure distribution for parabolic cavity of  $r/d=2.5$ , a)  $d=1-3$  mm, b)  $d=4-6$  mm and c)  $d=7-10$  mm

### 5.2.3 The Effect of Parabolic Cavity on Surface Heat Transfer Rates

The surface heat flux distribution over a hemisphere cylinder follows the pressure distribution trends. The stagnation point heat flux is dramatically reduced by the presence of shallow parabolic cavity. This reduction is due to the formation a pair of recirculating fluid regions in the stagnation region which insulates the stagnation region from the high enthalpy freestream flow. The heat flux along the cavity rises sharply along the surface up to the sharp lip. At sharp lip, a discontinuous and detrimental rise in the heat flux is seen which is probably due surface slope discontinuity and volumetric inefficiency of the

control volume at the intersection of the cavity surface and the outer surface. Across the sharp lip, the surface heat flux drops discontinuously to very low values. This discontinuous heat flux jump across the infinitely sharp lip can be smoothed by the use of rounded lip. Figures 5.22-5.24 show the surface heat flux distribution for blunt body with various parabolic cavities with  $r/d$  values of 1.5, 2 and 2.5 respectively

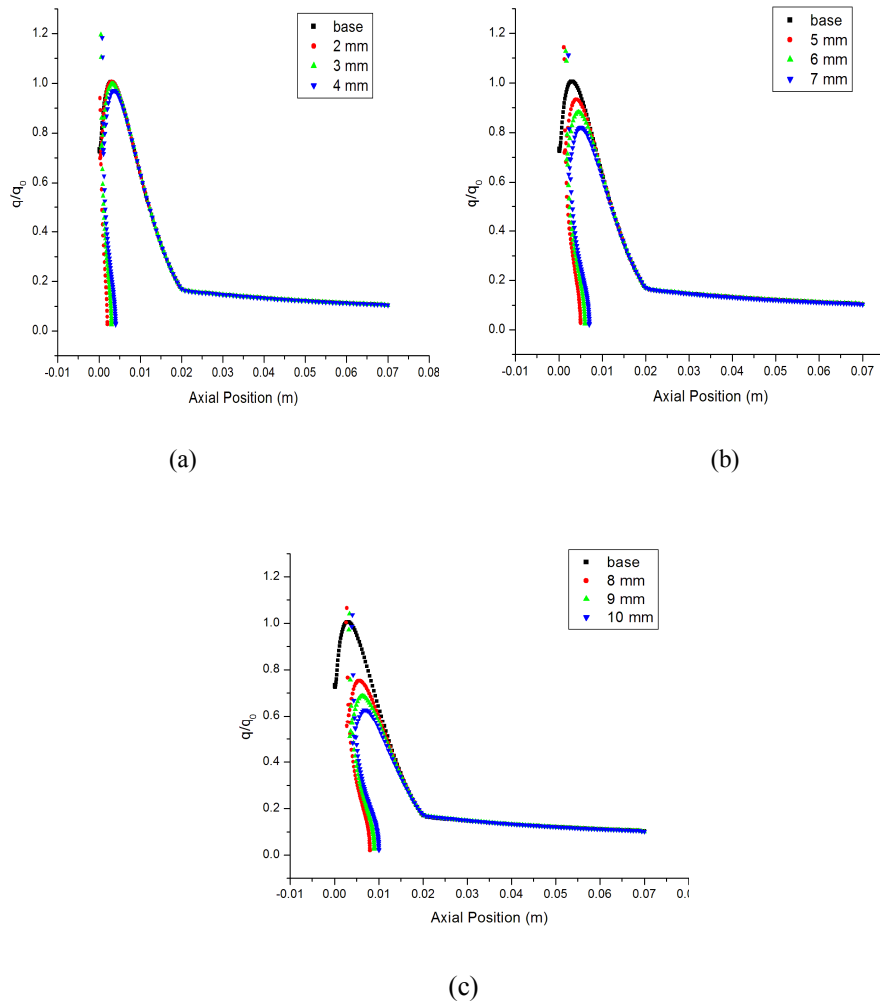


Figure 5.22 Surface heat flux distribution for parabolic cavity with  $r/d=1.5$ , a)  $d=2-4$  mm, b)  $d=5-7$  mm and c)  $d=8-10$  mm.

The surface heat flux drop at the sharp lip is observed to be proportional to the depth or the lip radius of the parabolic cavity with larger drop for wider and

deeper cavities. Downstream of the lip, the heat flux along the hemispherical surface increases on the outer surface to a new maximum. After the maximum, the surface heat flux decreases continuously along the hemispherical portion of the nose up to the hemisphere-cylinder junction. The heat flux reduction stalls at the junction with very small drop along the length of the cylinder.

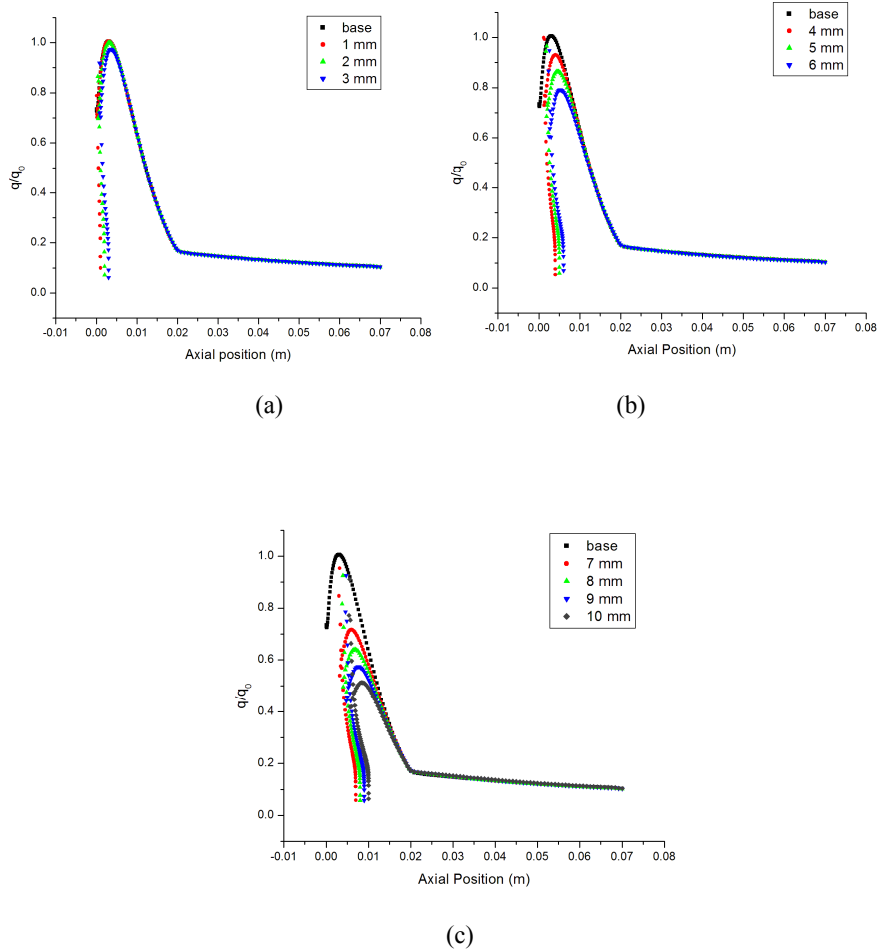


Figure 5.23 Surface heat flux distribution for parabolic cavity with  $r/d=2$ , a)  $d=1-3$  mm, b)  $d=4-6$  mm and c)  $d=7-10$  mm.

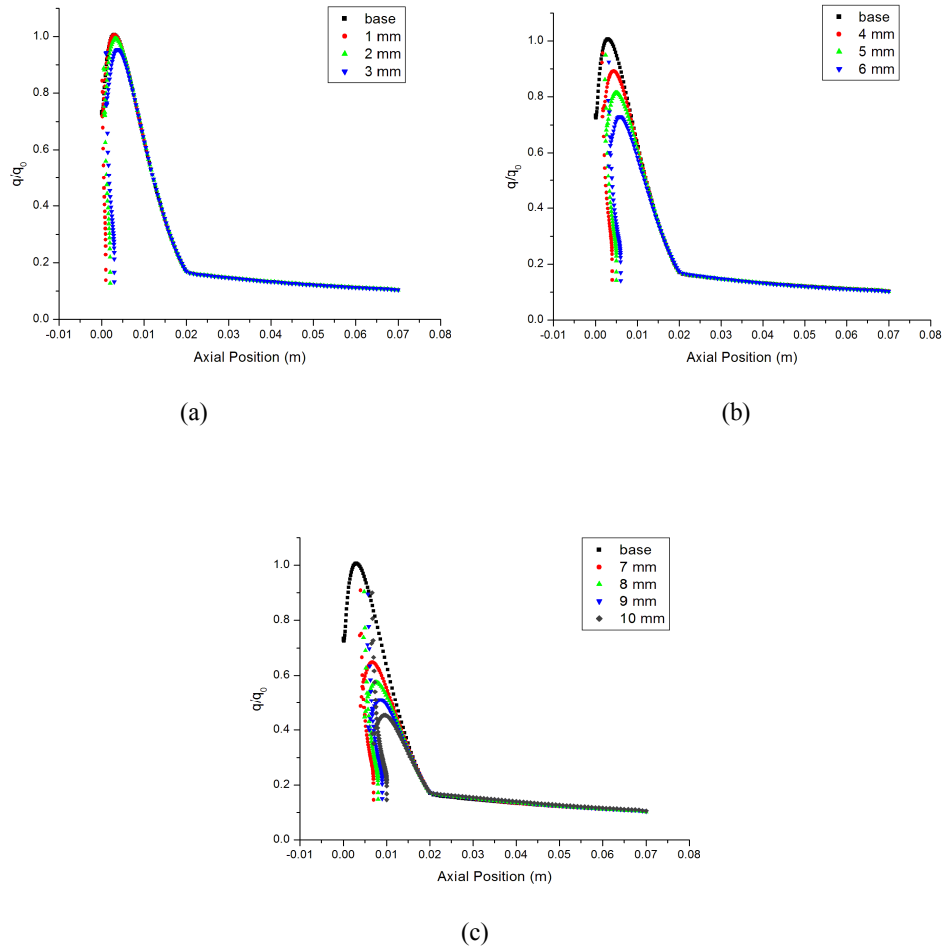


Figure 5.24 Surface heat flux distribution for parabolic cavity with  $r/d=2.5$ , a)  $d=1-3$  mm, b)  $d=4-6$  mm and c)  $d=7-10$  mm.

As can be seen from above Figs. 5.22-5.24, the radius of cavity at the lip is the key parameter in the surface heat flux distribution. Larger the cavity radius at the lip, lesser is the post lip peak heat flux. The peak surface heat flux on the outer surface of the various configurations with forward facing parabolic cavity is shown in Fig. 5.25. The surface heat fluxes in Fig. 5.25 are non-dimensionalized with the peak heating rate of the base configuration i.e a hemisphere cylinder without cavity.

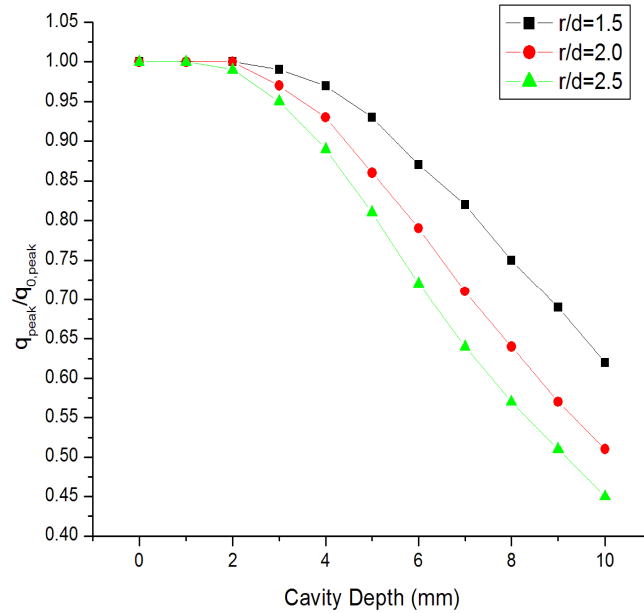


Figure 5.25 Peak heat fluxes on the outer surface for various cavity configurations

The advantage of deploying a forward facing parabolic cavity of various  $r/d$  ratios and depths can be summarized in terms of reductions in total heat transfer rates, area weighted average (AWA) of heat fluxes and peak heat fluxes. Figures 5.26 and 5.27 respectively show the total heat transfer rates and the AWA heat fluxes and peak heat fluxes for various cavity models investigated. The values in Figs. 5.26 and 5.27 are normalized with respect to the values for the base configuration.

As can be seen from Figs. 5.26-5.27, the aerodynamic heating parameters remain unchanged for very small cavities with depth up to 3 mm. For cases with cavity deeper than 3 mm a significant drop in all aerodynamic heating parameters is observed. These reductions increase almost linearly with the cavity depth and the deepest cavity shows the best aerodynamic heat reduction capability. For the same cavity depth, the cavity the larger mouth radius, more is the heat flux reduction and lesser heat transfer rates. Among the cases investigated the deepest cavity with  $r/d$  ratio of 2.5 and depth 10 mm produced a 26% reduction in total heat transfer rates, 25 % reduction in AWA



heat flux and 55% reduction the peak heat flux on the outer surface as compared to the values for the base configuration.

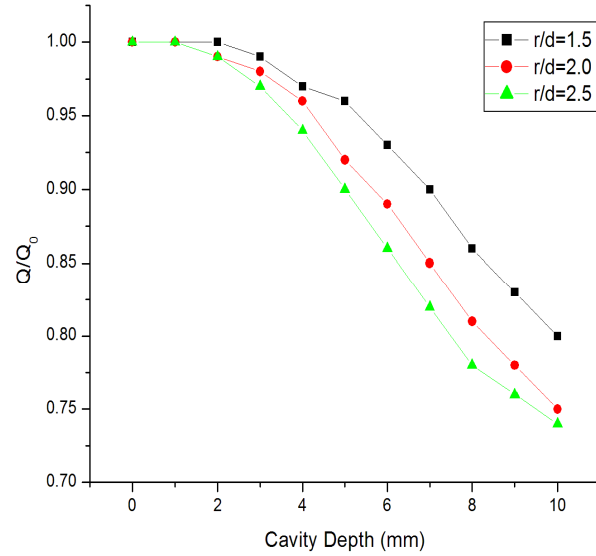


Figure 5.26 Total heat transfer rates for various cavity models

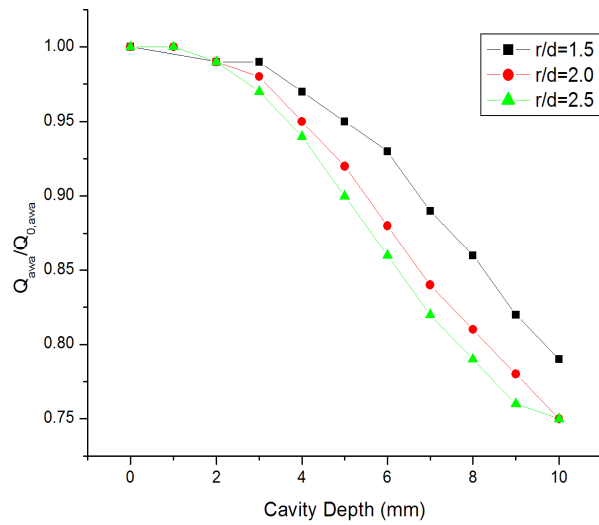
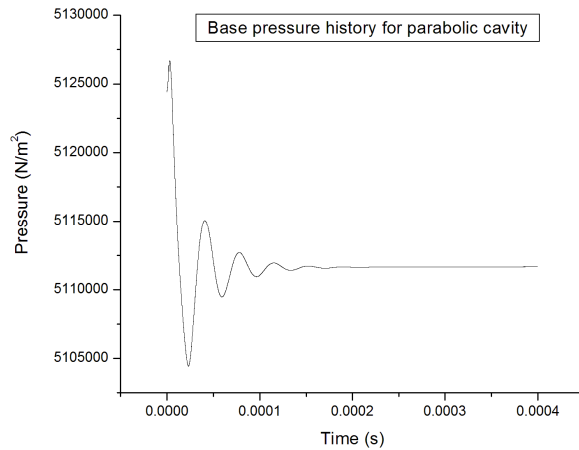


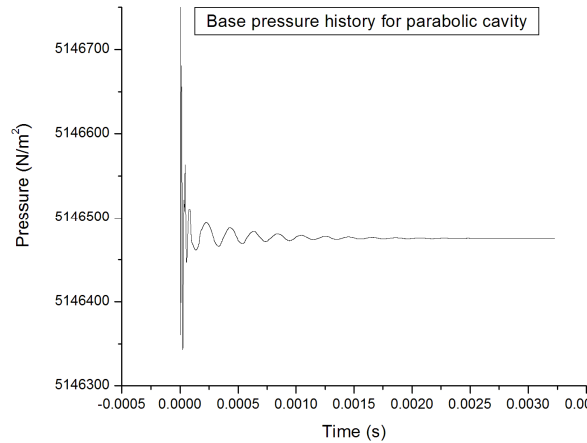
Figure 5.27 AWA heat fluxes for various cavity models

### 5.2.4 The Effect of Flow Unsteadiness

For all the shallow parabolic cavities investigated, the flow attains a steady state with all unsteady fluctuations in flowfield are completely damped out at larger physical time. The transient fluctuations of the cavity base pressure for three different cavities are shown Fig. 5.28. Figure 5.28 shows the result of time accurate time marching from the steady state solution with a time step of  $1 \times 10^{-7}$  second.



(a)



(c)

Figure 5.28 Base pressure history for parabolic cavities with a)  $r/d=1.5$ ,  $d=7$  mm and b)  $r/d=2.5$ ,  $d=4$  mm

All cavities attain the steady state at different time from the start depending on the depth of the cavity. As a consequence existence of steady state flowfield at zero degree angles of attack, the transient drags also converge their steady state values. The steady state drag of the blunt body remains unchanged with increase in depth the cavities, however a slight increase is seen for very wide cavities with r/d ratio of 2.5.

The same is true for the surface heat flux and total heat transfer rates. The distribution of mean surface heat flux for unsteady flow and surface heat fluxes for steady flow are identical.

### 5.3 THE EFFECT OF CONICAL CAVITY

#### 5.3.1 Flowfield around hemisphere cylinder with conical cavity

The flowfield for shallow conical cavities with semi-vertex angle of  $45^\circ$  shows the presence of two strong vortices inside the cavity. Figure 5.29 shows the primary vortices formed inside the conical cavity for configuration with a depth 4 mm and base radius of cone as 4 mm.

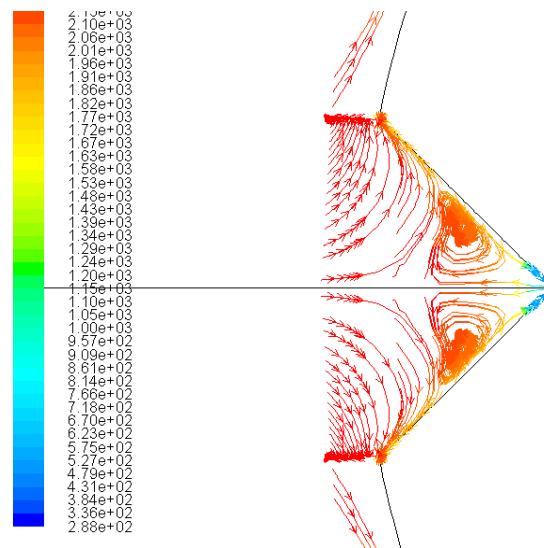


Figure 5.29 Primary vortices inside shallow conical cavities

As the depth of cavity is increased for same semi vertex angle, the primary vortices are pushed deep inside the cavity and aligned along the side walls of the cavity as shown in Fig. 5.30

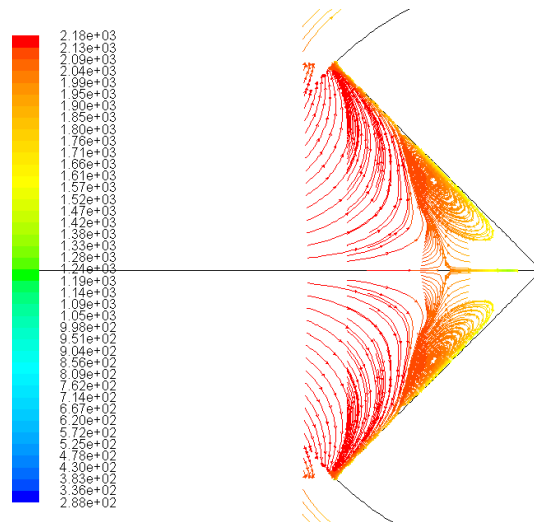


Figure 5.30 Pathlines for Cavity  $\alpha=45^\circ$ ,  $d= 20$  mm

This makes the streamline from the strike the sharp lip tangentially thus reducing the deceleration of the fluid particles. As the semi-vertex angle is decreased, the vortices move towards the axis of the body and away from the slant walls of the cones as shown in Fig. 5.31.

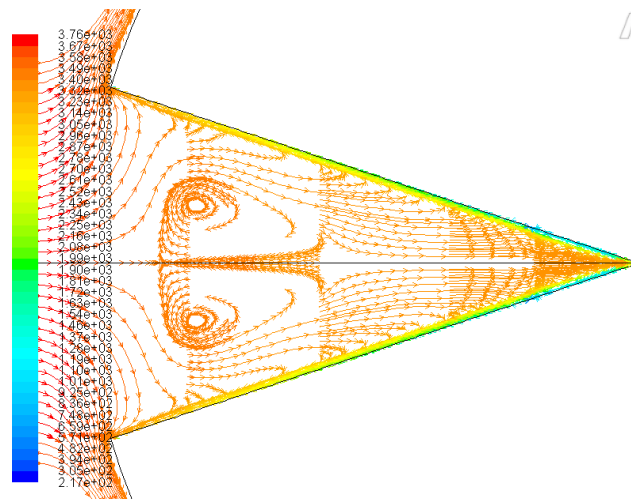


Figure 5.31 Pathlines for cavity with  $\alpha=18.45^\circ$ ,  $d=18$  mm

For sufficiently deep cavities the vortices become elongated and aligned parallel to the axis of the cavity. The deeper the conical cavity for a given semi-vertex angle, more elongated are the vortices inside the cavity. The elongated vortices for deep and small angle cones fills almost all the volume inside the cavity pushing the incoming high enthalpy flow away from the cavity as shown in Fig. 5.32. Thus for small angle cones with sufficient depth, only a negligible portion of the external flow enters the cavity and external flow impinges directly on the sharp lip and results in higher crowding as well as larger deceleration of the high enthalpy air, thus a higher heating rates are observed for small angle conical cavities.

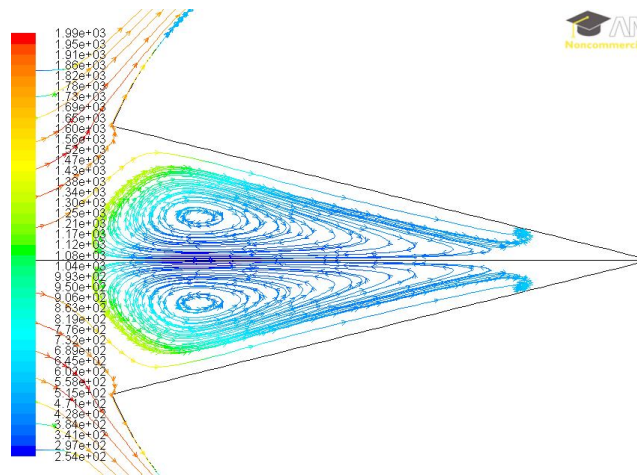


Figure 5.32 Vortices inside conical cavity  $\alpha=14^\circ$ ,  $d= 32$  mm

The velocity, pressure and the temperature fields for a hemisphere cylinder remains unaffected by the presence of very small depth conical cavity at nose as shown in Fig. 5.33 (a-c) which shows Mach number, pressure and temperature contours for configuration with a conical cavity of a depth 6 mm and lip radius 3 mm. The fluid inside the cavity is under stagnation conditions, rotating and moving at very low mach numbers and the pressure equal to the stagnation pressure. A temperature gradient however, could be observed along the axis of cavity, with post shock temperature rising slightly and then decreasing to low values near the walls.

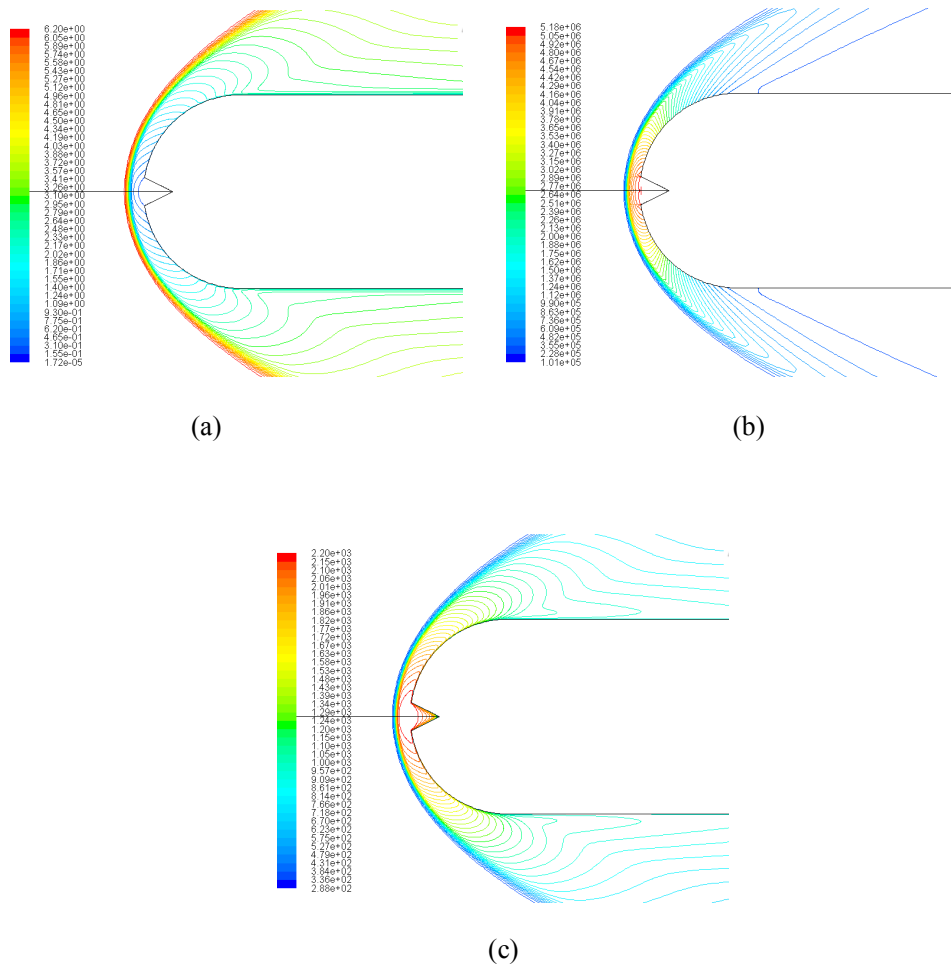


Figure 5.33 Contours of a) Mach number, b) Pressure and c) Temperature for conical cavity with  $\alpha=26.6^\circ$ ,  $d=6$  mm

For deeper cavities with small semi vertex angles, a slightly higher pressure, above post shock pressure can be seen in the vicinity of the sharp lip. The high temperature fluid inside these cavities however, is restricted to a small region near the entrance of the cavity. The post shock temperature falls gradually along the axis of the cavity to very low values before dropping sharply at the cold wall. The Mach number, pressure and temperature contours for a typical configuration with deep conical cavity are shown respectively in Fig. 5.34 (a) – (c).

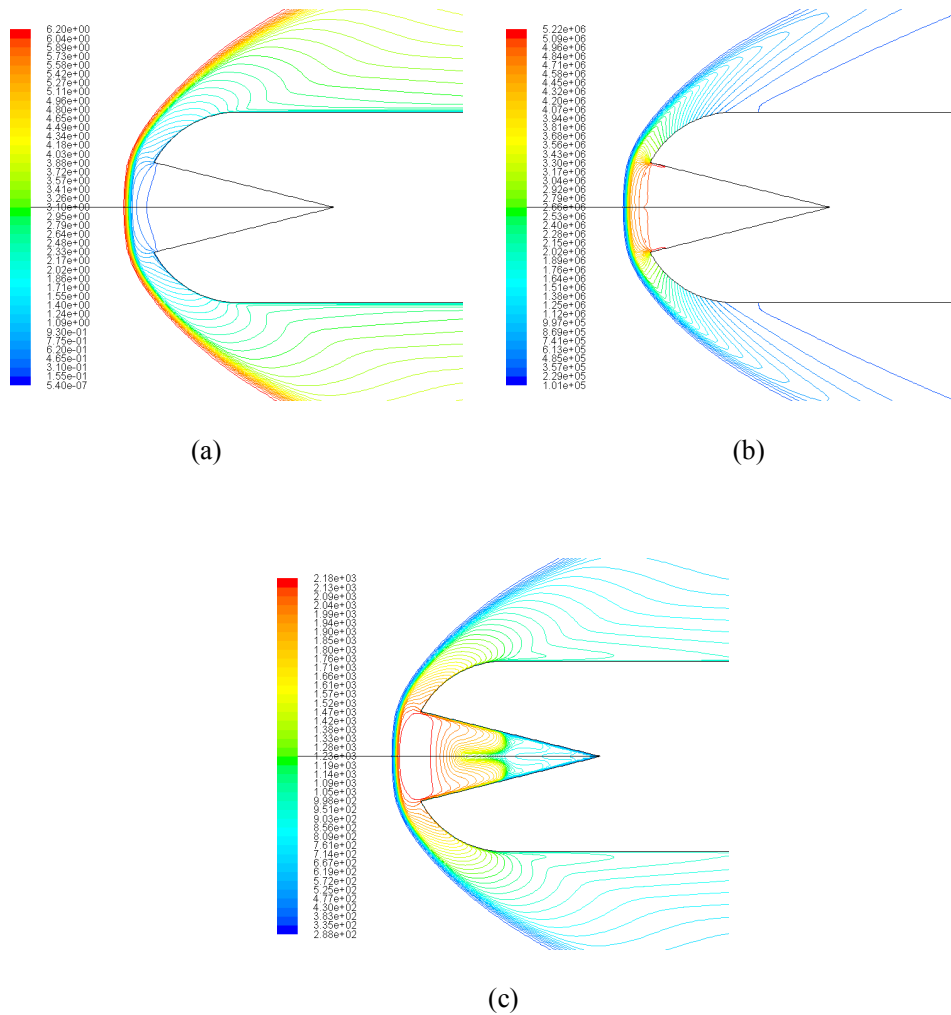


Figure 5.34 Contours of a) Mach number, b) Pressure and c) Temperature for conical cavity with  $\alpha=14^\circ$ ,  $d=40$  mm

### 5.3.2 Effect of Conical Cavity on Surface Pressure Distribution

The pressure distribution over the surface of hemisphere cylinder with a forward facing conical cavity is similar to that for a parabolic or ellipsoid cavity. The pressure all along the inner surface of the cavity remains constant and equal to the stagnation pressure for all cavity depths. The surface pressure distributions for cavity configurations with  $a/b = 1, 2, 3$  and  $4$  are shown in Figs. 5.35-5.38 respectively.

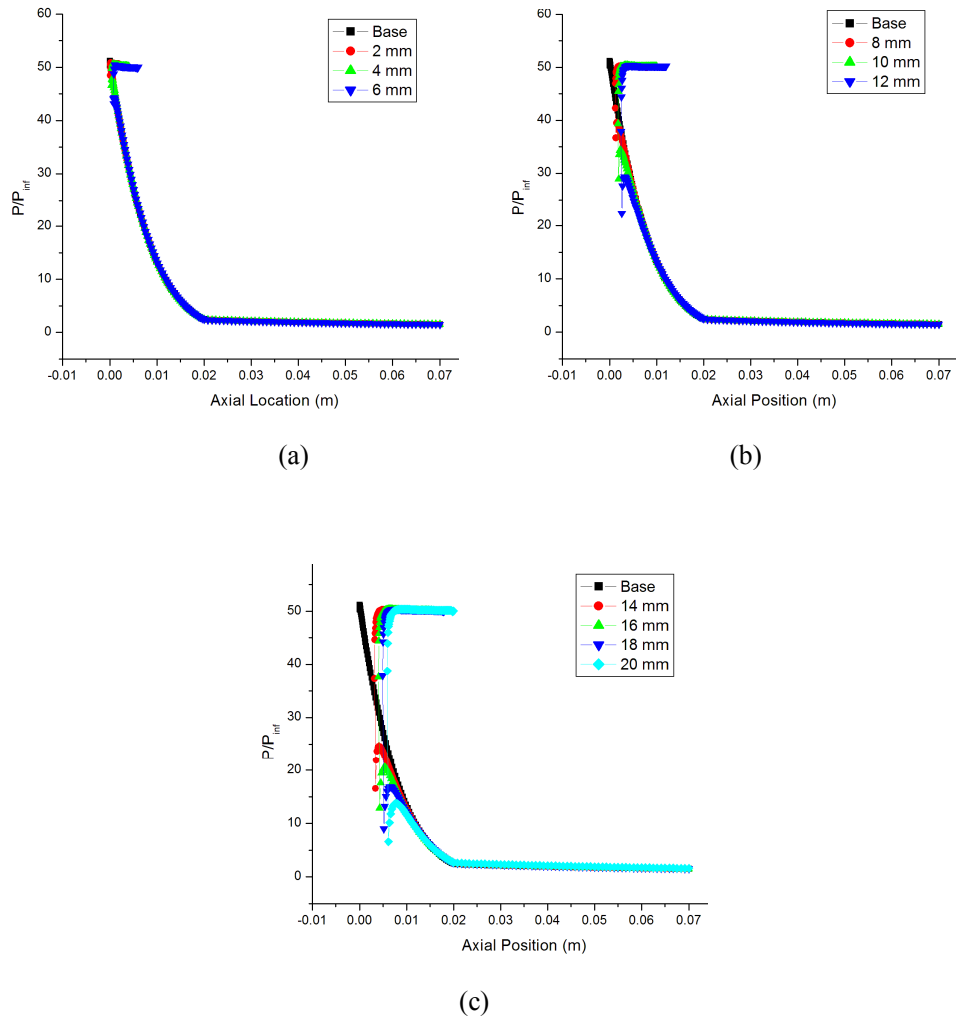


Figure 5.35 Surface pressure for conical cavity with  $\alpha=45^\circ$  and  $d=$  a) 2-6 mm, b) 8-12 mm and c) 14-20 mm

Though the surface pressure along the cavity is constant and equal for all cavity configurations, a sudden expansion seen at the sharp lip on outer surface is different for different cavity configurations. As can be observed from Figs. 5.35-5.38, the expansion at the sharp lip is highly dependent on the lip radius at the mouth of cavity, more the lip radius more is the pressure drop. For the cavity with widest mouth investigated, the pressure drops to about 15% of the stagnation values. After a sharp expansion at the lip, a small recovery in pressure is seen aft of the lip. In absolute terms, this recovery in pressure is similar for all cavity configurations. The slightly recompressed flow aft of the sharp lip goes for another gradual expansion along the outer hemispherical surface.



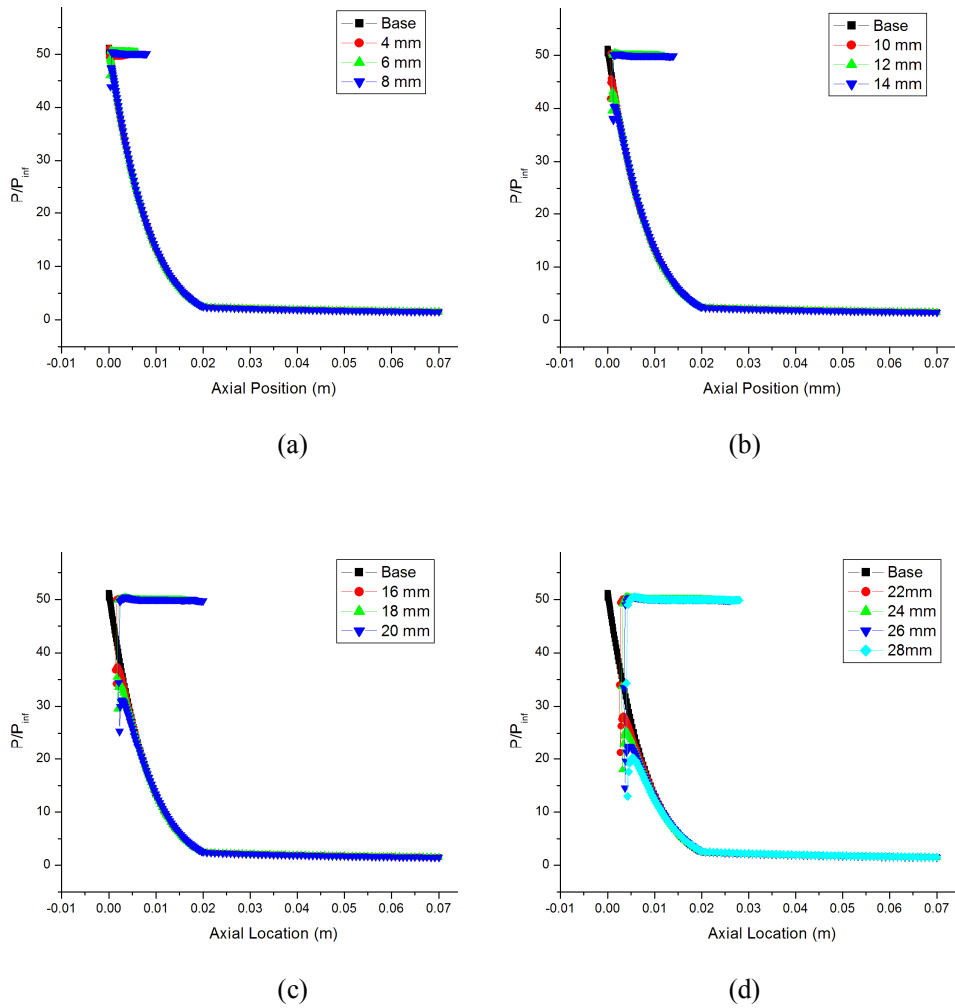
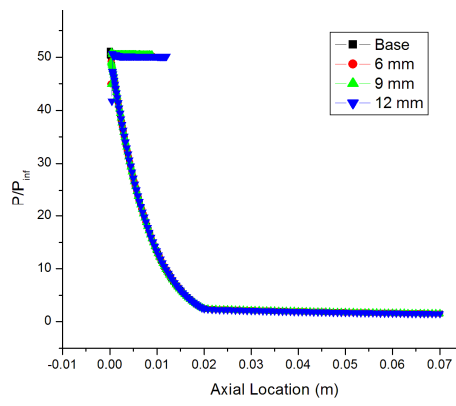
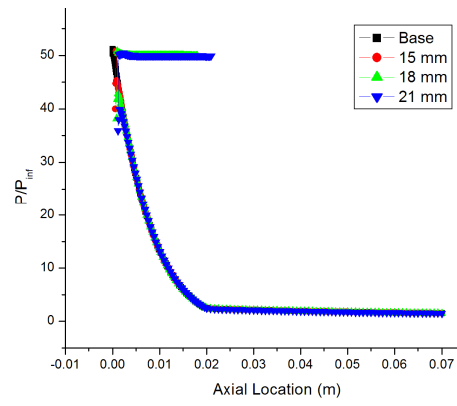


Figure 5.36 Surface pressure distribution for conical cavity with  $\alpha=26.56^\circ$  and  $d=$   
a) 4-8 mm, b) 10-14 mm, c) 16-20 mm and d) 22-28 mm

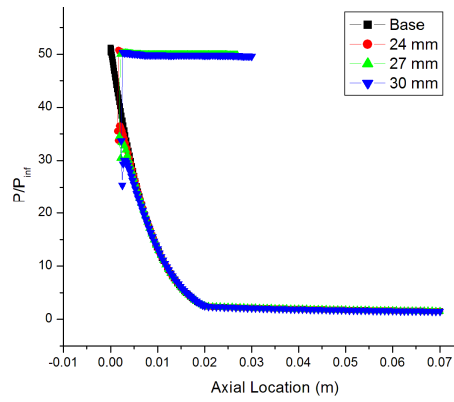
The pressure drop through this gradual expansion is same for all the cavity configurations and pressure after this expansion drops to about 5% of the stagnation values. The continuous expansion on the hemispherical portion of nose stalls at the hemisphere-cylinder junction. After the hemisphere-cylinder junction the pressure falls negligibly along the length of the cylinder.



(a)



(b)



(c)

Figure 5.37 Surface pressure distribution for conical cavity with  $\alpha=18.45^\circ$  and  $d=$   
a) 6-12 mm, b) 15-21 mm and c) 24-30 mm

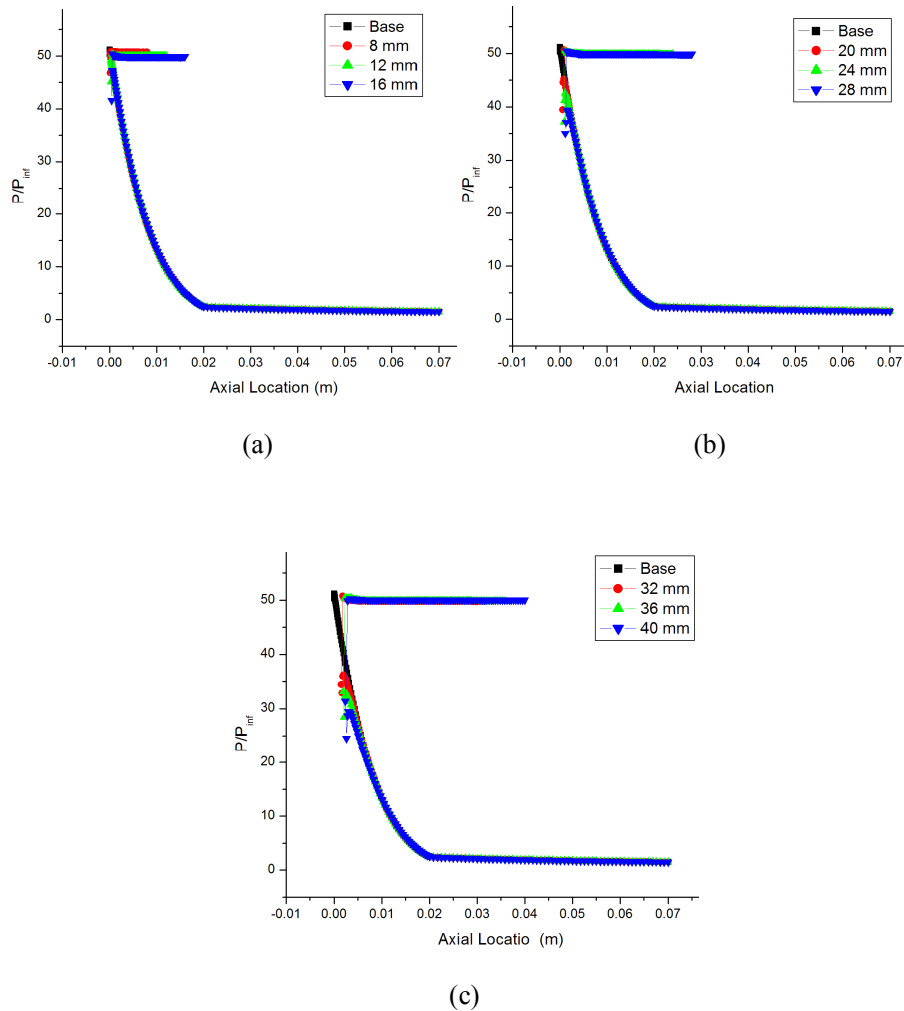


Figure 5.38 Surface pressure distribution for conical cavity with  $\alpha=14^\circ$  and  $d=$  a) 8-16 mm, b) 20-24 mm and c) 32-40 mm

### 5.3.3 Effect of Conical Cavity on Surface Heat Flux Distribution

The surface heat flux distribution over a hemisphere cylinder with a forward facing conical cavity follows the trends for the surface pressure distribution except on the inner cavity surface. The stagnation point heat transfer rate is dramatically reduced for all cases to negligible values because of the formation of a strong pair of vortices inside the cavity. This recirculating fluid zone insulates the stagnation point from the incoming stream and hence reduced heating rates. The heat flux along the inner cavity surface thereafter rises sharply to reach its peak value at the infinitely sharp lip. The value of this

peak heat flux depends on the cavity configuration particularly the lip radius of the conical cavity. Figures 5.39-5.42 show the surface heat flux distribution for models with various cavity depths having semi-vertex angles of  $45^\circ$ ,  $26.56^\circ$ ,  $18.4^\circ$  and  $14^\circ$  respectively. The numbers inside the legend in these figures represent the depth of conical cavity.

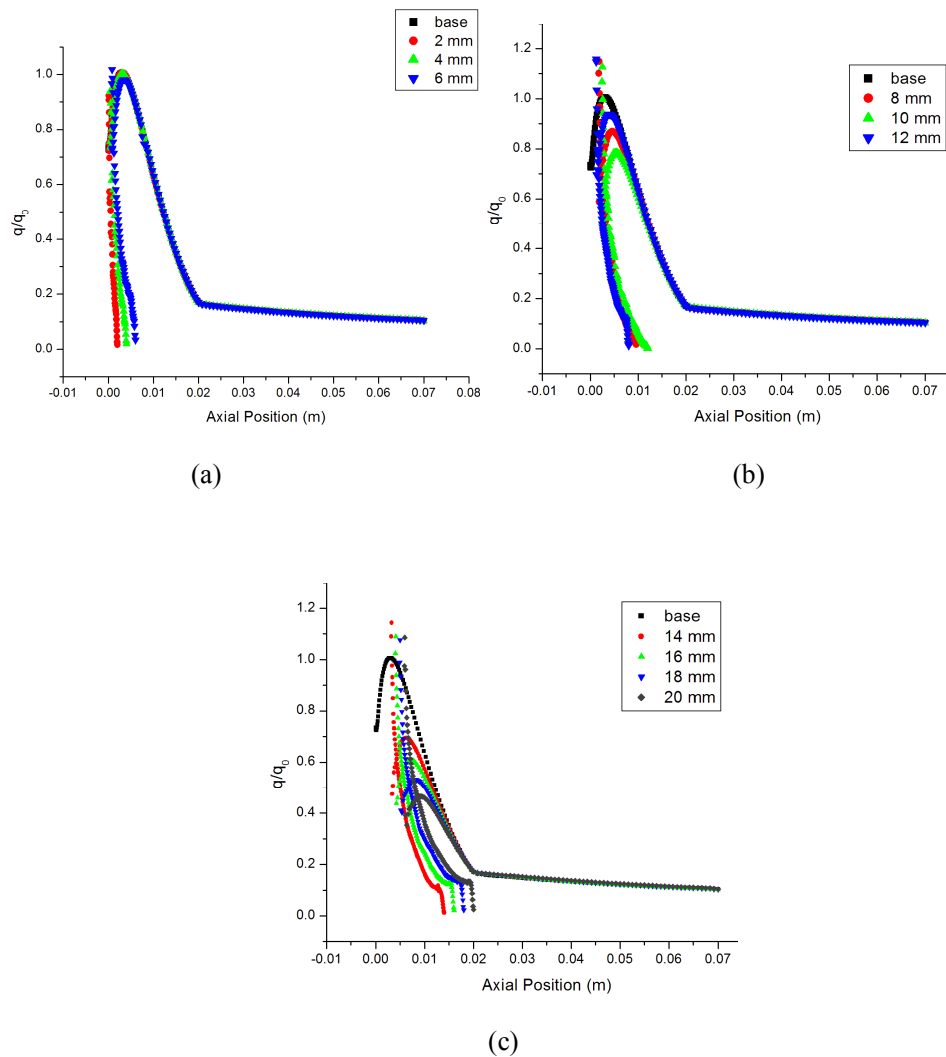


Figure 5.39 Surface heat flux distribution for conical cavities with  $\alpha=45^\circ$

As can be seen in Figs. 5.39-5.42, the peak heat flux at the sharp lip of small radius is lower than the peak heat flux for base configuration. The peak heat

flux for cavities with lip radius or the base radius of the cone  $b$ , larger than 5 mm, is 5-18% higher than that of base configuration.

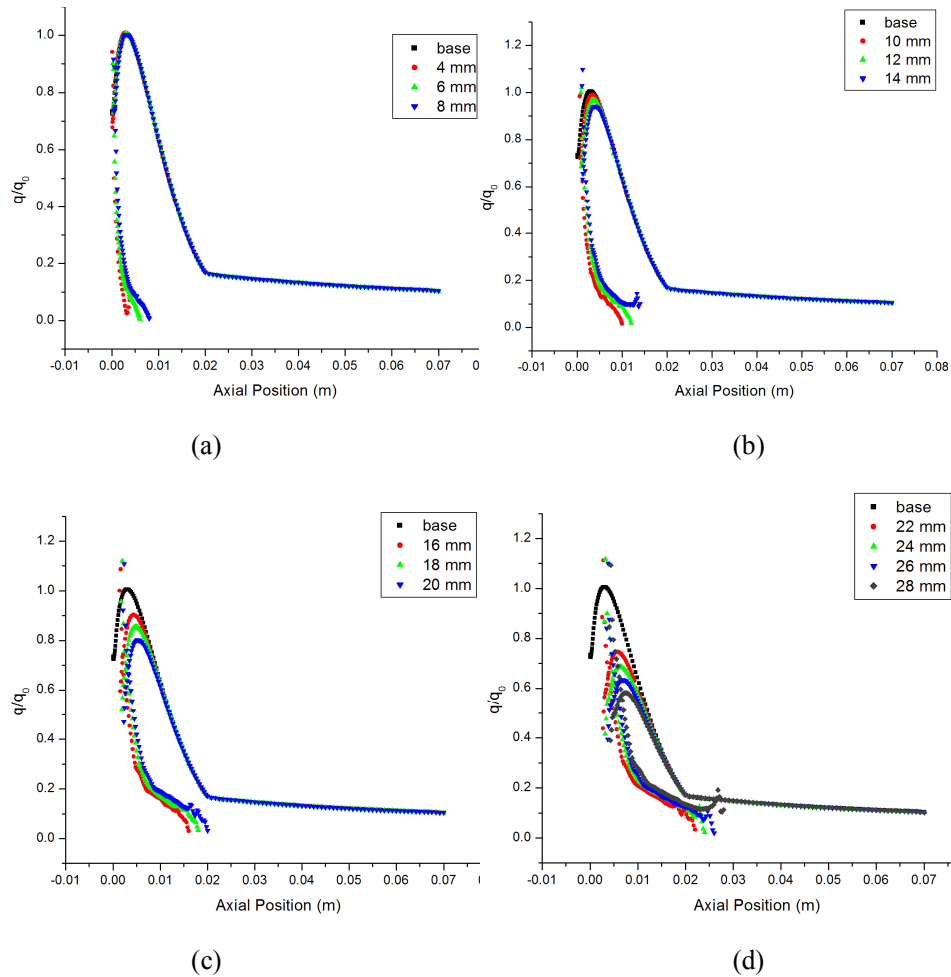


Figure 5.40 Surface heat flux distribution for conical cavities with  $\alpha=26.56^\circ$

After the peak rise in the heat flux at the sharp leap on the inner side, the surface heat flux drops discontinuously to very low values aft of the sharp lip. This drop can be associated with the sudden expansion of flow across the lip. From the low heating rates just on the start of the upper surface, the surface heat fluxes rise to another maximum on the hemispherical surface downstream of the sharp lip. This second peak heat flux on the outer surface is lower than the peak heat flux for the base configuration without cavity, and is highly dependent on both, the depth of cavity and the lip radius of the cavity. As can be

observed in Figs. 5.39-5.42, a lowered peak is achieved for increasing depth of the conical cavity as well as the increasing lip radii of these cavities. After the occurrence of the peak heat flux, the surface heating rates decreases smoothly along the hemispherical portion up to the hemisphere-cylinder junction. At this point the surface heat flux is reduced to about less than 20 % of the base peak heat fluxes in all cases. The smooth reduction in surface heat flux along the outer surface stalls at the hemisphere-cylinder junction. Post junction the surface heat flux is further reduced marginally along the length of the cylindrical portion.

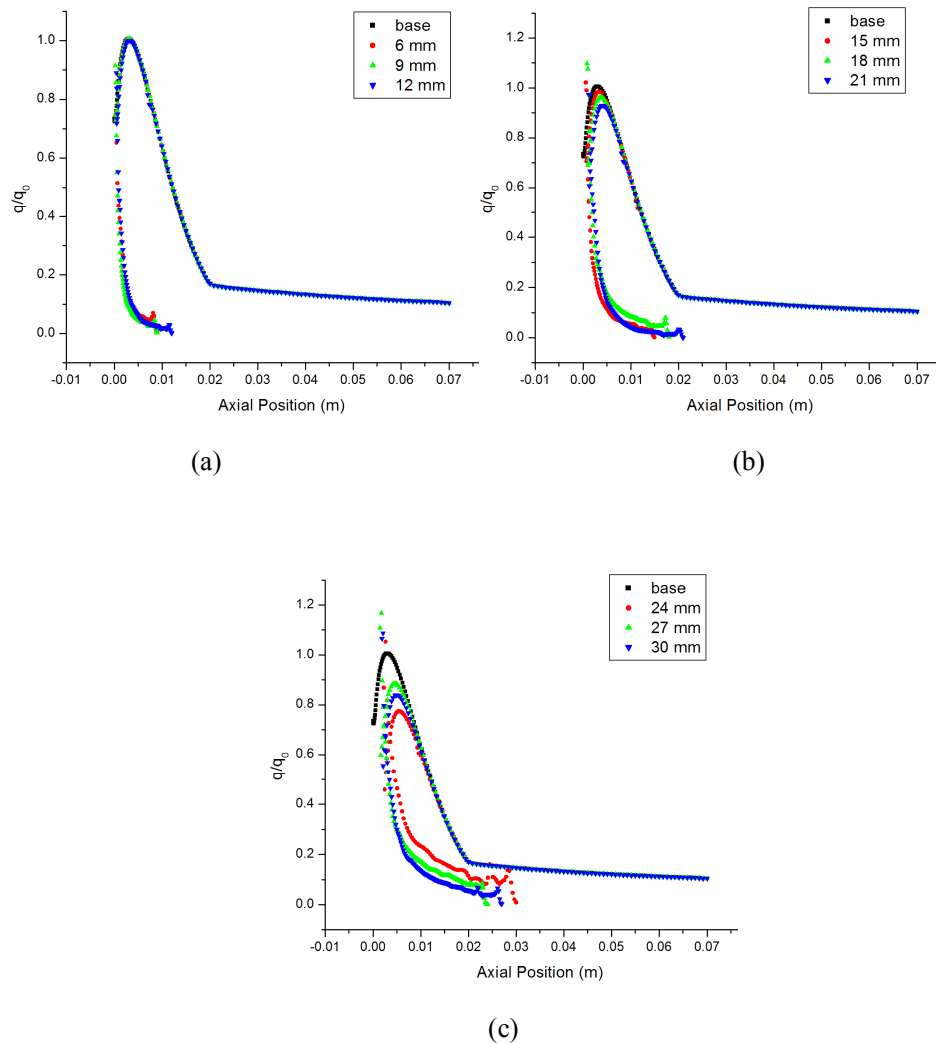


Figure 5.41 Surface heat flux distribution over conical cavity with  $\alpha=18.45^\circ$

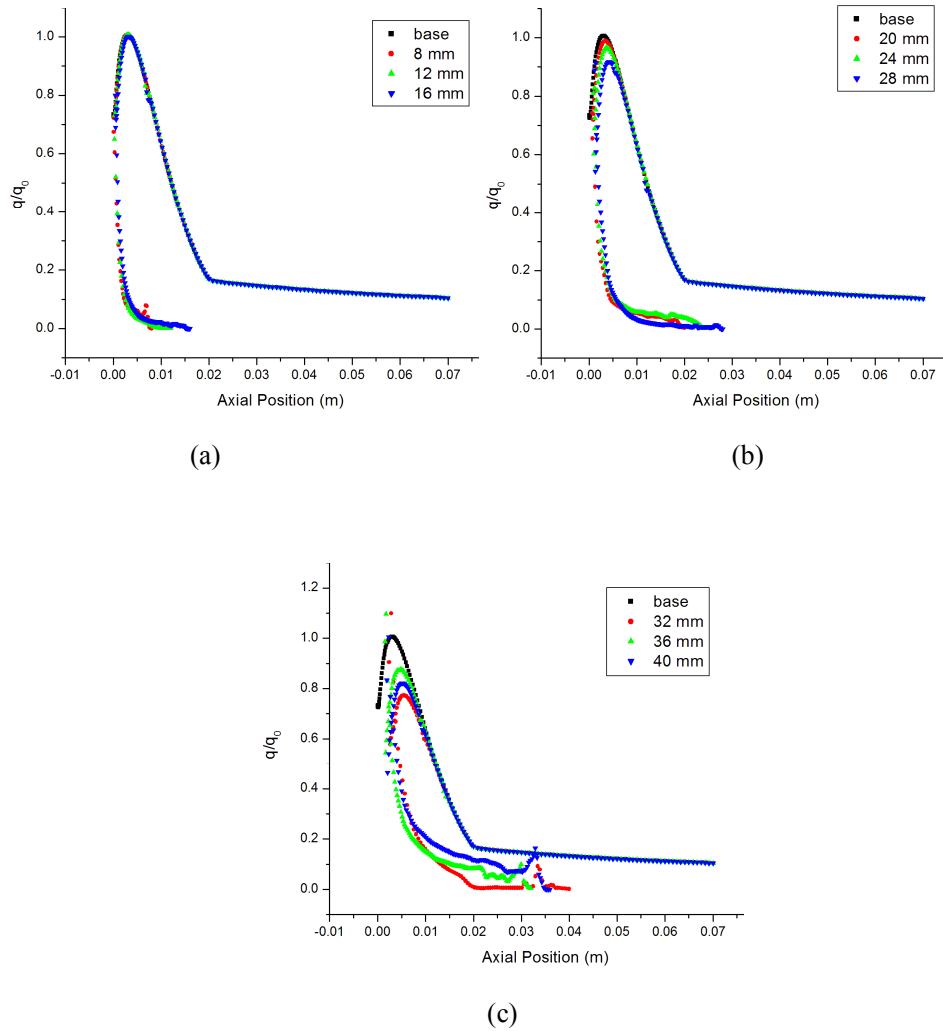


Figure 5.42 Surface heat flux distribution for conical cavity with  $\alpha=14^\circ$

The detrimental heating observed at the sharp lip in above figures can be reduced slightly by the use of rounded lips. More is the fillet radius of the lip; smoother is the transition of heat flux and pressure distribution across the lip. The advantage of using a conical cavity as a heat reduction mechanism is emphasized when the peak heat fluxes on only the outer surface on the body are compared to the peak heat flux for the base configuration without any cavity as shown in Fig. 5.43.

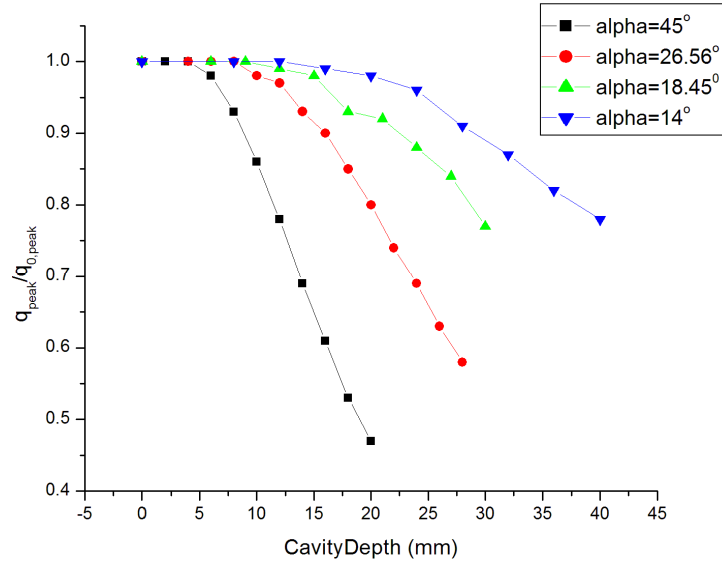


Figure 5.43 Peak heat flux on outer surface

In Fig. 5.43, the peak surface heat fluxes for various cavity configurations are non-dimensionalized with respect to the peak heat flux for the base configuration. Clearly, a greater reduction in surface heat flux is achieved by the use of deeper conical cavities. For the same depth of the cavity however, a larger reduction in peak heat fluxes is achieved for a larger lip radius or a larger vertex angle of the conical cavity. Among the range of cavity configurations investigated, the deepest cavity i.e. 20 mm with the largest lip radius produced a reduction of about 55% in the peak surface heat flux.

### 5.3.4 Effect of Conical Cavity on Total Heat Transfer Rates

The surface integral and the area weighted average of the heat flux distribution on the body of a hemisphere cylinder with various conical cavities are shown respectively in Fig. 5.44 and Fig. 5.45. The surface integration of the heat flux over the entire surface, also known as total heat transfer rates,  $Q$ , in Fig. 5.44 is non-dimensionalized with the total heat transfer rate for the base configuration  $Q_0$ . Also the AWA of surface heat fluxes is non-dimensionalized with the corresponding value of the base configuration.



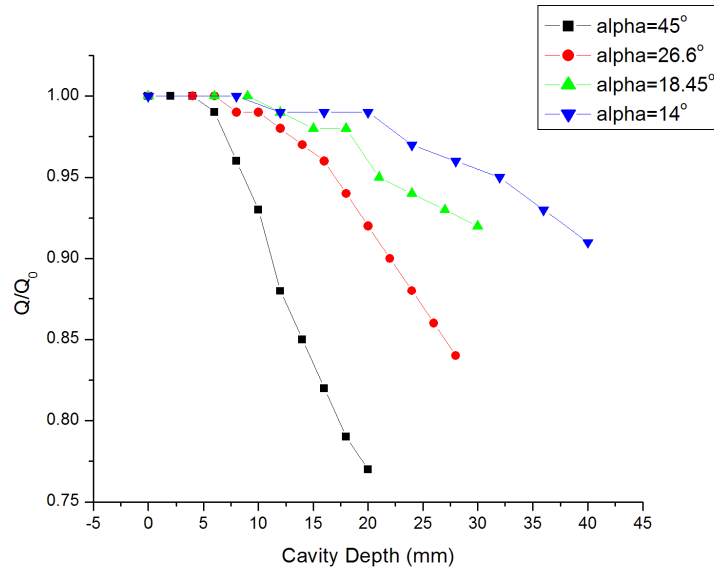


Figure 5.44 Total heat transfer rates for various conical cavity configurations

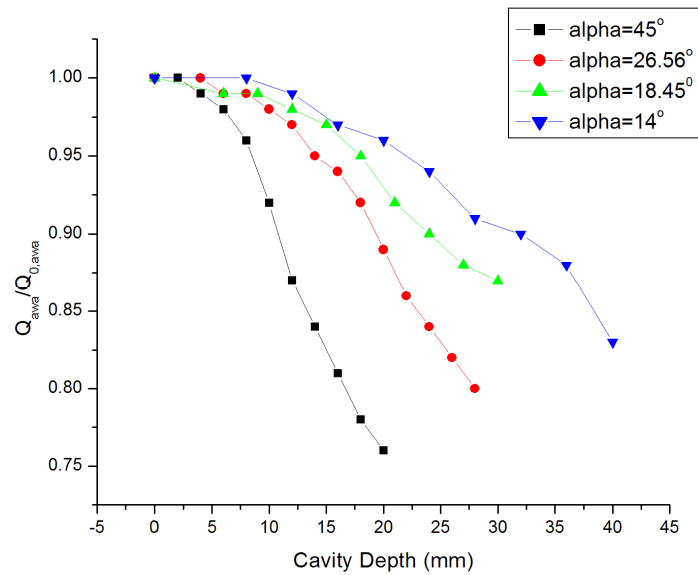


Figure 5.45 Area weighted average of surface heat transfer rates for various conical cavity configurations

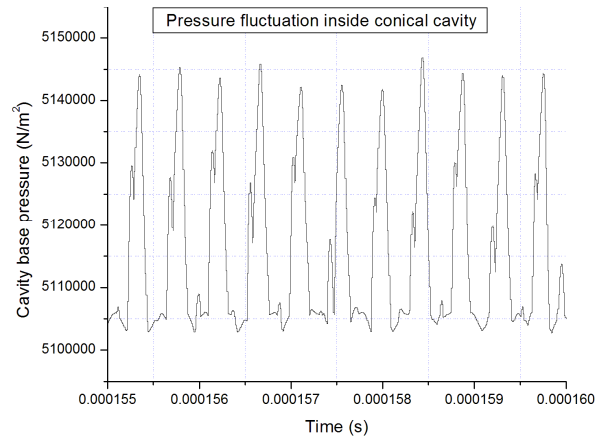
The trends for both total and AWA heat transfer rates are similar to those for peak heat flux. Advantage clearly lies with deeper cavities having a wide mouth opening. For the cavities investigated with widest mouth opening i.e.

$\alpha=45^\circ$ , a maximum reduction of 24% in both total transfer rates and the AWA of heat fluxes is achieved for deepest cavity.

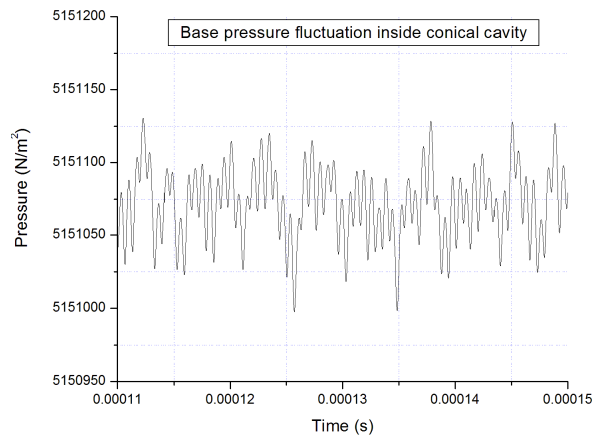
### 5.3.5 Effect of Flow Unsteadiness

Severe flow unsteadiness is seen for a hemisphere cylinder with forward facing conical for all cone angles. Though large initial fluctuations are highly damped at large times, a periodic oscillation about the mean values is seen in all flowfield variables. Fig. 5.46 shows the transient pressure fluctuations inside conical cavities of various cone angles. As can be seen from Fig. 5.46, the amplitude and frequency of pressure fluctuation decrease with a decrease in the semi vertex angle of the conical cavity. For large angle cavities, the base pressure is seen to oscillate to about  $\pm 5\%$  about its mean value while for small angle cones the pressure fluctuations are damped out with time and oscillates less than 0.1% about the mean values. The large amplitude oscillations seen for large angle cavities are due to inflow and outflow of fluid into and from the cavity. This also results in subsequent bow shock oscillation about its mean position with the frequency equal to the frequency pressure oscillation inside the cavity. For small angle conical cavities, a large region of recirculating fluid is trapped inside the cavity and does not flow out of cavity and hence the fluctuation of the cavity pressure is negligible.

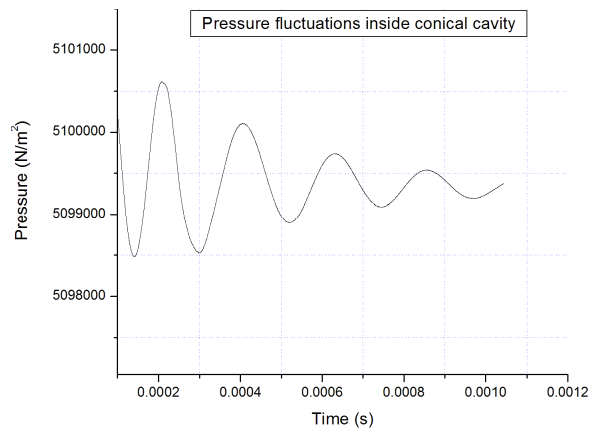
The fluctuation of cavity base pressure also results in the transient oscillations of aerodynamic drag and surface heat fluxes. The variation of aerodynamic drag directly follows the trend of pressure fluctuation as is expected. The drag variation of two typical configurations with large and small angle conical cavities is shown in Fig. 5.47. For all cavity configurations investigated the drag oscillation is less than 1percent of the mean unsteady value. The mean unsteady drag coefficient for various conical cavity configurations was found to be 1 to 4% lower than the steady state drag coefficient.



(a)



(b)



(c)

Figure 5.46 Cavity pressure fluctuation inside conical cavity with a)  $\alpha=45^\circ$ ,  $d=14\text{mm}$ , b)  $\alpha=26.56^\circ$ ,  $d=6\text{ mm}$  and c)  $\alpha=18^\circ$ ,  $d=27\text{ mm}$

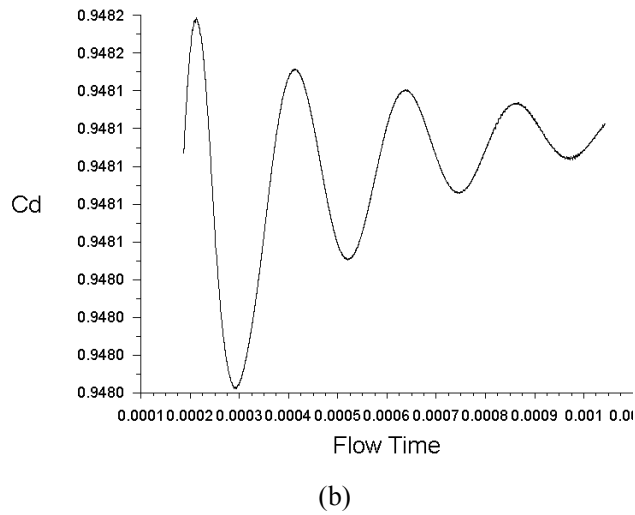
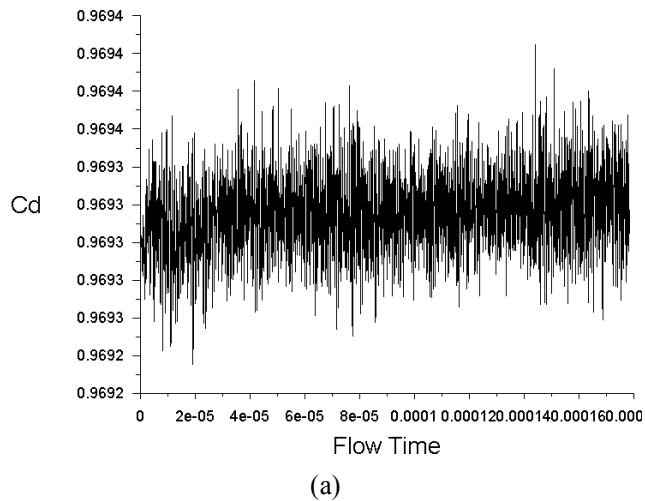
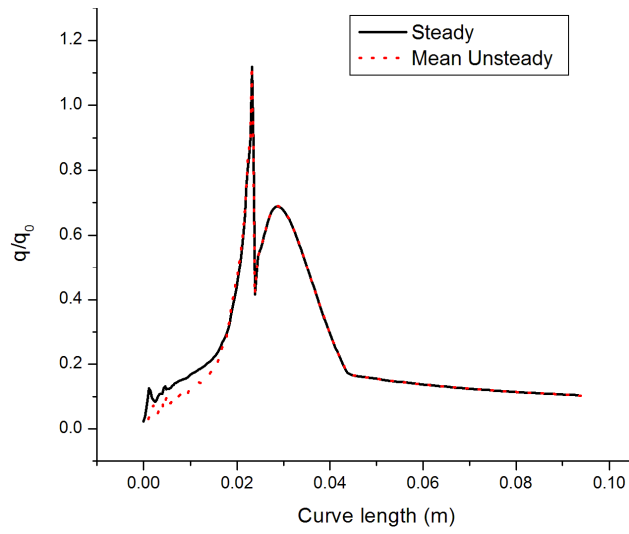


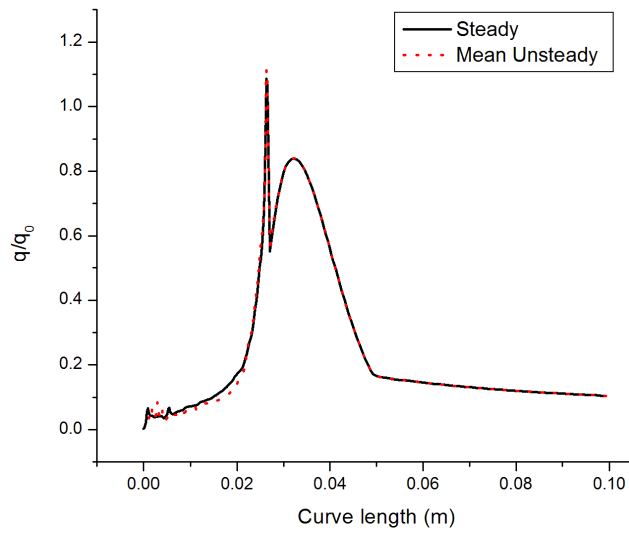
Figure 5.47 Drag oscillation for conical cavity with a)  $\alpha=45^\circ$ ,  $d=14\text{mm}$  and  
 b)  $\alpha=18^\circ$ ,  $d=27\text{ mm}$

The surface heat flux distributions for different conical cavities also show a similar oscillation patterns. The mean unsteady surface heat transfer rates however, do not differ too much from its steady state values. Figure 5.48 shows the mean unsteady surface heat flux distribution for two configurations with deep conical cavities. As can be seen in Fig. 5.48, the unsteady surface heat flux curve overlaps the steady state curve except inside the cavity where the flow unsteadiness decreases the mean heat fluxes. Also, a negligible difference can be seen at the sharp lip. This heat flux distribution ensure the

unsteady total heat transfer rates to differ from the steady state values by not more than 1%.



(a)



(b)

Figure 5.48 Comparison of unsteady and steady-state surface heat fluxes for conical cavity with a)  $\alpha=26.56^\circ$ ,  $d=24\text{mm}$  and b)  $\alpha=18^\circ$ ,  $d=27\text{mm}$

## 5.4 THE EFFECT OF HEMISPHERICAL CAVITY

### 5.4.1 Flowfield around hemisphere cylinder with hemispherical cavity

A forward facing hemispherical cavity is inserted at the nose of base model by subtracting a hemisphere with centre at the stagnation point of the base model and having radii of 2 mm to 18 m. The external flowfield around a hemisphere cylinder is unaffected by the presence of with a very small hemispherical cavity and a steady flow is obtained for all hemispherical cavity investigated. Intermediate transient results for models with small hemispherical cavities shows the presence of a pair of small vortices in the stagnation region inside the cavity as shown in Fig. 5.49.

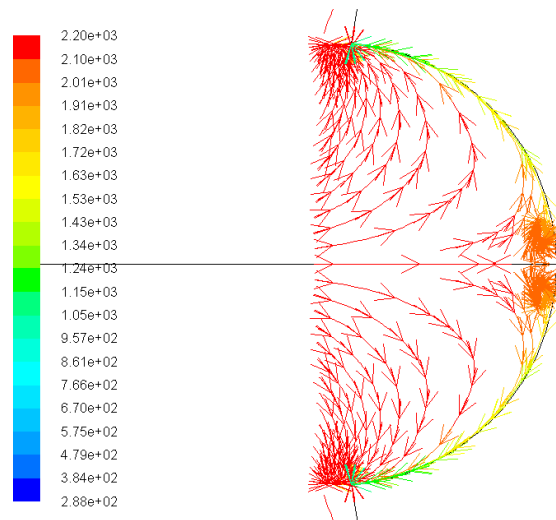


Figure 5.49 Streamlines inside a hemispherical cavity of 3 mm

As the flow progresses, the vortices become elongated, pushed to the walls and finally moves out of the cavity to have a uniform and steady flow inside the cavity as shown in Fig. 5.50. The steady state streamlines inside the cavity follow the curvature of the cavity nicely up to the sharp lip to have a very small deceleration of the fluid particles along the surface of cavity. Downstream of the sharp lip however, the flow separates for a fraction of curve length before reattaching again.

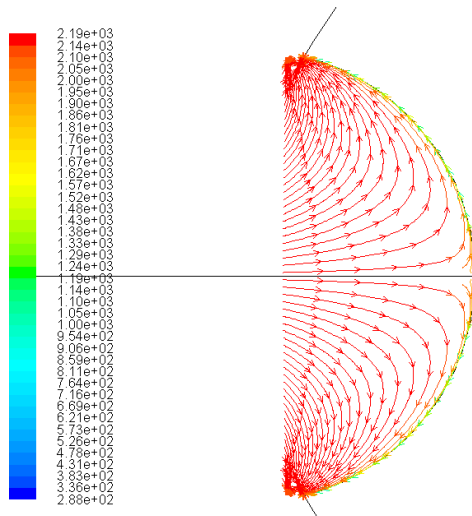


Figure 5.50 Streamlines inside hemispherical cavity of radius 10mm

The effect a forwards facing hemispherical cavity on flowfield around a hemisphere cylinder with can be best illustrated through the contours of flowfield variables. The pressure, temperature and Mach number contours for a hemisphere cylinder with a typically small hemispherical cavity are shown in Fig. 5.51 (a-c) respectively. For small cavities, the steady state bow shock wave shape is similar to that for the base model with air inside cavity at stagnation conditions. The air inside the cavity is moving at very low velocities with some reversed flow near the sharp lip and in the vortices. The stagnation temperature contour completely envelops these small hemispherical cavities with high temperatures seen even in the post lip expansion region. A very gradual expansion can be seen after the lip of the body with very little pressure drop.

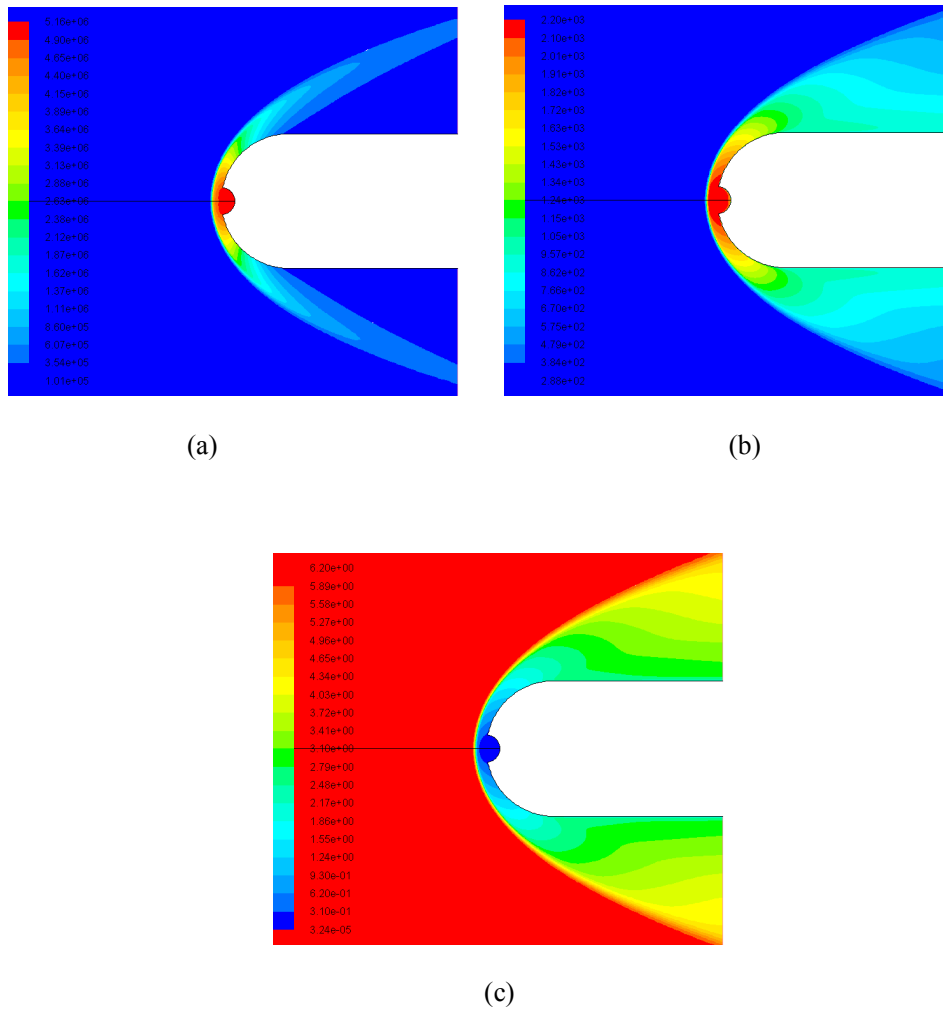


Figure 5.51 a) Pressure, b) Temperature and c) Mach number contours for 4 mm cavity

For large radii cavities, the flowfield is very different with normal shock extending up to the sharp lip of the cavity as shown in Figs. 5.52 (a-c). As can be seen in pressure contours, the expansion aft of the sharp lip is severe leading to a separated flow downstream of the sharp lip. The separated flow reattaches to form a mild reattachment shock downstream of the sharp lip with a recirculating fluid region between the separation and the reattachment point. The temperature inside the recirculating zone is low as compared to the surrounding forming a cool ring aft of the sharp. Also a slightly reduced temperature levels can be seen all along the cavity inner surface is giving a favourable heat



reduction. The fluid inside the cavity for all cases moves with very low Mach numbers of order less than 0.3.

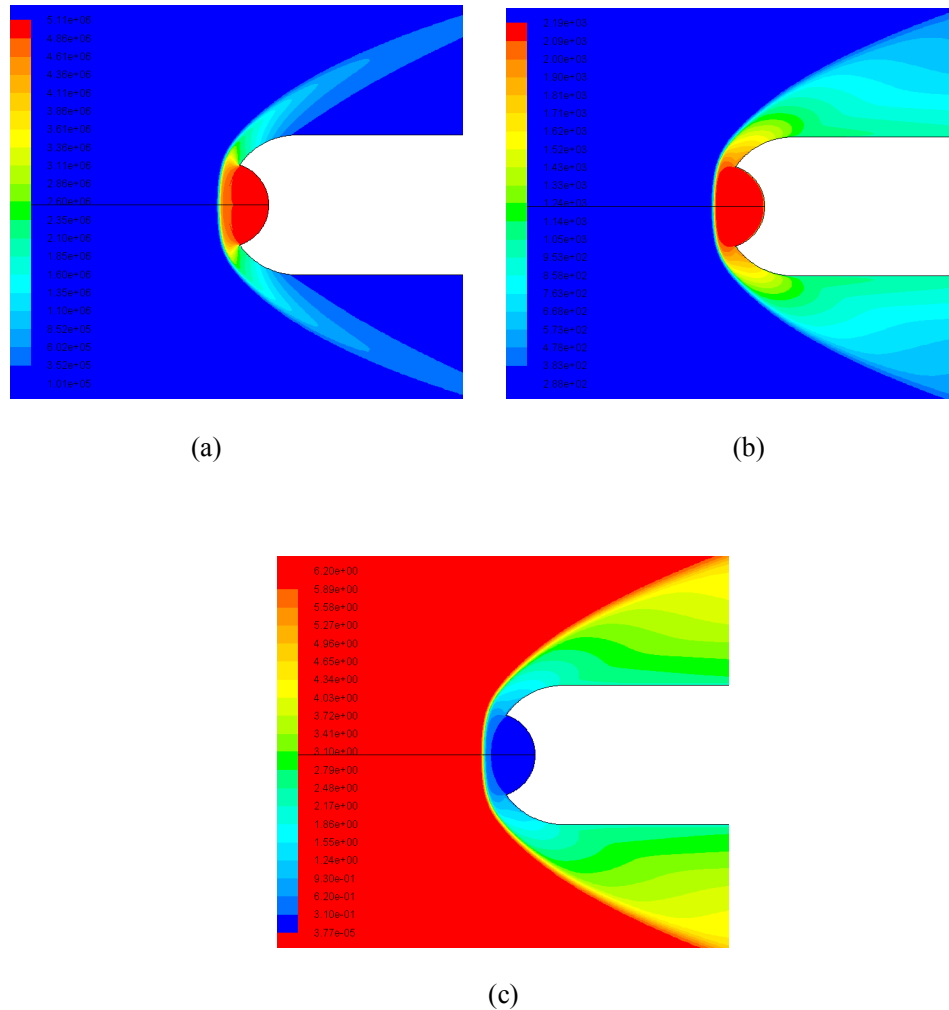


Figure 5.52 a) Pressure, b) Temperature and c) Mach number contours for hemisphere cylinder with 12 mm cavity

#### 5.4.2 Effect of hemispherical cavity on surface pressure distribution

The fluid inside the spherical cavity is almost stagnant moving out of the cavity at low speeds. The pressure on the cavity surface at the stagnation point is slightly lower than the stagnation pressure with a small increase in pressure along the length of the cavity. The maximum pressure along the cavity surface can be seen at the inner side of the sharp lip with values very close to the stag-

nation pressure value for hemisphere cylinder without cavity. Fig. 5.53 (a-f) shows the surface pressure distribution for various hemisphere cylinder configurations with different radii hemispherical cavities. As can be seen in Fig. 5.53, the low speed flow expands suddenly after the infinitely sharp lip through an expansion wave. The magnitude of the pressure drop across the expansion wave is found to be proportional to the depth or the lip radius of the cavity; with larger pressure drop for larger lip radius of the cavity. For the largest spherical cavity investigated, the pressure aft of the lip falls to about 5 % of the stagnation values.

A very small region of recirculating flow is formed on the surface aft of the lip due to this sudden expansion. The recirculating flow aft of the sharp lip is bounded downstream by a mild reattachment shock, which leads to some recovery in the surface pressure on the hemispherical portion. The compression ratio across this reattachment shock is same irrespective of the cavity radii. After achieving a lowered peak on the hemispherical portion the surface pressure falls gradually along the surface of the hemisphere cylinder to very low values. The surface pressure reduction stalls at the hemisphere-cylinder junction with very little pressure drop thereafter along the cylindrical surface. At the end of the cylinder length, the surface pressure attains low values close to freestream pressure values.

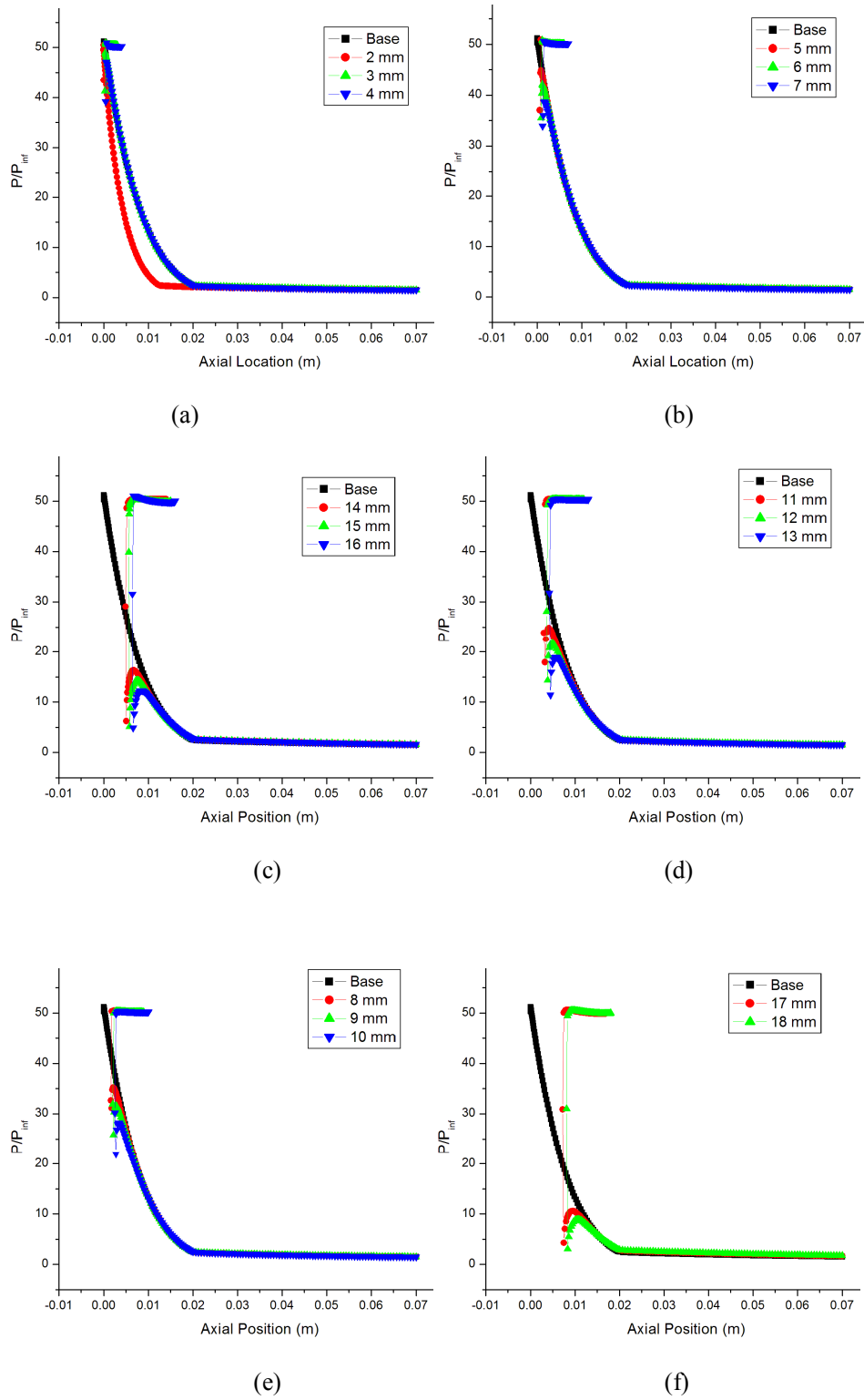
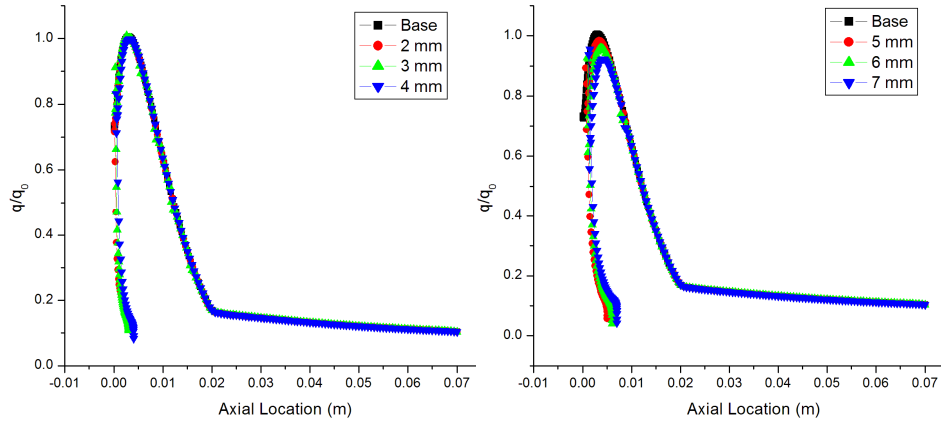


Figure 5.53 Surface Pressure distributions for various spherical cavities

### 5.4.3 Effect of hemispherical cavity on surface heat transfer rates

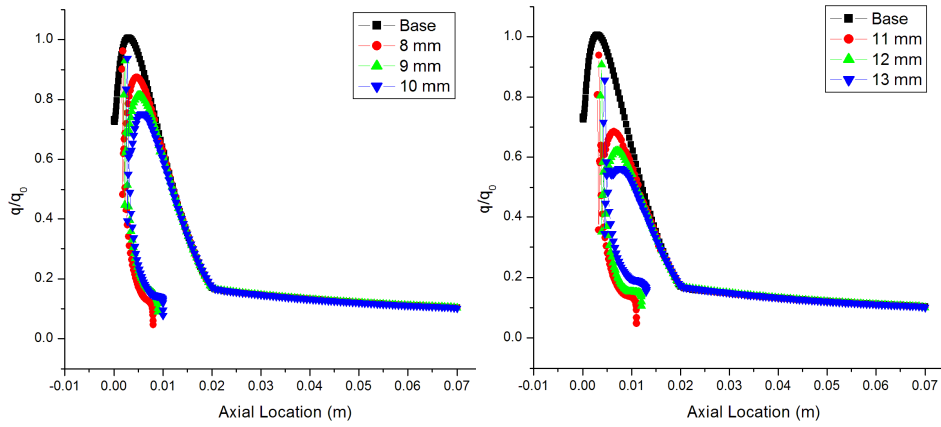
The surface heat flux distribution follows the surface pressure distribution trends except inside the cavity as shown in Fig. 5.54 (a-f). The stagnation point heat transfer rate is dramatically reduced due to the alignment of flow along the cavity surface. The flow thus, initially headed normally towards the cavity surface are diverted towards the cavity lip, increasing the surface heating away from the stagnation point. The heat fluxes along the inner cavity surface increases sharply reaching a peak at the sharp lip. The peak heat flux that occurs on the inner side of the sharp lip is however, found to be slightly less than the peak heat flux of the base model. The sudden expansion of fluid on the upper surface aft of sharp lip causes the surface heat flux to attain very low values immediately aft of sharp lip forming a cool ring in the vicinity of sharp lip. This drop in heating rates aft of the sharp lip is dependent on the lip radius of the cavity with the cavity configuration of the larger radii producing larger drop in surface heat fluxes.

After the low heating values aft of the sharp lip, the surface heat fluxes rises slightly along the convex hemispherical surface attaining a new peak on the outer surface. After attaining the peak value the surface heat flux decreases rapidly along the hemispherical surface to very low values at the hemisphere-cylinder junction. After the junction the surface heat fluxes are marginally reduced along the length of the cylinder.



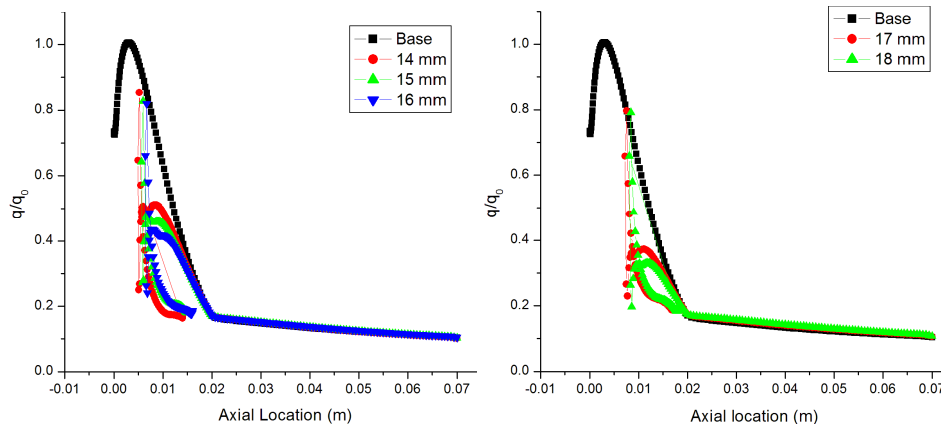
(a)

(b)



(c)

(d)



(e)

(f)

Figure 5.54 Surface heat flux distribution for various spherical cavity

The peak heating that occurs on the hemispherical outer surface of a model with cavity is lesser than the peak heating that occurs on the base hemisphere cylinder without cavity. This reduction in outer surface heat flux is further exaggerated for deeper and wider cavities as shown in Fig. 5.55. As can be seen from Fig. 5.55, a reduction of about 67 % in peak heating rates can be achieved with the deepest cavity of 18 mm radius.

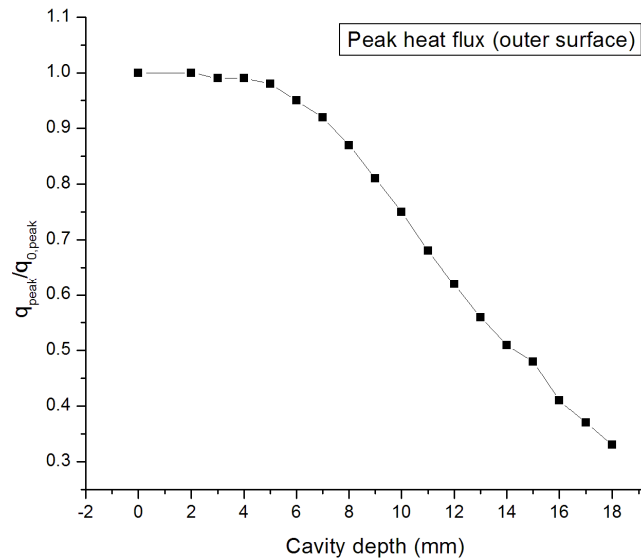
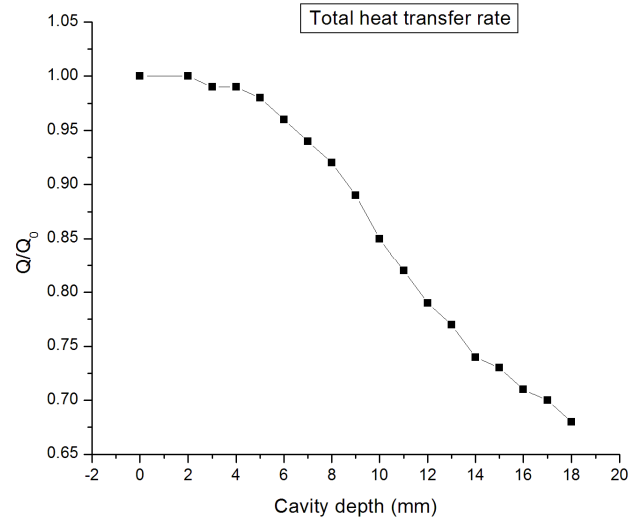
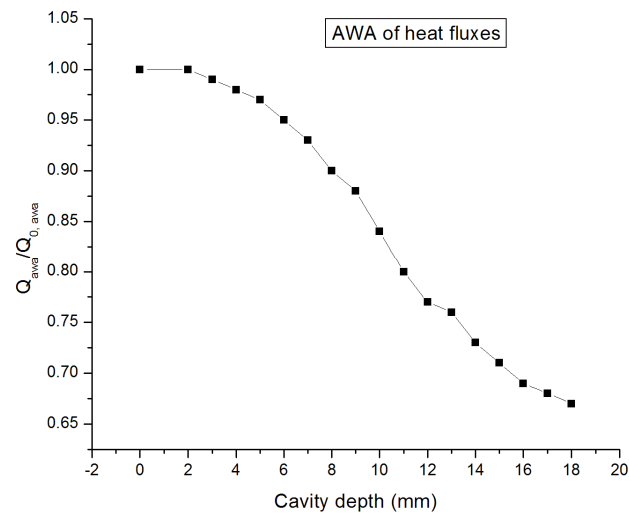


Figure 5.55 Peak surface heat flux for various cavity configurations

The overall applicability of forward facing spherical cavity in the reduction aerodynamic heating becomes apparent when the total heat transfer rates and the AWA of surface heat fluxes are compared to those for the model. Fig. 5.56 shows the total heat transfer rates and the AWA heat transfer rates for various cavity configurations, normalized with the respective quantities for the base model. Obviously, the models with deeper and wider cavity hold the advantage over the smaller cavity configurations. For the deepest and widest spherical cavity configuration studied, a maximum reductions of 32% and 33% in total heat transfer rates and AWA heat flux respectively was observed.



(a)



(b)

Figure 5.56 a) Total heat transfer rates and b) AWA of heat fluxes for various cavity depth

The use of very wide mouth cavity for aerodynamic heat reduction, however, does not seem to be a feasible solution especially for the ascent or cruise of missiles because of large pressure drag for such configurations. Fig. 5.57 shows the drag for various cavity configurations, non-dimensionalized with the drag of the base configuration. It is evident from Fig. 5.57, that medium

sized cavities can be used for heat reduction with any increment in associated drag.

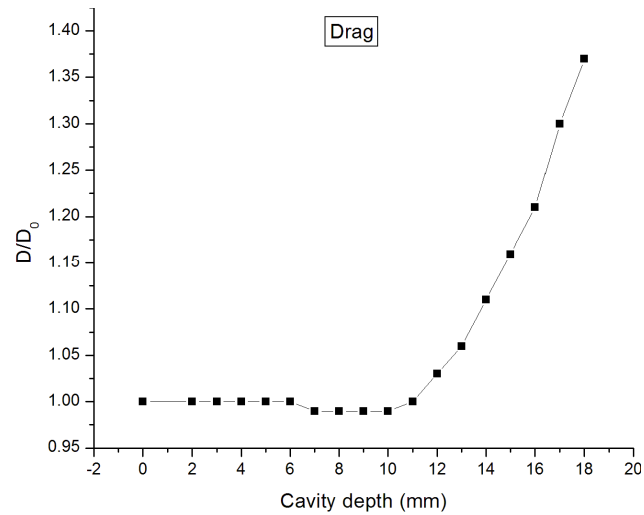


Figure 5.57 Variation of drag with spherical cavity depth

#### 5.4.4 Effect of Flow Unsteadiness

As with the hemisphere cylinder with a forward facing parabolic cavities, all flow unsteadiness around a hemisphere cylinder with a hemispherical cavities are damped out at larger times, well before 1 millisecond. The cavity base pressure convergence of a typical hemispherical cavity obtained with time marching from the steady state solution with a time step of  $1 \times 10^{-7}$  seconds is shown in Fig. 5.58.

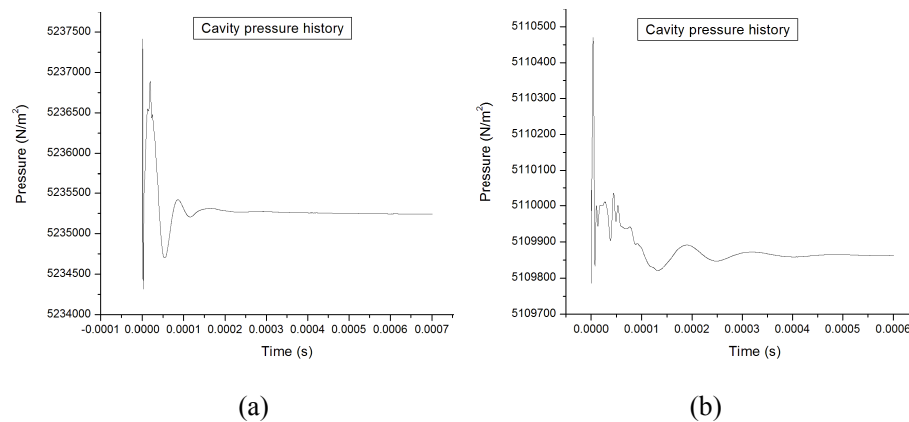


Figure 5.58 Cavity base pressure convergence for a)  $d = 4$  mm and b)  $d = 14$  mm



The convergence of base to a steady value also ensures the convergence of aerodynamic drag and the surface heat fluxes. The mean unsteady drag coefficient converges to a value 4% lower than the state drag coefficient. However, the total and the area weighted heat transfer rates for the unsteady cases are identical because of identical local surface heat fluxes as shown in Fig. 5.59.

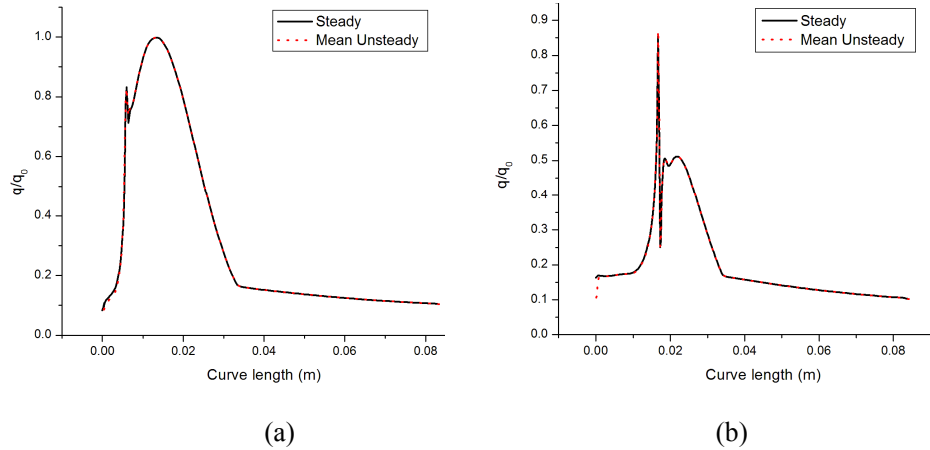


Figure 5.59 Mean unsteady heat fluxes for hemispherical cavity with  
a)  $d = 4$  mm and b)  $d=14$  mm

## 5.5 THE EFFECT OF DOUBLE DISK AEROSPIKE

### 5.5.1 The flowfield around a double disk aerospoke

The flowfield around a single disk aerospoke is well understood and discussed in Chapter 1. In the present thesis, aerospoke configurations with two hemispherical aerodisks were investigated for peak reattachment pressure and reattachment heat fluxes. All the aerodisk configurations investigated have an overall  $l/D$  ratio of 1, 1.25 and 1.5 with first disk of radii 4 mm, 5 mm and 6 mm. For all the cases investigated, a steady state solution was obtained with time derivatives vanishing to values less than  $1e^{-06}$ . The steady state flowfield shows the presence of a large region of dead air between the main body and the first aerodisk as shown in Fig. 5.60. The fluid inside this is recirculating in clockwise direction for a flow left to right, at a very low Mach numbers and is

separated from the main flow. Another recirculating fluid zone can be seen at junction of first aerodisk cap and second spike stem, i.e. at the nose of the first aerodisk cap. This region of recirculating flow in front of the hemispherical aerodisk cap is however, very small. Infinitesimally small regions of recirculating dead air flow can also be seen behind each of the hemispherical caps, with flow direction opposite to that in above mentioned zones.

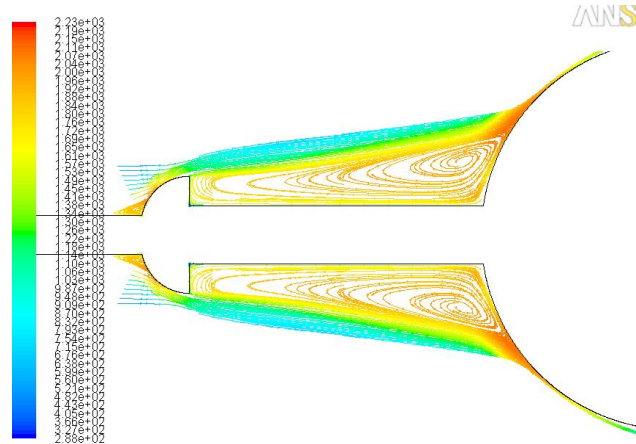
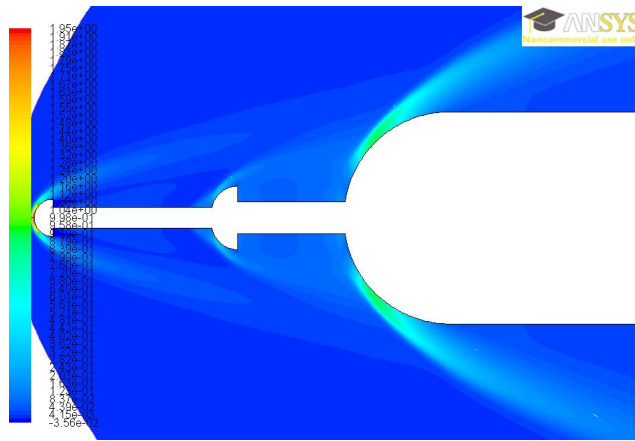
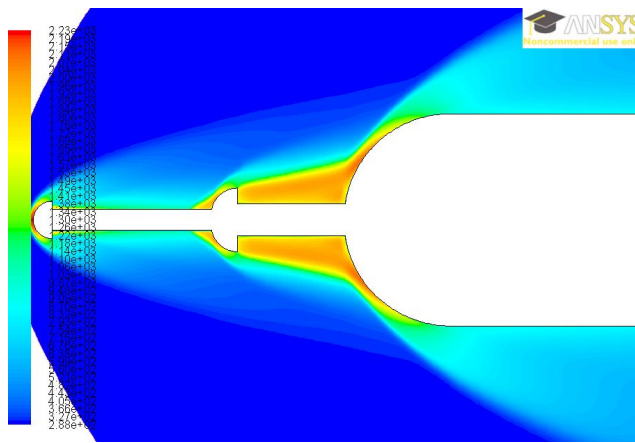


Figure 5.60 Recirculating Flow between the spike and the main body

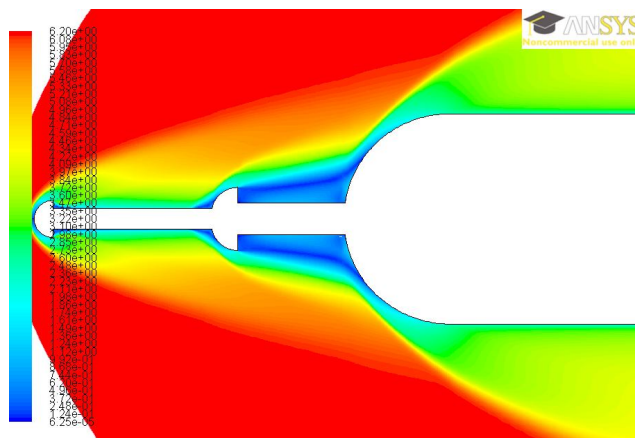
The presence of large recirculating region between the main body and first aerodisk cap makes the flow deflected from the cap of the first aerodisk to impinge on the shoulder of the main body as can be seen in Fig. 5.61 (a-c) which shows the pressure, temperature and Mach number contours for a hemisphere cylinder with double disk aerospike. The shock wave formed on the first aerodisk is however, weaker than it would in absence of the second aerodisk, thus producing lesser reattachment heating as compared to single cap aerospike. For very short aerospikes, the flow deflected from the cap of even the front aerodisk impinges on the main body shoulders. The result is a high pressure and temperature zone on the shoulders of main body as seen in Fig. 5.61.



(a)



(b)



(c)

Figure 5.61 Contours of a) pressure, b) Temperature and Mach number for Aerospike of  $r_1=6$  mm,  $r_2=3.5$  mm and  $l/d=1.5$

. At the front end of the aerospike, stagnation pressure and temperature are observed at the nose of the front hemispherical cap with subsonic Mach numbers. The flow expands slightly along the surface of hemispherical cap before undergoing a sudden expansion at the end of cap resulting in a very low pressure region between the two hemispherical caps. High pressure and temperature regions can also be observed on shoulders of the rear hemispherical aerodisk with an expanded flow in its wake. The formation of large recirculating fluid zone ensures the presence of relatively low temperature fluid in the vicinity of main body nose.

Though the recirculating fluid in front of the main body contains dead air which do not move out of the region, the fluid rotates at some finite velocities due to continuous tangential traction of topmost fluid layers by the external flow. The flow except in the recirculating regions and the front stagnation region is seen to be everywhere supersonic.

### **5.5.2 Effect of double disk aerospike on surface pressure distribution**

With the addition of double disk aerospike at the nose, the flow first sees the small hemispherical aerodisk as the blunt body and the pressure rises to stagnation pressure in accordance with the radius of the front hemispherical body. At zero angles of attack the peak pressure rise occur at the stagnation point of the front aerodisk, and the pressure falls drastically along the curve leading to region of separated and reversed flow in the wake of the first aerodisk. As the flow outside the wake, encounters the second aerodisk, there is a jump in the pressure, but not as substantial as the first one. Again, the pressure falls along the curve forming another region of recirculating flow between the second aerodisk and the main body. The most drastic rise in the pressure occurs at the reattachment point on the main body, which is located at approximately at the same region irrespective of the overall lengths of the aerospikes tested in the investigation. The deflected high energy flow from both aerodisks impinges on the main body at the reattachment point with detrimental rise in pressure. The surface pressure distribution trend is similar for all aerospike configurations investigated as shown in Figs. 5.62 -5.64. Figures 5.62-5.64 show the surface

pressure distribution for double disk aerospike configurations with radius of first hemispherical cap  $r_1=6\text{ mm}$ ,  $5\text{ mm}$  and  $4\text{ mm}$  respectively with  $l/D$  ratios of 1, 1.25 and 1.5. The different curves in each figure represent different ratios of length of first spike stem to length of second spike stem ( $l_1/l_2$ ). As can be seen from 5.62-5.64, the pressure rise on the shoulder of the hemispherical cap of the first aerodisk is almost independent of the distance between the two caps and the overall  $l/D$  ratio of the aerospike.

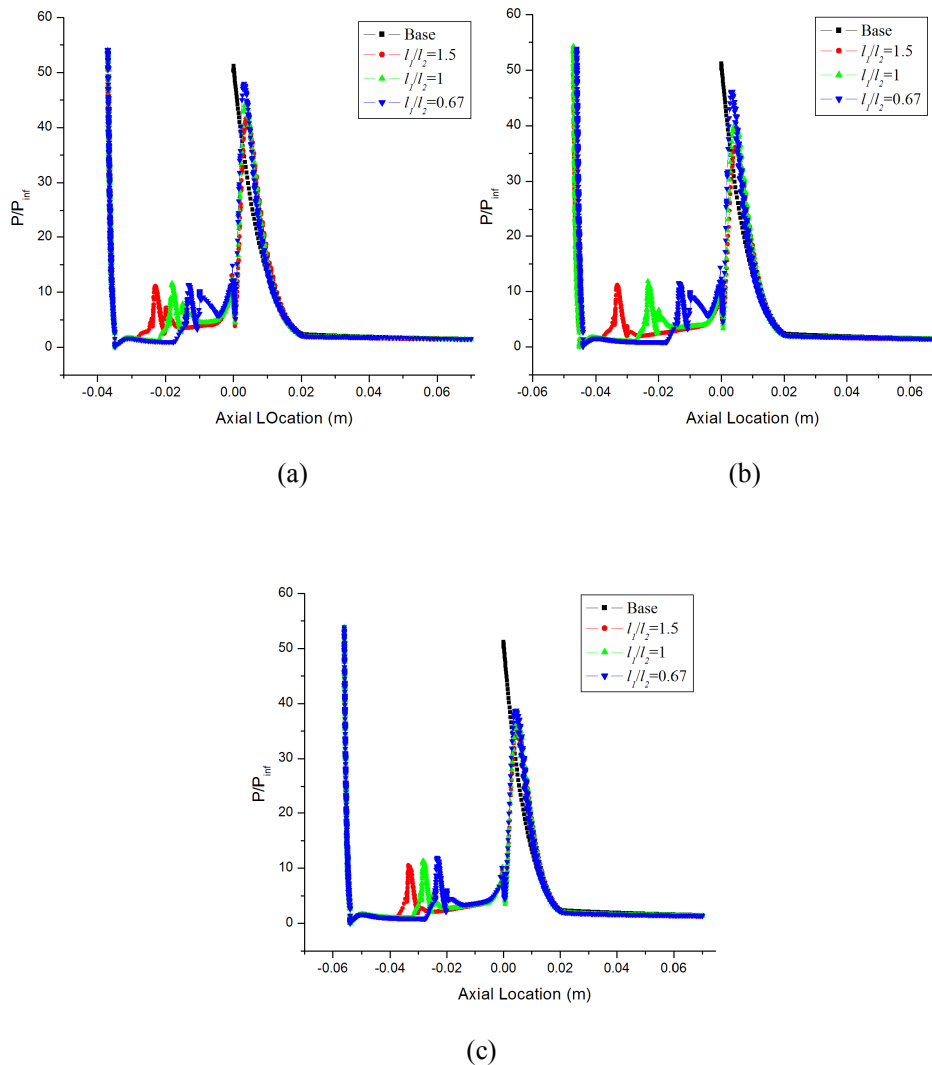


Figure 5.62 Surface pressure distribution for aerospike configurations with  $r_1=6\text{ mm}$ ,  $r_2=3.5\text{ mm}$  and a)  $l/D=1$ , b)  $l/D=1.25$  and c)  $l/D=1.5$

The peak pressure on hemispherical cap of the first aerodisk is roughly between nine to twelve times the freestream pressures with lower pressure rise for smaller radius of cap. The pressure rise that occurs on the reattachment point on the main body, on the other hand is highly dependent on the  $l/D$  ratio of the aerospike and the radius of the hemispherical caps.

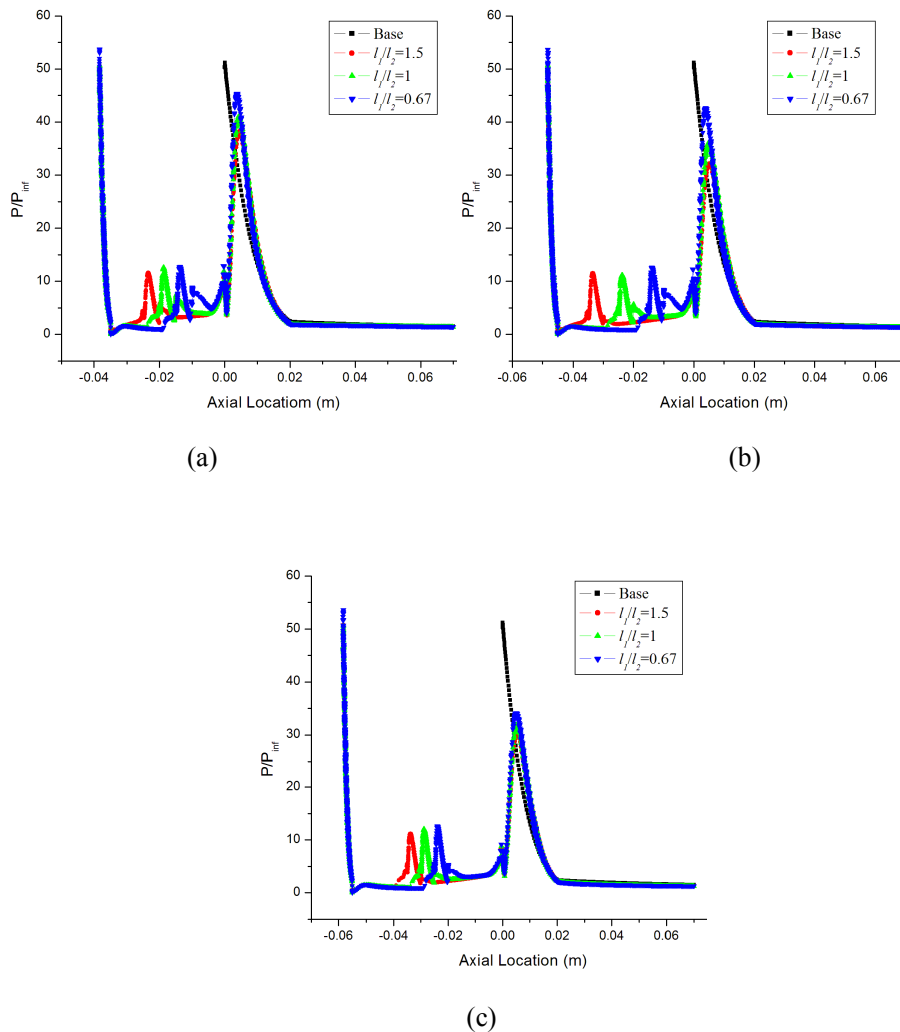


Figure 5.63 Surface pressure distribution for aerospike configurations with  $r_1=5$  mm,  $r_2=3$  mm and a)  $l/D=1$ , b)  $l/D=1.25$  and c)  $l/D=1.5$

The reattachment pressure which is always less than the peak pressure for the base model becomes lesser with the increasing overall  $l/D$  ratio and decreases further with decrease in the radii of the hemispherical caps, especially the first

cap. Among the cases investigated the aerospike configuration with  $r_1=4$  mm and a  $l/D$  value of 1.5 the reattachment pressure rise is reduced to about 50% of base model stagnation pressure. After the peak pressure rise at the reattachment point, the surface pressure on the main body falls rapidly along the hemispherical surface up to the hemisphere cylinder junction. Aft of the junction, the pressure gradient becomes very small with surface pressure attaining values close to the freestream value by the end of the cylinder length. The surface pressure distribution on the main body downstream of the reattachment point is similar for all cases investigated irrespective of the aerospike design.

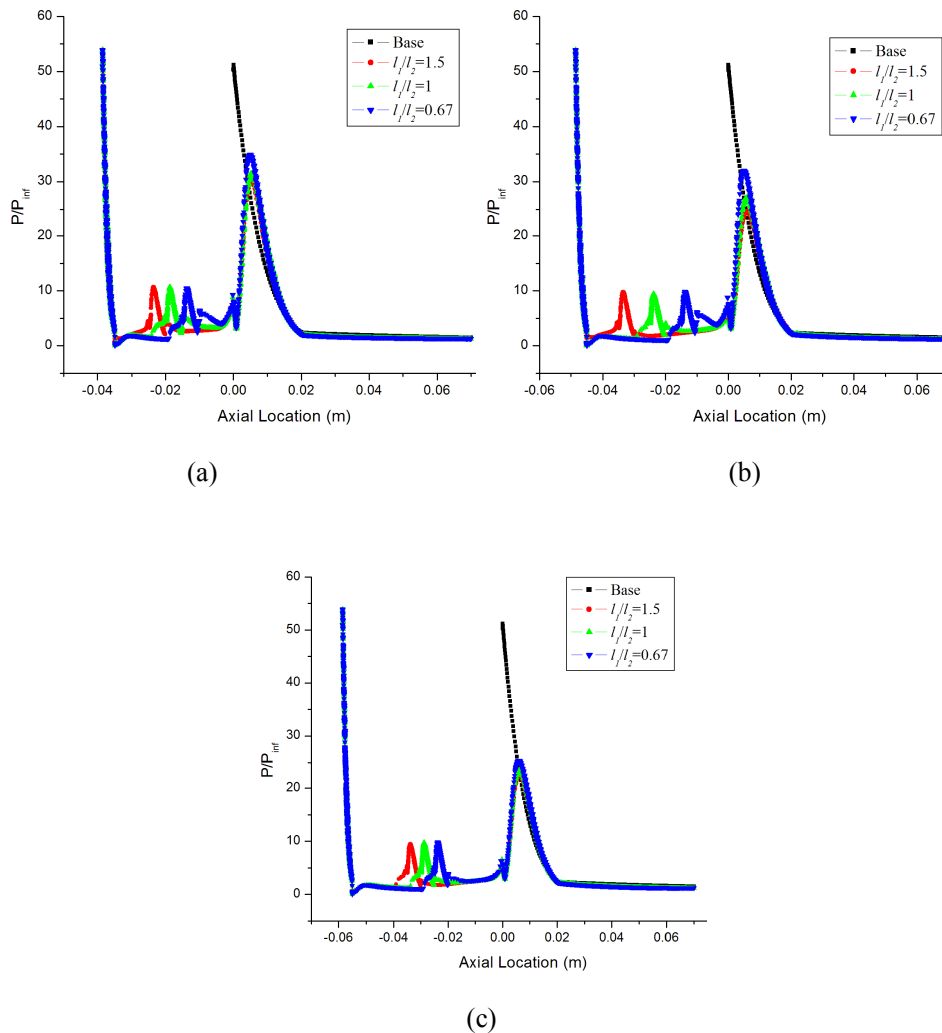


Figure 5.64 Surface pressure distribution for aerospike configurations with  $r_1=4$  mm,  $r_2=2.5$  mm and a)  $l/D=1$ , b)  $l/D=1.25$  and c)  $l/D=1.5$

### 5.5.3 Effect of Double Disk Aerospire on Surface Heat Fluxes

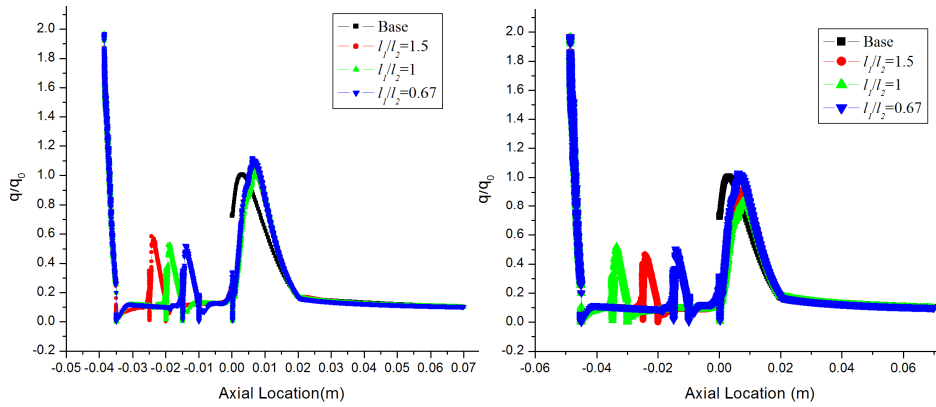
The surface heat flux distribution follows a trend similar to the pressure distribution. The formation of bow shock wave in front of the front spherical aerodisk results in large stagnation point heat fluxes which is higher than those for a hemisphere-cylinder without aerodisk. The smaller radius of the front aerodisk results in a large stagnation point heat transfer rates and shear stresses. These large wall fluxes fall sharply along the hemispherical cap surface and its wake to attain negligible values in the recirculation aft of the front hemispherical cap. The surface heat fluxes first increases slightly and then becomes constant along the length of spike between the two hemispherical aerodisk caps. Another drop in the surface heat flux is seen in front of the rear hemispherical cap due to presence of recirculating fluid zone at the spike stem and cap junction. Figures 5.65-5.67 show the steady state surface heat flux distribution pressure distribution for double disk aerospire configurations with radius of first hemispherical cap  $r_1=6\text{ mm}$ ,  $5\text{ mm}$  and  $4\text{ mm}$  respectively with  $l/D$  ratios of 1, 1.25 and 1.5.

The surface heat fluxes rises sharply along the hemispherical cap surface to appreciably high values on the shoulder of the rear disk. This heating of the rear hemispherical cap is though, substantially lower than the peak heating of both the front cap and the main body. The marginal heat flux jump on the rear disk shoulder vanishes again following an expansion and a region of recirculating flow on the aft of the cap. The surface heat flux values rise marginally along the spike length between the rear disk and the main body before plunging to very low values in the stagnation region of the main body insulated by a dead air region.

As can be seen from Figs. 5.65-5.67, a substantial rise in the surface heat fluxes occurs at the reattachment point of the main body where the flows separated from both the aerodisks coalesce. This reattachment heat flux rise is drastic; however, it is lower than that of the stagnation point heat flux for the same hemisphere-cylinder without any aerospikes for longer aerospikes. The peak reattachment heat flux is observed to be highly dependent on the radius of the first hemispherical cap as the configuration with  $r_1=4$  and  $5$  produced reat-

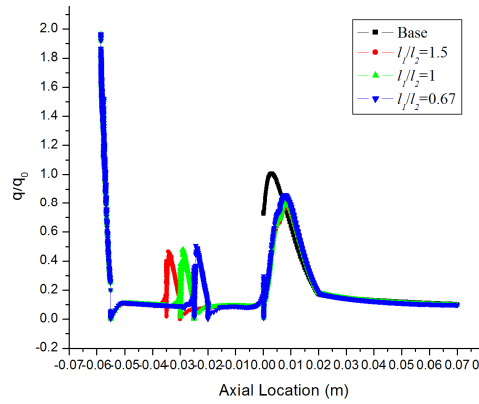


tachment heat flux greater than the peak heating of base model for all  $l/D$  values.



(a)

(b)



(c)

Figure 5.65 Surface heat flux distribution for aerospike configurations with  $r_1=6$  mm,  $r_2=3.5$  mm and a)  $l/D=1$ , b)  $l/D=1.25$  and c)  $l/D=1.5$

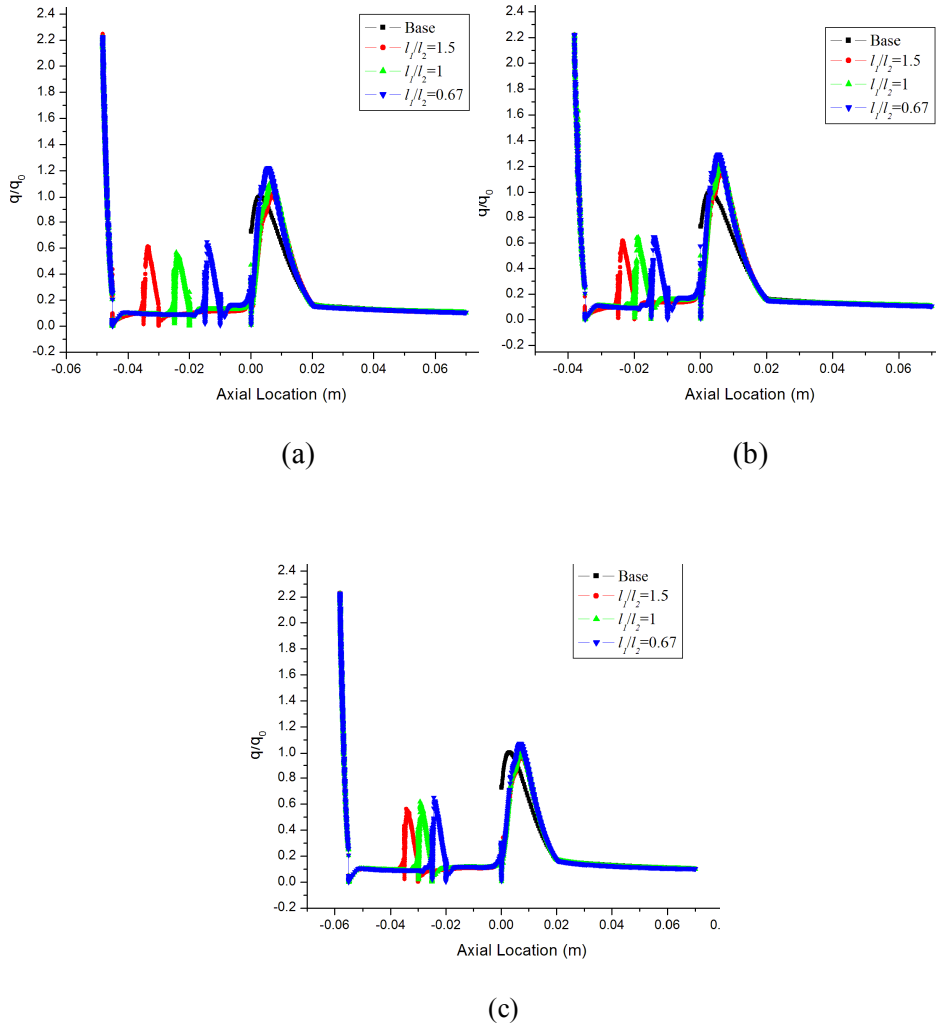


Figure 5.66 Surface heat flux distribution for aerospike configurations with  $r_1=5$  mm,  $r_2=3$  mm and a)  $l/D=1$ , b)  $l/D=1.25$  and c)  $l/D=1.5$

Certainly the larger hemispherical aerodisk provide better reduction in reattachment heat flux. For the same sizes of hemispherical caps on the other hand, the longer aerospikes provides more reductions in the peak reattachment heat fluxes. The relative position of the rear disk between the main body and the front cap also seems to have an effect the peak heating slightly with larger values of  $l_1/l_2$  showing more favourable heat reductions.

Post peak heating at the reattachment point, the surface heat fluxes diminishes sharply along the hemispherical surface up to the hemisphere cylinder

junction. The surface heat flux thereafter remains almost constant along the length of the cylinder with negligible drop.

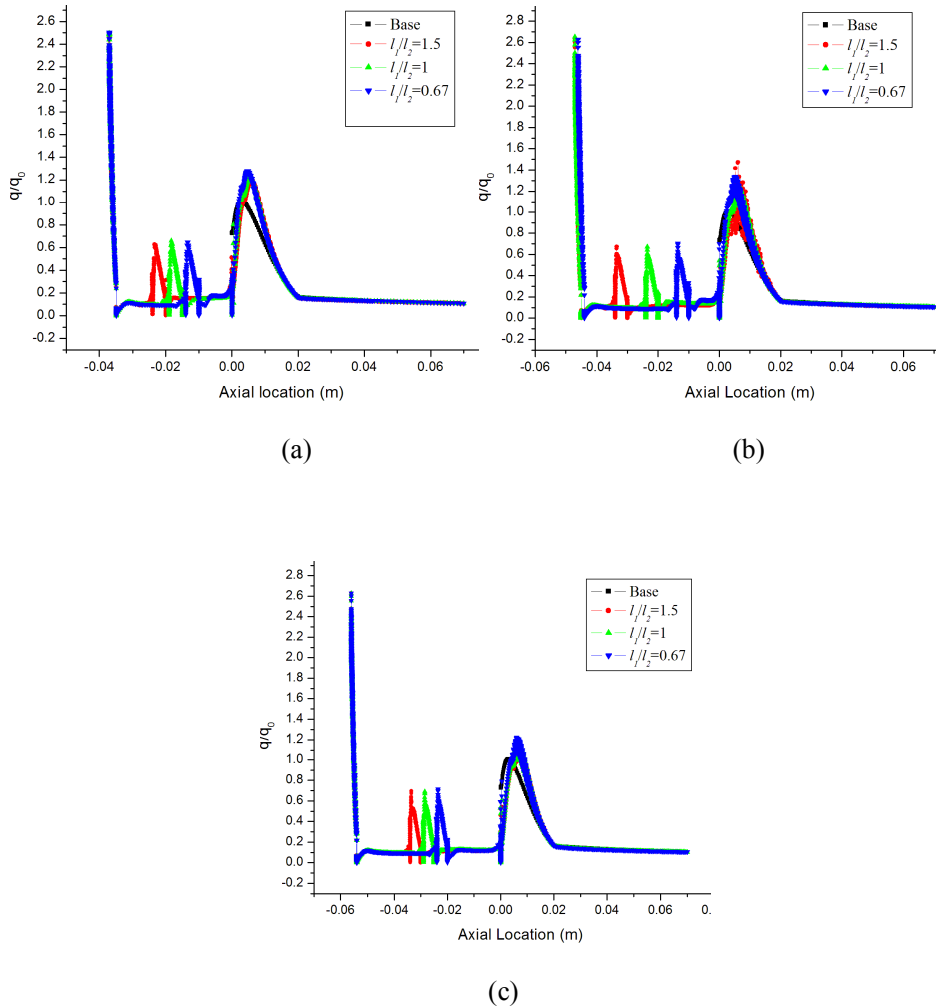


Figure 5.67 Surface heat flux distribution for aerospike configurations with  $r_1=4$  mm,  $r_2=2.5$  mm and a)  $l/D=1$ , b)  $l/D=1.25$  and c)  $l/D=1.5$

The applicability of using various double spike configurations becomes more apparent by comparing the reduction in aerodynamics heating and drag of the main body with different spike configurations with those for a blunt body without spike. Table 5A shows the percentage reductions in heat fluxes to the main body and drag for the double aerodisk configurations with radius of first

hemispherical cap  $r_1=6$  mm and radius of second hemispherical disk  $r_2 = 3.5$  mm.

Table 5 A: Reductions in Heat flux and Drag for Aerospikes with  $r_1=6$  mm and  $r_2=3.5$  mm

Cases	$l/D$	$l_1/l_2$	% Reduction in Total heat transfer rates	% Reduc- tion in peak heat flux	% Reduc- tion in drag
1	1.0	1.5	03	-03	29
2	1.0	1.0	05	-03	28
3	1.0	0.67	02	-12	22
4	1.25	1.5	13	16	42
5	1.25	1.0	10	09	38
6	1.25	0.67	05	-03	30
7	1.5	1.5	15	22	47
8	1.5	1.0	14	19	45
9	1.5	0.67	12	14	42

In Table 5A, the negative signs represent an increase in the corresponding parameter. Clearly, a small but significant reduction in heat fluxes is obtained for the longer aerospikes. Also, it can be observed that the reattachment heat flux is primarily dependent on the position of the bigger hemispherical disk. Case 7 which has an aerospoke configuration of  $l/D=1.5$ ,  $l_1/l_2=1.5$ , and radius of first cap  $r_1=6$ mm produced the most favourable reductions in both the aerodynamic heating and drag with 15%, 22% and 47% reductions in total heat transfer rates, peak heat flux and drag respectively. As mentioned earlier the spiked configurations with  $r_1=5$  or 4, did not produced any reduction the aerodynamic heating of the main body irrespective of the  $l/D$  ratio of the aerospikes and not presented in the table.

#### 5.5.4 Comparisons with a Single Aerodisk Aerospoke

The use of double disk aerospoke or a multiple disk aerospoke is certainly advantageous. The superiority of the double disk aerospoke over the single aerodisk aerospoke in reducing aerodynamic heating is clearly established when the surface heat flux distribution of both configurations are compared as

shown in Fig. 5.68. In Fig. 5.68 the local surface heat flux distribution for single aerodisk aerospike and double aerodisk aerospikes for different overall  $l/D$  ratio are presented.

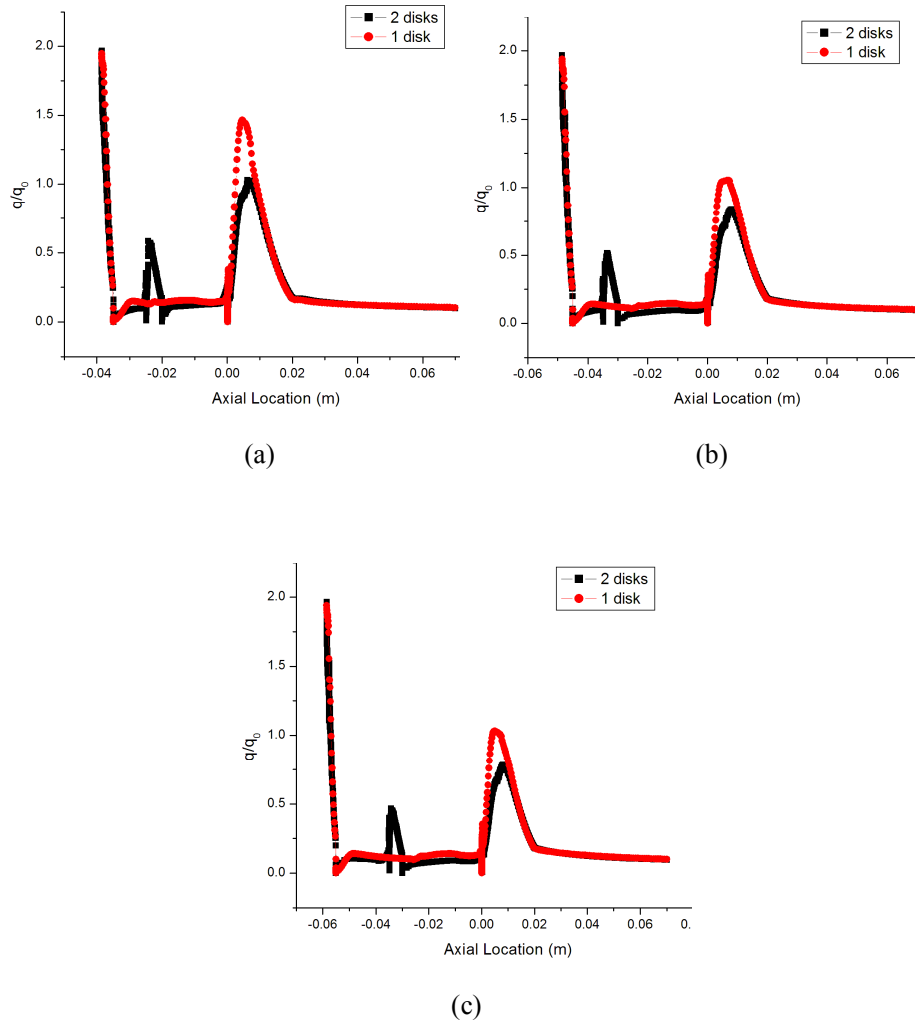


Figure 5.68 Surface heat flux distribution for aerospike configurations with  
a)  $l/D=1$ , b)  $l/D=1.25$  and c)  $l/D=1.5$

As can be seen in Fig. 5.68 the use of an additional intermediate hemispherical cap is quite beneficial in reducing the local surface heating of the main body, especially at the reattachment point. A significant reduction in peak reattachment heat flux is observed for aerospikes of all  $l/D$  ratios with corresponding reductions in total convective heat transfer rates is obtained as compared to the single aerodisk configuration of the same  $l/D$  ratio.

The double disk aerospike are effective not only for the reduction of aerodynamic heating, but also for drag reduction. The presence of an intermediate disk weakens the shock wave system by adding extra regions of recirculating fluid zone. This result in a reduced reattachment pressure on the shoulder and a reduced the dynamic pressure in front of the main body, lowering the drag of the body. The surface pressure distribution for the single and double disk aerospike are compared in Fig. 5.69. The pressure values in Fig. 5,69 are non dimensionalized with the freestream pressure.

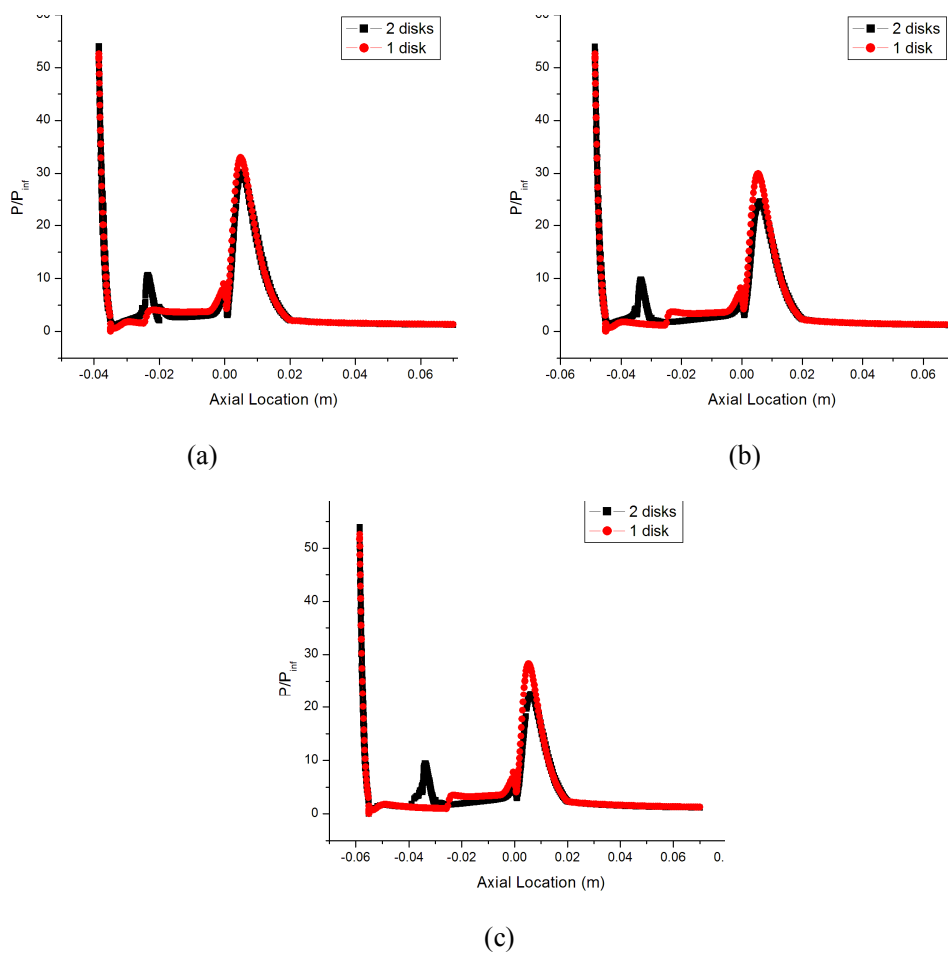


Figure 5.69 Surface pressure distributions for aerospike configurations with a)  $l/D=1$ , b)  $l/D=1.25$  and c)  $l/D=1.5$

The advantage of using two disk aerospike over a single disk aerospike can be tabulated as the reductions in drag and peak reattachment heat fluxes with the values for single disk aerospike as reference, as shown in Table 5B.

Table 5 B: Reductions in Aerodynamic Drag and Heating Parameters

$l/D$	% Reduction in Reattachment Heat Flux	% Reduction in Total Heat Transfer Rate	% Reduction in Drag
1.0	30	14	08
1.25	21	13	15
1.5	29	15	17

Thus aerospikes with two or multiple aerodisks can effectively used to manage the aerodynamic drag and heating problems for hypersonic projectiles.

## **6 RESULTS AND DISCUSSION FOR FLOW AT MACH 10.1**

All the real gas computations have been performed using Park's 5 species 17 reactions model at a freestream Mach number, pressure and temperature of 10.1, 16066 N/m<sup>2</sup> and 216.65 K respectively. This freestream condition, taken from a typical ballistic reentry trajectory has been chosen because of its representation of dense atmospheric which is the theme of this dissertation. Since the thermally perfect gas computations and the chemically reacting gas computations have been done at different sets of conditions, no direct attempt has been made to correlate the results obtained for the two different gas models.

### **6.1 THE EFFECT OF PARABOLIC CAVITY**

The structure of flowfield around a hemisphere cylinder with a forward facing parabolic cavity in chemically reacting air is same as in thermally perfect gas case. The shock wave standoff distance and the shock wave thickness however, decrease for the chemically reacting air along with larger pressure jump across the shock wave owing to higher Mach number. The temperature behind the bow shock is sufficiently high to dissociate the oxygen molecules almost completely and some percentage of nitrogen molecules as well in the stagnation region as shown in Fig. 6.1, which shows the contours of temperature for two different cavity configurations. As compared to the temperature contours for thermally perfect gas, the high temperature zone aft of the bow shock is limited to a very small region behind the shock and relatively cold fluid is seen along the cavity surface. The reason for this is the heat taken away by the dissociation of primarily oxygen molecules due to high temperatures.



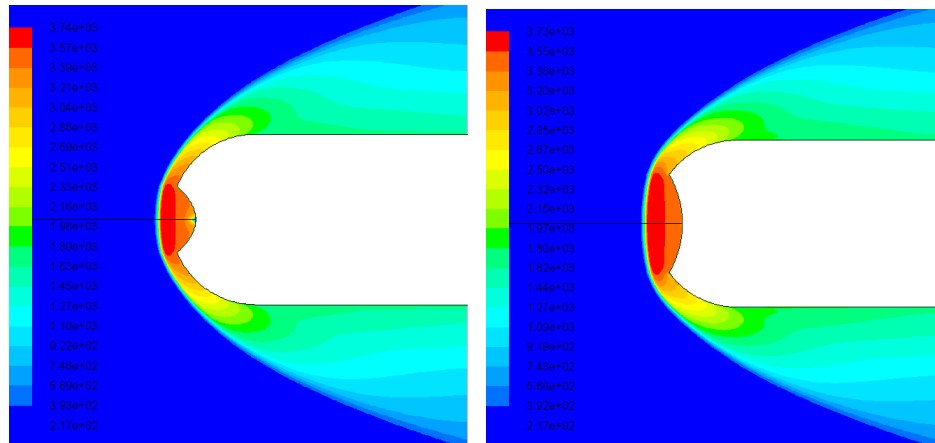


Figure 6.1 Temperature contours for parabolic cavities with a)  $r/d=1.5$ ,  $d=6$  mm and (b)  $r/d=2.5$ ,  $d=7$  mm

With the above temperature field, more than one-fourth of the oxygen in the cavity region is dissociated with some dissociation of nitrogen molecules as well. The contours of mass fractions of different species for the above two cavity configurations are shown in Figs. 6.2 and 6.3 respectively. As can be seen in Fig. 6.2, for parabolic cavity with small lip radius, most of the oxygen dissociation occurs in the vicinity of the sharp lip inside the cavity. The temperature in this region is high enough to enunciate the dissociation of even  $N_2$  molecules and recombination to form NO. In the stagnation region of these cavities however, very little dissociation takes place with negligible concentrations of O, N and NO. Almost all of the N atoms formed recombine with the O atoms to form NO radical leaving behind a very small amount N atoms entirely inside the cavity with few traces outside the lip forming a ring like structure.

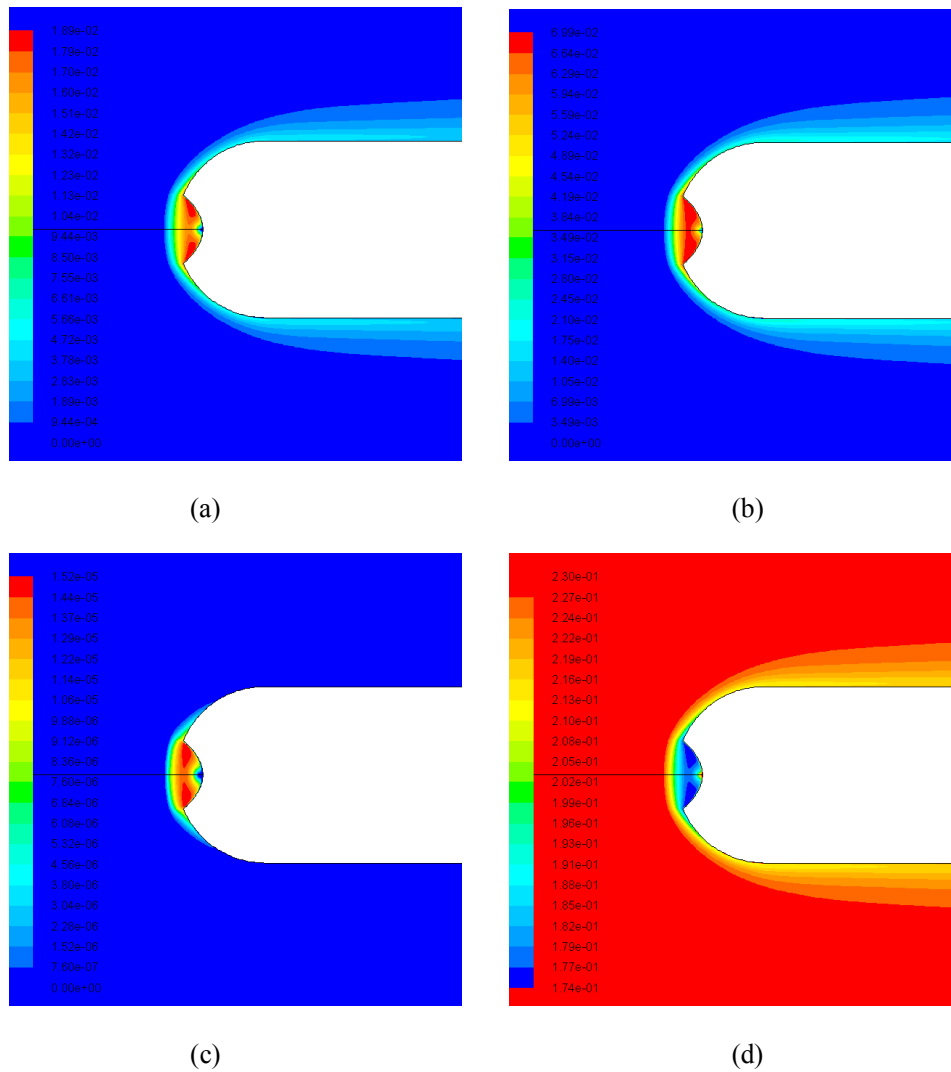


Figure 6.2 Contours of mass fractions of a) O, b)NO, c) N and O<sub>2</sub> for parabolic cavity with  $r/d=1.5$ ,  $d=6\text{mm}$

For large opening cavities, as shown in Fig. 6.3, the dissociation of oxygen and nitrogen is not concentrated just near the sharp lip; rather it is uniform within the cavity with uniform mass fractions of O, NO and O<sub>2</sub> inside the cavity. The traces of N again are seen only over a small region inside the cavity away from the stagnation point.

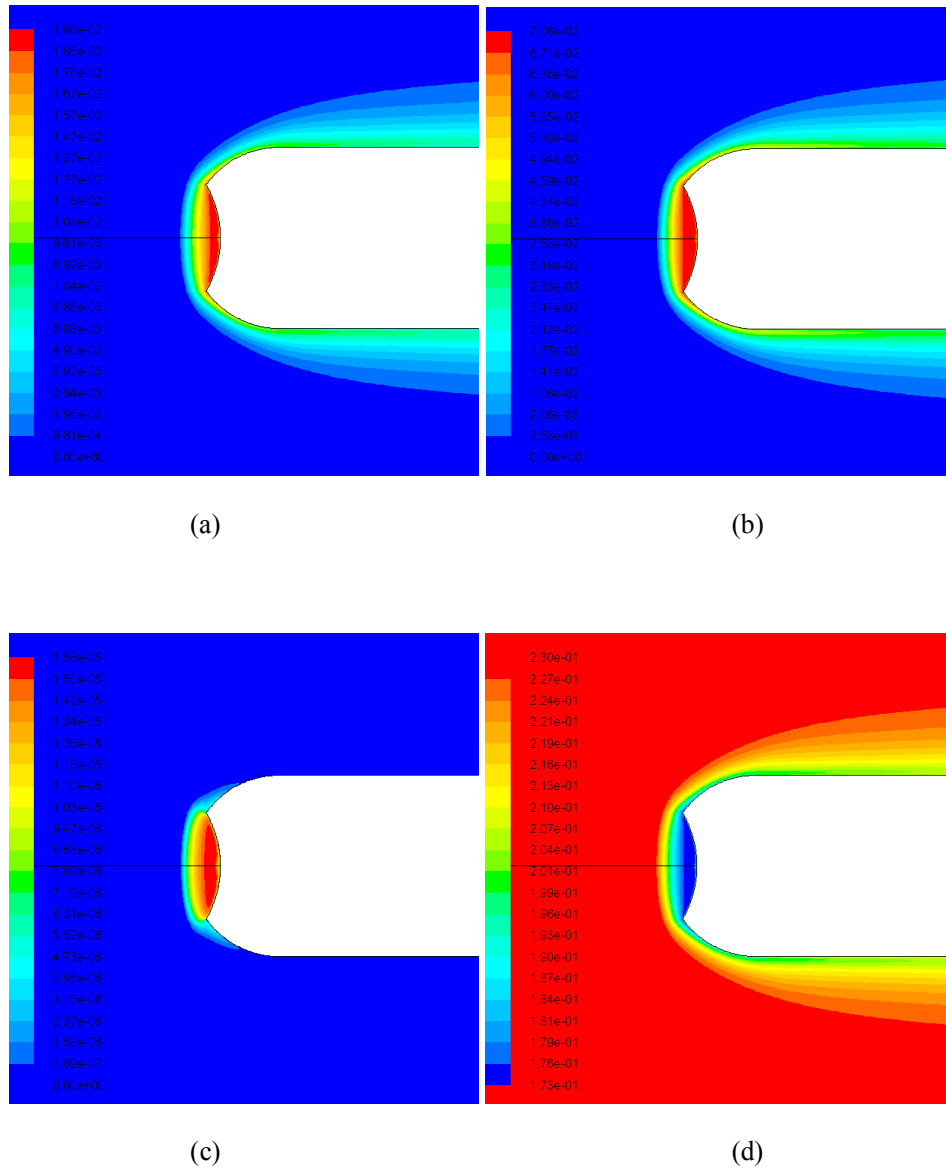


Figure 6.3 Contours of mass fractions of a) O, b)NO, c) N and O<sub>2</sub> for parabolic cavity with  $r/d=2.5$ ,  $d=7\text{mm}$

The dissociation of oxygen and nitrogen molecules in the post shock region absorbs an appreciable amount of thermal energy giving lesser convective heat transfer rates at same inflow conditions. The catalyticity of the walls however increases the wall heat transfer rates due to recombination of dissociated atoms. For the computations done in this research, the blunt body wall has been modelled as fully catalytic wall with species mass concentrations equal to the freestream values. All of above chemical reactions occur predominantly in the

shock layer and the stagnation region. The degree of dissociation of molecules and the association of atoms along the stagnation streamline is shown in Fig. 6.4 (a) and (b).

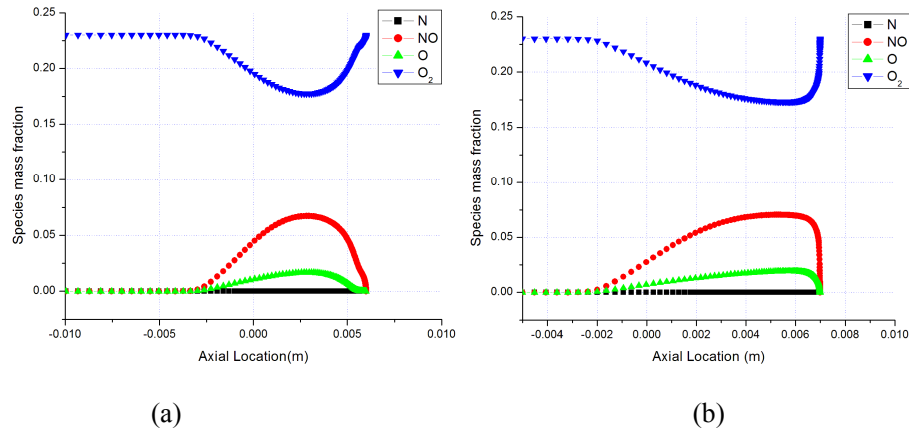
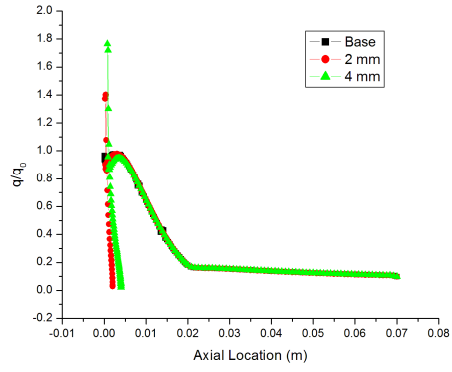
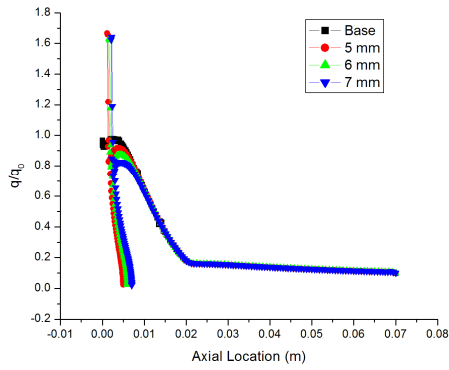


Figure 6.4 Species mass fraction along stagnation streamline for a)  $r/d=1.5$ ,  $d=6$  mm and b)  $r/d=2.5$ ,  $d=7$  mm

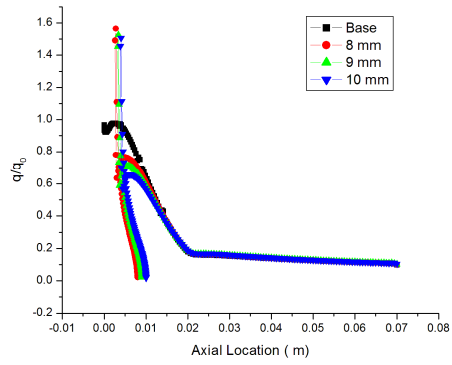
The effect of finite rate chemistry with fully catalytic walls seems to have decreased the effectiveness of forward facing parabolic cavity in reducing the surface heat transfer rates especially near the sharp lip as shown in Figs. 6.5-6.7. Figs. 6.5, 6.6 and 6.7 show the surface heat fluxes for various parabolic cavity configurations with  $r/d=1.5$ , 2 and 2.5 respectively with depth of cavity in the legend. As can be seen in Figs. 6.5-6.7, there is a detrimental rise in the surface heat flux at the sharp lip which much higher than those seen for thermally perfect gas. Except for the sharp lip, the surface flux distribution is similar to those obtained for perfect gas computations.



(a)



(b)



(c)

Figure 6.5 Surface heat flux distribution for various parabolic cavity configurations with  $r/d=1.5$

Another point of difference observed with regard to the surface heat flux distribution is that the heat flux drop aft of the sharp lip is lesser as compared to the perfect gas with marginally small rise in heat flux after the post lip drop. As with the thermally perfect gas computations, the stagnation point heat flux is substantially reduced by the presence of a parabolic cavity along with favourable reductions all along the body except for the sharp lip.

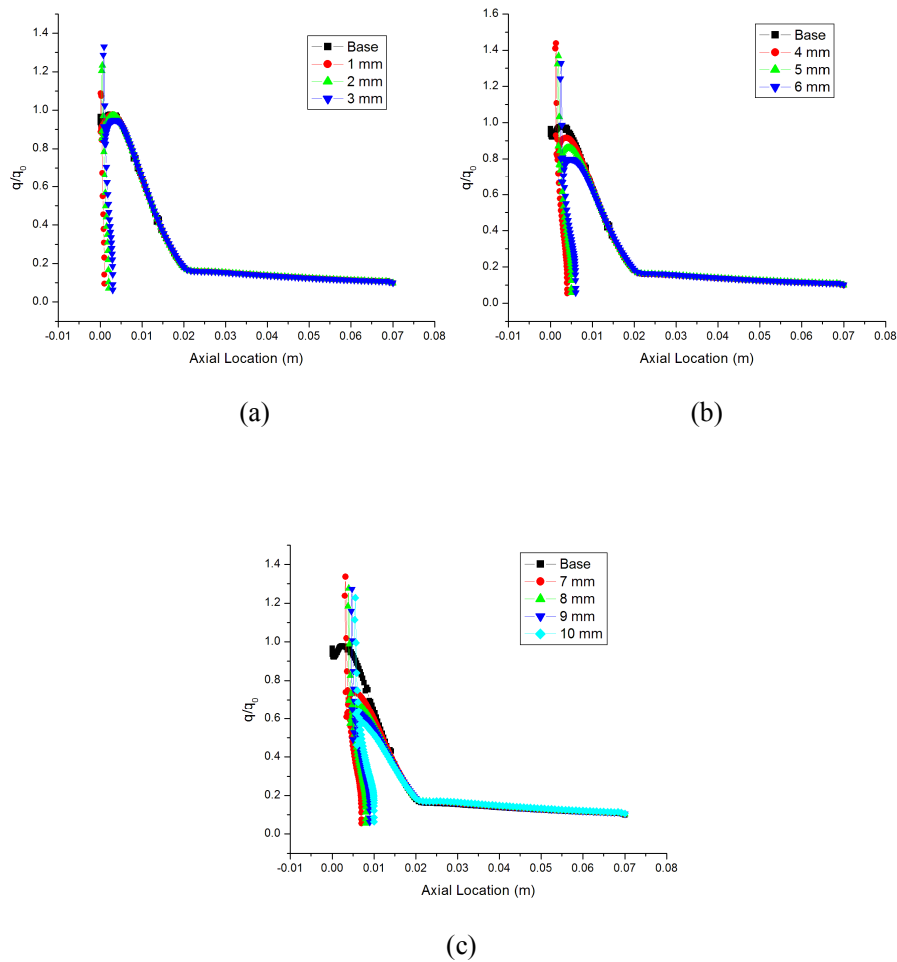


Figure 6.6 Surface heat flux distribution for various parabolic cavity configurations with  $r/d=2.0$

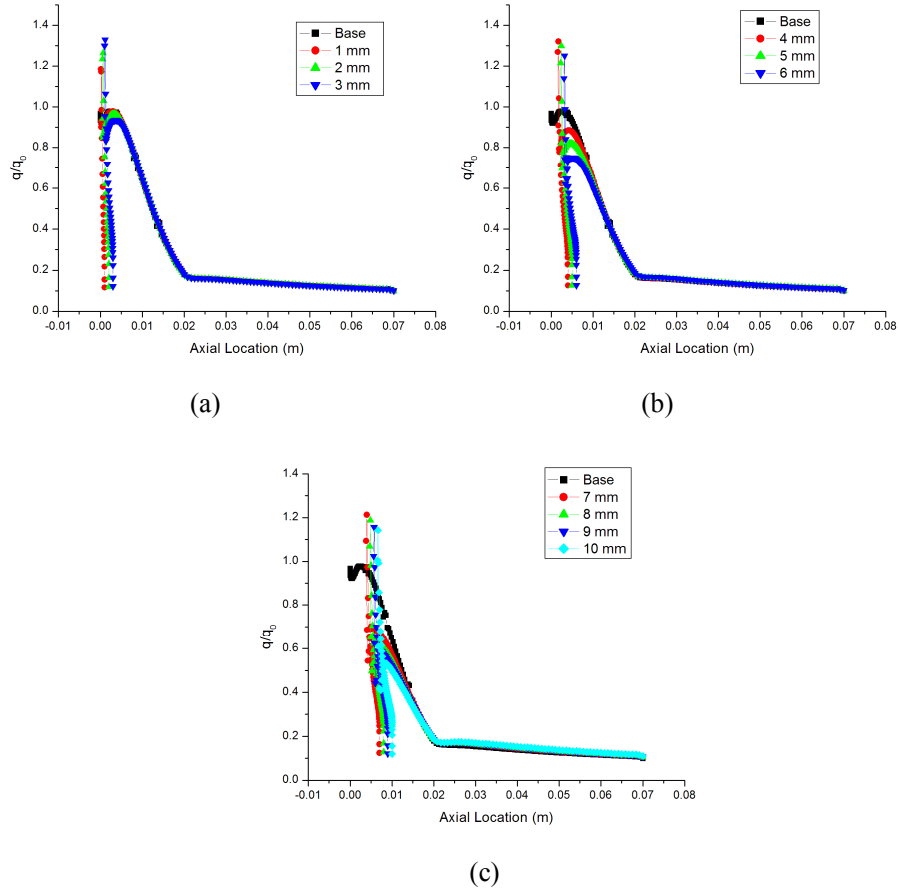


Figure 6.7 Surface heat flux distribution for various parabolic cavity configurations with  $r/d=2.5$

The reductions in peak heat fluxes can be appreciated if the peak heat flux on the outer surface for various cavity configurations is compared to the peak heating of the base body as shown in Fig 6.8. In Fig. 6.8, the surface heat fluxes are normalised with the peak heat flux for the base configuration. The trend is same as for the perfect gas considerations with deeper and wider cavities producing more reductions in the peak surface heat flux. The percentage reduction however, is slightly less here with the deepest cavity with an  $r/d$  value of 2.5 producing a reduction of 47%.

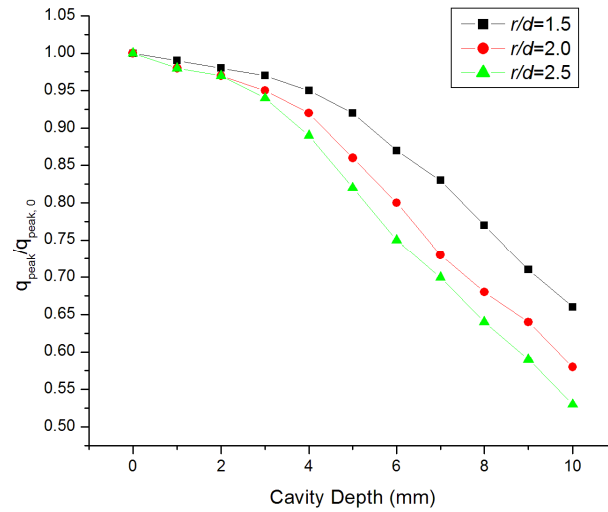
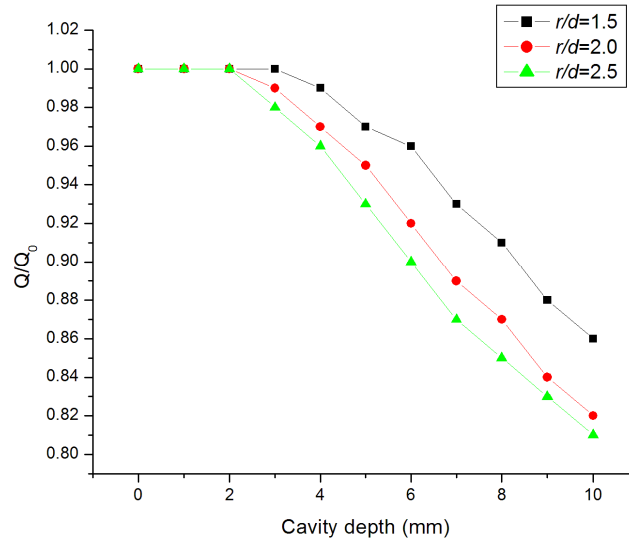


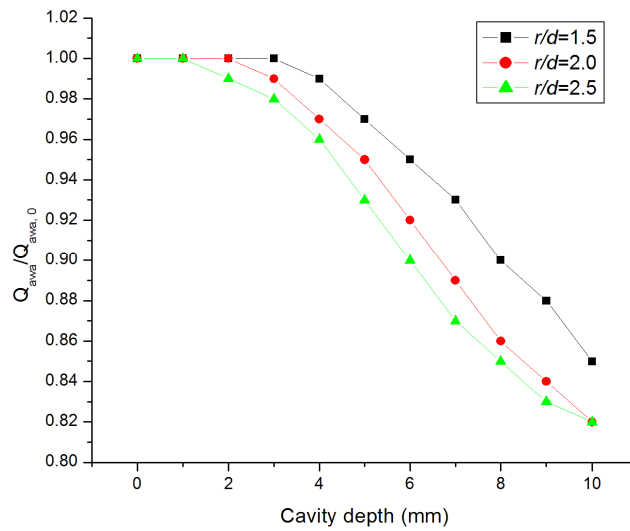
Figure 6.8 Post lip peak heat flux for parabolic cavity

The reduction in aerodynamic heating is often expressed in terms of reductions in the total heat transfer rates or the AWA of the heat fluxes as shown in Fig. 6.9 (a) and (b). As can be seen in Fig. 6.9, maximum reductions of 19 and 18 percent in the integral and the AWA of heat fluxes respectively is obtained for the deepest cavity investigated. The lower reductions in heat transfer rates observed in Fig. 6.9 are primarily due to the increase in local heating at the sharp due to wall catalyticity.





(a)



(b)

Figure 6.9 Non dimensionalized a) total heat transfer rates and b) AWA of surface heat fluxes for various parabolic cavity configurations

Finally, the drag of the hemisphere cylinder is observed to be unaffected by the presence of a parabolic cavity at the nose up to a lip radius of 14 mm after which it increases rapidly with increasing lip radius for all cavity depths as shown in Fig. 6. 10.

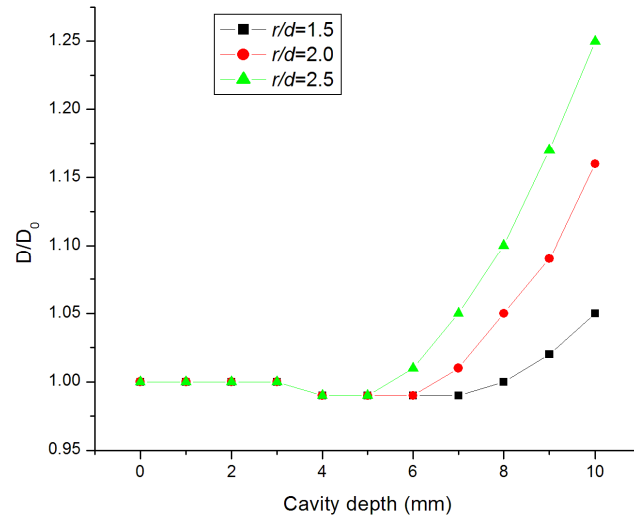


Figure 6.10 Normalized drag for various parabolic cavity configurations

## 6.2 EFFECT OF ELLIPSOID CAVITY IN CHEMICALLY REACTING AIR

The flowfield structure around a hemisphere cylinder with a forward facing ellipsoid cavity at Mach 10.1 is similar to that for at Mach 6.2 with a pair of large recirculating fluid zone inside the cavity. At Mach 10.1, however, the steady state shock wave comes closer to the body also becomes sharper as shown in Fig. 6.11 (a) and (b) which shows pressure contours for two different ellipsoid cavity configurations at Mach 10.1. As can be seen in Fig. 6.11, the flow inside cavity is entirely under stagnation conditions with an expansion wave at the sharp lip which is much gradual as compared to the Mach 6.2 case. Also a clear difference can be seen in the location of recompression shock on the shoulder which is again much sharper and does not extend beyond the hemisphere cylinder junction.

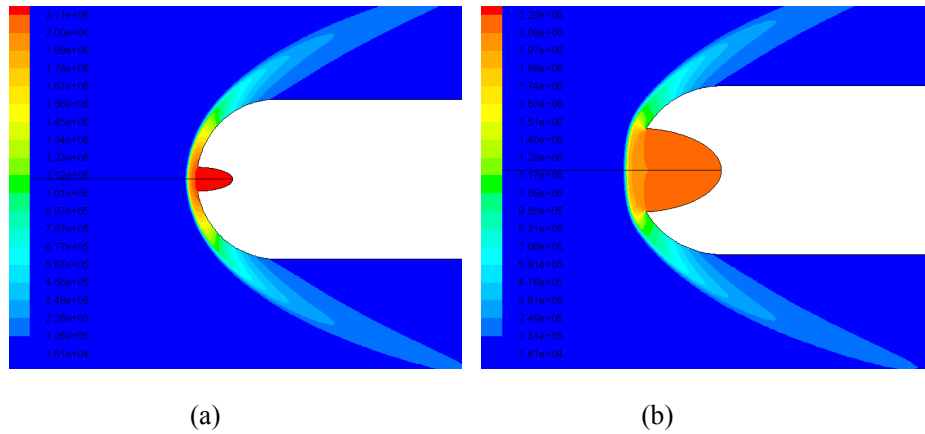


Figure 6.11 Contours of pressure for ellipsoid cavity with a)  $a/b=3$ ,  $d=9$  mm and  $a/b=2$ ,  $d=20$  mm

The post shock temperatures inside the stagnant cavity at mach 10.1 are high enough to enunciate the dissociation of  $O_2$  and  $N_2$  molecules which relaxes the temperatures slightly. Some of atomic oxygen and nitrogen combine at these elevated temperatures to produce NO radicals in the cavity region. Figure 6.12 shows the contours of mass fractions of different species for a typical ellipsoid. As can be seen in Figs. 6.12, most of the oxygen and nitrogen dissociation occur inside the cavity in the vicinity of the sharp lip. For a Mach number of 10.1, about 25% of  $O_2$  in post shock region near the lip is dissociated with some traces of N atoms also seen forming a ring at the sharp lip. For the deep cavities with wider mouth opening, the region of  $O_2$  dissociation can be seen deep into the cavity with concentrations of dissociated atoms and radical forming a very wide ring covering the inner surface of the lip.

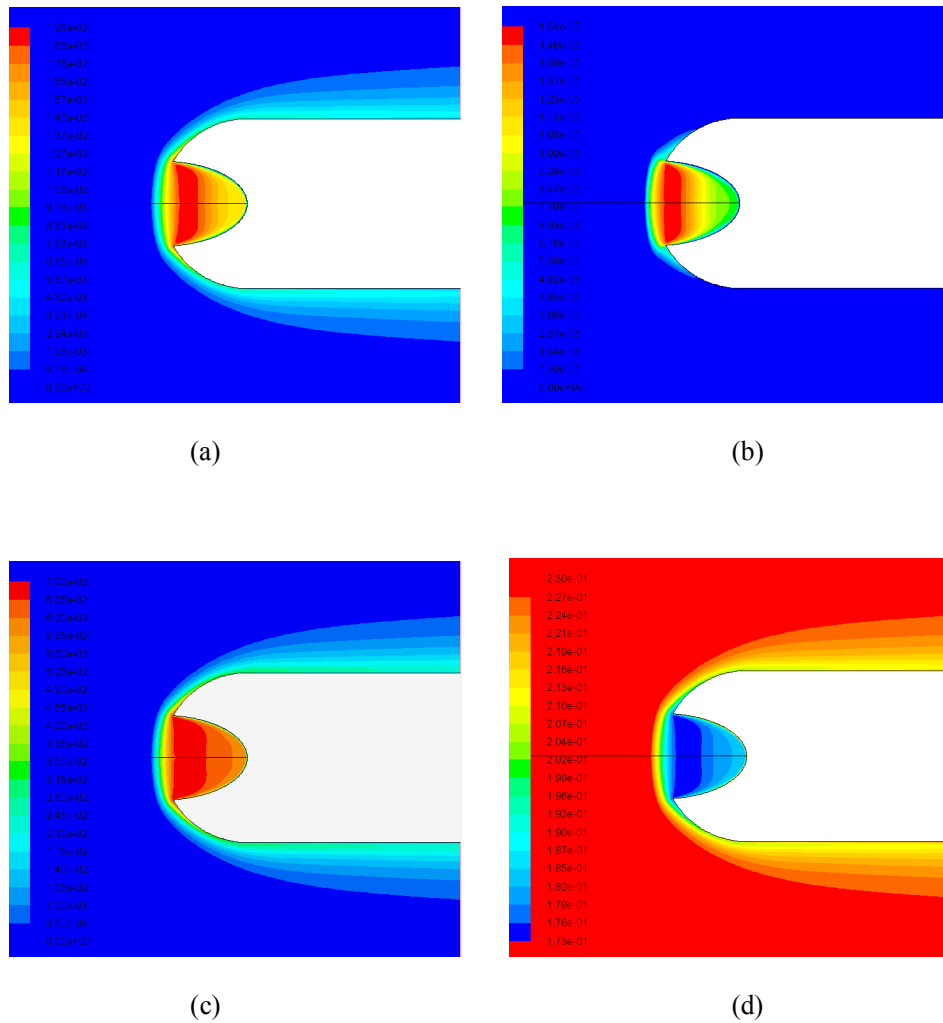


Figure 6.12 Mass fractions of a) O, b) N, c) NO and d) O<sub>2</sub> for ellipsoid cavity with a/b=3 and d=9 mm

The degree of dissociation of various molecules and radicals and the recombination of various atoms in shock layer and in the stagnation region can be more efficiently represented as the variation of mass fractions of these species along the stagnation streamline as shown in Fig. 6.13 (a-b).

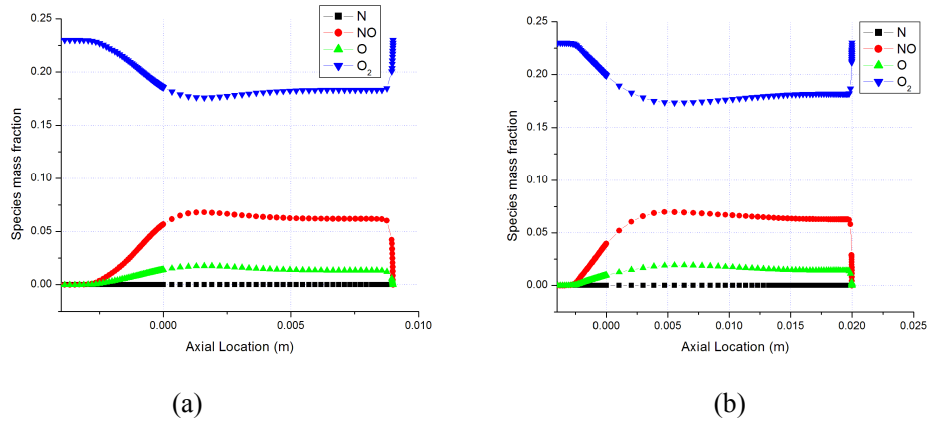


Figure 6.13 Variation of species mass fraction along the stagnation streamline for ellipsoid cavity with a)  $a/b=3$ ,  $d=9$  mm and b)  $a/b=2$ ,  $d=20$  mm

As can be seen from Fig. 6.13 (a-b), the degree of dissociation of oxygen does not vary with the depth of lip radius of the cavity. The thickness of the ring of dissociated species however increases with increasing depth or lip radius of the ellipsoid cavity. In other words; more volume of air molecules is dissociated with increasing depth and mouth opening of the cavity giving lower total heating rates. The species mass fractions fall to the freestream values due to super catalytic wall assumption with increased aerodynamic heating of the surface due to heat of recombination.

The pressure distribution over a hemisphere cylinder with a forward facing ellipsoid cavity at Mach 10.1 is similar to that at Mach 6.2, however with increased pressure ratio across the bow shock. The surface heat flux distribution on the other hand is slightly different with no sudden drop in heat fluxes aft of the sharp lip as shown in Figs. 6.14-6.16. Figures 6.14, 6.15 and 6.16 show the surface heat flux distribution for various ellipsoid cavity configurations with  $a/b$  ratio of 3, 2 and 1.5 respectively. The heat flux values in these curves have been non-dimensionalized with the peak surface heat flux for the base configuration while the numbers in the legend represents the depth of the ellipsoid cavity.

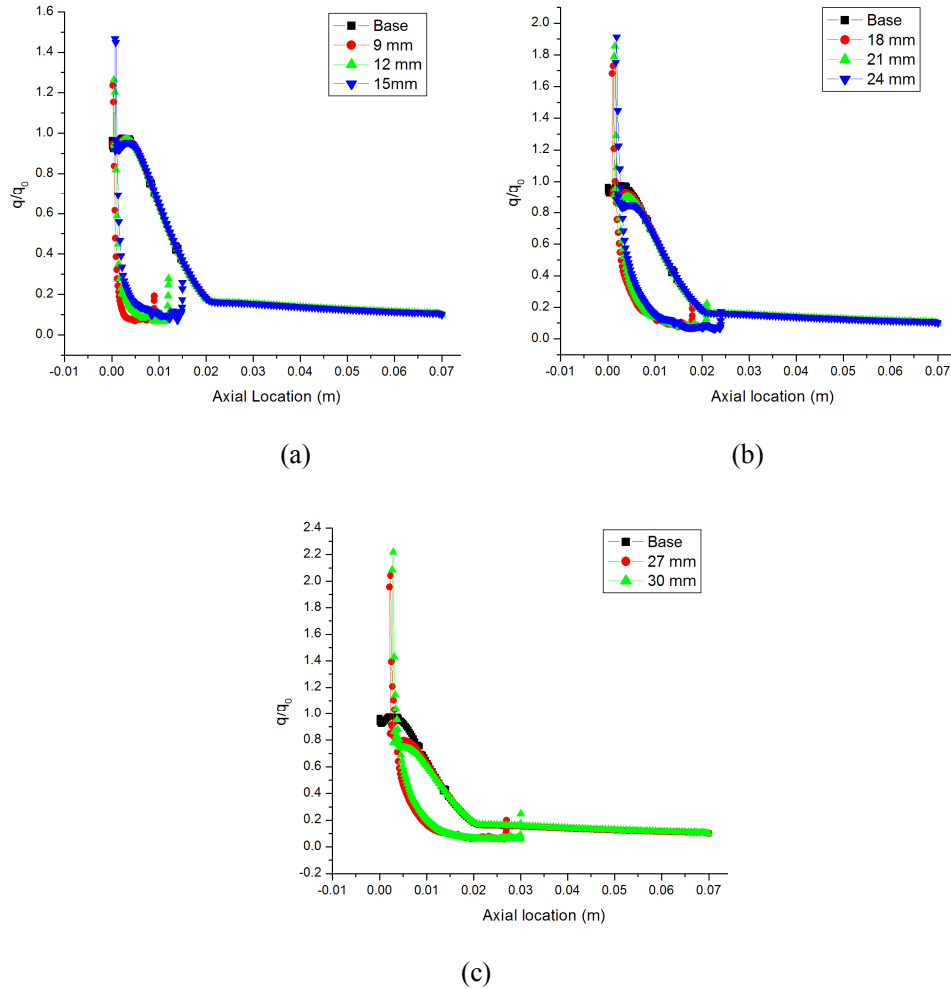


Figure 6.14 Surface heat flux distribution for various cavity configurations with  $a/b=3$

As can be in Figs. 6.14 -6.16, the peak heat flux rise at the sharp leap is more severe as compared to the low Mach number case with a local heating at the sharp lip rising to more than 100% higher than the peak heating of the base configuration, especially for the cavities with large mouth opening. Immediately after the sharp lip, the surface heat flux fall to close the peak heating of the base configuration. The local heating rates fall thereafter to slightly lower values before rising again to another peak on the hemispherical portion and then falling continuously along the hemispherical surface up to the hemisphere cylinder junction.

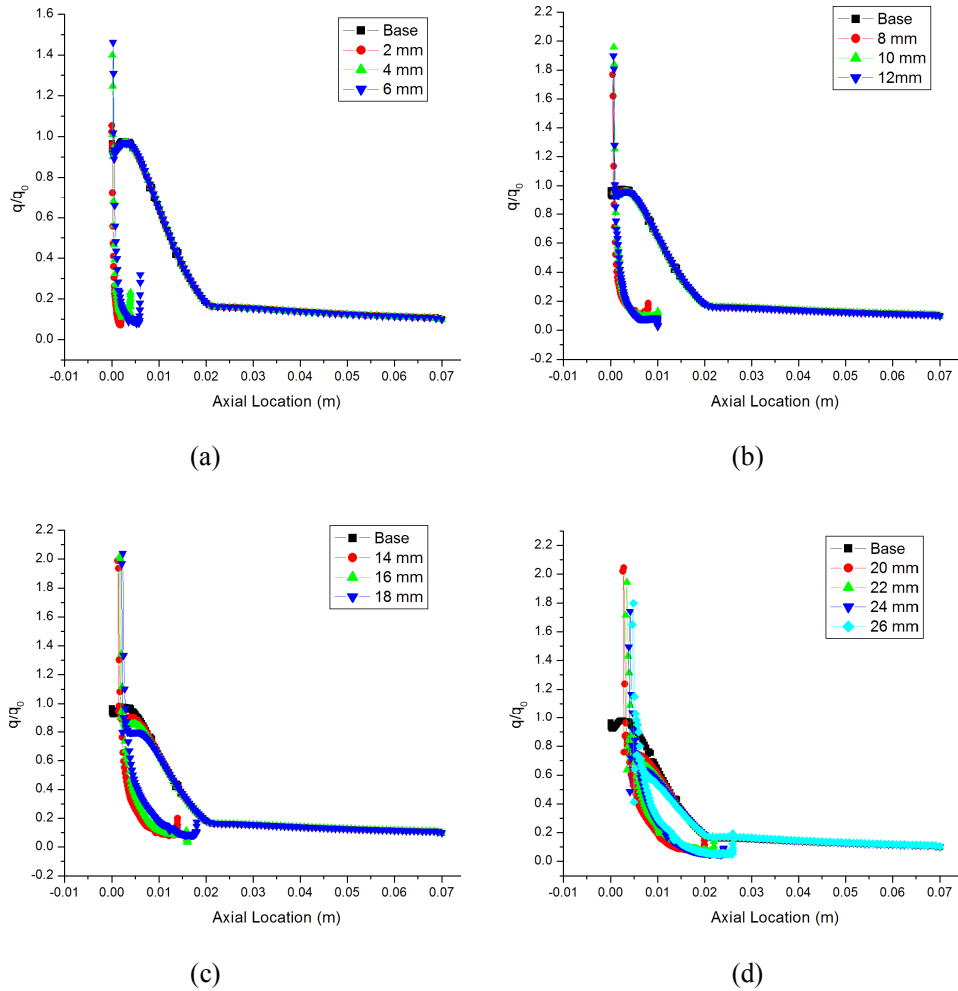


Figure 6.15 Surface heat flux distribution for various cavity configurations with  $a/b=2$

The second maximum on the hemispherical portion however, is not seen in the case of ellipsoid cavities with large lip radii. For these wider mouth cavities the surface heat fluxes fall continuously after the sharp lip up to the hemisphere cylinder junction. The large heating rates seen immediately aft of the sharp lip is probably due to the absence of any recirculating fluid zone after the lip, as was the case with Mach 6.2.

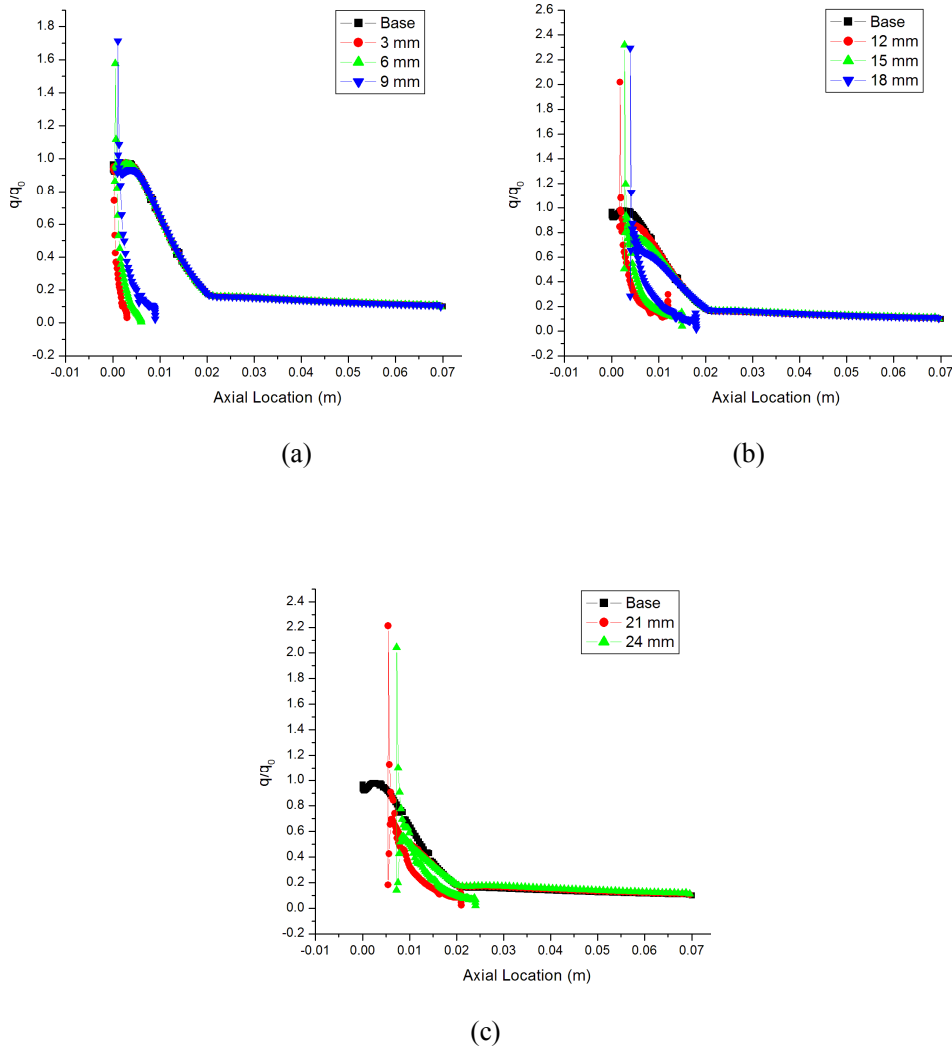


Figure 6.16 Surface heat flux distribution for various cavity configurations with  $a/b=1.5$

Though the combination of Mach number flowfield and full catalyticity of the wall diminishes the heat reduction capabilities of a forward facing ellipsoid cavity, some insight of the heat reduction achieved can be demonstrated via Fig. 6.17. Figure 6.17 shows the normalized local outer surface heat flux at a point 5 mm aft of the sharp lip for various ellipsoid cavity configurations. The particular point is chosen primarily as the peak local heating aft of the sharp lip for most configurations occur at this point irrespective of the depth of cavity.



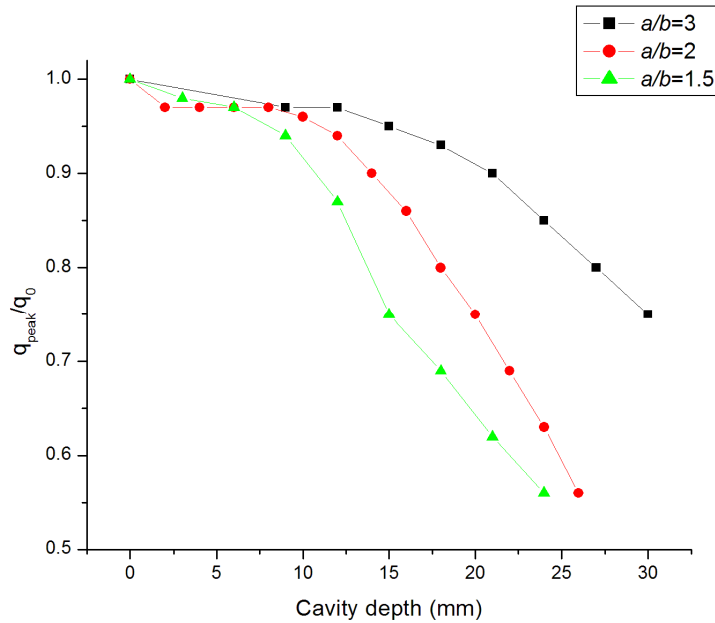
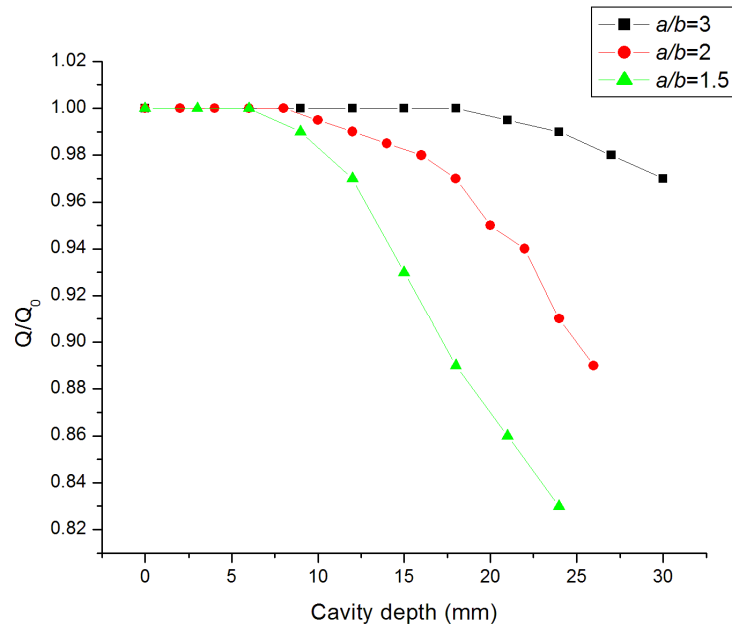


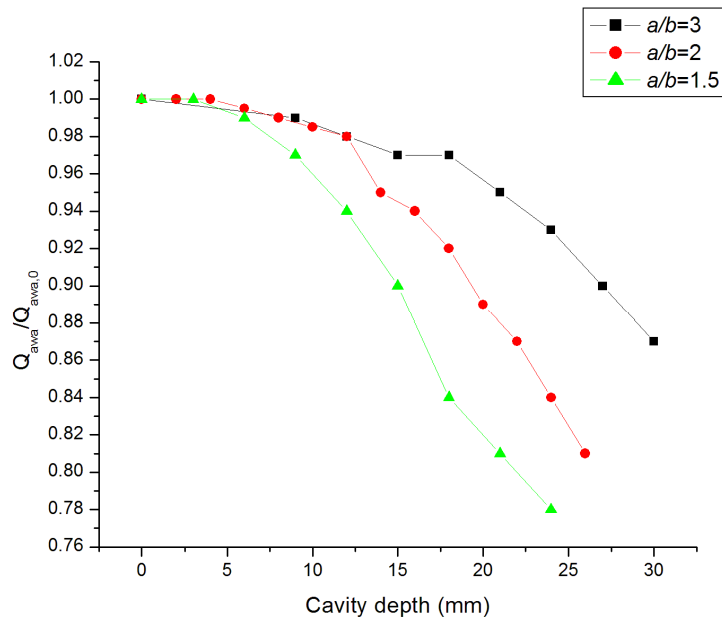
Figure 6.17 Local surface heat flux at a point 5 mm aft of sharp lip

The peak heating on the convex hemispherical surface decreases with an increase in the depth or the lip radius of the cavity, as is observed from Fig.6.17. For the same depth of the cavity, the configuration with larger lip radius shows lower peak heat flux while for the configurations with same cavity lip radius, the one with deeper cavity provided the higher heat flux reduction. Among the ellipsoid cavity configurations investigated, the deepest cavity with a/b ratio of 1.5 produced a maximum local heat flux reduction of 45 %.

The ability of a passive device like a forward facing cavity in reducing aerodynamic heating is often judged by the reductions obtained in either the total heat transfer rates or the area weighted average of the surface heat fluxes of over the whole body. Figure 6.18 (a) and (b) respectively show the total heat transfer rates and the AWA of heat fluxes for various cavity configurations, non-dimensionalized with their respective values for the base configuration.



(a)



(b)

Figure 6.18 Non-dimensionalized a) total heat transfer rates and b) AWA heat fluxes for various ellipsoid cavity configurations at Mach 10.1

The trends for reductions in aerodynamic heating parameters are similar to those obtained for local peak heating, with deeper cavities with wider mouth

producing larger reductions. As can be seen in Fig. 6.18, ellipsoid cavities with  $a/b$  ratio of 3 shows almost negligible reductions in steady state total heat transfer rates, however with appreciable reduction in AWA of heat fluxes. This reduction is mostly due to the increase in surface area of the configuration rather than being a result of reduced effective heating on the upper surface. The cavities with  $a/b$  ratios of 2 and 1.5, with depths more than 10 mm on the other hand seems to favourably reduce both the total heat transfer rates and the AWA of heat fluxes. For the deepest and widest ellipsoid cavity configurations investigated, reductions of 17% and 22% is seen in total heat transfer rates and the AWA heat fluxes respectively.

Finally, the steady-state drag of a hemisphere cylinder with forward facing ellipsoid seems to be unaffected by the depth rather dependent on the lip radius of the cavity as shown in Fig. 4.20. For lip radius of up to 14 mm the drag remains constant with even slight drop for moderately deep cavities due to reversed direction of shear stresses inside the cavity. The aerodynamic drag for configurations with lip radii larger than 14 mm however, rises abruptly for all cavity depths.

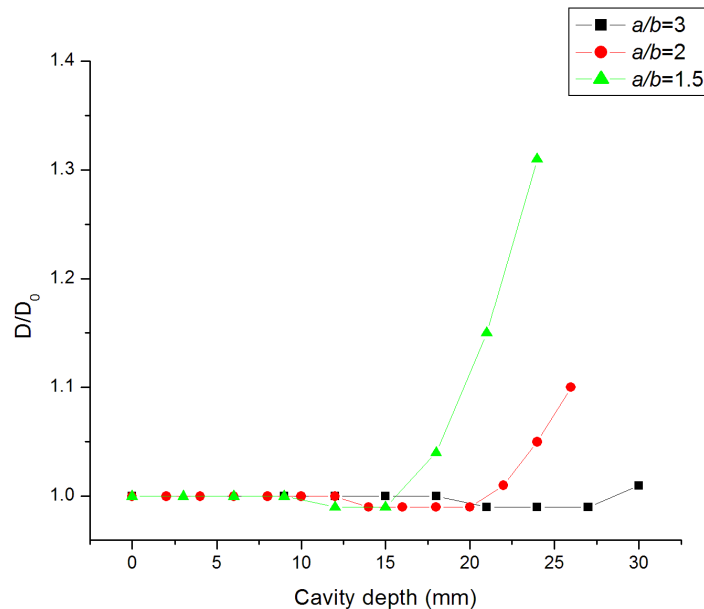


Figure 6.19 Non-dimensional drag for various ellipsoid cavity models

### 6.3 EFFECT OF FORWARD FACING CONICAL CAVITIES

The flowfield structure around a hemisphere cylinder with a forward facing conical cavity at Mach number 10.1 differs with that at Mach 6.2 in that the bow shock is sharper and closer to the body. Figure 6.20 and 6.21 show the pressure and temperature contours for wide angle and low angle conical cavity configurations respectively. As can be seen in Figs. 6.20 and 6.21, for both angles the conical cavity is entirely engulfed by the sonic zone with stagnant pressure and temperatures inside the cavity. The maximum pressure seen for deeper cavities are marginally larger than those for shallow cavities because longer stagnation line. The region of maximum temperature however, is seen to be limited to the lip region only due to formation of recirculating fluid region inside the cavity which insulates the external flow from reaching deep into the cavity.

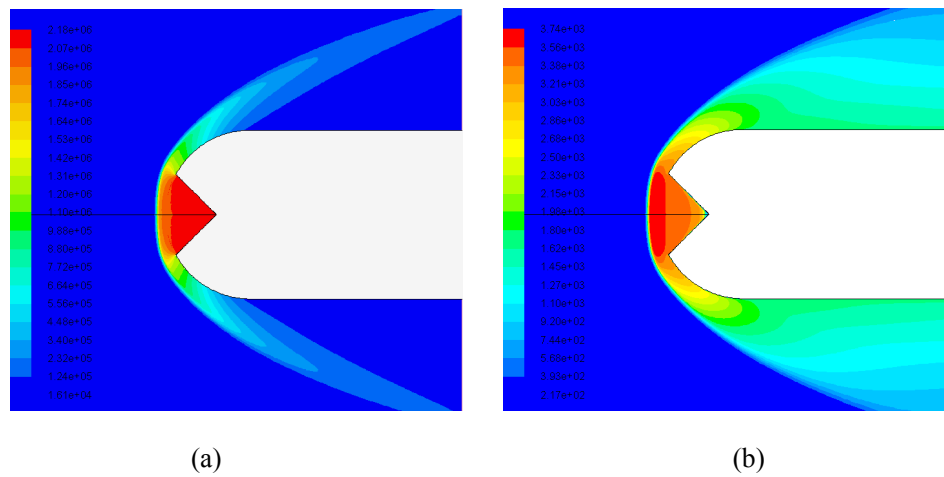


Figure 6.20 Contours of a) pressure and b) temperature for a conical cavity model with  $\alpha=45^\circ$  and  $d=12$  mm

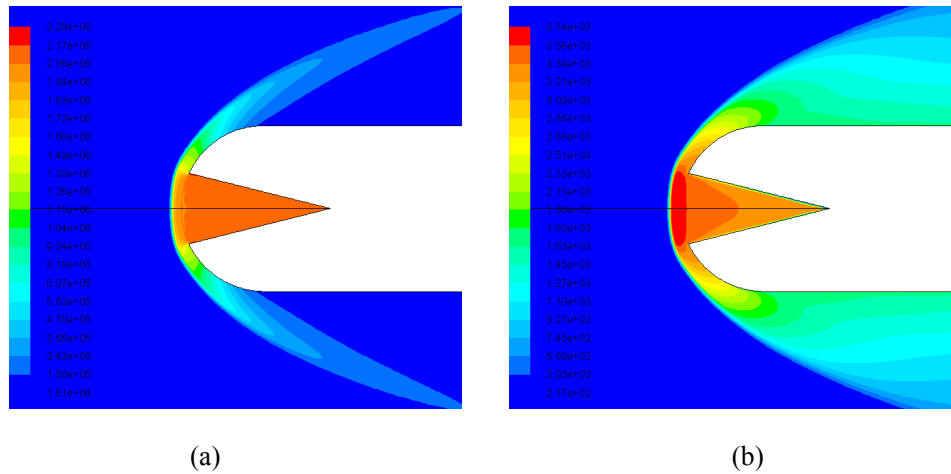


Figure 6.21 Contours of a) pressure and b) temperature for a conical cavity model with  $\alpha=14^\circ$  and  $d=36$  mm

As can be seen in the temperature contours, the temperature in the shock layer and inside the cavity is sufficiently high bring about a substantial dissociation of  $O_2$  molecules and even start the dissociation of  $N_2$  molecules. Almost all of the N atoms recombine with the readily available O atoms under the influence of existing aerothermal environment to form NO radicals. This leaves behind only traces of N atoms in the flowfield around the hypersonic vehicle. The presence and steady state distribution of various species in the flowfield over a hemisphere cylinder with a typical forward facing conical cavity is shown in Fig. 6.22.

As can be seen in Fig. 6.22 (a)-(d), the dissociation air molecules primarily occurs inside the cavity in the vicinity of cavity lips with the concentrations of newly born species decreasing outwards gradually and inwards. The newly form species, thus form a thick ring of atoms and radicals at the lips inside the cavity. A similar distribution of different constituent species is seen for all cavity configurations with the ring in wider mouth cavities penetrating deep into the cavity.

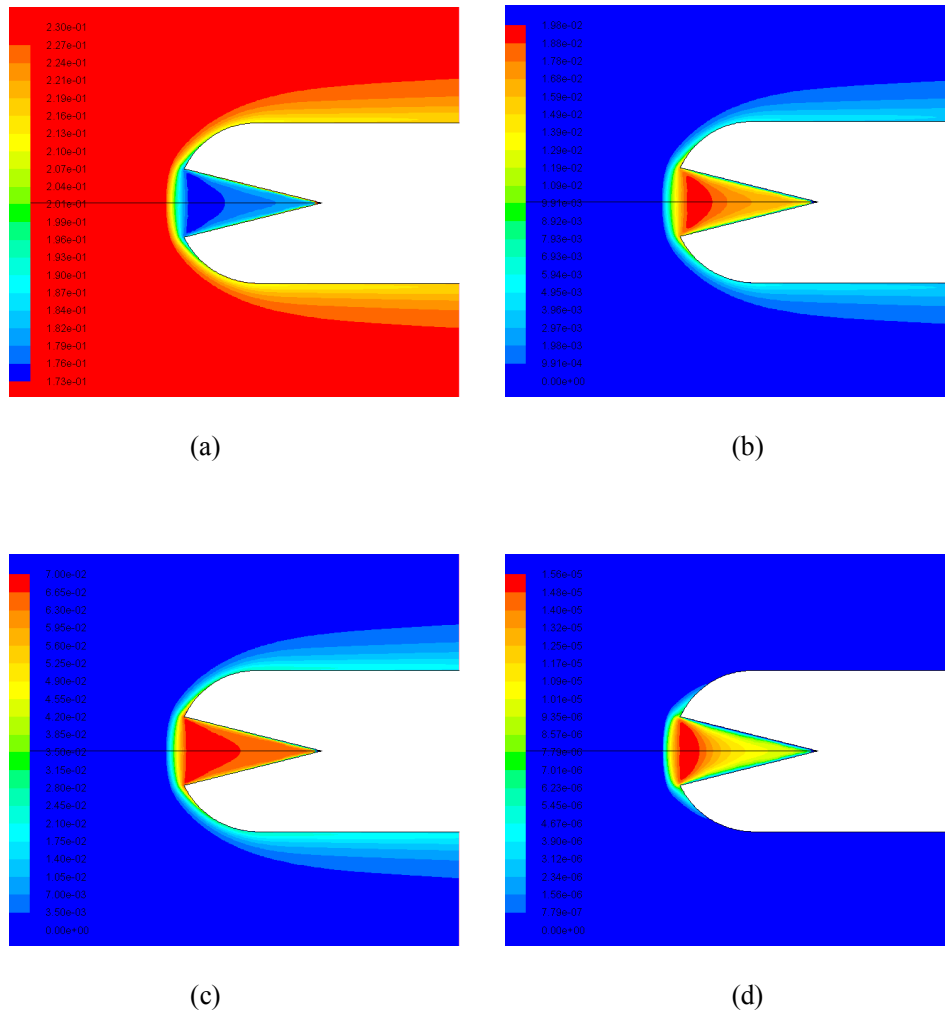


Figure 6.22 Contours of mass fractions of a)  $O_2$ , b)  $O$ , c)  $NO$  and  $N$  for a conical cavity model with  $\alpha=14^\circ$  and  $d=36$  mm

The steady state distribution of different constituent species along the stagnation streamline for few typical conical cavity configurations are shown in Fig 6.23 (a-d). As can be seen in Fig. 6.23, the maximum degree of dissociation of oxygen molecules more all cases is similar with approximately 24% of the oxygen inside the cavity dissociated. The mass fractions of different species along the stagnation streamline remains constant throughout the depth of the cavity before attaining freestream values at the fully catalytic wall. This makes the thickness and volume of dissociated air increasingly large with increase in either the depth or the lip radius of the cavity.

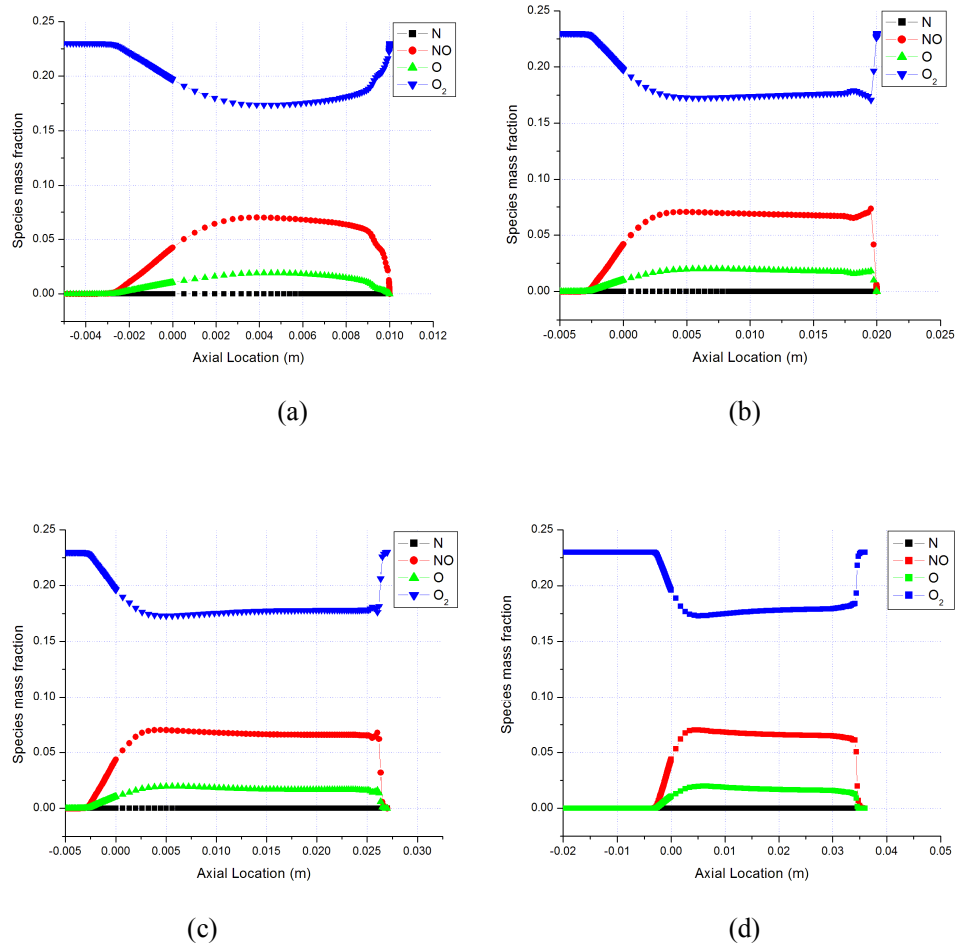


Figure 6.23 Variation of species mass fractions along the stagnation streamline for conical cavity with a)  $\alpha=45^\circ$ ,  $d=10\text{mm}$ , b)  $\alpha=26.6^\circ$ ,  $d=20\text{mm}$ , c)  $\alpha=18.4^\circ$ ,  $d=27\text{mm}$  and d)  $\alpha=14^\circ$ ,  $d=36\text{mm}$

For very large angle conical cavities the variation of degree of dissociation at the cavity inlet and at cone apex is much smoother as compared to small angle conical cavities. This is probably due to the formation of a very small recirculating region of fluid right at the apex of the cone with small semi-vertex angles.

The dissociation of O<sub>2</sub> and N<sub>2</sub> molecules in the cavity takes a large amount of heat in the form of heat of reaction and the enthalpy of formation of new species. The recombination of the atomic species to give back the molecular

component at the wall, on the other hand, releases a similar quantity of heat energy. The surface heat flux distribution for various conical cavity configurations at Mach 10.1 under chemically reacting aerothermal conditions with fully catalytic walls is shown in Figs. 6.24-6.27. Figures 6.24, 6.25, 6.26 and 6.27 show the surface heat flux values, non-dimensionalized with the peak heat flux for the base model, for models with conical cavities of semi vertex angles  $45^\circ$ ,  $26.6^\circ$ ,  $18.4^\circ$  and  $14^\circ$  respectively. The numbers appearing in the legend of these figures represent the depth of the cavity.

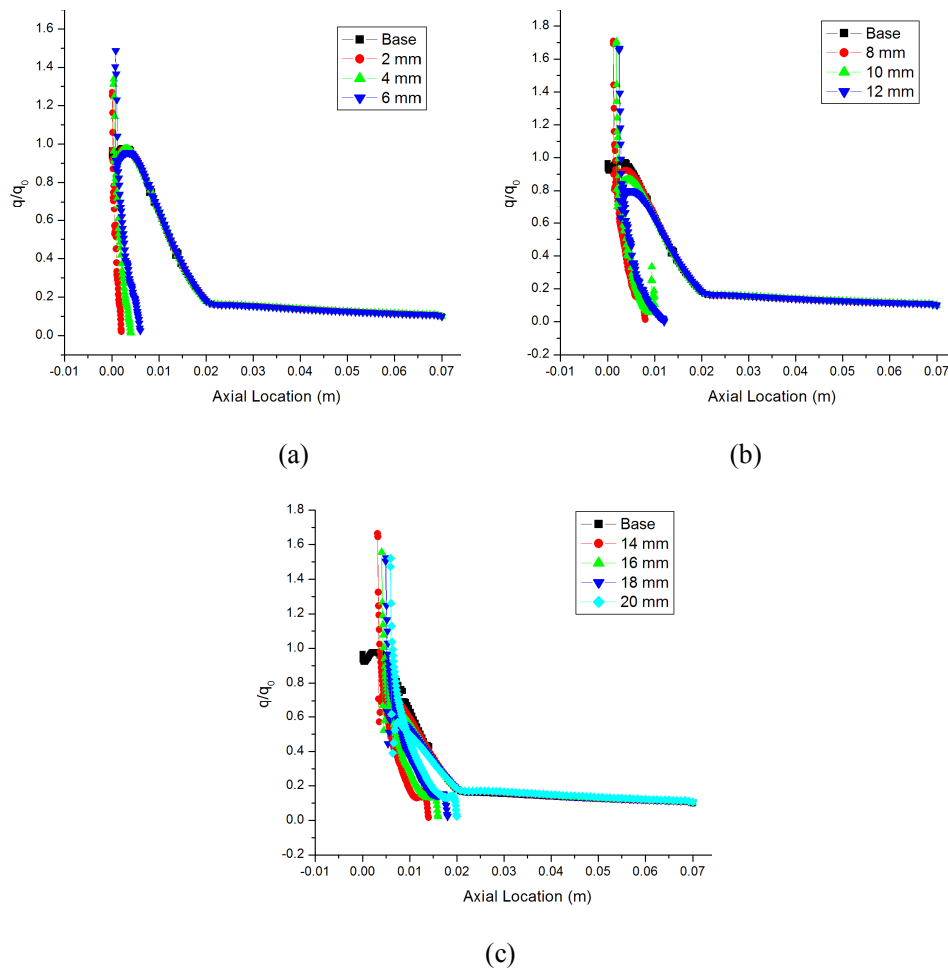


Figure 6.24 Surface heat flux distribution for models with conical cavity of  $\alpha=45^\circ$



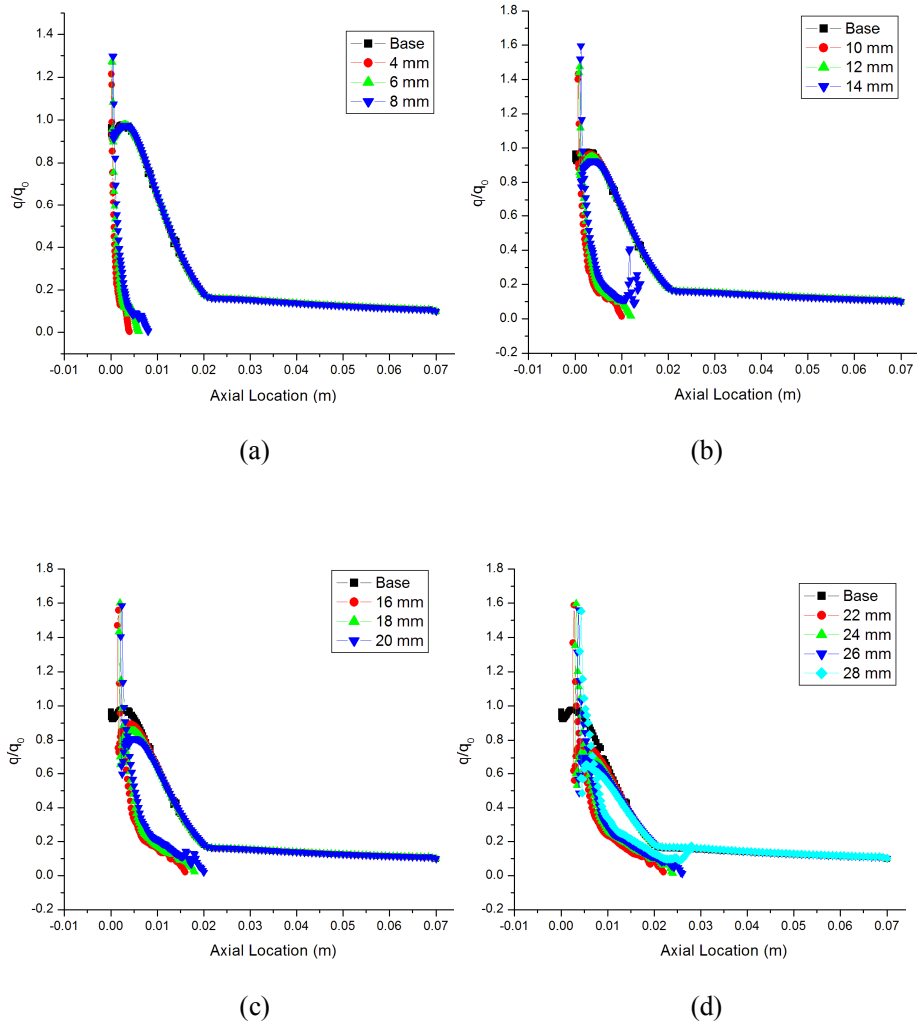


Figure 6.25 Surface heat flux distribution for models with conical cavity of  $\alpha=26.6^\circ$

As can be seen in Figs. 4.24-4.27, the lip radius or the base radius of the conical cavity plays an important role in the peak heating at the sharp lip. For conical cavity configurations with lip radii less than 5 mm the steady state bow shock shape is similar to that of a hemisphere cylinder without any cavity and thus the heating in the vicinity of the sharp lip is not severe with only about 20% rise above the base body peak heat fluxes.

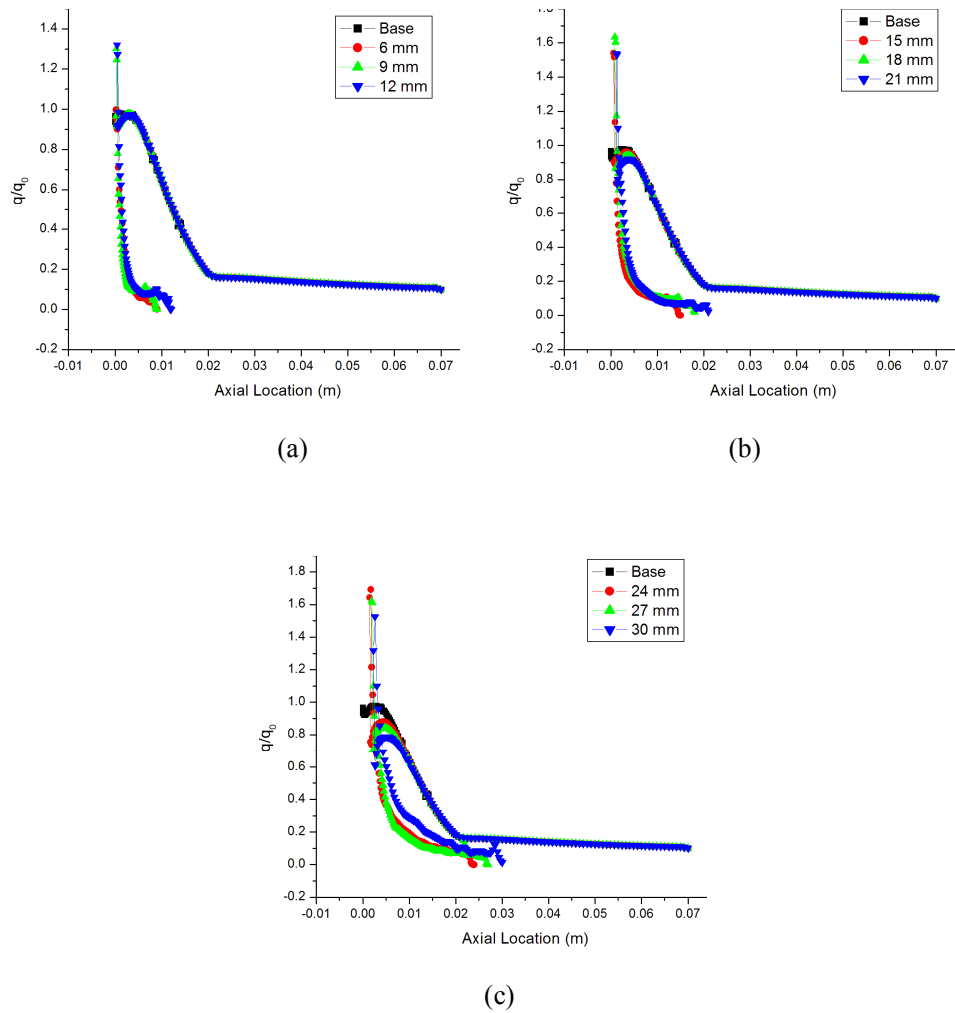


Figure 6.26 Surface heat flux distribution for models with conical cavity of  $\alpha = 18.4^\circ$

For cavities with lip radii more than 5 mm however, the flow first meets the sharp lip thus producing a detrimental rise in the heat flux at the sharp lip. The heat flux at the sharp lip of these large mouth cavities is nearly 40-80% higher than the peak heat flux of the base configuration. As compared to the cavity models of other shape, the stagnation heat flux is very low because of inability of external flow to reach the apex of the cone. The local surface heat fluxes inside the cavity remains at low values for a major portion of the cavity surface before attaining very high values at the lip. The magnitude of heating inside the cavity is observed to increase only slightly by decreasing the cone angle of cavity.

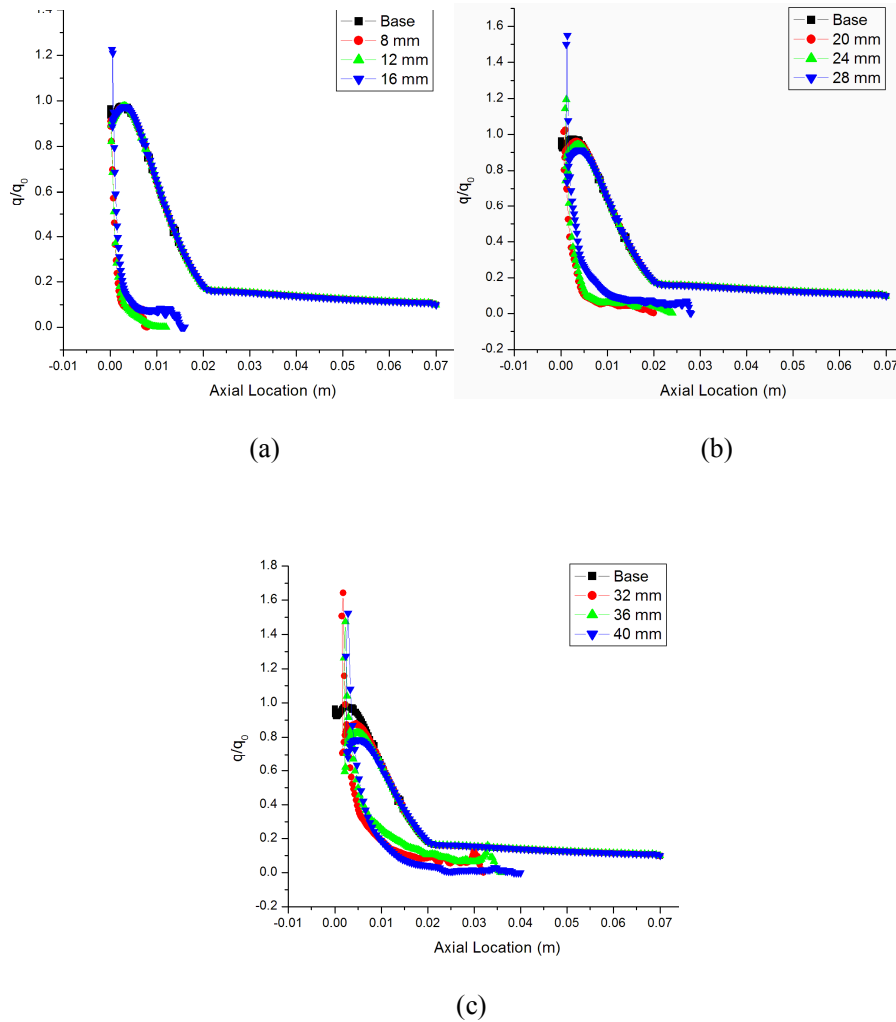


Figure 6.27 Surface heat flux distribution for models with conical cavity of  $\alpha = 14^\circ$

As with the perfect gas computations the surface heat fluxes falls dramatically aft of the sharp lip owing to the expansion on the upper surface. The surface heat flux at the sharp lip on the upper surface falls to values below the peak heating of the base model. The formation of compression wave after the expansion sees an increase in the heat fluxes which reaches another maximum on the convex hemispherical surface. This maximum heating is generally lower than the peak heating of the base model and depends on the semi vertex angle of the cone and the depth of cavity as shown in Fig. 6.28.

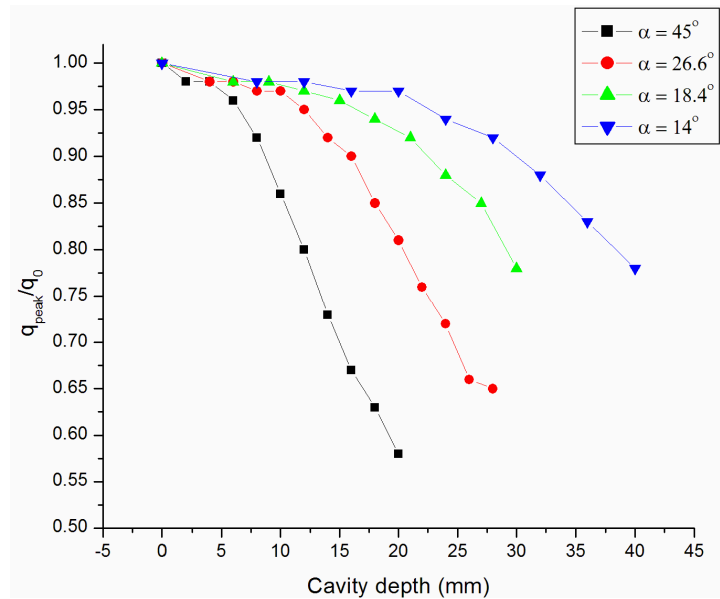
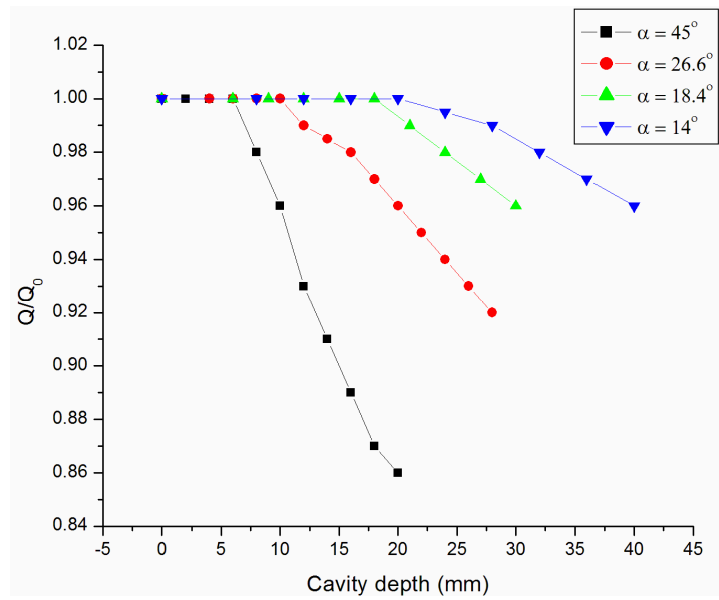


Figure 6.28 Peak local heat flux on the outer surface of conical cavity models

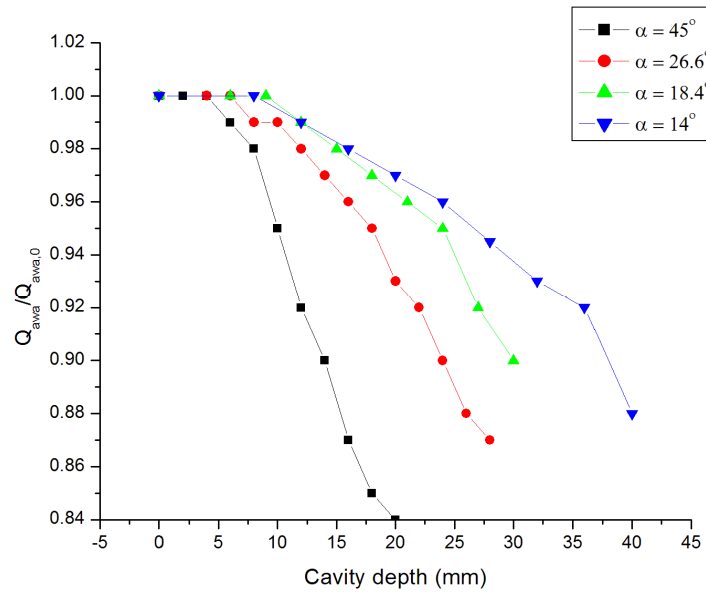
As can be seen in Fig. 6.28, deeper cavities provide a better steady state heat reduction in the outer surface peak heat flux for all lip radii and semi-vertex angles. For the same depth of the cavity, the cavity with larger lip radius or larger semi-vertex angle provides a larger heat reduction in surface peak heat fluxes. Among the conical cavity models investigated, the deepest cavity with a semi vertex angle of  $45^\circ$  provided the highest reduction of 44% in the outer surface peak heat flux.

The reduction in key aerodynamic heating parameters like the Total heat transfer rates and the Area Weighted Average of heat fluxes also provide a measure of the effectiveness of a forward facing conical cavity in the thermal management of aerodynamic heat loads. Figures 6.29 (a) and (b) respectively show the total heat transfer rates and the AWA heat flux for various conical cavity configurations, non-dimensionalized with their respective values for the base configuration. As can be seen in Fig. 6.29 (a) and (b), no reduction is seen in either of these quantities for cavity configurations with small lip radius i.e. below 5 mm. For cavities with larger lip radius, significant reductions both the heat transfer quantities were observed for all semi-vertex angles cavity depths. These reduction in the total heat transfer rates and the AWA heat fluxes in-

increases with increase in the depth of cavity as well as with increase in semi-vertex angle of the cone.



(a)



(b)

Figure 6.29 a) Total heat transfer rates and b) AWA heat fluxes for various conical cavity configurations at Mach 10.1

Among the various conical cavity configurations investigated the deepest cavity with semi vertex angle of  $45^\circ$  produced reductions of 15% and 16% respectively in the total heat transfer rates and the AWA heat fluxes. These reductions are lower than those obtained for conical cavities at Mach 6.2, primarily because of the assumption of a fully catalytic wall for chemically reacting flow at Mach 10.1.

Finally the steady state drag of a hemisphere cylinder seems to be unchanged by the presence of a conical cavity at nose for cavities up to a lip radius of 12 mm as shown in Fig. 6.30. In fact in Fig. 6.30, a very small reduction in drag is seen for very small angle conical cavities due to reversed flow direction inside the cavity which reduces the viscous drag. For conical cavities with very wide mouth opening an increase in drag is also seen.

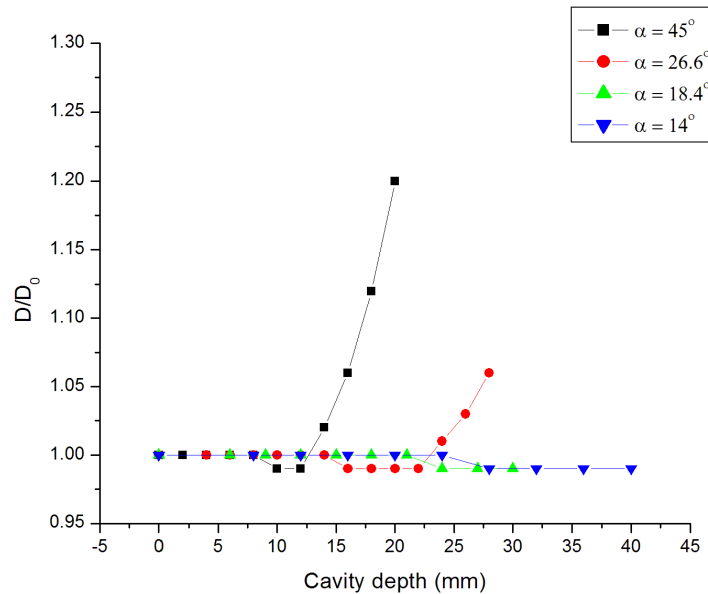


Figure 6.30 Non dimensional drag for various cavity models

#### 6.4 EFFECT OF FORWARD FACING HEMISPHERICAL CAVITY

The steady state flowfield structure inside the hemispherical cavity and the non-dimensional pressure distribution trends over a hemisphere cylinder with a forward facing cavity at Mach 10.1 is found to be similar to that at Mach 6.2.

The absolute pressure and temperature ratio across the bow shock wave is however, much higher for Mach 10.1 as shown in Figs. 6.31 and 6.32. Figure 6.31 and 6.32 show the contours of pressure and temperature for hemisphere cylinder a forward facing hemispherical cavity of radii 2 and 8 mm respectively. As can be seen in Figs. 6.31 and 6.32, besides being more curved towards the body, the bow shock wave at mach 10.1 is much sharper and closer to the body as compared to the bow shock for Mach 6.2.

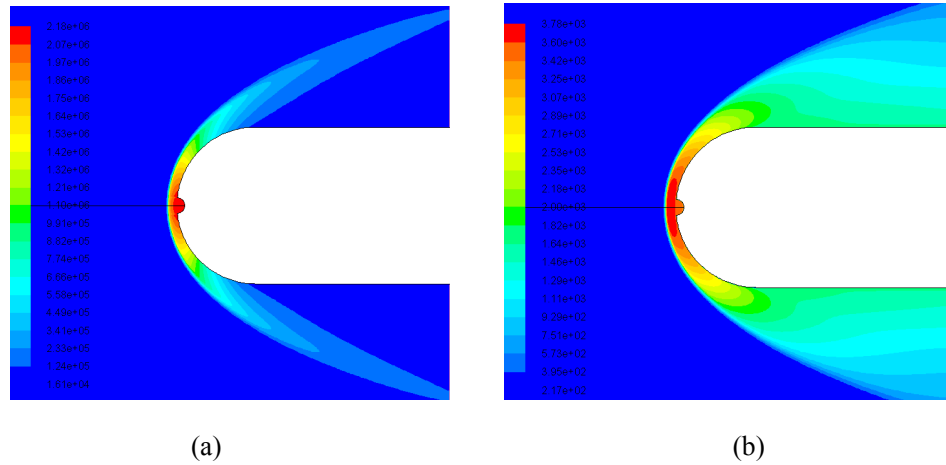


Figure 6.31 Contours of a) pressure and b) temperature for 2 mm spherical cavity model at Mach 10.1

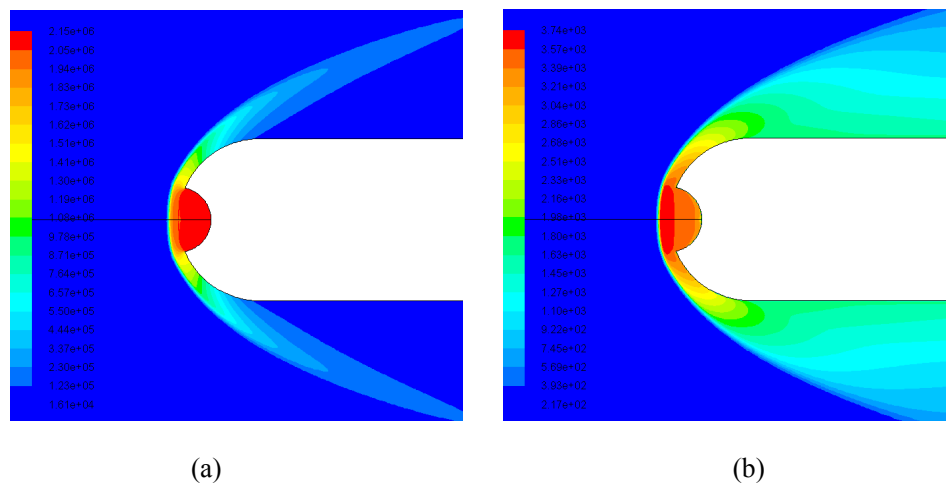


Figure 6.32 Contours of a) pressure and b) temperature for 8 mm spherical cavity model at Mach 10.1

As can be seen from the contours of pressure and temperature, the pressure inside the entire cavity region is at stagnation conditions, however, the temperature inside the cavity decreases along the stagnation streamline towards the surface giving favourable reductions in the stagnation point heating. The post shock temperature in the vicinity of the sharp lips, however, is sufficiently large to bring about the dissociation of  $O_2$  and  $N_2$ . The atomic oxygen and nitrogen combine to form NO which dissociates again in this high temperature zone. The contours of various species present in the flowfield of a hemisphere cylinder with a typical hemispherical cavity, except  $N_2$ , are shown in Fig. 6.33.

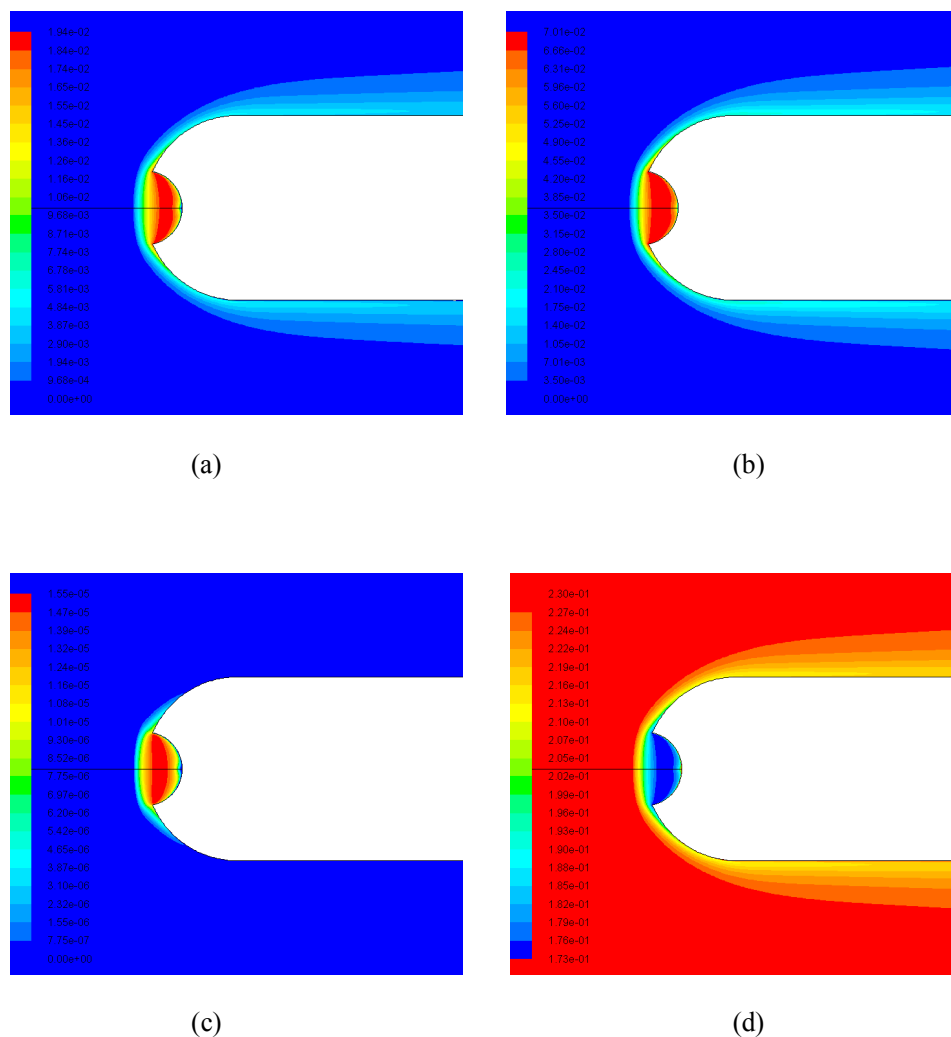


Figure 6.33 Contours of mass fractions of a) O, b) NO, c) N and d)  $O_2$  for a hemispherical cavity model of depth 8 mm



As can be seen in Fig. 6.33, about one-fourth of Oxygen inside the cavity is dissociated along with dissociation of a very small fraction of Nitrogen. The newly born species show their presence almost entirely inside the cavity with only traces outside the shock layer. This is especially true for the N atoms which seen only inside the cavity and in the post shock region. In Fig. 6.3, a small region of high mass fraction of  $O_2$  molecule is seen at the stagnation point due to formation of a very small recirculating fluid zone and the species mass fraction of all species falling to the freestream values due to fully catalytic wall assumption. This trend is seen for all hemispherical cavity configurations as shown in Fig. 6.34 (a) and (b), which shows the variation of mass fractions of NO and  $O_2$  respectively along the stagnation streamline of cavities of radii 2 mm, 8 mm and 16 mm. The extended region of dissociated species for deeper cavity ensures larger reduction total convective heat transfer rates.

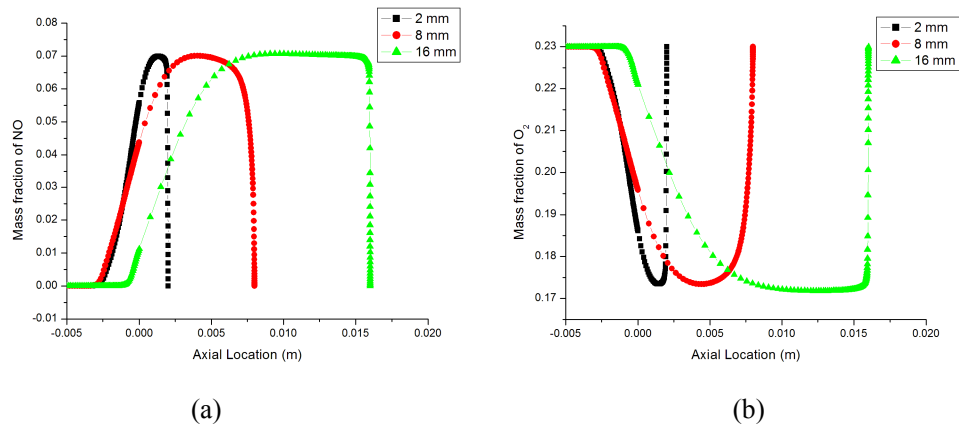
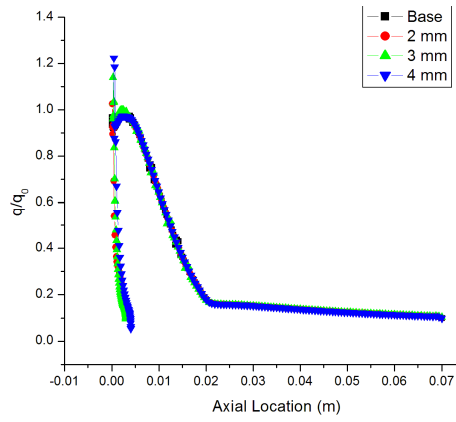


Figure 6.34 Variation of species mass fractions of a) NO and b)  $O_2$  along the stagnation streamline for hemispherical cavity models

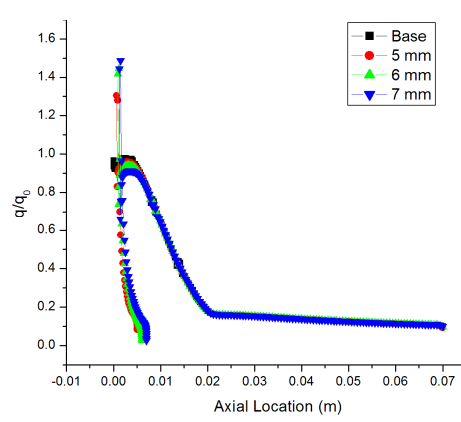
The inclusion of multispecies chemically reacting air model at Mach 10.1 alters the aerodynamic heating of the blunt body significantly. A significant portion of the kinetic energy contained in the air molecules is utilized in dissociation of various molecules with lower increase in the thermal energy. The assumption of fully catalytic wall however, increases the surface heat flux due to the heat of recombination of various atomic species. The variation of local

surface heat flux for various hemispherical cavity configurations at Mach 10.1 is shown in Fig. 6. As can be seen Fig. 6.35, the presence of a hemispherical cavity at the stagnation point reduces the local surface heat flux at all locations except at the sharp lip for cavities of all radii. These reductions in heat fluxes along the outer surface of the projectile are however lower than those observed at Mach 6.2 perfect gas case.

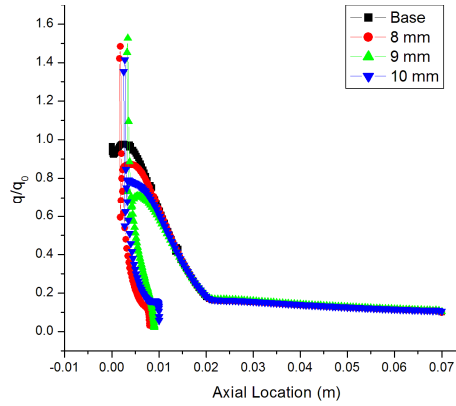
Another difference as compared to Mach 6.2 case can be observed in that the drop in surface heat fluxes aft of the sharp lip is not very high due to formation of relatively small separation bubble aft of the sharp lip. The heat transfer rate at the stagnation point is especially reduced to negligible values by the presence of such cavities for both computations. As can be seen in Fig. 6.35, for a very small cavity radius, the peak heating at the sharp lip is not severe with less than 20 % increase as compared to peak heating of base model. This is because the bow shock shape and external flow structure for these small radii cavity configurations is similar to that for the base model. For hemispherical cavities of moderate depth however, the peak heating rate at the sharp lip is severe with values at approximately 30-60% higher than the peak heating of the base configuration. Some respite in lip heating is seen at very wide mouth cavities due to changes in flow structure inside the cavity.



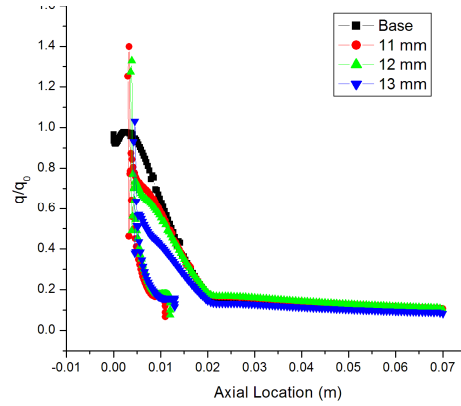
(a)



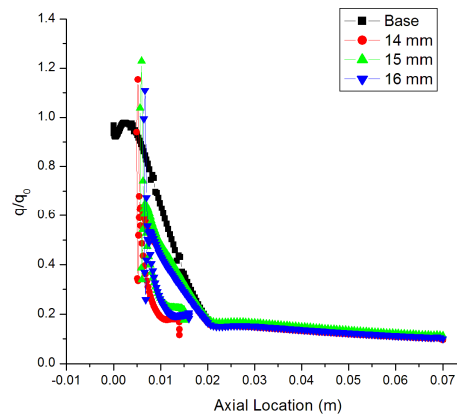
(b)



(c)



(d)



(e)

Figure 6.35 Surface heat flux distribution over a hemisphere cylinder with hemispherical cavity of different radii

The advantage of deploying a forward facing hemispherical cavity at the nose of a blunt body can be expressed as the reduction in peak surface heat flux on the outer surface as shown in Fig. 6.36 wherein the heat flux values are normalized with respect to the peak heating of the base configuration. As can be seen in Fig. 6.36, the peak heat flux occurring on the convex shoulder of a hemisphere is reduced favourably by the presence of hemispherical cavity at nose. These reductions are higher for larger radius of cavity with the hemispherical cavity of radius 18 mm producing a reduction of 52%.

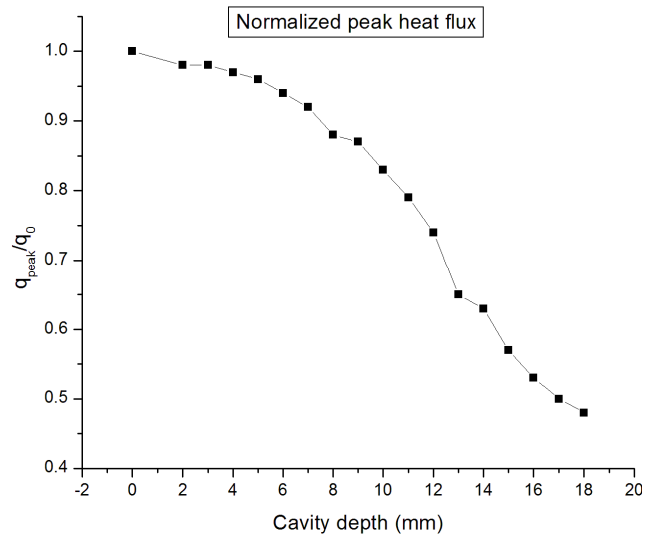
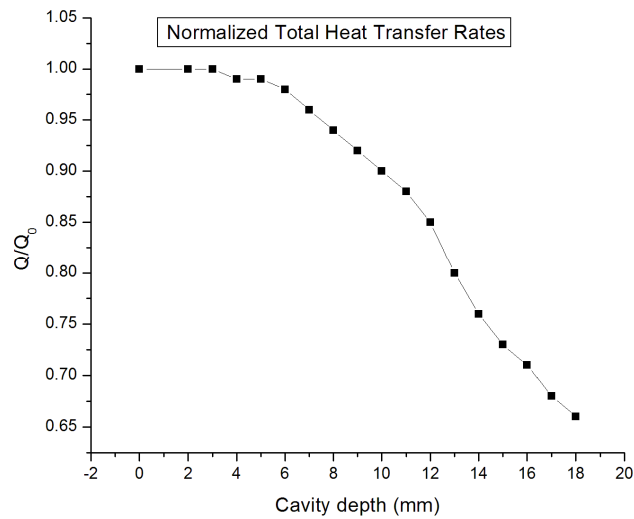


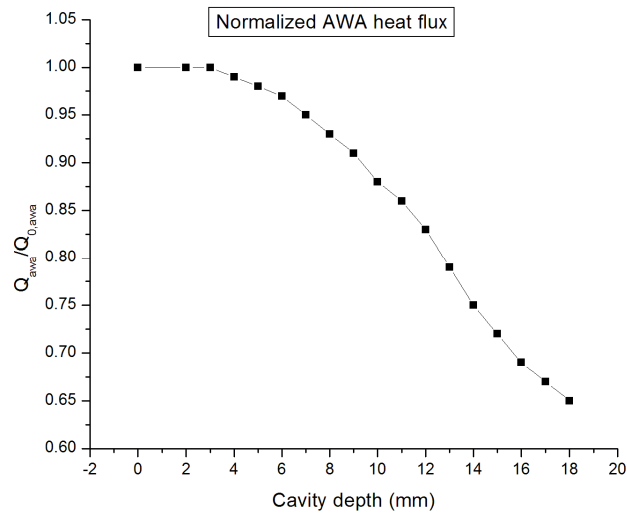
Figure 6.36 Peak surface heat flux on the outer surface of various cavity models

It is often convenient to demonstrate the usefulness of a cavity configuration in reducing aerodynamic heating by observing the reductions obtained in the total heat transfer rates and the AWA heat fluxes. The normalized values of Total convective heat transfer rates and the AWA heat fluxes for various hemispherical cavity configurations are compared respectively in Fig. 6.37 (a) and (b). As can be seen Fig. 6.37, no reductions in either of these quantities is obtained for cavities of radius 5 mm, primarily because of outer surface pressure and heat flux distribution being similar to that of base configuration. The reduction obtained in the stagnation point heat transfer rate for these small

cavities, is neutralized by the increase in local heat flux at the sharp lip and thus no real change in Total heat transfer rate or AWA heat flux is seen. The heat reduction advantage becomes apparent for large radius cavities with larger cavities producing higher reduction in both these quantities because of favourable reductions in heat flux on both concave cavity and convex hemispherical surfaces.



(a)



(b)

Figure 6.37 a) Total heat transfer rates and b) AWA heat flux for various hemispherical cavity configurations

Among the spherical cavity configurations investigated, the deepest or the largest cavity of radius 18 mm produced reductions of 34% and 36% in Total heat transfer rates and AWA heat fluxes respectively.

Lastly, the drag of a hemisphere cylinder seems to be unaffected by the presence of small to moderate depth hemispherical cavity at nose as shown in Fig. 6.38, which shows the drag for various hemispherical cavity configuration, normalized with the drag of the base model. Even, a very small reduction in drag could be observed for cavities of radii 6 to 10 mm, primarily because of increase in component of shear stress in the forward direction inside the cavity. For large hemispherical cavities with radii more than 12 mm, a significant increase in drag can be seen in Fig. 6.38. This is a direct consequence of large expansion on the on the upper surface and large frontal stagnation area for these cavity configurations. For the deepest hemispherical cavity investigated, an increase of 45% in drag is observed.

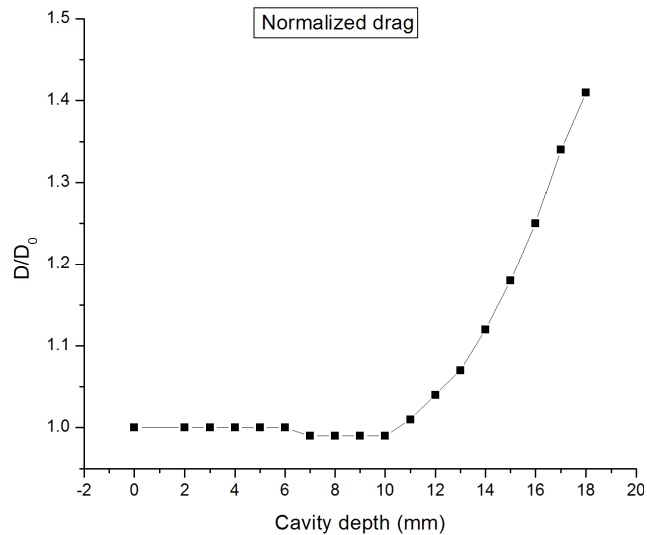


Figure 6.38 Normalized drag for various hemispherical cavity models

## 6.5 EFFECT OF DOUBLE DISK AEROSPIKE

At Mach 10.1, the shock wave gets closer to the body of a hemisphere cylinder with a double disk aerospike, especially at the shoulders. The struc-

ture of the steady state flowfield otherwise, matches closely with the flowfield structure at mach 6.2 as shown in Fig. 6.39 (a) - (b). Fig. 6.39 (a) and (b) respectively shows the contours of Mach number and temperature for a typical double disk aerospike configuration with  $l/D = 1.5$ , at Mach 10.1. As can be seen in Fig. 6.39, a large region of dead air is formed between the second aerodisk and the main body with relatively cool air recirculating at low velocities. Because of the small radius of the front aerodisk, however the bow shock wave is highly curved and a region of very high temperature can be seen at the front aerodisk.

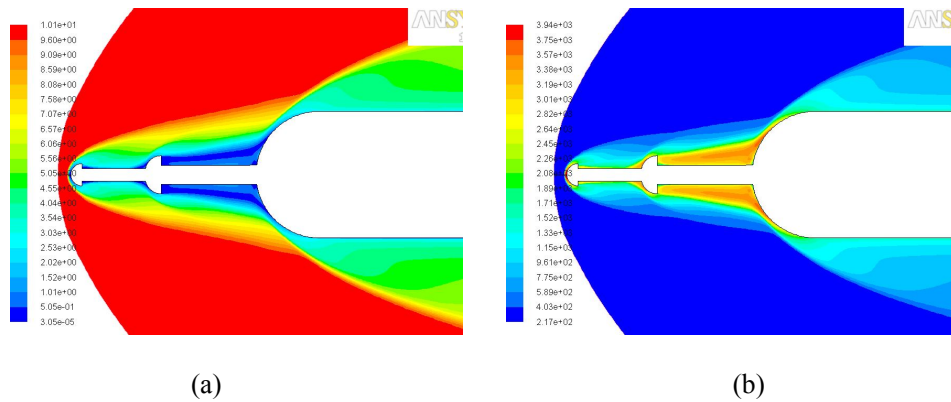


Figure 6.39 Contours of a) Mach number and b) Temperature for a double disk aerospike at Mach 10.1

The steady state flowfield shows the presence of a single primary vortex between the rear aerodisk and the main body with two secondary vortices. The shape, size and location of these vortices, formed at the junctions of the rear aerospike stem with the rear aerodisk and the main body, depend highly on the size and location of the rear aerodisk. For the longer aerospikes investigated, both the two secondary vortices are small in size with the primary vortex containing most fluid in the dead region. For decreasing radius of the rear aerodisk the secondary vortices in long aerospikes diminish in further in size. The dead air region for longer aerospikes is thus thinner and the flow from the rear aerodisk impinges smoothly on the shoulder of the main body without being deflected as shown in Fig. 6.40 (a). For aerodisk configurations with small

distance between the rear disk and the main body, the secondary vortex in the wake of the aerodisk grows in sizes and pushes in the primary vortex towards the main body. The primary vortex is no longer stretched longitudinally, but more circular in shape and bulged out. Due this bulging of the primary vortex the external flow from the rear aerodisk is deflected upwards on the main body shoulder as shown in Fig. 6.40(b). Fig. 6.40 (a) and (b) show the diving streamline for respectively a long and a short aerospike.

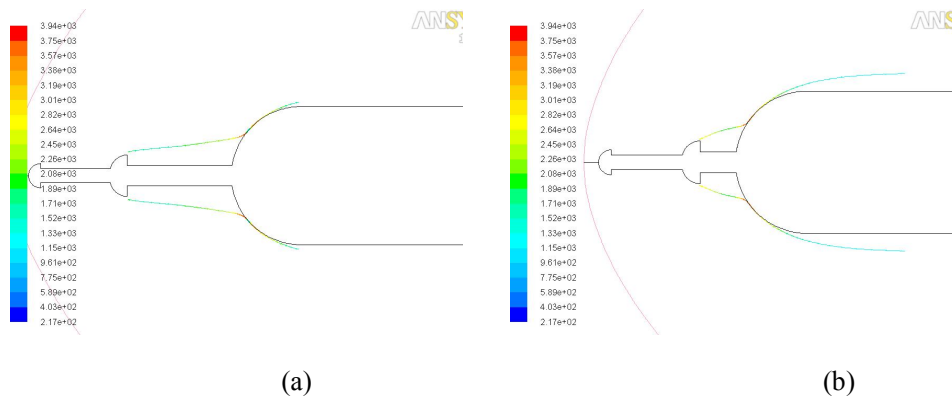


Figure 6.40 Diving streamlines for aerodisk with a)  $l/D = 1.5$  and b)  $l/D = 1$

Besides the system vortices between the rear aerodisk and the main body two small regions of recirculating fluid can also be seen between the front aerodisk and rear aerodisk. These recirculating fluid regions are located at the junctions of spike stem with the rear aerodisk and front aerodisk. The pressure and temperature in these recirculating fluid regions are highly reduced while the flow deflected from the aerodisks external to them impinge on the shoulder to give large pressure rise at the reattachment point. The variation of surface pressure for various aerodisk configurations investigated is shown in Figs. 6.41 and 6.42. Figs. 6.41 and 6.41 show the normalized pressure distribution for aerodisk aerospikes with radius of rear aerodisk 6 mm and 4 mm respectively for various  $l/D$  ratios.



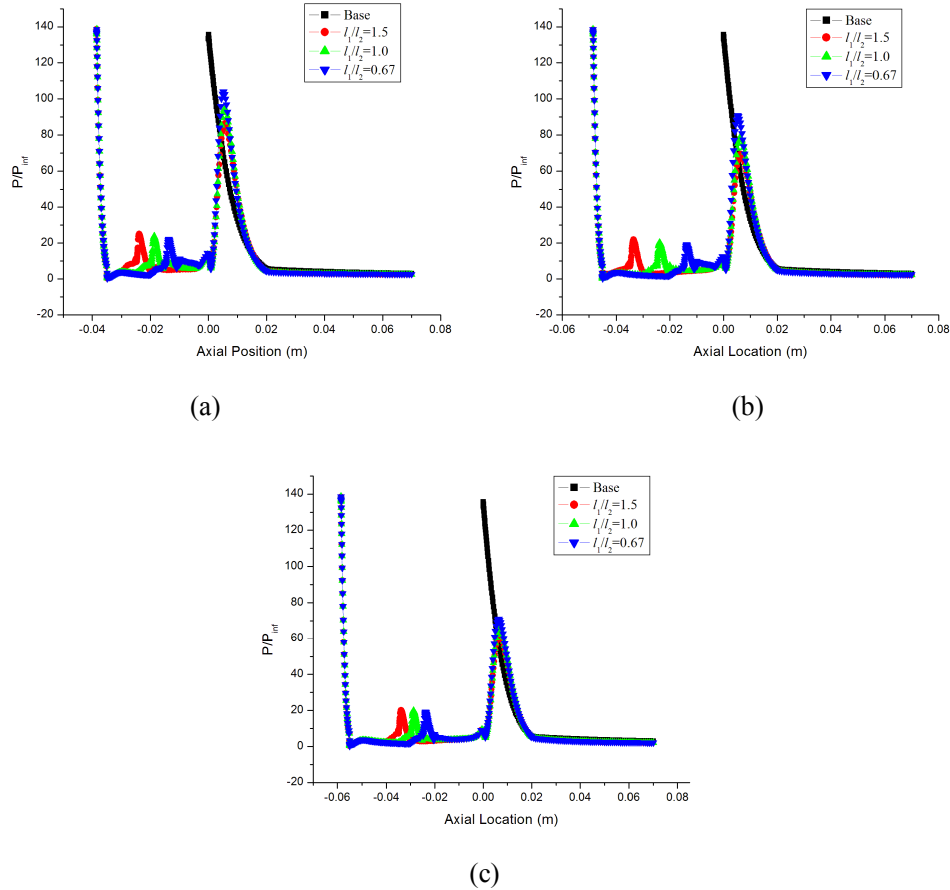


Figure 6.41 Surface pressure distribution for aerodisk configuration with  $r_f = 6$  mm and a)  $l/D = 1.0$ , b)  $l/D = 1.25$  and c)  $l/D = 1.5$

As can be seen in Fig 6.41, the surface pressure distribution over an aerodisk configuration with radius of rear disk equals to 6mm and radius of front disk equal to 3.5 mm is similar to that at Mach 6.2. The stagnation pressure at the front aerodisk falls rapidly along the convex aerodisk surface and following a major expansion attains very low values in the wake of the front aerodisk. The surface pressure remains constant along the stem of the front aerospike before rising to appreciable value on the shoulders of the rear aerodisk. The surface pressures fall once again in the dead air region between the rear aerodisk and the main body. The pressure rises along the convex surface of the main body thereafter reaching a maximum at the reattachment point where the flow detached from the aerodisks impinge.

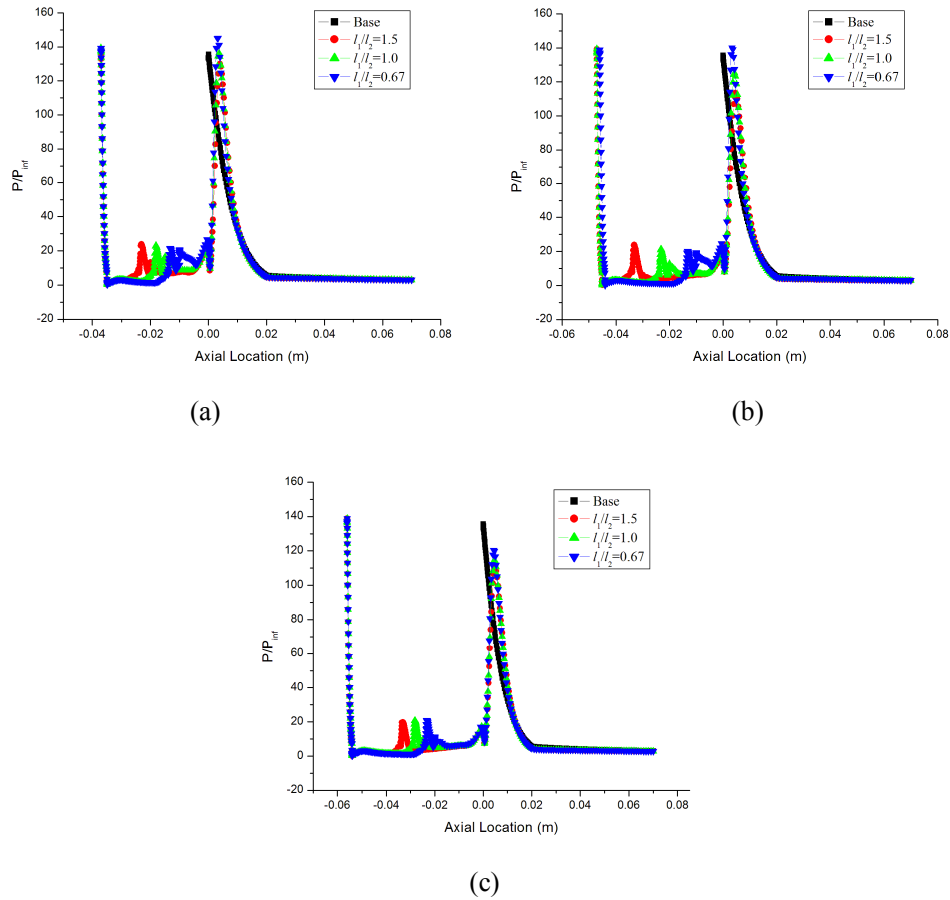


Figure 6.42 Surface pressure distribution for aerodisk configuration with  $r_1 = 5$  mm and a)  $l/D = 1.0$ , b)  $l/D = 1.25$  and c)  $l/D = 1.5$  at Mach 10.1

The pressure rise at the reattachment point is however, the substantially lower than the stagnation pressure of the base model. The surface pressure distribution for aerodisk configuration with radius of rear aerodisk equal to 4 mm and radius of second aerodisk equal to 2 mm at Mach 10.1 is somewhat different from that at Mach 6.2, as can be seen in Fig. 6.42. The pressure rise at the reattachment point for these small radius aerodisk configurations is severe with reattachment pressure close to the stagnation pressure. Only a slight reduction in reattachment pressure is seen for longer aerospikes with  $l/D = 1.5$ .

The large pressure rise at the reattachment point causes a severe local heating of the main body, even for longer aerospike as shown in Figs. 6.43 and

6.44, which respectively show the surface heat flux distribution for aerodisk configuration with  $r_1=6\text{mm}$  and  $4\text{mm}$ . The small radius of the front aerodisk causes a severe stagnation point heat flux resulting dissociation of molecular oxygen as well as nitrogen. The surface heat flux distribution follows the pressure distribution trends along the length of spike to remain at low values except at the shoulder of the rear aerodisk.

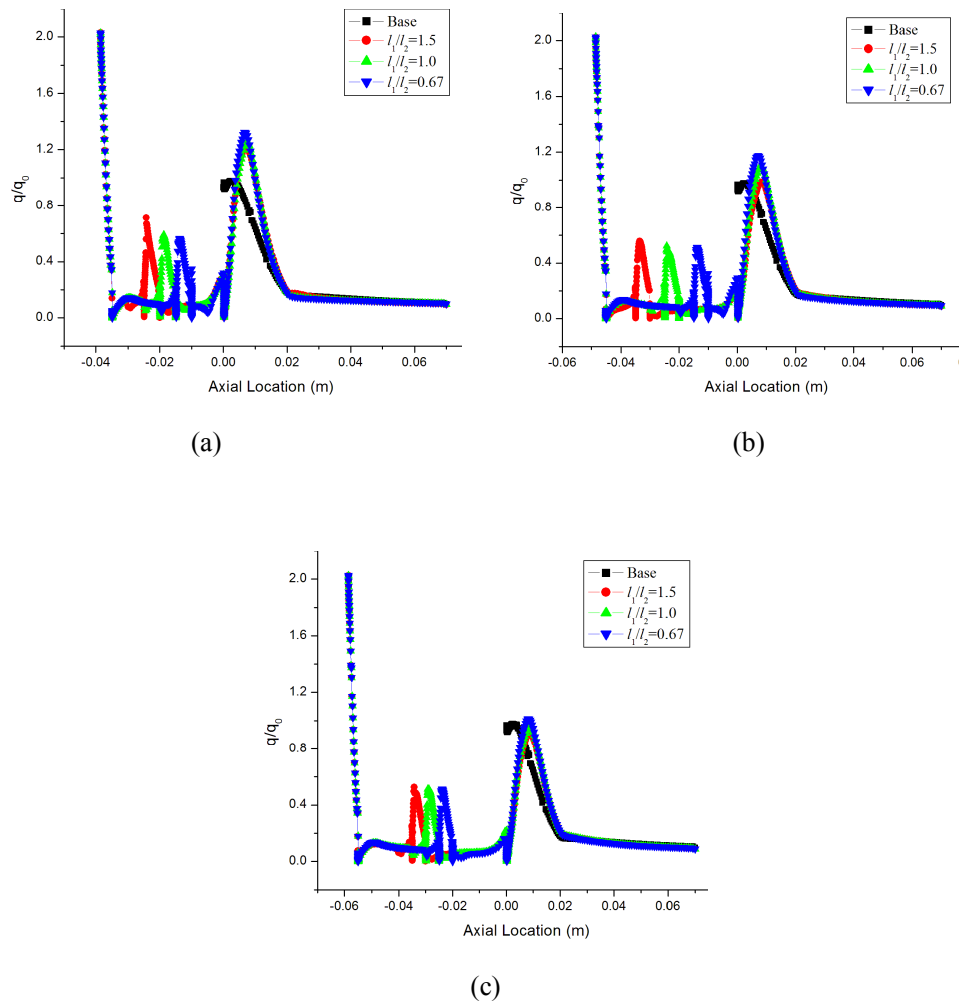
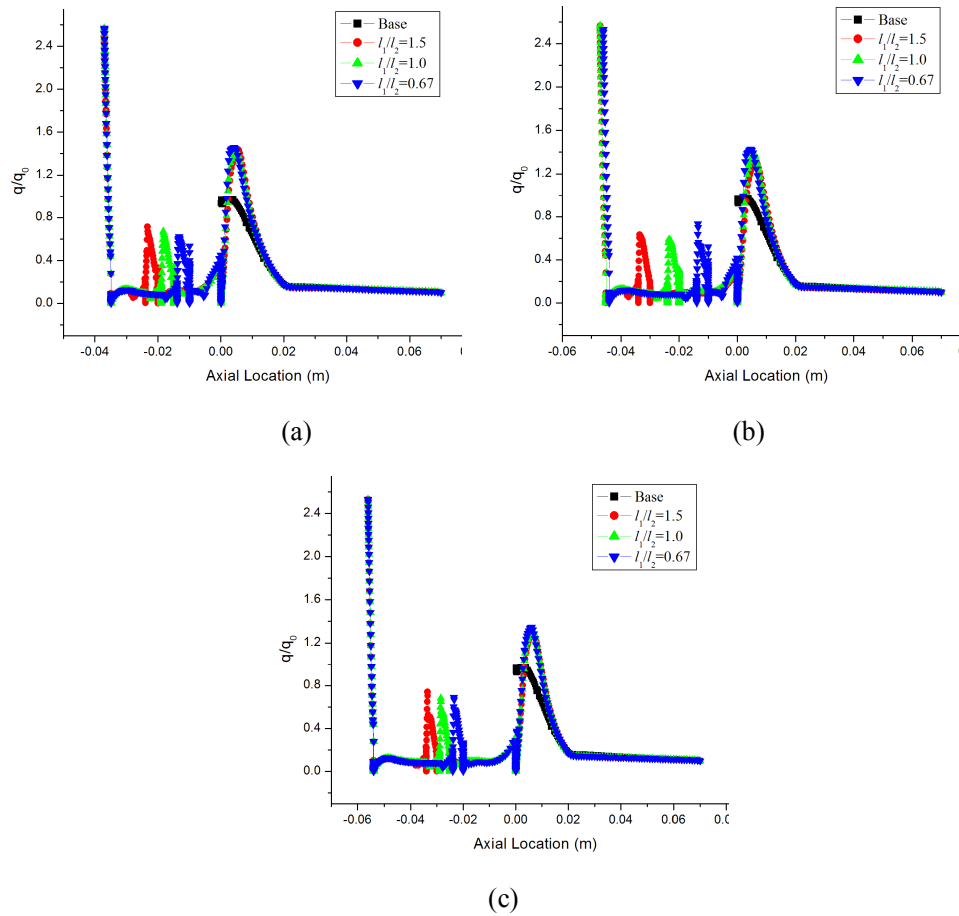


Figure 6.43 Surface heat flux distribution for aerodisk configuration with  $r_1=6\text{mm}$ ,  $r_2=3.5\text{mm}$  and a)  $L/D=1$ , b)  $L/D=1.25$  and c)  $L/D=1.5$



**Figure 6.1** Surface heat flux distribution for aerodisk configuration with  $r_1=4$  mm,  $r_2=2$  mm and a)  $l/D=1$ , b)  $l/D=1.25$  and c)  $l/D=1.5$

After very low values near the main body stagnation region, the local surface heat flux rises sharply to peak values, which for almost all cases investigated is more than the peak heating of the base configuration. This severe heating at Mach 10.1 is primarily because of two reasons, firstly due to small wave angle at this mach number the flow deflected from both the aerodisks impinges directly onto the reattachment point on the main body and secondly due to the assumption of fully catalytic wall, the heat of recombination at the walls increases the surface heat fluxes substantially. As can be seen from Figs. 6.43 and 6.44, reattachment heat flux for various aerospike configurations is 20 to 60 percent higher than the stagnation point heating of the base configuration. The only exception observed is the case aerospike configuration with  $r_1=6$

mm,  $r_2=3.5$  mm and  $l/D=1.5$ , where in the reattachment heat flux is marginally lower than the peak heating of the base model.

As can also be observed Fig 6.44, the reattachment heating worsens for smaller radii of aerodisks. The aerospike configurations of  $r_1=5$  mm and  $r_2=2.5$  mm show heating results intermediate to those shown in Figs. 6.43 and 6.44 and hence not presented here. Besides good heat reduction capabilities, a double disk aerospike configuration with large radii caps also show better drag reduction capabilities as compared to double disk aerospike configuration with smaller radii caps. The reductions in AWA heat fluxes and drag obtained by mounting a double disk aerospike in a chemically reacting flow at Mach 10.1 is presented in Table 6A. Table 6A shows results only for the configurations with  $r_1=6$ mm and  $r_2=3.5$  mm, as other configurations shows large increase in peak heat fluxes with only small reductions in drag. The negative sign in Table 6A indicate an increase in respective quantity.

Table 6 A: Reductions in Heat flux and Drag for Aerospike Configurations at Mach 10.1

Cases	$l/D$	$l_1/l_2$	% Reduction in AWA of heat flux	% Reduction in peak heat flux	% Reduction in drag
1	1.0	1.5	-0.03	-0.21	0.27
2	1.0	1.0	-0.02	-0.26	0.24
3	1.0	0.67	-0.04	-0.33	0.20
4	1.25	1.5	0.04	-0.10	0.34
5	1.25	1.0	0.08	0.01	0.39
6	1.25	0.67	0.00	-0.18	0.26
7	1.5	1.5	0.11	0.09	0.44
8	1.5	1.0	0.09	0.04	0.42
9	1.5	0.67	0.07	-0.02	0.39

As with the Mach 6.2 flow, case 7 with  $l/D=1.5$ ,  $r_1=6$  mm,  $r_2=3.5$  mm and  $l_1/l_2=1.5$  s observed to be the optimal configuration with 11% and 9% reductions in AWA heat fluxes and peak heat fluxes respectively with 44% reduction in aerodynamic drag.

## 7 CONCLUSION AND FUTURE WORK

The effectiveness of various nose mounted passive devices like cavities of elliptic, parabolic, spherical and conical shapes and aerospike with two hemispherical aerodisks in reducing the total heat transfer rates and AWA heat fluxes to a hemisphere cylinder is investigated computationally using the research edition of a commercially available Navier-Stokes solver. Besides above two quantities, the effect of these devices on the local surface heat flux and pressure distribution and aerodynamic drag have also been analysed. All the above computations have been performed at zero degree angle of attack for two sets of freestream conditions using axisymmetric assumption to minimize computational expenses. The first set of computations have been done at standard sea level atmosphere with freestream Mach number of 6.2 while the second set of computations have done at standard atmosphere at 13.3 km altitude and a freestream mach number of 10.1. The numerical experiments at Mach 6.2 has been done assuming a thermally perfect gas air model while the computation at Mach 10.1 is done assuming air to be a chemically reacting mixture of five species viz. NO, NO, O, O<sub>2</sub> and N<sub>2</sub> in thermal equilibrium using Park's chemistry model with fully catalytic wall. To simulate worst case heating scenario and to minimize the error associated with laminar to turbulent transition, a fully turbulent flow has been modelled using SA turbulence model.

### 7.1 CONCLUSION

The major findings on the effect of forward facing cavity at Mach 6.2 are as summarized below:

- The use of forward facing cavity reduces the stagnation point heating by more than 80% for all shapes and sizes of cavity.
- For all cavity configurations, the peak local heating occurs on the inner surface of the cavity at the sharp lip. The local heat flux at the infinite-

ly sharp lip for most of the cases is higher than the peak heating of the base configuration.

- The maximum lip heating at Mach 6.2 is seen for deep ellipsoid cavities wherein the local heating is up to 80% higher than the peak heating of the base.
- The spherical and parabolic cavity showed the minimum heating at the sharp lip with peak heating at sharp lip 30-40% lower than the peak heating of base model.
- The peak heating on the outer convex surface which occurs aft of the reattachment shock, decreases with increasing depth of cavity and the lip radius of cavity. For the same depth of cavity, the configuration with larger lip radius shows lesser peak heating on the outer surface.
- With the deepest and widest ellipsoid cavity, a maximum reduction of 64% in outer surface peak heating was observed at Mach 6.2. For Mach 10.1, however, the hemispherical cavities show best outer surface heat flux reduction of a maximum 55%.
- Total heat transfer rates and the AWA heat fluxes to the hemisphere cylinder decreases with increasing depth of the cavities as well as with increasing lip radius.
- The deepest hemispherical, parabolic, ellipsoid and conical cavities investigated showed reductions of 32%, 26%, 26% and 23% respectively in total convective heat transfer rates at Mach 6.2.
- The deepest hemispherical, parabolic, ellipsoid and conical cavities investigated showed reductions of 33%, 25%, 30% and 24% respectively AWA heat fluxes at Mach 6.2.
- For the same depth, the parabolic cavities produce the maximum reduction in total heat transfer rates and AWA heat flux as well while the conical cavities showed the least reductions.
- The drag of a hemisphere cylinder is negligibly affected by the presence of a forward facing cavity. In fact for some moderate depth

cavities, the drag is reduced by 2-4% owing to the direction of the viscous traction inside the cavity.

- The drag of the projectile increases for lip radius of more than 12 mm and drags of as much as 50% higher than the base configuration can be seen for very wide cavities.

The major findings on the effect of forward facing cavity at Mach 10.1 are as summarized below:

- The effectiveness of forward facing cavities in reducing aerodynamic heating is reduced at Mach 10.1 with the assumption of fully catalytic wall.
- At Mach 10.1, about 24% of oxygen and 4% of nitrogen in the stagnation region is dissociated. Most of this dissociation occurs at the mouth of the cavity in the vicinity of sharp lip.
- The local heating at the sharp lip worsens at Mach 10.1, with deep ellipsoid showing peak heating of as high as 2.7 times the peak heating of base configuration.
- The least heating at the sharp lip is seen for wide parabolic cavity with a worst heating of only 1.5 times the base configuration peak heating.
- A favourable reduction in peak heating on the outer convex surface is seen for all cavity configurations with parabolic, hemispherical, conical and ellipsoid cavities showing reductions of as high as 47%, 52%, 42% and 44% respectively.
- The total heat transfer rates at Mach 10.1 can be reduced by up to 44%, 19%, 14% and 17% for hemispherical, parabolic, conical and ellipsoid cavity respectively.
- The AWA heat fluxes were reduced by up to 35%, 18%, 16% and 22% for hemispherical, parabolic, conical and ellipsoid cavity respectively.
- The trends for drag are same as with Mach 6.2 flow with drag equal to the drag of the base configurations for all cavity shape and depths for



lip radius up to 6 mm. The drag for cavity configurations of all shapes reduces slightly for lip radii of 7 to 12 mm and increases thereafter significantly for lip radii larger than 12 mm.

And finally, the major findings on the effect of double disk aerospike are as summarized below:

- The peak reattachment pressure on the main body is reduced to 50 % of the base body stagnation pressure by the use of double disk aerospikes with overall length to diameter ratio of 1.5.
- For shorter spikes with length to diameter ratio of 1, the peak reattachment pressure is only marginally smaller than the stagnation pressure of the base body.
- At Mach 6.2, the reattachment heat flux on the main body is larger than the peak heating of the base configurations for radius of rear cap less than 6 mm irrespective of the length of aerospike.
- For the double disk aerospike configuration with radius of rear cap 6 mm, the peak reattachment heat flux and the total heat transfer rates are reduced by 22% and 15 % respectively for  $l/D$  ratio of 1.5.
- At Mach 10.1, the effectiveness of double disk aerospike in reducing reattachment heat flux is significantly reduced with even the best aerospike configuration of  $l/D=1.5$  and radius of rear cap 6 mm providing only 11% and 9% reductions in AWA heat fluxes and peak heat fluxes respectively.
- For shorter aerospikes at Mach 10.1, increase in all the aerodynamics heating parameters is seen.
- Favourable drag reductions are observed for all aerodisk aerospike configurations with longer aerospikes providing as high as 47% and 44% reductions in drag at Mach 6.2 and 10.1 respectively.
- Among the double disk aerospike configurations investigated the one with  $l/D=1.5$ ,  $r_1=6$  mm,  $r_2=3.5$  mm and  $l_1/l_2=1.5$  is observed to be the

optimal configuration with 9% and 44% reductions in peak heat fluxes and drag respectively at Mach 10.1 and respective reductions of 22% and 47% at Mach 6.2

Based on the above observations, the author would like to suggest the use of shallow parabolic cavities as a passive heat reduction mechanism as they provide substantial reduction in all aerodynamic heating parameters without increasing the drag of the vehicle as well as retaining the volumetric efficiency of the nose cone to carry payloads. Even the transient simulations suggest the bow shock oscillation for the parabolic cavities has smaller amplitude as compared to other cavity shapes. For hypersonic projectiles designed to have a small drag, sufficiently long double disk aerospike should be deployed at the nose as they reduce the reattachment heat flux even under turbulent flow conditions with suitable reductions in drag as well. Any practical implementation of the above nose configurations would however, require a detailed static and dynamic stability analysis of the complete vehicle at all flight angles.

## **7.2 FUTURE WORK**

Based on the amount of computational work accomplished and numerical modeling assumptions made in this investigation, the following areas require a further investigation:

- The effectiveness of forward facing cavities and aerospike in reducing heat at various angles of attack other than zero needs to be investigated. This would require a full three dimensional modeling of the problem.
- The effect of rounding the cavity lips on the effectiveness of various forward facing cavities in reducing aerodynamic heating needs to be investigated.
- Since only double disk aerospike with hemispherical disks were investigated, the effect of multiple disk aerospike with disks of different shapes like flat plate, sphere, cone etc., demands a separate investigation.

- Since the stagnation point during an actual flight keeps on changing, the effect of non-axisymmetric cavities and aerospikes on aerodynamic heating would prove to be crucial.
- A thorough experimental investigation requires to be done in order to validate the findings of the current investigation.
- The static and dynamic stability analysis of the full length vehicle with fins needs to be carried out before any practical implementation of above configurations is realized

## REFERENCES

- [1] Anderson, J. D. (2005). *Introduction to Flight*. New York: McGraw Hill Inc.
- [2] Anderson, J. D. (1989). *Hypersonic and High Temperature Gas Dynamics*. New York: McGraw Hill Inc.
- [3] Anderson, J. D. (2005). *Fundamentals of Aerodynamics* (Fifth Edition ed.). McGraw Hill Inc.
- [4] Moss, J. N., & Bird, G. A. (1984). Direct simulation of transitional flow for hypersonic re-entry conditions. AIAA Paper 1984-0223.
- [5] Lees, L. (2003). Hypersonic Flow . *Journal of Spacecrafts and Rockets* , 40 (5), 700-735.
- [6] Lees, L. (1956). Laminar Heat Transfer Over Blunt-Nosed Bodies at Hypersonic Speeds. *Jet Propulsion* , 26 (4), 259-269.
- [7] Fay, J. A., & Riddell, F. R. (1958). Theory of Stagnation point heat transfer in dissociated air. *Journal of the Aeronautical Sciences* , 25 (2), 73-85.
- [8] Allen, H. J., & Eggers, A. J. (1953). *A Study of the Motion and Aerodynamic Heating of Ballistic Missiles Entering the Earth's Atmosphere At High Supersonic Speeds*. NACA TR-1381.
- [9] Ladoon, D. W., Schneider, S. P., & Schmisser, J. D. (1998). Physics of Resonance in a Supersonic Forward-Facing Cavity. *Journal of Spacecraft and Rockets* , 35 (5), 626-632.
- [10] Engblom, W. A., Yuceil, B., Goldstein, D. B., & Dolling, D. S. (1996). Experimental and Numerical Study of Hypersonic Forward-Facing Cavity Flow. *Journal and Spacecrafts and Rockets* , 33 (3), 353-359.
- [11] Engblom, W. A., Goldstein, B., Ladoon, D., & Schneider, S. P. (1997). Fluid Dynamics of Hypersonic Forward-Facing Cavity Flow. *Journal of Spacecrafts and rockets* , 34 (4), 437-444.

- [12] Huebner, L. D., & Utreja, L. R. (1993). Mach 10 Bow-Shock Behavior of a Forward-Facing Nose Cavity . *Journal of Spacecraft and Rocket* , 30 (3), 291-297.
- [13] Huebner, L. D., Mitchel, A. M., & Boudreax, E. L. (1995). Experimental Results on the Feasibility of An Aerospike For Hypersonic Missiles. AIAA 95-0737.
- [14] Bogdonohoff, S. M., & Vas, I. E. (1959). Preliminary investigations of spiked bodies at hypersonic speeds. *Journal of the Aerospace Sciences* , 26 (2), 65–74.
- [15] Panaras, A. G., & Drikasis, D. (2009). High-speed unsteady flows around spiked blunt bodies. *Journal of Fluid Mechanics* , 632, 69-96.
- [16] Heppenheimer, T. A. (2007). *Facing the Heat Barrier: A History of Hypersonics*. NASA SP-2007-4232.
- [17] Crawford, D. H., & McCauley, W. D. (1956). *Investigation of the laminar aerodynamic heat transfer characteristics of a hemisphere-cylinder in the Langley 11" Hypersonic Tunnel at Mach number of 6.8*. NACA-TN-1323.
- [18] Stine. H. A., & Wanlass, K. (1954). *Theoretical and Experimental Investigation of Aerodynamic heating and isothermal heat transfer parameters on a hemispherical nose with laminar boundary layer at supersonic Mach numbers*. NACA- TN-3344.
- [19] Diaconis, N. S., Wisniewski, R. J., & Jack, J. R. (1957). *Heat Transfer and Boundary Layer Transition on Two Blunt Bodies at Mach number 3.1*. NASA Technical Note 4099.
- [20] Stoney, W. E., Jr. (1958). *Aerodynamic Heating of Blunt Nose shapes at Mach numbers up to 14*. NACA RM-L58E05a.
- [21] Reller, J. O. (1960). *Heat Transfer To Blunt Axially Symmetric Bodies* . NASA TM-X-391.
- [22] Sinclair, M., Walter, S., & Warren, R. (1961). *Hypervelocity Stagnation Point Heat Transfer*. NASA -R61SD185.
- [23] Griffith, J., & Lewis, C. H. (1963). *A Study of Laminar Heat Transfer to Spherically Blunted Cones and Hemisphere-Cylinders at Hypersonic Conditions*. AEDC-TDR-63-102.

- [24] Bushnell, D. M., Jones, R. A., & Huffman, J. A. (1968). *Heat transfer and Pressure distribution on a spherically blunted 25° half-angle cone at Mach 8 and angles of attack up to 90°*. NASA TN D-4792.
- [25] Marvin, J. G., & Akin, C. M. (1965). *Pressure and Convective Heat transfer Measurement in a Shock Tunnel Using Several test gases*. NASA TN-D-3017.
- [26] Baker, R. L., & Kramer, R. F. (1982). *Reentry Vehicle Nose tip Design for Minimum Total Heat Transfer*. SD-TR-82-25.
- [27] Andrushchenko, V. A., Syzranova, N. G., & Shevelev, Y. D. (2007). An estimate of the heat fluxes to the surface of blunt bodies moving at hypersonic velocity in the atmosphere. *Journal of Applied Mathematics and Mechanics*, 71 (5), 747–754.
- [28] Sravanan, S., Jagdeesh, G., & Reddy, K. P. J. (2009). Convective heat-transfer rate distributions over a missile shaped body flying at hypersonic speeds. *Experimental Thermal and Fluid Science*, 33, 782–790.
- [29] Cooper, M., Beckwith, I. E., Jones, J. J., & Gallagher, J. J. (1958). *Heat transfer Measurement on a concave Hemispherical Nose Shape with unsteady Flow effects at mach Numbers of 1.98 and 4.5*. NACA RM-L58D25a.
- [30] Hopko, R. N., & Strauss, H. K. (1958). *Some Experimental Heating Data on Convex and Concave Hemispherical Nose Shapes and Hemispherical Depressions on a 30° Blunted Nose Cone*. NACA RM-L58A17a.
- [31] Stallings, R. S., & Burbank, P. B. (1959). *Heat-Transfer And Pressure Measurements On A Concave-Nose Cylinder For A Mach Number Range Of 2.49 To 4.44*. NASA TM X-221.
- [32] Tyner, T. W. (1959). *Some Experimental Heating Data on a 5.0-Inch-Diameter Flat Face with Hemispherical Depressions*. NASA TM X-68.
- [33] Nestler, D. E. (1981). An experimental study of cavity flow on sharp and blunt cones at Mach 8. AIAA Paper 1981-0335.
- [34] Sambamurthi, J. K., Huebner, L. D., & Utreja, L. J. (1987). Hypersonic flow over a cone with nose cavity. AIAA Paper 1987-1193.

- [35] Perng, S. W., & Dolling, D. S. (1997). Attenuation of pressure oscillations in high speed cavity flow through geometry changes. AIAA Paper 1997-1802.
- [36] Kim, J. D., & Park, S. O. (2000). Unsteady characteristics of hypersonic forward facing cavity flow. AIAA Paper 2000-3925.
- [37] Silton, S. I., & Goldstein, D. B. (2005). Use of an axial nose-tip cavity for delaying ablation onset in hypersonic flow. *Journal of Fluid Mechanics*, 528, 297–321.
- [38] Bazyma, L., & Kuleshov, V. (2007). Numerical and experimental investigation of cylinder cavity flows. *Proceedings of the Institution of Mechanical Engineers, Part G: Journal of Aerospace Engineering*, 221:253, DOI: 10.1243/09544100JAERO144.
- [39] Seiler, F., Srulijes, J., Pastor, M. G., & Mangold, P. (2007). Heat Fluxes inside a Cavity Placed at the Nose of a Projectile Measured in a Shock Tunnel at Mach 4.5. *New Results in Numerical and Experimental Fluid Mechanics, VI, NNFM 96*, 309–316.
- [40] Sravanan, S., Jagdeesh, G., & Reddy, K. P. J. (2009). Investigation of Missile Shaped Body with Forward-Facing Cavity at Mach 8. *Journal of Spacecraft and Rockets*, 46 (3), 577-591.
- [41] Lu, H., & Liu, W. (2012). Numerical Simulation in Influence of Forward-Facing Cavity on Aerodynamic Heating of Hypersonic Vehicle. *Procedia Engineering*, 29, 4096 – 4100.
- [42] Gauer, M., & Paull, A. (2008). Numerical Investigation of a Spiked Blunt Nose Cone at Hypersonic Speeds. *Journal of Spacecraft and Rockets*, 45 (3), 459-471.
- [43] Alexander, S. R. (1947). *Results of tests to determine the effect of a conical windshield on the drag of a bluff body at supersonic speeds.* NACA RM-L6K08a.
- [44] Mair, W. A. (1952). Experiments on separation of boundary layers on probes in front of blunt-nosed bodies in a supersonic air stream. *Philosophy Magazine, Series 7*, 43 (243), pp. 695–716.
- [45] Jones, J. J. (1952). *Flow separation from rods ahead of blunt noses at Mach number 2.7.* NACA RM L52E05a.

- [46] Piland, P. O., & Putland, L. W. (1954). *Zero-lift drag of several conical and blunt nose shapes obtained in free flight at Mach number of 0.7 to 1.3*. NACA RM L54A27.
- [47] Stadler, J. R., & Neilson, H. V. (1954). *Heat transfer from a hemisphere cylinder equipped with flow separation spikes*. NACA TN 3287.
- [48] Jones, J. J. (1955). *Experimental drag coefficients of round noses with conical wind shields at Mach Number 2.72*. NACA RM L55E10.
- [49] Beastall, D., & Turner, J. (1957). *The effect of a spike protruding in front of a bluff body at supersonic speeds*. Aeronautical Research Council, R. & M. No. 3007.
- [50] Hermach, C. A., Kraus, K., & Reller, J. O. (1957). *Reduction in temperature-recovery factor associated with pulsating flows generated by spike-nosed cylinders at a Mach number of 3.50*. NACA RM A56L05.
- [51] Crawford, D. H. (1959). *Investigation of the flow over a spiked-nose hemisphere cylinder*. NASA TN-D-118.
- [52] Maull, D. J. (1960). Hypersonic flow over axially symmetric spiked bodies. *Journal of Fluid Mechanics* , 8 (4), 584–592.
- [53] Wood, C. J. (1961). Hypersonic flow over spiked cones. *Journal of Fluid Mechanics* , 12 (4), 614–624.
- [54] Holden, M. (1966). Experimental studies of separated flows at hypersonic speeds. Part I—separated flows over axisymmetric spiked bodies. *AIAA Journal* , 4 (4), 591–599.
- [55] Khlebnikov, V. S. (1986). Distribution of heat flux on the surface of a sphere with a forward separation zone. *Fluid Dynamics* , 21 (4), 654–658.
- [56] McGhee, R. J., & Staylor, W. F. (1969). *Aerodynamic investigation of sharp cone-cylinder spikes on 120° blunted cones at Mach numbers of 3, 4.5, and 6*. NASA TN D- 5201.
- [57] Staylor, W. F. (1970). *Flow-field investigation for large-angle cones with short spikes at a Mach number of 9.6*. NASA TN D-5754.



- [58] Yamauchi, M., Fujii, K., & Higashino, F. (1995). Numerical investigation of supersonic flows around a spiked blunt body. *Journal of Spacecraft and Rockets* , 32 (1), 32–42.
- [59] Mehta, R. C. (2002). Numerical analysis of pressure oscillations over axi-symmetric spiked blunt bodies at Mach 6.8. *Shock Waves* , 11 (3), 431–440.
- [60] Motoyama, N., Mihara, K., Miyajima, R., Watanuki, T., & Kubota, H. (2001). Thermal protection and drag reduction with use of spike in hypersonic flow. AIAA paper 2001-1828.
- [61] Milicev, S. S., & Pavlovic, M. D. (2001). Influence of spike shape at super-sonic flow past blunt-nosed bodies: experimental study. *AIAA Journal* , 40 (5), 1018–1020.
- [62] Milicev, S. S., Pavlovic, M. D., Ristic, S., & Vitic, A. (2002). On the influence of spike shape at supersonic flow past blunt bodies. *Mechanics, Automatic Control and Robotics* , 3 (12), 371–382.
- [63] Menezes, V., Sravanan, S., & Reddy, K. P. J. (2002). Shock tunnel study of spiked aerodynamic bodies flying at hypersonic Mach numbers. *Shock Waves* , 12 (1), 197–204.
- [64] Menezes, V., Sravanan, S., Jagdeesh, G., & Reddy, K. P. (2003). Experimental investigations of hypersonic flow over highly blunted cones with aerospikes. *AIAA Journal* , 41 (10), 1955–1966.
- [65] Gopalan, J., Menezes, V., Reddy, K. P. J., Hashimoto, T., Sun, M., Saito, T., & Takayama, K. (2005). Flow Fields of a Large-Angle, Spiked Blunt Cone at Hypersonic Mach Numbers. *Trans. Japan Soc. Aero. Space Sci.* , 48 (160), pp. 110-116
- [66] Maru, Y., Kobayashi, H., Takeuchi, S., & Saito, T. (2007). Flow Oscillation Characteristics in Conical Cavity with Multiple Disks. *Journal of Spacecraft and Rockets* , 44 (5), 1012-1020.
- [67] Kobayashi, H., Maru, Y., & Fukiba, K. (2007). Experimental Study on Aerodynamic Characteristics of Telescopic Aerospikes with Multiple Disks. *Journal of Spacecraft and Rockets* , 44 (1), 33-41.

- [68] Kalimuthu, R., Mehta, R. C., & Rathakrishnan, E. (2008). Experimental investigation on spiked body in hypersonic flow. *The Aeronautical Journal* , 112 (1136), 593–598.
- [69] Kalimuthu, R., Mehta, R. C., & Rathakrishnan, E. (2010). Drag reduction for spike attached to blunt nosed body at Mach 6. *Journal of Spacecraft and Rockets* , 47 (1), 219–222.
- [70] Gauer, M., & Paull, A. (2008). Numerical investigation of a spiked blunt nose cone at hypersonic speeds. *Journal of Spacecraft and Rockets* , 45 (3), 459–471.
- [71] D'Humieres, G., & Stollery, J. L. (2010). Drag reduction on a spiked body at hypersonic speeds. *The Aeronautical Journal* , 14 (1152), 113–119.
- [72] Ahmed, M., & Qin, N. (2010). Drag reduction using aerodisks for hypersonic hemispherical bodies. *Journal of Spacecraft and Rockets* , 47 (1), 62–80.
- [73] Wang, Z., Lv, H., & Zhang, A. (2010). Numerical Analysis of Thermal Protection and Drag Reduction with Use of Spike. *IEEE 978-1-4244-6044-1/10*.
- [74] Ahmed, M. Y., & Qin, N. (2010). Metamodels for aerothermodynamic de-sign optimization of hypersonic spiked blunt bodies. *Aerospace Science and Technology* , 14, 364–376.
- [75] Gerdroodbary, M. B., & Hosseinalipour, S. M. (2010). Numerical simulation of hypersonic flow over highly blunted cones with spike. *Acta Astronautica* , 67, 180–193.
- [76] McBride, B. J., Gordon, S., & Reno, M. A. (1993). *Coefficients for calculating Thermodynamic and Transport Properties of Individual Species*. NASA-TM-4513.
- [77] Gupta, R. N., Lee, K., Thompson, R. A., & Yos, M. (1991). *Calculations and curve fits for Thermodynamic and transport properties for equilibrium air to 30000 K*. NASA Reference Publication 1260.
- [78] Wilcox, D. C. (2006). *Turbulence Modeling for CFD* (3rd ed.). La Canada, CA: DCW Industries, Inc.

- [79] Spalart, P. R., & Allmaras, S. R. (1992). A One-Equation Turbulence Model for Aerodynamic Flows. AIAA Paper 92-0439.
- [80] Spalart, P. R., & Allmaras, S. R. (1994). A One-Equation Turbulence Model for Aerodynamic Flows. *La Recherche Aerospatiale* , 1, pp. 5-12.
- [81] Menter, F. R. (1994). Two-equation eddy-viscosity turbulence models for engineering applications. *AIAA Journal* , 32 (8), 1598–1605.
- [82] Paciorni, R., Dieudonne, W., Degrez, G., Charbonnier, J. M., & Deconinck, H. (1997). Validation of the Spalart-Allmaras Turbulence Model for Application in Hypersonic Flows. AIAA Paper 97-2023.
- [83] Roy, C. J., & Blottner, F. G. (2001). Assessment of One- and Two-Equation Turbulence Models for Hypersonic Transitional Flows. *Journal of Spacecraft and Rockets* , 38 (5), 699-710.
- [84] Roy, C. J., & Blottner, F. G. (2001). Further Assessment of One- and Two-Equation Turbulence Models for Hypersonic Transitional Flows. AIAA Paper 2001-0210.
- [85] Roy, C. J., & Blottner, F. G. (2006). Review and assessment of turbulence models for hypersonic flows. *Progress in Aerospace Sciences*, 42, 469–530.
- [86] Roy, C. J., & Blottner, F. G. (2001). Review and assessment of turbulence models for hypersonic flows: 2D/ Axisymmetric Cases. AIAA Paper 2001-0210.
- [87] Anderson, J. D. (1995). *Computational Fluid Dynamics with Applications*. McGraw Hill Inc.
- [88] Hutchinson, B. R., & Raithby, G. D. (1986). A Multigrid Method Based on the Additive Correction Strategy. *Numerical Heat Transfer* , 9, 511–537.
- [89] *Theory Guide: Ansys Fluent, ver. 14.0*. (2011). Ansys Inc., USA.
- [90] Brandt, A. (1979). *Multi-level Adaptive Computations in Fluid Dynamics*. AIAA. Williamsburg, VA: Technical Report AIAA-79-1455.
- [91] Barth, T. J., & Jespersen, D. (1989). The design and application of upwind schemes on unstructured meshes. *AIAA 27th Aerospace Sciences Meeting*. Reno, Nevada: Technical Report AIAA-89-0366.

- [92] Schmidt, J. W., & Turkel, E. (1981). Numerical Solution of the Euler Equations by Finite Volume Methods Using Runge-Kutta Time-Stepping Schemes. *AIAA 14th Fluid and Plasma Dynamics Conference*. Palo Alto, California: Technical Report AIAA-81-1259.
- [93] Steger, J. L., & Warming, R. F. (1981). Flux vector splitting of the inviscid gas dynamic equations with applications to finite-difference methods. *Journal of Computational Physics* , 40, 263–293.
- [94] Roe, P. L. (1986). Characteristic-based schemes for the Euler equations. *Annual Review of Fluid Mechanics* , 18, 337–365.
- [95] Liou, M. S., & Steffen, C. J., Jr. (1993). A new flux splitting scheme. *Journal of Computational Physics* , 107 (1), 23–39.
- [96] Liou, M. S. (1996). A sequel to AUSM: AUSM+. *Journal of Computational Physics* , 129, 364–382.
- [97] Liou, M. S. (2010). The Evolution of AUSM Schemes. *Defence Science Journal* , 60 (6), 606-613.
- [98] Moradi, H. V., & Hosseinalipour, S. M. (2006). On the performance of AUSM based schemes in hypersonic with equilibrium gas effects. AIAA Paper 2006-7962.
- [99] Bertin, J. J. (1994). *Hypersonic aerothermodynamics*. Washington: AIAA Education Series, AIAA.
- [100] Park, C. (1989). A review of reaction rates in high temperature air. AIAA Paper 89-1740.
- [101] Sarma, G. S. (1995). Aerothermochemistry for hypersonic technology. *VKI Lecture series 1995-04*.
- [102] Gardiner, W. C. (1984). *Combustion Chemistry*. Springer-Verlag, Berlin.
- [103] Shinn, J. L., Moss, J. N., & Simmonds, A. L. (1982). Viscous Shock Layer Heating Analysis for the Shuttle Windward Plane Finite Recombination Rates. AIAA 82-0842.
- [104] Dunn, M. G., & Kang, S. W. (1973). *Theoretical and Experimental Studies of re-entry Plasma*. NASA CR-2232.

- [105] Park, C. (1993). Review of Chemical-Kinetic Problems of Future NASA Mission, I: Earth Entries". *Journal of Thermophysics and Heat Transfer* , 7 (3), 385-398.
- [106] Hassan, B., Kuntz, D. W., & Potter, D. L. (1998). Coupled Fluid/Thermal Prediction of Ablating Hypersonic Vehicles. AIAA Paper 98-0168.
- [107] Kurbastkii, K. A., & Montanari, F. (2007). Application of Pressure-Based Coupled Solver to the Problem of Hypersonic Missiles with Aerospikes. AIAA 2007-462.
- [108] Tannehill, J. C., & Mugge, P. H. (1974). *Improved Curve Fits for the Thermodynamic Properties of Equilibrium Air Suitable for Numerical Computation Using Time-Dependent or Shock-Capturing Methods*. NASA CR-2470.

## APPENDIX A: AXISYMMETRIC NAVIER –STOKES EQUATIONS

The axisymmetric Navier Stokes equations applicable to unsteady hypersonic flow can be written in strong conservations form as given in equation (A.1),

$$\frac{\partial \vec{W}}{\partial t} + \frac{\partial(\vec{F}_c - \vec{F}_v)}{\partial x} + \frac{\partial(\vec{G}_c - \vec{G}_v)}{\partial y} = \vec{S} \quad (\text{A.1})$$

where  $\vec{W}$  is the unknown state vector,  $\vec{F}_c$  and  $\vec{F}_v$  respectively are the inviscid and viscous flux vectors along axial direction,  $\vec{G}_c$  and  $\vec{G}_v$  respectively are the inviscid and viscous flux vectors along the radial direction and  $\vec{S}$  is the source vector. The elements of the column vectors appearing in equation (1) are given by equation (A.2).

$$\vec{W} = \begin{bmatrix} \rho \\ \rho u \\ \rho v \\ \rho E \end{bmatrix}, \quad \vec{F}_c = \begin{bmatrix} \rho u \\ \rho u^2 + p \\ \rho uv \\ (\rho E + p)u \end{bmatrix}, \quad \vec{F}_v = \begin{bmatrix} 0 \\ \tau_{xx} \\ \tau_{xy} \\ u\tau_{xx} + v\tau_{xy} - q_x \end{bmatrix}, \quad \vec{G}_c = \begin{bmatrix} \rho v \\ \rho v u \\ \rho v^2 + p \\ (\rho E + p)v \end{bmatrix},$$

$$\vec{G}_v = \begin{bmatrix} 0 \\ \tau_{yx} \\ \tau_{yy} \\ u\tau_{yx} + v\tau_{yy} - q_y \end{bmatrix} \quad \text{and} \quad \vec{S} = \frac{1}{y} \left\{ \begin{bmatrix} 0 \\ \tau_{yx} \\ \tau_{yy} - \tau_{\theta\theta} \\ u\tau_{yx} + v\tau_{yy} - q_y \end{bmatrix} - \begin{bmatrix} \rho v \\ \rho uv \\ \rho v^2 \\ (\rho E + p)v \end{bmatrix} \right\} \quad (\text{A.2})$$

The shear stresses and the heat fluxes in equation (A.2) are in turn given by equations (A.3) and (A.4) respectively,

$$\tau_{xx} = \frac{2}{3} \mu \left( 2 \frac{\partial u}{\partial x} - \frac{\partial v}{\partial y} - \frac{v}{y} \right); \quad \tau_{yy} = \frac{2}{3} \mu \left( 2 \frac{\partial v}{\partial y} - \frac{\partial u}{\partial x} - \frac{v}{y} \right);$$

$$\tau_{\theta\theta} = \frac{2}{3}\mu\left(2\frac{v}{y} - \frac{\partial u}{\partial x} - \frac{\partial v}{\partial y}\right) \quad \text{and} \quad \tau_{xy} = \mu\left(\frac{\partial u}{\partial y} + \frac{\partial v}{\partial x}\right) \quad (\text{A.3})$$

$$q_x = -k\frac{\partial T}{\partial x} \quad \text{and} \quad q_y = -k\frac{\partial T}{\partial y} \quad (\text{A.4})$$

In above equations,  $x$ ,  $y$  and  $\theta$  represents the axisymmetric coordinates with  $u$  and  $v$  are the corresponding velocity components in axial and radial directions. Additional equations required to close the above system of equations are given equation (A.5),

$$E = e + \frac{u^2 + v^2}{2}; \quad e = c_v T \quad \text{and} \quad p = \rho RT \quad (\text{A.5})$$

The molecular viscosity  $\mu$  appearing in equation (A.3) is computed using the Sutherland formula while the thermal conductivity  $k$  is derived from the kinetic theory.

## APPENDIX B: PUBLICATIONS

1. Yadav, R., & Ugur, G. (2012). Aerothermodynamics of a generic reentry vehicle with a series of aerospikes at nose. *63rd International Astronautical Congress*. Naples.
2. Yadav, R., & Ugur, G. (2012). Aerothermodynamics of hemispherical cylindrical blunt vehicle with a flow through duct. *63rd International Astronautical Congress*. Naples, Italy.
3. Yadav, R., Guven, U., Velidi, G., & Sunderraj, K. (2012). Effect of eccentricity on the heat transfer rates of a reentry vehicle with a concave windward surface. *63rd International Astronautical Congress*. Naples, Italy.
4. Yadav, R., Guven, U., & Bhat, S. (2012). Effect of Nose Cavity on the Heat Transfer Rates to the Surface of an Aeroshell Descending Through Martian Atmosphere. *63rd International Astronautical Congress*. Naples, Italy.
5. Yadav, R., Guven, U., Velidi, G., & Sunderraj, K. (2012). Effect of nose cavity on the heat fluxes to reentry vehicle in Titan's atmosphere. *63rd International Astronautical Congress*. Naples, Italy.
6. Yadav, R., & Guven, U. (2013). Aerodynamic Heating of Hypersonic Projectile with Concave Nose. *Advances in Aerospace Sciences and Applications*, 2 (2), 110-116.
7. Yadav, R., & Guven, U. (2013). Aerothermodynamics of a hypersonic projectile with a forward facing ellipsoid cavity at nose. *Advances in Aerospace Sciences and Application*, 2 (1), 39-44.



## MANUSCRIPTS UNDER PEER REVIEW

1. Rajesh Yadav and U. Guven, Aerothermodynamics of a hypersonic vehicle with double-disk aerospike at nose. *Aerospace Science and Technology (AESCTE-D-12-00407)*.
2. Rajesh Yadav and U. Guven, Aerothermodynamics Of Generic Reentry Vehicle With A Series Of Aerospikes At Nose. *Acta Astronautica, AA-D-13-00072*.
3. Rajesh Yadav and U. Guven, Aerothermodynamics of a Hypersonic Vehicle with a Forward-Facing Parabolic Cavity at Nose. *Proc. I. Mech. E., Journal of Aerospace Engineering, JAERO1839*.
4. Rajesh Yadav and U. Guven, Aerodynamic Heating of a Hypersonic Projectile with Forward Facing Ellipsoid Cavity at Nose, *Journal of Spacecrafts and Rockets, AIAA ID 2013-01-A32605*.

## APPENDIX C: FORTRAN CODE FOR COMPUTATION OF LAMINAR HEATING RATES

```
Program Laminar_Heating

Implicit None

!declaration of global variables

Real M_1, M_2                ! Mach numbers upstream and down
                               !stream of shock wave

Real pr_ratio,temp_ratio

Real p_1, p_2                !pressures

Real rho_1, rho_2, rho_w     !densities

Real T_1, T_2, T_w, T_stag   ! Temperature

Real a_1,u_1,h_2,h_w

Real r0, Q0                  !Nose radius, Stagnation point Heat flux,

Real, parameter::gama=1.4

Real, parameter :: R=287

Real, parameter :: pi=3.141593

Character yes, shape, c

Real angle,theta_c

!*****

Print*, "***** Welcome *****"

Print*

Print*, "***UNIVERSITY OF PETROLEUM AND ENERGY STUDIES ***"

Print*

Print*, "***** Author-->Rajesh Yadav *****"
```

```

Print*
Print*, "*****Under the Guidance of: Prof. U. Guven *****"
Print*
Print*, "This code computes the laminar stagnation point heat transfer rate"
Print*, "based on Fay-Riddell Correlation"
Print*, "Surface heat flux distribution is computed based on Lee's Theory"
Print*
Print*, "The code provides solution for both ideal gas and real gas in      &
      Thermo-chemical equilibrium"
Print*

500  Print*, "Please enter the freestream Conditions"
      Print*
      Print*, "Mach Number"
      Read*, M_1
      Print*

      Print*, "Static pressure in N/m2"
      Read*, p_1
      Print*
      Print*, "Static Temperature in K"
      Read*, T_1
      Print*
      Print*, "Wall Temperature in K"
      Read*, T_w

```

```

Print*

a_1=sqrt (gama*R*T_1)
u_1=M_1*a_1
rho_1=Density(p_1,T_1)
h_w=1005*T_w

Print*,"Freestream conditions"
Print*,"Pressure=",p_1
Print*,"Temperature=",T_1
Print*,"Density=",rho_1
Print*,"Mach=",M_1
Print*,"Velocity=",u_1
Print*
Print*,"Is air perfect gas?"
Print*
Print*,"Type Yes or No"
Print*

!*****

!The main program
do while (yes.ne."y".and.yes.ne."no")
    Read*, yes
    If(yes=="y".OR.yes=="Y")then
        Print*
        Print*,"Gama=1.4"
        Call perfect_gas

```

```

elseif(yes=="n".OR.yes=="N")then

Call real_gas(p_1,rho_1,T_1,u_1,p_2,rho_2,T_2,h_2)

rho_w=real_den(p_2,T_w,h_w)

print*,"Density at walls=",rho_w,"kg/m3"

Goto 100

else

print*,"Please enter either yes or no"

endif

enddo

!*****

100  Print*

Print*,"Post-shock parameters"

Print*,"Pressure=",p_2

Print*,"Temperature=",T_2

Print*,"Density=",rho_2

Print*

Print*,"Enter the nose radius in m"

Read*,r0

call Fay_Riddell(Q0,r0,p_2,p_1,T_2,T_w,rho_2,rho_w)

print*,"Stagnation Point Heat Transfer Rate,Q0=",Q0,      "W/m2"

Print*

Print*,"Is your blunt body spherical or blunt cone?"

Print*

Print*,"Press s for spherical and c for cone"

```

```

Read*, shape
If(shape=="S".or.shape=="s")then
Call Lee_sphere
elseif(shape=="C".or.shape=="c")then
Print*, "Please enter semivertex angle in degrees"
Print*
Read*, angle
theta_c=angle*pi/180
call Lee_cone
else
Print*, "Wrong choice"
endif
Print*, "Do you want to continue with new model?"
Read*, c
If(c=="y")then
Goto 500
Endif

```

! The main program ends here

!\*\*\*\*\*

CONTAINS

! Calculation of post shock parameters

Subroutine perfect\_gas

! This subroutine calculates the post shock pressure, density, mach number and temperature for perfect gas case

$$M_2 = \sqrt{\frac{1 + ((\gamma - 1)/2) * M_1^{**2}}{\gamma * M_1^{**2} - (\gamma - 1)/2}}$$

```

pr_ratio=1+2*gama*(M_1**2-1)/(gama+1)

temp_ratio=pr_ratio*(2+(gama-1)*M_1**2)/((gama+1)*M_1**2)

p_2=pr_ratio*p_1

T_2=temp_ratio*T_1

rho_2= Density(p_2,T_2)

T_stag=T_1*(1+((gama-1)/2)*M_1**2)

rho_w= Density(p_2,T_w)

Print*,"Post shock Mach No=",M_2

Print*,"Density at wall=",rho_w

End Subroutine perfect_gas

!*****

Subroutine Fay_Riddell(Q,rad,p_e,p1,t_e,t_w,ro_e,ro_w)

! This subroutine calculates the stagnation point heat transfer rates for given
spherical nose using Fay-Riddell Correlation for laminar flows

!

!  $\dot{q}_0 = \frac{0.763}{Pr_w^{0.6}} (\rho_e \mu_e)^{0.4} (\rho_w \mu_w)^{0.1} \sqrt{\frac{du_e}{dx}} (h_{0e} - h_w) \left[ 1 + (Le^{0.52} - 1) \left( \frac{h_D}{h_{0e}} \right) \right]$ 

! Le=1 has been assumed

!Variable declaration for Fay-Riddell Correlation

Real,intent(OUT):: Q

Real vel_grad

Real,intent(IN):: rad,p_e,p1,ro_e,ro_w,t_e,t_w

Real, parameter::Pr=0.71

Real mu_e, mu_w

Real, parameter::cp=1005      !specific heat for freestream air

```

```

mu_e=Sutherland(t_e)
mu_w=Sutherland(t_w)
vel_grad=(1/rad)*sqrt(2*(p_e-p1)/ro_e)
      Q= (0.763/Pr**0.6)*((ro_e*mu_e)**0.4)*((ro_w*mu_w)**0.1)  &
      *cp*(t_e-t_w)*sqrt(vel_grad)
end subroutine      Fay_Riddell

!*****

Function Sutherland(T)
! This function calculates the viscosity for given temperature based on
! Sutherland Formula. The reference viscosity at 288.16 K is taken to be
! 1.7895 x 10-5
! This function is called by Subroutine Fay_Riddell
Real T ,Sutherland
      Sutherland=0.000017894*((T/288.16)**1.5)*((288.16+110)/(T+110))
End Function Sutherland

!*****

Function Density(p,T)
! This function calculates the density using equation of state for perfect gas.
! This is called by subroutine Perfect_gas
Real Density, p, T
      Density=p/(R*T)
End Function Density

!*****

Subroutine Lee_sphere

```



!\*\*\*\*\*

! This subroutine calculates the surface heat flux distribution for the hemi  
!spherical nose using formula given by Lester Lees

$$\dot{q}_w = \frac{\left(\frac{1}{2}\right)\left(\frac{p_w}{p_s}\right)\left(\frac{u_e}{u_\infty}\right)\left(\frac{r}{r_0}\right)}{\left[\int_0^{\xi} \left(\frac{p_w}{p_s}\right)\left(\frac{u_e}{u_\infty}\right)\left(\frac{r}{r_0}\right)^2 d\xi\right]^{1/2}} \left[\frac{u_\infty^2 \rho_s}{2(p_s - p_\infty)}\right]^{1/4}$$

!\*\*\*\*\*

Real theta(51), d\_theta

Real D(51)

Real q\_ratio(51)

integer i

d\_theta=pi/100

open (1,file="lee.dat")

write (1,10)

10 Format (T4,'curve length',T20,'qw/q0')

do i=1,51

theta(i)=0.0+(i-1)\*d\_theta

D(i)=(1-1/(gama\*M\_1\*\*2))\*(theta(i)\*\*2-theta(i)\*sin(4\*theta(i))/2 &  
+ (1-cos(4\*theta(i)))/8)+(4/(gama\*M\_1\*\*2)) &  
\*(theta(i)\*\*2-theta(i)\*sin(2\*theta(i))+(1-cos(2\*theta(i)))/2)

if(i==1)then

q\_ratio(i)=1.0

```

else
q_ratio(i)=(1/sqrt(D(i)))**2*theta(i)*sin(theta(i))*      &
((1/(gama*M_1**2))*(cos(theta(i)))**2+(1/(gama*M_1**2)))
endif

write(1,*)theta(i)*r0, q_ratio(i)*Q0
Print*, "Curve length", "Surface heatFlux"
Print*, theta(i), q_ratio(i)*Q0
enddo

Print*, "The surface heat flux distribution has been written to file &
lee.dat"

Print*, "The file can be plotted with Tecplot/Matlab/Excel"

End subroutine Lee_sphere

!*****
Subroutine Lee_cone
! This subroutine calculates the surface heat flux distribution for the conical
! portion of a sphere-cone using Lee's theory
Real A, B, D
Real q_ratio(51), s_tip (51), s(51), Rb, del_s
integer j
Print*, "Please enter the base radius"
Print*
Read*, Rb

del_s=(Rb/sin(theta_c)-r0/tan(theta_c))/50

```

```

D=(1-1/(gama*M_1**2))*((pi/2-theta_c)**2-(pi/2-theta_c)      &
*sin(4*(pi/2-theta_c))/2 +(1-cos(4*(pi/2-theta_c)))/8)      &
+(4/(gama*M_1**2))*((pi/2-theta_c)**2-(pi/2-theta_c)*      &
sin(2*(pi/2-theta_c)+(1-cos(2*(pi/2-theta_c)))/2)

A=0.866*sqrt((1-1/(gama*M_1**2))*(sin(theta_c))**2           &
+1/(gama*M_1**2))*sqrt(pi/2-theta_c)

B=0.1876/(((sin(theta_c))**2)*((1-1/(gama*M_1**2))*         &
((sin(theta_c))**2)+1/(gama*M_1**2)))*D-((1/tan(theta_c))**3)

open(1,file="blunt_cone.dat")
write(1,20)
20  Format(T4,'curve length',T20,'qc/q0')

do j=1,51
s_tip(j)=r0/(tan(theta_c))+(j-1)*del_s
s(j)=(pi/2-theta_c)*r0+(j-1)*del_s
q_ratio(j)=A*(s_tip(j)/r0)/sqrt(B+(s_tip(j)/r0)**3)
write(1,*)s(j), q_ratio(j)*Q0
print*,s(j),q_ratio(j)*Q0
print*
enddo

Print*,"The surface heat flux distribution has been written to file &

```

```

blunt_cone.dat"

Print*, "The file can be plotted with Tecplot/Matlab/Excel"

End subroutine Lee_cone

!*****

Subroutine real_gas(p1,rho1,t1,u1,p2,rho2,t2,h2)

! This subroutine calculates the post shock parameters for real gas in Thermo
chemical equilibrium by iterative solution of one dimensional Euler equations

! Declaration of variables

Real,intent(IN):: p1,rho1,t1,u1

Real,intent(OUT):: p2,rho2,h2,t2

Real u2,h1

integer i

      h1=1005*t1

Print*, "Please guess post shock velocity for iterative calculation of post shock
properties"

Print*

Print*, "Enter any subsonic value 10-100 m/s"

Read*,u2

      rho2=rho1*u1/u2

!*****

      do i=1,50      !Sufficient iteration for convergence for all conditions

      h2=h1+0.5*u1**2*(1-(rho1/rho2)**2)

      p2=p1+(rho1*u1**2)*(1-rho1/rho2)

      rho2= real_den(p2,rho2,h2)

      enddo

      t2=temp(rho2,p2)      !

```

$$u2=rho1*u1/rho2$$

end subroutine real\_gas

!\*\*\*\*\*

function real\_den(p,rho2,h)

! This function calculates the density of a real gas for given values of pressure  
! and enthalpy based on polynomial correlation by Tanehill and Munge

Real,intent(IN)::p

Real real\_den,rho2

Real,intent(IN)::h

Real gbar,x,y,z

Real c1,c2,c3,c4,c5,c6,c7,c8,c9,c10,c11

y=log(rho2/1.225)

x=log(p/101325)

z=x-y

If(y>-0.5.AND.z<=0.3)then

c1=1.4

c2=0

c3=0

c4=0

c5=0

c6=0

c7=0

c8=0

c9=0

c10=0

c11=0

elseif(y>-0.5.AND.z>0.3.AND.z<=1.15)then

c1=1.42598

c2=0.000918

c3=-0.092209

c4=-0.002226

c5=0.019772

c6=-0.036600

c7=-0.0077469

c8=0.043878

c9=-15.0

c10=-1.0

c11=-1.04

elseif(y>-0.5.AND.z>1.15.AND.z<=1.6)then

c1=1.64689

c2=-0.062133

c3=-0.334994

c4=0.063612

c5=-0.038332

c6=-0.014468

c7=0.073421

c8=-0.002422

c9=-15.0

```
c10=-1.0  
c11=-1.360  
elseif(y>-0.5.AND.z>1.6)then
```

```
c1=1.48558  
c2=-0.453562  
c3=-0.152096  
c4=0.303350  
c5=-0.459282  
c6=0.448395  
c7=0.220546  
c8=-0.292293  
c9=-10.0  
c10=-1.0  
c11=-1.60
```

```
elseif(y>-4.5.AND.y<=-0.5.AND.z<=0.3)then
```

```
c1=1.4  
c2=0  
c3=0  
c4=0  
c5=0  
c6=0  
c7=0  
c8=0  
c9=0
```

c10=0

c11=0

elseif(y>-4.5.AND.y<=-0.5.AND.z>0.3.AND.z<=0.98)then

c1=1.42176

c2=-0.000366

c3=-0.083614

c4=0.000675

c5=0.005272

c6=-0.115853

c7=-0.007363

c8=0.146179

c9=-20.0

c10=-1.0

c11=-0.860

elseif(y>-4.5.AND.y<=-0.5.AND.z>0.98.AND.z<=1.38)then

c1=1.74436

c2=-0.035354

c3=-0.415045

c4=0.061921

c5=0.018536

c6=0.043582

c7=0.044353

c8=-0.049750



c9=-20.0

c10=-1.04

c11=-1.336

elseif(y>-4.5.AND.y<=-0.5.AND.z>1.38.AND.z<=2.04)then

c1=1.49674

c2=-0.021583

c3=-0.197008

c4=0.030886

c5=-0.157738

c6=-0.009158

c7=0.123213

c8=-0.006553

c9=-10.0

c10=-1.05

c11=-1.895

elseif(y>-4.5.AND.y<=-0.5.AND.z>2.04)then

c1=1.10421

c2=-0.033664

c3=0.031768

c4=0.024335

c5=-0.178802

c6=-0.017456

c7=0.080373

c8=0.002511

c9=-15.0

c10=-1.08

c11=-2.65

elseif(y>-7.AND.y<=-4.5.AND.z<=0.398)then

c1=1.4

c2=0

c3=0

c4=0

c5=0

c6=0

c7=0

c8=0

c9=0

c10=0

c11=0

elseif(y>-7.AND.y<=-4.5.AND.z>0.398.AND.z<=0.87)then

c1=1.47003

c2=007939

c3=-0.244205

c4=-0.025607

c5=0.872248

c6=0.049452

c7=-0.764158

c8=0.000147

c9=-20.0

c10=-1.0

c11=-0.742

elseif(y>-7.AND.y<=-4.5.AND.z>0.87.AND.z<=1.27)then

c1=3.18652

c2=0.137930

c3=-1.89529

c4=-0.103490

c5=-2.14572

c6=-0.272717

c7=2.06586

c8=0.223046

c9=-15.0

c10=-1.0

c11=-1.041

elseif(y>-7.AND.y<=-4.5.AND.z>1.27.AND.z<=1.863)then

c1=1.63963

c2=-0.001004

c3=-0.303549

c4=0.0016464

c5=-0.852169

c6=-0.101237

c7=0.503123

c8=0.04358

c9=-10.0

c10=-1.0

c11=-1.544

else

c1=1.55889

c2=0.055932

c3=-0.211764

c4=-0.023548

c5=-0.549041

c6=-0.101758

c7=0.276732

c8=0.046031

c9=-15.0

c10=-1.0

c11=-2.250

endif

$$\text{gbar} = c1 + c2*y + c3*z + c4*y*z + (c5 + c6*y + c7*z + c8*y*z) /$$

&

$$(1 + \exp(c9*(x + c10*y + c11)))$$

```
real_den=(p/h)*(gbar/(gbar-1))
```

```
end function real_den
```

```
!*****
```

```
function temp(den,pr)
```

```
!This function calculates the temperature for a real gas for supplied values of  
!density and pressure using the polynomial correlation by Tanehill and Munge
```

```
Real,intent(IN)::pr
```

```
Real,intent(IN)::den
```

```
Real temp
```

```
Real d1,d2,d3,d4,d5,d6,d7,d8,d9,d10,d11,d12
```

```
Real x,y,z
```

```
    y=log(den/1.225)
```

```
    x=log(pr/101325)
```

```
    z=x-y
```

```
!Shorting of coefficients of polynomial
```

```
If(y>-0.5.AND.Z>0.48.AND.Z<=0.9)then
```

```
    d1=0.27407
```

```
    d2=0
```

```
    d3=1.00082
```

```
    d4=0
```

```
    d5=0
```

```
    d6=0
```

```
    d7=0
```

d8=0  
d9=0  
d10=0  
d11=0  
d12=0

elseif(y>-0.5.AND.Z>0.9)then

d1=0.235869  
d2=-0.043304  
d3=1.17619  
d4=0.046498  
d5=-0.143721  
d6=-1.37670  
d7=0.160465  
d8=1.08988  
d9=-0.083489  
d10=-0.217748  
d11=-10.0  
d12=-1.78

elseif(y>-4.5.AND.y<=-0.5.AND.Z>0.48.AND.Z<=0.9165)then

d1=0.281611  
d2=0.001267  
d3=0.990406  
d4=0

d5=0

d6=0

d7=0

d8=0

d9=0

d10=0

d11=0

d12=0

elseif(y>-4.5.AND.y<=-0.5.AND.Z>0.9165.AND.Z<=1.478)then

d1=0.457643

d2=-0.034272

d3=0.819119

d4=0.0046471

d5=0

d6=-0.073233

d7=-0.169816

d8=0.043264

d9=0.111854

d10=0

d11=-15.0

d12=-1.28

elseif(y>-4.5.AND.y<=-0.5.AND.Z>1.478.AND.Z<=2.176)then

d1=1.04172

d2=0.041961

d3=0.412752

d4=-0.009329

d5=0

d6=-0.434074

d7=-0.196914

d8=0.264883

d9=0.100599

d10=0

d11=-15.0

d12=-1.778

elseif(y>-4.5.AND.y<=-0.5.AND.Z>2.176)then

d1=0.418298

d2=-0.252100

d3=0.784048

d4=0.144576

d5=0

d6= -0.20015

d7=-0.639022

d8=0.716053

d9=0.206475

d10=0

d11=-10.0

d12=-2.4



elseif(y>-7.AND.y<=-4.5.AND.Z>0.30.AND.Z<=1.07)then

d1=2.72964

d2=0.003725

d3=0.938851

d4=-0.01192

d5=0

d6=0.682406

d7=0.089153

d8=-0.646541

d9=-0.070769

d10=0

d11=-20.0

d12=-0.82

elseif(y>-7.AND.y<=-4.5.AND.Z>1.07.AND.Z<=1.57)then

d1=2.50246

d2=-0.042827

d3=1.12924

d4=0.041517

d5=0

d6=1.72067

d7=0.268008

d8=-1.25038

d9=-0.179711

d10=0

d11=-20.0

d12=-1.33

elseif(y>-7.AND.y<=-4.5.AND.Z>1.57.AND.Z<=2.24)then

d1=2.44531

d2=-0.047722

d3=1.00488

d4=0.034349

d5=0

d6=1.95893

d7=0.316244

d8=-1.01200

d9=-0.151561

d10=0

d11=-20.0

d12=-1.88

else

d1=2.50342

d2=0.026825

d3=0.838860

d4=-0.009819

d5=0

d6=3.58284

```

d7=0.533853
d8=-1.36147
d9=-0.195436
d10=0
d11=-20.0
d12=-2.47
endif

temp=288.16*exp((d1+d2*y+d3*z+d4*y*z+d5*z**2)+(d6+d7*y      &
+d8*z+d9*y*z+d10*z**2)/(1+exp(d11*(z+d12))))
end function temp

!*****

End program Laminar_Heating

```

## **CURRICULAM VITAE**

The author graduated from the Aeronautical Society of India in 2005, with a specialization in Aerodynamics. He joined the University of Petroleum and Energy Studies as Sr. Technical Assistant in 2006 and currently serving as Lab Superintendent in Aerospace Laboratories of the University. He concurrently continued his education and received Master degree in Information Technology from KSOU with specialization in Modeling and Simulation. The author is a graduate member of the Aeronautical Society of India and has qualified GATE three times with All India Ranks of 8, 19 and 12 in the years 2006, 2007 and 2009 respectively.